UNIVERSITAT POLITÈCNICA DE VALÈNCIA

DEPARTAMENTO DE COMUNICACIONES

PhD Dissertation

Reconfigurable Devices using Liquid Crystal at Microwave Frequencies in Substrate Integrated Waveguide

Juan Rafael Sánchez Marín

Supervisors
Dr. Carmen Bachiller Martín
Dr. Vicente E. Boria Esbert

Thesis submitted to the Departamento de Comunicaciones,
in partial fulfillment of the requirements for:
Título de Doctor por la Universitat Politècnica de València
Valencia, September 2019

“Toma una dirección apasionada
y nadie podrá contigo.
Y sobre todo recuerda que,
si aprendes a caerte,
aprenderás a levantarte,
y si aprendes a morir,
aprenderás a vivir."

La Dama de 94 años
Finales que merecen una historia
Albert Espinosa

A mi María,
y a mi hermano,
que siempre camina conmigo.

Acknowledgement

Es difícil creer que haya llegado este momento, el fin de mi etapa de investigación predoctoral. Echando la vista atrás solo puedo recordar que esta etapa comenzó en el momento más duro de mi vida. La alegría de conseguir un contrato FPU se vio truncada en un minuto. Por eso, aquí quiero agradecer a todas las personas que me han dado fuerzas para seguir luchando y llegar a donde estoy.

En primer lugar, a Carmen por su apoyo incondicional y por guiarme en el mundo de la investigación y muchas veces en el personal. Con ella la investigación siempre ha sido más fácil y los momentos duros más llevaderos. Sin ti esto no hubiera sido posible. A Vicente por acogerme en el GAM y darme la oportunidad de adentrarme en el mundo de la investigación.

A mis compañeros del GAM que hacen que los días de trabajo sean más llevaderos. Sobre todo, quiero agradecer a Vicente Nova su gran disposición a trabajar, su apoyo en los momentos buenos y en los de bajón ya que, a pesar de su pesimismo perpetuo, siempre está con ganas de ayudar.

A mi familia y amigos que en la distancia siempre me han apoyado y me han dado fuerzas para seguir, aunque a veces no entendieran bien a qué he dedicado mi tiempo estos años. A mi ángel de la guarda, que nunca olvido y siempre está conmigo, y allá donde estés te haré sentir orgulloso.

Por último, a María, mi compañera de viaje, que es el pilar fundamental de mi vida, ya que sin ella no habría tenido la fuerza suficiente para emprender este camino.

Resumen

La cantidad de servicios de telecomunicación se ha incrementado signiticativamente en las últimas décadas. El uso de teléfonos inteligentes, así como el Internet de las Cosas, está generando una saturación del espectro electromágnetico. Por tanto, los requisitos de los sistemas de microondas han cambiado para adaptarse a estos nuevos avances.

Para satisfacer estas necesidades, se busca el desarrollo de dispositivos de bajo coste, volumen, peso y consumo. Además, interesa que sean espectralmente eficientes y fácilmente integrables con otros dispositivos. Entre todos los dispostivos de microondas, los filtros son elementos clave dentro de los sistemas de comunicaciones móviles e inalámbricas. Es por ello que el diseño de filtros que cumplan con los requisitos mencionados se ha convertido en un tema de gran interés. Para dar respuesta a este problema ha surgido la tecnología de Guía de Onda Integrada en Sustrato (*Substrate Integrated Waveguide (SIW)*), que permite la implementación de filtros con un reducido tamaño y fácilmente integrables con otros dispositivos en tecnología planar. Dicha tecnología presenta unas prestaciones en cuanto a manejo de potencia y pérdidas mejores que la tecnología de circuito impreso (*Printed Circuit Board (PCB)*), aunque no llegan a ser iguales que las de la guía de onda clásica.

Por otro lado, la saturación espectral también lleva al estudio de filtros con respuestas variables en frecuencia, es decir, que puedan cambiar su frecuencia central y ancho de banda con el fin de adaptarse a las necesidades del sistema.

Por ello, el objetivo general de esta Tesis es el análisis y diseño de nuevos filtros reconfigurables en tecnología integrada. El trabajo empieza con el estudio de los fundamentos de los filtros de microondas hasta llegar al diseño de resonadores reconfigurables en tecnología *SIW* usando el cristal líquido como material de reconfiguración.

En primer lugar, se ha estudiado la influencia que los cambios en el valor de la permitividad dieléctrica en el interior de las estructuras filtrantes pueden tener en la respuesta de las mismos. En particular, se desarrollan filtros alternando secciones de línea con y sin dieléctrico dentro de una *SIW* vacía, *Empty Substrate Integrated Waveguide (ESIW)*.

Una vez hecho esto, se procede al estudio de materiales que tengan un valor de permitividad dieléctrica variable de alguna forma. En concreto, se ha realizado la caracterización de

diferentes mezclas de cristal líquido a la frecuencia de microondas. Dicho material cambia su valor de permitividad cuando se le aplica un campo eléctrico o magnético.

Dado que para la reconfiguración de la respuesta de los filtros se requiere de una estructura desacoplada en baja frecuencia, es decir, con más de un conductor, se ha desarrollado una estrategia para el desacoplo de la estructuras *ESIW*, la tecnología *Decoupled Empty Substrate Integrated Waveguide (DESIW)*.

Por último, se han diseñado resonadores en dicha tecnología *DESIW*, que se han llenado de cristal líquido y aplicado unos campos de polarización, consiguiendo variar su respuesta en frecuencia. Dichos resonadores constituyen el elemento básico para el desarrollo de filtros de microondas. Es por ello que el conocimiento obtenido en la Tesis es una buena base para futuros trabajos esta tecnología que permitan conseguir filtros de altas prestaciones.

Resum

La quantitat de serveis de telecomunicació s'ha incrementat significativament en les últimes dècades. L'ús de telèfons intel·ligents, així com la internet de les coses, està generant una saturació de l'espectre electromagnètic. Per tant, els requisits dels sistemes de microones han canviat per a adaptar-se a aquests nous avanços.

Per a satisfer aquestes necessitats, se cerca el desenvolupament de dispositius de baix cost, volum, pes i consum. A més, interessa que siguen espectralment eficients i fàcilment integrables amb altres dispositius. Entre tots els dispositius de microones, els filtres són elements clau dins dels sistemes de comunicacions mòbils i sense fil. És per això que el disseny de filtres que complisquen els requisits esmentats s'ha convertit en un tema de gran interès. Per a donar resposta a aquest problema ha sorgit la tecnologia de Guia d'Ona Integrada en Substrat (*Substrate Integrated Waveguide (SIW)*), que permet la implementació de filtres amb una reduïda grandària i fàcilment integrables amb altres dispositius en tecnologia planar. Aquesta tecnologia presenta unes prestacions quant a maneig de potència i pèrdues millors que la tecnologia de circuit imprès (*Printed Circuit Board (PCB)*), encara que no arriben a ser iguals que les de la guia d'ona clàssica.

D'altra banda, la saturació espectral també porta a l'estudi de filtres amb respostes variables en freqüència, és a dir, que puguen canviar la seua freqüència central i l'amplada de banda amb la finalitat d'adaptar-se a les necessitats del sistema.

Per això, l'objectiu general d'aquesta tesi és l'anàlisi i el disseny de nous filtres reconfigurables en tecnologia integrada. El treball comença amb l'estudi dels fonaments dels filtres de microones, fins a arribar al disseny de ressonadors reconfigurables en tecnologia *SIW* usant el cristall líquid com a material de reconfiguració.

En primer lloc, s'ha estudiat la influència que els canvis en el valor de la permitivitat dielèctrica a l'interior de les estructures filtrants poden tenir en la resposta d'aquestes. En particular, es desenvolupen filtres que alternen seccions de línia amb dielèctric i sense dins d'una *SIW* buida, *Empty Substrate Integrated Waveguide (ESIW)*.

Una vegada fet això, es procedeix a l'estudi de materials que tinguen un valor de permitivitat dielèctrica variable d'alguna forma. En concret, s'ha realitzat la caracterització de

diferents mescles de cristall líquid a la freqüència de microones. Aquest material canvia el seu valor de permitivitat quan se li aplica un camp elèctric o magnètic.

Atès que per a la reconfiguració de la resposta dels filtres es requereix una estructura desacoblada en baixa freqüència, és a dir, amb més d'un conductor, s'ha desenvolupat una estratègia per al desacoblament d'estructures *ESIW*, la tecnologia *Decoupled Empty Substrate Integrated Waveguide (DESIW)*.

Finalment, s'han dissenyat ressonadors en aquesta tecnologia *DESIW*, que s'han omplit de cristall líquid i aplicat uns camps de polarització, i s'ha aconseguit variar la seua resposta en freqüència. Aquests ressonadors constitueixen l'element bàsic per al desenvolupament de filtres de microones. És per això que el coneixement obtingut en la tesi és una bona base per a futurs treballs d'aquesta tecnologia que permeten aconseguir filtres d'altes prestacions.

Abstract

The number of telecommunication services has increased significantly in recent decades. The use of smartphones, as well as the Internet of Things, is generating a saturation of the electromagnetic spectrum. Therefore, the requirements of microwave systems have changed to adapt to these new developments and related challenges.

For achieving these needs, the development of devices with low cost, volume, weight and power consumption is sought. In addition, it interests to be spectrally efficient, to offer high performance, and to be easily integrated with other devices. Among all microwave devices, filters are key elements within mobile and wireless communication systems. In this context, the design of filters that meet the aforementioned requirements has become a topic of great interest. For solving this problem, Substrate Integrated Waveguide (SIW) technology has emerged, which allows the implementation of filters with a small size and to be easily integrated with other devices in planar technology. This technology has better power handling and loss performance than Printed Circuit Board (PCB) technology, although they do not have the performance of the classic waveguide counterpart.

On the other hand, the spectral saturation also leads to the study of filters with tunable frequency response, that is, they can change their central frequency and bandwidth, in order to fulfil the changing system requirements.

Therefore, the general objective of this PhD Thesis work is the analysis and design of new reconfigurable filters in integrated technology. The work begins with the study of the basics of microwave filters until the design of reconfigurable resonators in SIW technology, using Liquid Crystal (LC) as reconfiguration material.

Firstly, the influence that the change of the dielectric permittivity value inside the filtering structures have on the frequency response has been studied. Particularly, filters have been obtained by alternating line sections with and without dielectric material inside an empty SIW (Empty Substrate Integrated Waveguide (ESIW)).

Once this is done, it is proceed to the study of materials that have a variable dielectric permittivity value. Specifically, the characterization of different LC mixtures at microwave frequencies has been carried out. This material changes its permittivity value when an electric

or magnetic bias field is applied.

A low-frequency decoupled structure is required for the reconfiguration of filters, that is, structures with more than one conductor. For that, a strategy for decoupling ESIW structures has been developed, i.e, the Decoupled Empty Substrate Integrated Waveguide (DESIW) technology.

Finally, some resonators have been designed in DESIW technology, which have been filled with LC. The use of LC allows to tune their frequency response. These resonators are basic elements for the development of microwave filters. So that, the knowledge obtained in this Thesis work is a good basis for future works in this technology that allow for achieving high performance filters.

Index

List of Figures

List of Tables

Acronyms

AC Alternating Current.

ADLS Alternating Dielectric Line Sections.

AFM Atomic Force Microscopy.

CAD Computer Aided Design.

CSIW Corrugated Substrate Integrated Waveguide.

DC Direct Current.

DESIW Decoupled Empty Substrate Integrated Waveguide.

ESICL Empty Substrate Integrated Coaxial Line.

ESIW Empty Substrate Integrated Waveguide.

FDTD Finite-Difference Time-Domain.

FEM Finite Elements Method.

FSS Frequency Selective Surface.

GAM Generalized Admittance Matrix.

GGW Groove Gap Waveguide.

IL Insertion Loss.

LC Liquid Crystal.

PCB Printed Circuit Board.

PEC Perfect Electric Conductor.

PMC Perfect Magnetic Conductor.

RF Radio Frequency.

SIC Substrate Integrated Circuit.

SIW Substrate Integrated Waveguide.

VNA Vector Network Analyzer.

Chapter 1

Introduction

1.1 Motivation

Traditionally, the passive microwave devices of communication systems have been developed either in waveguide or in planar technology. Each technology has some advantages and disadvantages. However, in modern communication systems, there is a remarkable demand for high performance, multi-functional, low cost and compact devices. In this context, filters have a high impact on the system performance, cost and compactness. The movement to integrable microwave devices, (with the involved size reduction, low manufacturing cost, high reliability and low power consumption) has started a long-distance race in the development of devices based on Substrate Integrated Waveguide (SIW) [2]. This is a rectangular waveguide synthesized in a planar substrate with linear arrays of metallized via holes. The features of this technology are between those of planar (microstrip or stripline) and non-planar structures (metallic waveguides), making it a perfect candidate for the development of all sort of microwave devices.

Traditionally, these devices are designed and work properly for a certain frequency band. Nevertheless, among the growing demand of communications systems, the reconfiguration of these devices is an important trend in the microwave world. There is a huge demand on the possibility of changing the electromagnetic response according to the system requirements. This is a travel initiated many years ago, but its implementation is not easy. Regarding the system performance, reconfigurability of RF devices is a key issue, since it enables adapting the electromagnetic characteristics to the changing environment and evolving requirements. Different solutions can be applied to achieve the reconfiguration.

This Thesis arises from the need of developing methods for the reconfiguration of microwave filters on SIW technology, in order to have more tunability together with better

frequency response, compactness, and integration with other components. The development core is the analysis of the influence of the dielectric permittivity value in the features of those SIW filters, and the study of the reconfiguration when the dielectric properties change dynamically, as in the case of Liquid Crystal (LC) [3]. Furthermore, the Thesis presents a significant contribution in the design of reconfigurable microwave devices: the characterization of LC mixtures and its use for tuning filtering structures.

1.2 State of the Art

Microwave filters are essential components in any high frequency telecommunications system, they are present in both transmitter and receiver subsystems. Their basic function is to remove unwanted frequency components of an RF signal, and to let the transmission of the desired ones.

The use of SIW technology has become common in many high frequency applications [2]. The SIW technology has appeared in response to the emerging problem of integration of planar and non-planar circuits for high-frequency applications, since it allows the integration of waveguides on the same dielectric substrate used for the synthesis of planar transmission lines and circuits [4]. The advantage of this scheme is clear: the whole circuit (planar circuits, transitions and waveguides) can be implemented by standard PCB manufacturing techniques.

Although its performance is better in terms of quality factor than other planar circuits, SIW is not yet comparable with waveguide technology. In order to approach to the quality factor of the waveguide, different lines of work are being established to remove the dielectric substrate that provides significant loss. One of these strategies is based on the new Empty-SIW (ESIW) transmission line [5], consisting of emptying, metallizing, and covering a planar substrate with top and bottom conductor covers. The structure is completed with a specific broadband transition from a microstrip line.

The need for reconfigurable devices has also led to different strategies. Many of them include the possibility of introducing a DC bias voltage in the device, acting on additional elements capable of modifying their response [6]. For instance, the use of discrete electronic components (PIN Diodes [7–9], Varactor Diodes [10–12], MEMS Switches [13–15], etc.) is typically accomplished, since they are small enough to be integrated and can be designed for several applications. Another method of frequency tuning is the use of tunable materials [16–19]. They are materials whose electrical properties (permittivity, permeability, or conductivity) can be controlled by the application of an external bias field (either electric or magnetic).

In most cases, this involves that the structure must be composed by more than one sin-

gle conductor. This is not the case of a waveguide structure, which is completely closed with a single conductor. The decoupling of waveguides has been tried in several ways. The Corrugated-SIW [20] is a simple decoupled structure which provides similar results to the standard SIW in terms of insertion loss, because both are supported on a dielectric substrate. The Groove Gap Waveguide (GGW) [21] is also a promising structure, but its manufacturing process and integration with planar substrates may be more complex.

LC is a material whose permittivity can be controlled by the application of a bias electromagnetic field. It constitutes a state of matter between solids and liquids. It has a certain degree of order like solids and flows like liquids. These facts provide LC its particular properties: it has a very high anisotropy (electric, optical, magnetic) being a flowing material. LC mixtures are known for more than 120 years, but their practical application (mainly in the optic field) has been found in the last 30 or 40 years [22]. They currently dominate the market of flat screens and hence their economic importance is great. Nevertheless, their applications at microwave frequencies is very recent [23].

Throughout the last 30 years a great variety of LC displays have been developed with one thing in common: they all change their optical response by applying an electric field. In the same mode, LC can be applied at microwave frequencies for developing RF devices, modifying their frequency response with the presence of an external electric or magnetic field [24]. The process is achieved by the change of the dielectric properties of the LC, caused by the variation of the macroscopic organization of its molecules. Strictly speaking, LC responds at the molecular level, but not as an electronic component. Since it is a flowing material, LC requires a closed container. So that, the use LC for reconfiguration in microwave devices is limited to closed structures.

1.3 Objective of the thesis and working plan

The final objective of this PhD Thesis is the development of microwave reconfigurable filters in Substrate Integrated Waveguide using Liquid Crystal. This topic has been chosen since it presents two novel aspects that are of great practical application: on the one hand, the filters based on SIW are smaller and lighter, and easily integrable with other planar structures, but with better features. On the other hand, the reconfiguration using LC, which so far has not been widely used at microwave frequencies, allows to have a continuous tunable filter, obtaining the frequency response of several fixed-response filters in only one device. The strategy consists of decoupling an ESIW device and filling it with LC. Then, a low frequency electric field is applied to change the dielectric permittivity of the LC molecules and consequently, change the frequency response of the filter.

In order to achieve the goal of this thesis, the next work planning is followed:

- **Study of the background technology.** A comprehensive task of bibliography search is carried out, which helps to establish the need and relevance of the work to be performed. Specifically, a study of some different types of filters used in high frequency communications is developed: including classical rectangular waveguide technology, planar filters, and Substrate Integrated Circuit (SIC) technology. A literature review about all of them is performed in order to know the possibilities to make a reconfigurable filter. The use of Liquid Crystal and its properties is further investigated, since one of the aims of this thesis is the analysis and design of filters filled with this material.

  Moreover, a research about methods of material characterization is completed in order to select the best for characterizing LC mixtures.

- **Analysis of filters filled with a dielectric material by sections.** Before designing a filter with LC, it is needed to know how the partial presence of a dielectric material inside of an Empty Substrate Integrated Waveguide affects the frequency response. In this case, filters based on directly coupled resonant sections are implemented, where resonant sections are obtained with dielectric filled line sections and the coupling between them is obtained with empty line sections. A filter is obtained that consists of alternating line sections with and without dielectric material. For the analysis and design of this type of filters the following activities are proposed:

  - Development of a modal analysis tool based on forcing continuity of electromagnetic fields in the discontinuity between the dielectric material and the air.
  - Use of the developed analysis tool in the automated design of filters with alternating dielectric sections.
  - Integration of the tool with the well known optimization algorithms (as genetic algorithms [25] or the Simplex method [26]) to get a Computer Aided Design.
  - Design of filters for different specifications and comparison in terms of accuracy and efficiency.

- **Characterization of the properties of the Liquid Crystal.** One of the problems that appears during the development of the work is the lack a good characterization of the dielectric properties of LC mixtures at microwave frequencies. So, it is necessary to perform the characterization of these properties at the desired frequency bands. The split-cylinder resonator method has been used for this purpose. This method consists of comparing the measured resonance frequency and Q-factor of a resonant cylinder with

and without a sample of the material under analysis [27]. A modal and a numerical method have been employed for extracting the dielectric permittivity values and the loss tangent from these measurements.

- **Decoupling of single conductor closed structures.** ESIW technology can be employed for designing filters that can be filled with LC since they are closed and empty structures. Nevertheless, ESIW is, by definition, a waveguide thus a single conductor structure. The decoupling of this structure must be conducted to enable the application of an electromagnetic bias field over the LC molecules for changing their properties.

- **Manufacturing, measurement and reconfiguration**. Some of the designed prototypes have been manufactured, considering all the technological issues such as the filling and confinement of LC and the application of the electromagnetic bias field. A measuring set-up that includes the RF excitations and bias field is developed, and the reconfiguration of the frequency response is measured. The results are compared with simulations to verify the feasibility of the proposed methodology.

1.4 Structure of the thesis

The thesis is divided into the following chapters:

- **Chapter 1.** This chapter is the introduction to the thesis and presents the motivation and the state of the art, the detailed objectives to be achieved and the working plan to accomplish them.

- **Chapter 2.** This chapter presents the bibliographic search work that has been carried out, studying the different structures that can behave like filters and the technologies used for implementing them, as well as the analysis techniques that have been used. The following technologies have been studied:

  - Classic metallic waveguides or new structures as Ridge waveguide [28] and Groove Gap Waveguide [21]. These structures can be used for developing H-plane directly coupled cavities filters, either loaded or not with dielectric posts, or even in evanescent mode.
  - Planar structures that implement end-coupled [29], parallel-coupled [30], hairpin-line [31], interdigital [32], combline [33], and stubs [34] bandpass filters.

  - Substrate Integrated Circuit (SIC) [35] and, inside this large family, the Substrate Integrated Waveguide (SIW) [2], the Empty Substrate Integrated Waveguide (ESIW) [5], and the Empty Substrate Integrated Coaxial Line (ESICL) [36].

  Among all these technologies, the SICs, and, specifically, the SIW and ESIW have been chosen because they are the most suitable for the thesis purpose. The results they provide, their advantages and disadvantages, the improvements they need and the way to make them reconfigurable are studied.

  A brief review of the reconfiguration methods available for SIW technology is done, including PIN diodes [7], RF MEMS [13], varactor diodes [10], ferrite sections [37], and Liquid Crystal (LC) [19]. The LC has been chosen for its novelty and dielectric properties, moreover a depth analysis of its properties is performed.

  Finally, an overview of the different dielectric characterization methods is carried out, since the dielectric properties of many LC mixtures are not well characterized at microwave frequencies in the bibliography.

- **Chapter 3.** The influence of a dielectric material inside an empty integrated filter is studied. For that, a depth description of the analysis, design, and manufacturing of a new filtering structure proposed in the Thesis is carried out. This filter is based on alternating line sections with and without dielectric material. The filtering response of the manufactured prototypes is discussed, studying also their out-of-band response.

- **Chapter 4.** Next, the characterization of the dielectric properties of the LC is performed, obtaining the dielectric anisotropy (extreme values of dielectric permittivity and loss tangent) of this tunable material. Four different mixtures of LC are measured at three different frequency points.

- **Chapter 5.** This chapter deals with the last part of the work carried out: the design, manufacturing and measurement of continuously reconfigurable filters. For that, firstly, an analysis and design of decoupled microwave structures integrated in a planar substrate is done. Transmission lines and one-pole filters are manufactured in this technology. The one-pole filters are filled with different LC mixtures, and biased with electric and magnetic fields for tuning their response.

- **Chapter 6.** The thesis ends by establishing the main conclusions extracted from the work performed, as well as the possible future research lines that could be followed as a continuation of the developed work.

Chapter 2

Theoretical basics of reconfigurable microwave filters

2.1 Microwave filters

Microwave filters are essential components in the front-end of high frequency telecommunications systems. They are two-port networks that allow a signal transmission in a certain range of frequencies, their passband, and attenuate as much as possible, the signal outside this range, their stopband [1].

Nowadays, these devices are used in many applications like via satellite television, or radar systems, but mostly in cellular radio communications. Cellular radio has stringent filter requirements both in the base stations and in mobile handsets [38].

Moreover, the progressive increase in the electromagnetic spectrum saturation has resulted in a continuous increment of the operation frequency. This increment and the development of sophisticated high frequency applications require producing microwave circuits with advanced performance [39]. Referring to filters, the possibility of minimal insertion loss and high selectivity on compact circuits has been always a key feature to efficiently remove noise and interfering signals outside the passband. Other features currently required for these electronic components, such as agile frequency reconfiguration, are a result of the most recent trends towards developing high frequency multifunction devices [40].

A lot of research work has been done in the analysis and design of microwave filters, nevertheless the basics of the analysis and design process is common, regardless either the filter topology or the technology used for its implementation. There is wide bibliography about the processes of synthesis and optimization [38, 41] and it does not seem appropriate to do an exhaustive analysis of them. The process of designing any type of filter is composed

of three fundamental steps.

The first one is to know the specifications that must be always respected. Among all of them, the most prominent specifications are the number of cavities, the return loss, the insertion loss in the passband, and the rejected band.

Next, it comes the synthesis process, where the most appropriate topologies and technologies are chosen to meet the specifications, and the design parameters are determined. The synthesis process culminates by obtaining an “initial point", it means, the initial values of the design parameters. These values are generally obtained by using the analytic equations of the proposed topology.

Finally, the initial values will be modified in the optimization process until the required specifications are obtained. In this step, all the manufacturing considerations related to the technology must be taken into account in order to have a design as much similar as possible to reality. Generally, the optimization process of microwave devices is carried out through an automated Computer Aided Design (CAD) tool, since the complexity of the structures makes its manual design impossible. Besides, when designing a complex structure, the number of parameters increases, making inefficient the optimization of all the parameters at once, so it is convenient to apply a segmentation strategy. The segmentation strategy consists of dividing the structure under analysis in a set of blocks, transforming the process of design in a set of steps, in which a reduced number of parameters are optimized [42]. In this way, the efficiency of the process is increased (if the structure presents symmetry the efficiency is even higher), since the number of steps in the process can be reduced. After having optimized the block structure, the design ends with a last step, in which all the parameters are slightly adjusted at the same time. This is done through an optimization that starts from the initial point given by the dimensions obtained in the previous steps.

As mentioned before, the topology and technology of the filter must be chosen in the first step of the designing process. There are many topologies for implementing filters but they depend mostly of the used technology. A review of the most common technologies employed for manufacturing microwave filters (waveguide, planar or Substrate Integrated Circuit) and their typical topologies is included next.

2.1.1 Waveguide filters

A metallic waveguide is a structure that propagates an electromagnetic wave in a particular direction by confining its energy. A waveguide consists of either circular or rectangular hollow metallic pipes of uniform cross-section [38]. Metallic waveguides filters are the most widely used for satellite communications, since they present great electromagnetic shielding (radiation loss is completely removed), low insertion loss, ability to carry out high power sig-

nals and high quality factor [43]. The problem of this technology is that it is not appropriate to mass production due to the complexity of manufacturing and integration processes.

In this technology, the traditional structures are H-plane directly coupled cavity filters [44], as shown in Figure 2.1. These filters are based on half-wavelength resonators coupled through shunt inductive irises symmetric to both E- and H-plane. There are also other kind of irises that are only symmetric to the E-plane [45].

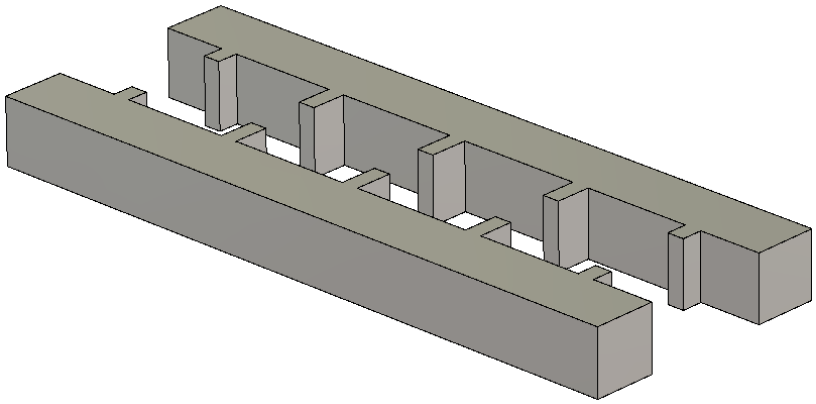

Figure 2.1: H-plane directly coupled cavity waveguide filter.

Different approaches are developed to reduce volume and mass [46]. For example, H-plane filters loaded with dielectric posts inside the cavities that act as resonators (see Figure 2.2). They can be either cylinders or square posts passing completely through the guide, with a stable permittivity for the operation bandwidth. At the operating frequency, most of the electromagnetic energy is stored within the dielectric. This causes the fields outside of dielectric worsen rapidly with distance. The resonance frequency is strongly controlled by both the dimensions and the electric permittivity of the dielectric material, whereas the quality factor is determined by the loss tangent of the dielectric.

Another topology for the coupling windows in rectangular waveguide filters consists of inserting screws or posts in the waveguide. They can be metallic or dielectric and act as inductive irises. The waveguide sections between the screws operate as half-wavelength resonators [38]. The operation principle is the same one that in the H-plane directly coupled cavities filter, consisting of bandpass resonators separated by shunt inductive posts.

Evanescent H-plane filters are a breakthrough in the design of high-performance filters. They are smaller and provide significant improvements in bandwidth rejection regarding directly coupled cavities filters [47, 48]. These structures work below the cutoff frequency of the waveguide. For theses H-plane filters, the single existing mode in the waveguide is an

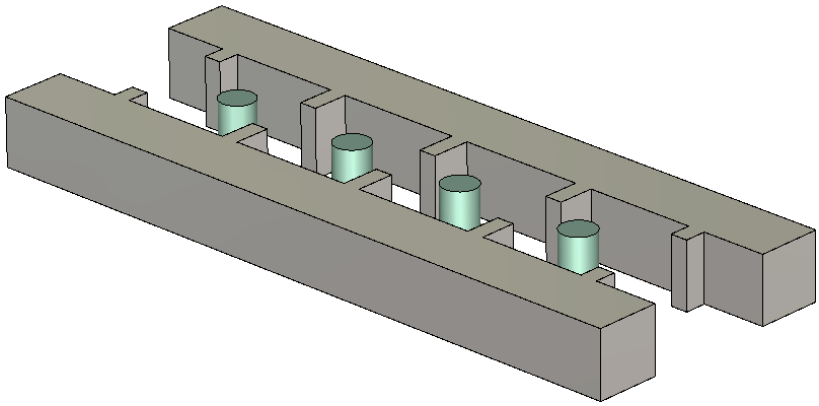

Figure 2.2: H-plane directly coupled cavity waveguide filter loaded with dielectric posts.

evanescent TE_{10} mode. They can be obtained thanks to the insertion of capacitive elements (metal or dielectric posts) introduced at appropriate intervals within the evanescent waveguide as depicted in Figure 2.3. These elements act as resonators in the cutoff waveguide, while the distance between them behaves as the coupling element [49]. The resonators can be positioned centred or off-centred on the longitudinal axis of the filter. The off-center posts enable crossed coupling between non-consecutive posts, allowing to implement transmission zeros. The dielectric posts can also be made double, thus obtaining a different field distribution inside the structure [50].

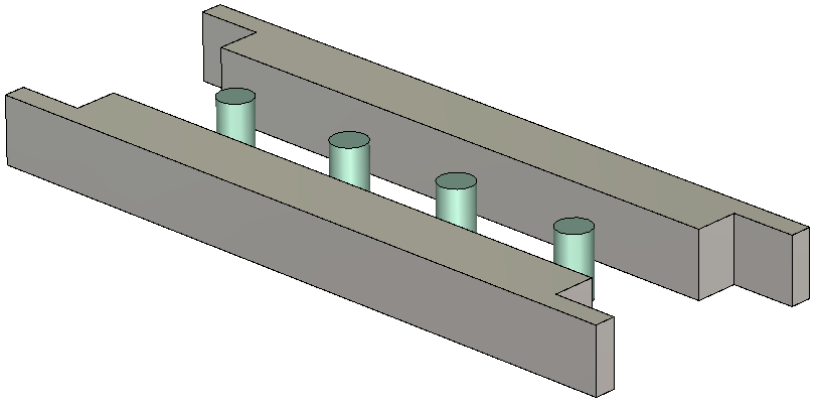

Figure 2.3: H-plane evanescent waveguide filter loaded with posts.

The ridge waveguide [28] is an alternative that has lower cut-off frequency and greater higher-mode separation than a plain rectangular waveguide of the same dimensions. A higher monomode bandwidth can be obtained using this technique. The ridge waveguide is per-

formed by adding conducting ridges along the longitudinal axis of the top and/or bottom walls of a rectangular waveguide (see Figure 2.4).

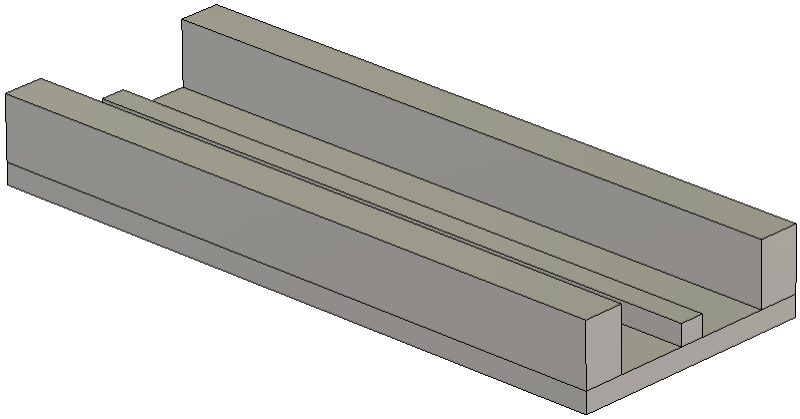

Figure 2.4: Ridge waveguide.

Recently, in order to solve the problem of electric contact in the joints between the two parts of a hollow waveguide when the frequency increases, Groove Gap Waveguide (GGW) technology has been developed [21]. In this technology, electric contact between the two metallic surfaces is not needed. The basic geometry of the GGW, shown in Figure 2.5, comprises two parallel conducting surfaces separated by a small gap. One of them is a Perfect Electric Conductor (PEC) surface, and the other one is a Perfect Magnetic Conductor (PMC) surface. The PMC surface can be implemented by periodic metallic pins [51]. The waveguide is formed inside the gap between the two surfaces. The gap is usually filled with air, but it can also be, fully or partly, filled with a dielectric material.

All of the aforementioned waveguide filters have excellent behaviour, but usually there is a slight deviation in the frequency response due to manufacturing tolerances. This deviation can be corrected by using tuning screws to adjust the frequency response. However, the problem of all these waveguide topologies is the difficulty to integrate the devices with power circuits. In order to solve this problem, and due to the need for low-cost technologies with high performance and suitable for mass production, planar technology (Printed Circuit Board (PCB)) was arisen.

2.1.2 Planar filters

A planar device is manufactured by using a PCB. This structure consists of a conducting strip on the top of a dielectric substrate and a metallic layer on the bottom of the substrate

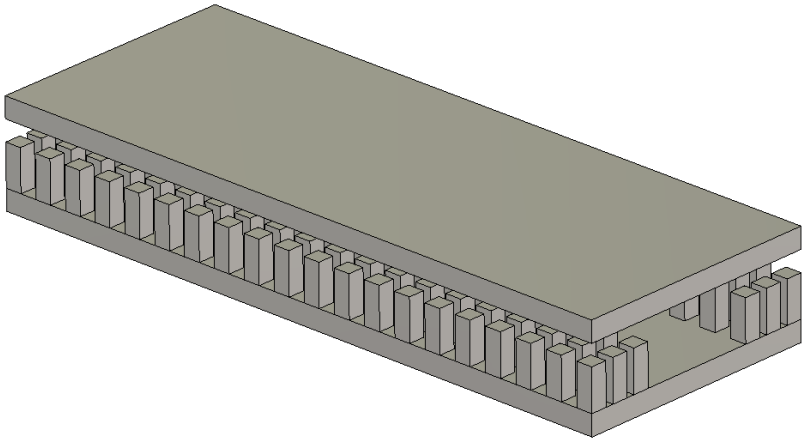

Figure 2.5: Layout of the Groove Gap Waveguide.

acting as ground. The field propagates in two media: the air and the dielectric substrate. This technology has many advantages for implementing microwave filters, since it reduces the volume, weight, and power consumption of telecommunications equipments.

There are several filtering topologies that can be implemented in a planar structure [52], some of them are reviewed next.

One of the most common planar filter is based on end-coupled half-wavelength microstrip resonators. The general configuration of these filters consists of a series of capacitively coupled resonant elements. These resonators are open-end microstrip transmission lines of half-wavelength [29], see Figure 2.6. The capacitive coupling from one resonator to the other appears in the gap between the two adjacent open ends. In this case, the gap can be represented by admittance inverters. They tend to reflect high impedance levels at the extremes of each resonator. This causes the resonators to exhibit a shunt-type resonance [53].

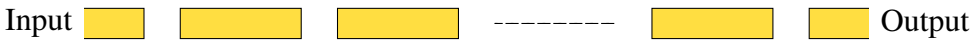

Figure 2.6: General end-coupled microstrip bandpass filter.

In order to have filters with a wider bandwidth than the described end-coupled microstrip filters, there is an alternative consisting of parallel-coupled microstrip resonators. The general structure of these microstrip bandpass filters uses half-wavelength line resonators positioned parallel to each other along half of their length [30], see Figure 2.7. This parallel arrangement gives relatively large coupling levels for a given spacing between resonators, hence the bandwidth can be increased.

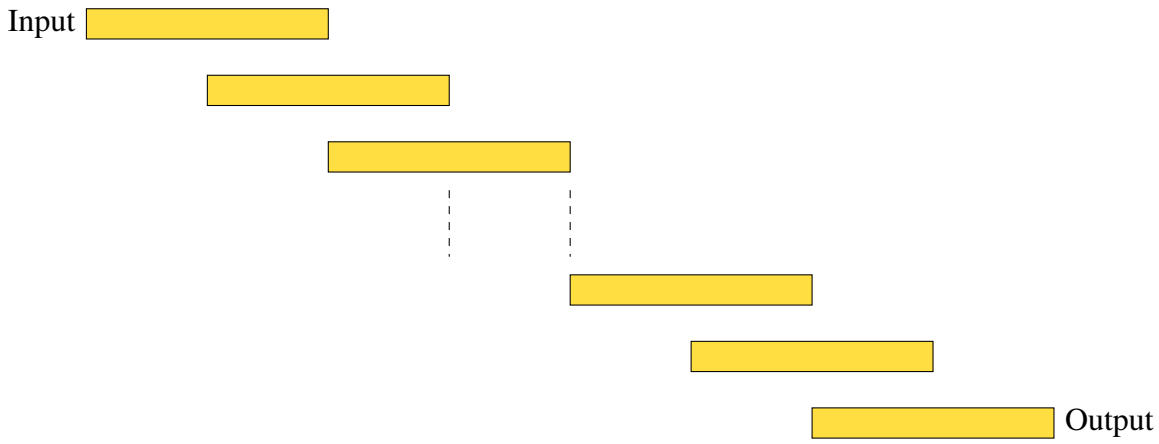

Figure 2.7: General parallel-coupled microstrip lines bandpass filter.

For reducing the size and the loss of the previous filters, there are other topologies such as the ones of the the hairpin filters. On the one hand, these filters are compact because conceptually they are obtained by folding the resonators of the parallel-coupled lines filter into a “U" shape [31], see Figure 2.8. However, to fold the resonators, it is necessary to take into account the reduction of the coupled-line lengths, which reduces the coupling between resonators. Also, if the two arms of each hairpin resonator are closely spaced, they operate as a pair of coupled lines themselves, which can have an effect on the coupling as well. On the other hand, they have lower insertion loss because the radiation field in folded resonators is cancelled out [54].

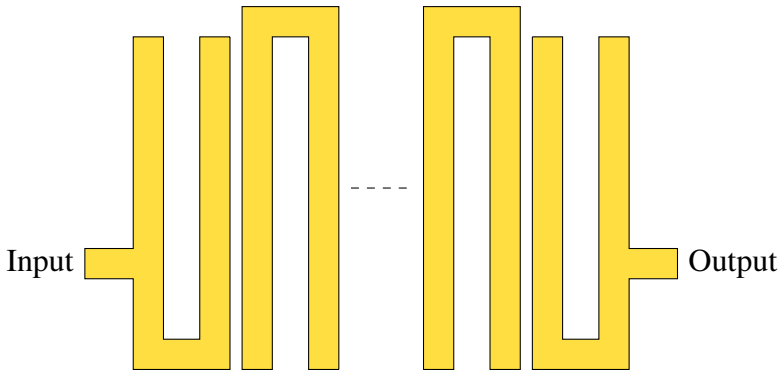

Figure 2.8: General hairpin-line microstrip bandpass filter.

Another structure is the interdigital filter. This filter configuration consists of an array of transmission line resonators, each one of them has a quarter-wavelength length at the midband frequency [32], see Figure 2.9. The resonators are short-circuited at one end and

open-circuited at the other end, with alternative orientation. In general, the physical dimensions (length and width) of the resonators can be different. Coupling is achieved by means of the fringing field between adjacent resonators.

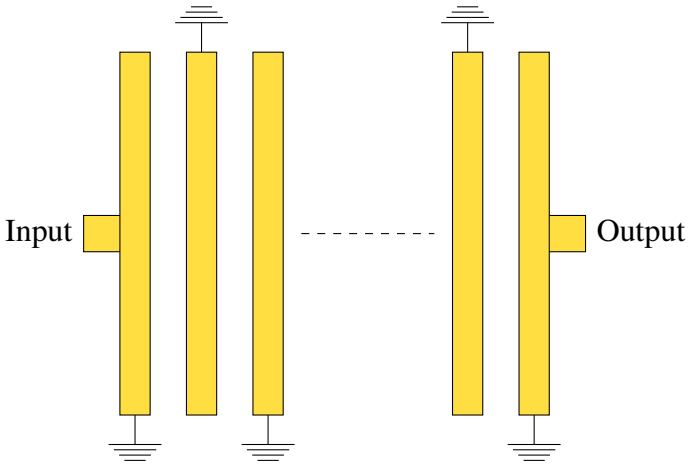

Figure 2.9: General interdigital bandpass filter.

One step further on planar filters is the design of combline filters. In this topology, the resonators consist of transmission line elements short-circuited at one end and terminated with a lumped capacitance at the other one, see Figure 2.10. The resonators length will be less than a quarter-wavelength by the presence of the capacitors [33].

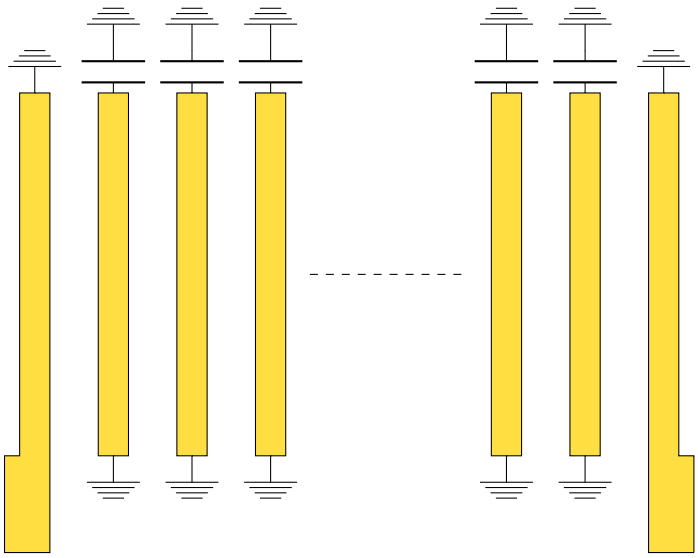

Figure 2.10: General combline bandpass filter.

Finally, the last presented topology is the stub filter [34]. These stubs can be shunt short-circuited stubs of a quarter-wavelength length or shunt open-circuited stubs of half-wavelength length, see Figure 2.11. These stubs act as resonators and they are connected by transmission lines of a quarter-wavelength length for short- and open-circuited stubs.

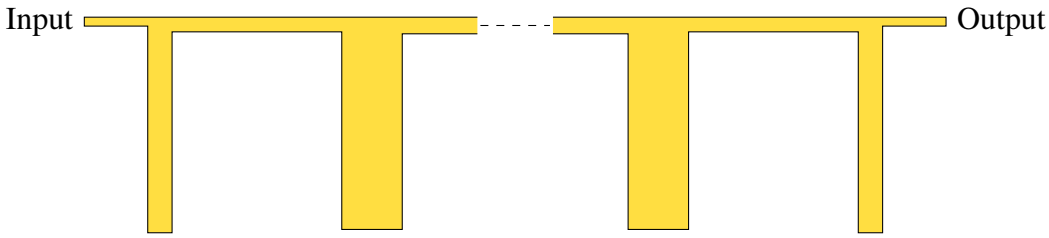

Figure 2.11: General bandpass filter with stubs.

However, all of these planar filters have worse performance than waveguide technology filters, such as high loss, low quality factor, and hence low filtering selectivity. In order to overcome weaknesses and limitations of both waveguide technology and planar circuit technology, and to ease the integration between both technologies, a new generation of high-frequency integrated circuits was proposed: Substrate Integrated Circuit (SIC).

2.1.3 Substrate Integrated Circuits

In 2001, an ingenious and revolutionary concept known as Substrate Integrated Circuit was proposed [2]. The foundation of the SIC is to synthesize non-planar structures with planar dielectric substrates. Within this large family of integrated circuits, the Substrate Integrated Waveguide (SIW) can be found.

SIW is a mixed technology waveguide-printed circuit which solves perfectly the shortcomings associated with traditional technologies. It integrates a rectangular waveguide in a planar substrate [2]. This is an “artificial" waveguide synthesized by two parallel rows of metallized via holes, joining two planar conductors separated by a dielectric substrate, see Figure 2.12. If the pitch between consecutive posts is smaller or equal to twice the vias diameter, the leakage loss is negligible. In this case, the SIW can be replaced by an equivalent rectangular waveguide filled with dielectric of permittivity ε_r.

SIW combines the best features of both metallic waveguide and planar structures. It respects the original specifications of the waveguide filters but getting integrated structures, which are much smaller, significantly cheaper, and easier to manufacture. The SIW devices have lower loss and higher quality factor than their equivalent ones in traditional planar technologies. In addition, the synthesis of SIW enables the efficient realization of broadband

transitions with planar circuits [4, 55]. So that, the integration of planar circuits and SIW circuits in the same substrate can be achieved using a low cost planar technique production [56].

Moreover, SIW structures have the advantage of fast full-wave simulation, as PEC boundary conditions can be applied during calculations. This is not possible for open structures, where a radiation boundary condition is necessary. This fact considerably reduces the computational time, which is of great importance during optimization in the design process.

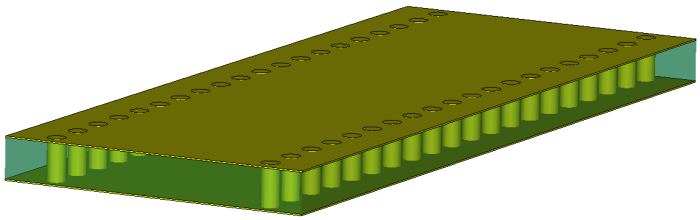

Figure 2.12: Layout of Substrate Integrated Waveguide.

The filter topologies that can be used in this technology are the same ones employed with rectangular waveguides [57]. The traditional H-plane directly coupled cavities filter is the most extended topology, where cavities and irises are performed by equispaced metallized via holes. Different shapes of these cavities are proposed in the bibliography: the classical rectangular ones [58], circular cavities [59], hexagonal cavities that combine the flexibility of rectangular cavities and the performance of circular ones [60], or isosceles triangles [61].

Evanescent H-plane filters can also be implemented in SIW techonology [62]. These filters have better performance in spurious suppression and smaller size than conventional coupled cavities SIW filters.

Recently, a new technology has appeared, the Empty Substrate Integrated Waveguide (ESIW) [5], which is an improvement of SIW. In this case, the body of the waveguide is performed by emptying a rectangular hole in a planar substrate, which is metallized. So, the side walls are continuous metallic walls instead of rows of metallized via holes, see Figure 2.13, a top and a bottom metallic covers close the three layered structure. The electromagnetic field travels in the vacuum confined by upper, lower and lateral metallic walls.

The absence of substrate, increases the quality factor and selectivity of the devices, so that, the performance of the ESIW is very close to that of the rectangular waveguide. Moreover, the advantages of low cost, easy manufacturing, and integration with planar circuits are maintained.

The design equations of waveguide technology for filter design [53] can be used, since ESIW is a perfect rectangular waveguide embedded in a PCB. The method based on equiv-

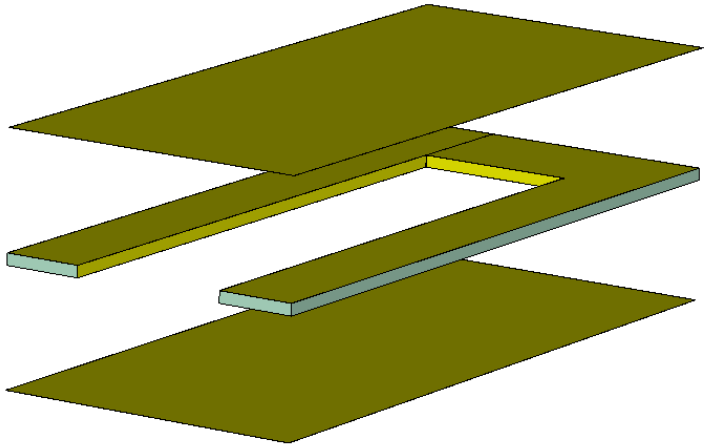

Figure 2.13: Layout of an Empty Substrate Integrated Waveguide.

alent circuits with inverters and resonators for designing H-plane directly coupled cavities filter is widely used for this structure.

Following the same idea, an empty coaxial line integrated in a substrate is proposed in [36], the Empty Substrate Integrated Coaxial Line (ESICL). This coaxial line is entirely built using PCBs. The integration of a coaxial line into an empty substrate permits to obtain non-dispersive and shielded lines with low loss, low radiation, and suitable for wideband applications. The layout of this structure is depicted in Figure 2.14.

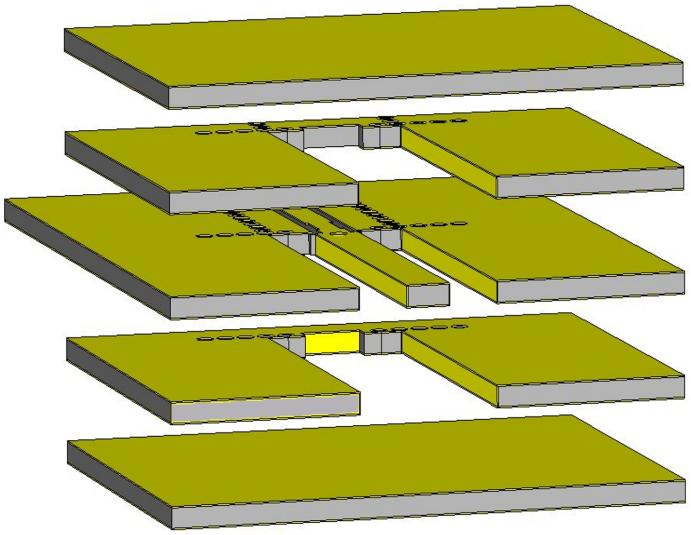

Figure 2.14: Layout of an Empty Substrate Integrated Coaxial Line.

In order to design filters with this configuration, the traditional wideband bandpass filters with planar lines can be applied [52]: the resonators of the filter are implemented with shorted stubs of a quarter-wavelength length. These resonators are coupled through impedance inverters, which are synthesized with quarter-wavelength length line sections.

A common problem for all of them (waveguide, planar structures and SICs) is that the manufactured device may not have the desired frequency response. This may be caused by the manufacturing tolerances or by the electromagnetic features of the employed materials. Therefore, it is desirable to tune the device response after manufacturing, that is, to adjust the center frequency and the bandwidth to meet the initial specifications.

Additionally, all the filters mentioned so far are designed to operate at a single frequency and bandwidth. The tuning only allows adjustment of the frequency response to meet specifications, i.e, they cannot change the electromagnetic response over a certain frequency range. These filters do not have the ability to reconfigure their operating parameters, i.e. center frequency and bandwidth.

In the high demanding communication systems scenarios, it is useful that the main filters features can be adjusted in a controlled manner, such as the center frequency, bandwidth and/or selectivity, thus replacing the need for multiple devices and improving system reliability as a whole. In addition, this permits reduction in size, weight, complexity and cost of the systems. Since the reconfiguration feature of filters is one of the fundamental pillars of this work, different possibilities to achieve a reconfigurable filter are studied below.

2.2 Reconfiguration methods

For reconfiguration in SIW technology, different elements can be used, as integrated electronic devices or tunable materials [6].

On the one hand, the use of discrete electronic components has been popularized due to advances in packaging and miniaturization, which allow its integration in RF devices.

- **PIN Diodes**. They are semiconductor elements [7] that can act as a variable resistor in RF frequencies. Its resistance varies as a function of the applied voltage. On the one hand, if the PIN diode is in forward bias mode (positive voltage), it is equivalent to a series resistor with a small inductance behaving as a short circuit. On the other hand, if the PIN diode is in reverse mode (negative voltage), it is equivalent to a capacitor in parallel with a resistor behaving as an open circuit.

  In [8, 9], posts are introduced inside the SIW cavities to achieve a fully tunable filter. There is an optimum location for the posts that provides fine tuning and allows adapta-

tion of several states. Such requirements are achieved by connecting and disconnecting the posts to the top metal layer of the SIW. The PIN diodes located in this layer are responsible for that switching task. To achieve this switching a Direct Current (DC) with different polarization is applied to the diodes. The activation of the posts in a symmetrical way achieves a greater tuning range.

- **RF MEMS**. Radio Frequency MicroElectroMechanical Systems are actuators that can change certain parameters using the mechanical movement of certain microscopic parts of the device, which is activated by an electric signal [13]. They can be used for ohmic or capacitive contact with the RF circuit.

  RF MEMS have some advantages regarding PIN diodes, as lower insertion loss, higher isolation, lower DC power consumption, and relative power handling [6]. However, there are some disadvantages, as higher cost, lower reliability, and high activation voltages.

  In [14], RF MEMS are used as variable capacitors to change the electric length of the filter stubs and, consequently, the central frequency and the bandwidth. In the case of SIW technology, its usage is similar to PIN diodes. For instance, in [15], a tunable filter is developed by using via-posts and RF MEMS switches placed at various locations within the cavities. To change the resonance frequency of the cavity, the tuning posts are connected and disconnected from the top wall, by properly closing RF MEMS switches. This provokes a cavity field perturbation that changes the resonance frequency.

- **Varactor Diodes**. They are variable capacitors whose capacitance can be controlled through a bias voltage. As in previous cases, one or some varactor diodes are inserted in the cavity of a filter for tuning it. This diode is connected to a variable DC voltage. Depending on the applied voltage, the capacitance varies and, therefore, the resonance frequency, as developed in [10, 11]. They can also be used for other microwave devices as phase shifters [12].

On the other hand, the employment of tunable materials avoids the drawback of the placement of discrete elements over a circuit. These materials change their electromagnetic properties (permittivity, permeability or conductivity) when a bias electric or magnetic field is applied.

- **Ferrite Sections**. Ferrite slabs are used in recent years for designing many components, such as phase shifters [63], isolators [64], tunable filters [65], and so on. In

these components, a small section of ferrite is introduced, on which an external magnetic field is applied. This produces a variation in the inductance of the ferrite and thus a variation in the parameters of the device (propagation constants, resonance frequency, etc.). Hence, devices can be reconfigured only by applying a DC bias field to the ferrite section. This reduces the complexity of the control system compared to traditional methodologies. This approach has numerous applications in advanced RF devices whose essence is stability and simple tuning.

In [66], a ferrite-loaded SIW switch is proposed. It consists of rectangular ferrite slabs loaded on the sidewall slots of a SIW. When a DC magnetic bias is applied to the ferrite slabs, the equivalent width of the ferrite-loaded SIW is changed, contributing to the tuning. In [67] and [37], the same principle is used for designing a tunable resonator and a bandpass filter, respectively.

- **Liquid Crystal**. LC is a material that can change its permittivity when an electric or magnetic field is applied. LC is located in the cavities of the filters, in order to reconfigure their electromagnetic response. By applying an electric or magnetic field, the permittivity of the LC varies and therefore parameters such as central frequency and bandwidth change. In [16–19], LC is used for developing phase shifters or tunable resonators.

Moreover, a combination of different tunable methods can be used. In [68, 69], a combination of varactors and ferrites is used inside a SIW cavity. By applying a bias voltage in the varactor and a current in the ferrites, several parameters are improved at the same time. This enables greater control over parameters such as resonance frequency, bandwidth or the phase-shift of the resonator.

In this work, the method that has been chosen for implementing the reconfiguration features is the LC, thus a depth review of this material is done next.

2.3 Fundamentals of Liquid Crystal

Liquid Crystal (LC) is an anisotropic liquid material that presents an intermediate matter state between crystalline solids and isotropic liquids, called mesophase. In this state, the LC mixtures designed for the telecommunications sector present a series of properties of molecular mobility. These properties, together with their dielectric anisotropy, allow to adjust their dielectric permittivity within a range of continuous values, by using an electric or magnetic biasing signal.

The reason of these properties is due to the inner construction of the LC molecules, in particular its great asymmetric shape [3]. These organic molecules present asymmetry between their two main axis, having a rod-like shape (calamitic LC) or a disk-like shape (discotic LC), as shown in Figure 2.15.

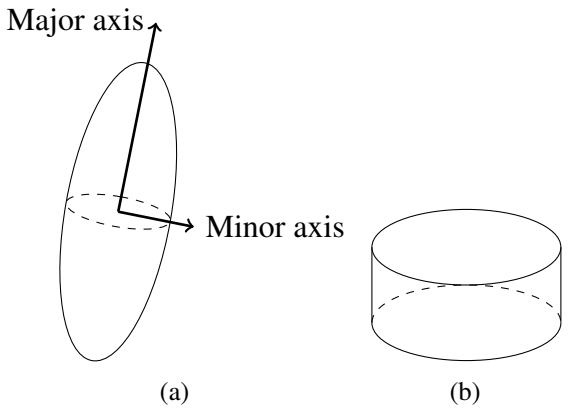

Figure 2.15: Molecules of the two main types of LC used in telecommunications applications. (a) Calamitic LC . (b) Discotic LC.

In this section, the fundamental properties of the calamitic or rod-like shape LC are presented, since they are the most commonly used in telecommunications applications.

As mentioned before, the characteristics of the mesophase state provide multiple properties for implementing reconfigurable microwave devices, since this state has certain features from solid and liquid states.

On the one hand, in the crystalline solid state, the molecules present great intermolecular forces that hold them together in a well defined position (positional order) and have a tendency to maintain an orientation (orientational order).

On the other hand, when the temperature increases, the matter transforms into a liquid state, where the molecules can freely move, thus not presenting either positional or orientational order.

LC presents, within a certain temperature range, an intermediate state where the molecules still have orientational order but no positional order. Thanks to the asymmetry of the molecules, the matter presents non-homogeneous intermolecular forces in all directions of space. This allows the molecules to freely move in certain dimensions like a liquid, but prevents their rotation in certain axes, since the molecules lay down on each other, limiting the movement and causing an orientation in a specific direction as in the crystalline solid state.

Since the properties of this type of material are mostly caused by the characteristics of its molecules, it is interesting to know their parts and their implication in the different properties.

The molecules of an LC of calamitic type are formed by three well differentiated parts (see Figure 2.16), which allows to obtain the orientational and positional orders, while enabling the orientation with an electromagnetic field.

- **Head**: the molecule has a permanent dipole in its upper part. This enables the induction of an electrostatic force that can rotate the molecules of an LC bulk in the direction of this field. In short, this head gives the ability to control the pointing direction of the molecules of a volume of LC by the application of an electric or magnetic field.

- **Core**: the head is attached to a rigid core of a cylindrical shape, which provides a high orientational order. The molecules, minimizing the total matter energy, tend to stack in parallel, although they can rotate around, and move along the direction of their long axis.

- **Tail**: the molecule has a flexible tail that diminishes intermolecular forces in certain directions, thus increasing the freedom to move in different directions. This provides a low positional order to the matter. Without this part, the matter would simply transform from crystalline solid to isotropic liquid without the mesophase state.

In conclusion, the rigid parts favours both orientational and positional orders while the flexible parts do not. With balanced rigid and flexible parts, the molecule exhibits LC phases.

Figure 2.16 shows a typical calimitic LC molecule: the three parts of the molecule, the chemical formulation and a graphic representation of the 4-Octyl-4-biphenylcar- bonitrile or $CH_3(CH_2)_7C_6H_4C_6H_4CN$ LC molecule. The biphenyl is the rigid core and the hydrocarbon chain is the flexible tail.

Each part of the the molecule is essential to achieve the mesophase state. On the one hand, a high asymmetric core would result in a significant increase in the positional order (restricting the molecule orientation), and a high symmetrical core would result in a decrease in orientational order. On the other hand, a too flexible tail decreases the orientational order, but a rigid one increases the positional order.

The same LC presents different intermolecular force distributions as a function of the temperature. These states are considered subphases within the mesophase. In the specific case of calamitic LCs there are two phases: smectic and nematic. The smetic phase appears at a lower temperature than the nematic one and, the particles are oriented by domains or zones. The nematic phase is the common and simplest LC phase. In this case, at the macroscopic scale, the long axes for all the molecules are oriented in one direction, designated by a vector called director $\overrightarrow{n}$.

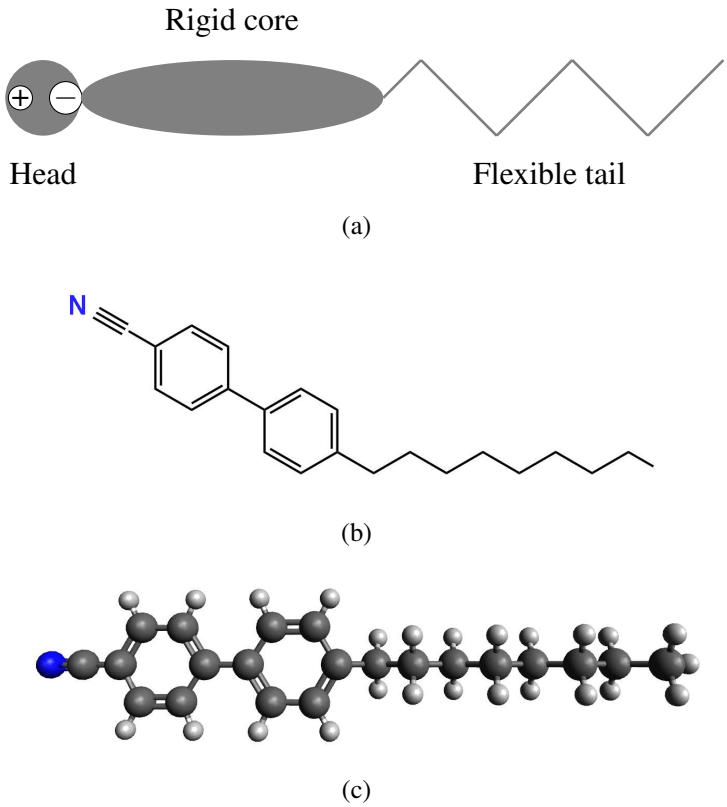

Figure 2.16: Calamitic LC molecule. (a) Scheme of the three parts of the molecule. (b) Schematic formulation. (c) 3D representation of the molecule.

In practice, nematic LCs are used, since it is possible to control the orientation of their total set of molecules. However, both the mesophase and its nematic subphase are limited in temperature, hence an important characteristic to take into account in the choice of an LC is precisely its temperature range in the nematic phase.

2.3.1 Polarization and dielectric anisotropy

The shape of the molecules of the LC does not only allow them to have a mesophase state, but also having different values of permittivity depending on their orientation. This anisotropy of the material can be explained in a very graphic way regarding the distribution of charges that are induced in the LC molecules under the presence of an electric field, since the mechanism of dielectric polarization that predominates at microwave frequencies is the polarization by dipole alignment.

As illustrated in Figure 2.17, the application of an electric field to two LC molecules

oriented perpendicularly, would cause the movement of the free charges of their core. This movement will excite a dipole moment in opposition to the field that has created the charges. In an LC volume, as depicted in Figure 2.18, the interaction of the sum of each dipole moment with the electromagnetic field that has created them is modeled in Maxwell Equations as dielectric permittivity. As can be seen in Figure 2.17, these dipole moments are clearly different in the two orientations of the molecule. The dipole moment excited in a molecule oriented parallel to the electric field is greater than the one excited in a molecule oriented perpendicular to the electric field [70]. This difference in dipole moments (relative orientation between the molecule and the electric field) is translated into different values of dielectric permittivity and, therefore, in the dielectric anisotropy.

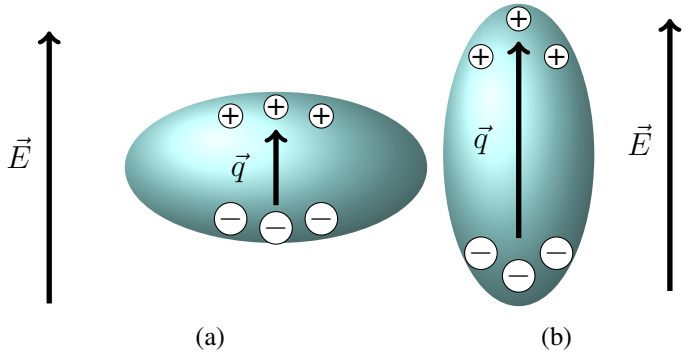

Figure 2.17: Induced charges distribution in an LC molecule by the presence of an electric field in its main axis. (a) Minor axis. (b) Major axis.

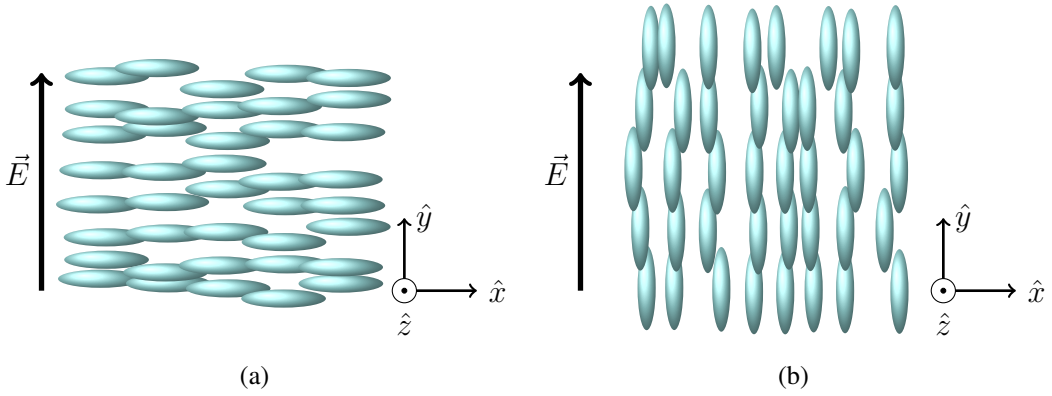

Figure 2.18: LC bulk in its two extreme polarization states or dielectric permittivity. (a) Perpendicular dielectric permittivity ($\varepsilon_{r\perp}$). (b) Parallel dielectric permittivity ($\varepsilon_{r\perp}$).

Since the permittivity of an LC material depends on the orientation of its molecules with respect to the electric field, two extreme permittivity values can be defined.

On the one hand, the propagation of a wave whose electric field $\overrightarrow{E}$ is orthogonal to the director $\overrightarrow{n}$ (see Figure 2.18(a)) will result in the lowest extreme permittivity. This is the relative orthogonal dielectric permittivity, $\varepsilon_{r\perp}$.

On the other hand, a wave with a polarization of the electric field $\overrightarrow{E}$ parallel to the director $\overrightarrow{n}$ (see Figure 2.18(b)) will result in a higher permittivity value. This is the relative parallel dielectric permittivity, $\varepsilon_{r\parallel}$.

Any change in the direction of propagation or polarization of the field will result in a relative intermediate value between the two extremes. With these parameters, the dielectric anisotropy of the material is defined in (2.1) as the maximum variation of the dielectric permittivity.

$$\Delta\varepsilon = \varepsilon_{r\parallel} - \varepsilon_{r\perp} \tag{2.1}$$

This property, together with the positonal and orientational orders of the molecules of the LC in mesophase, provides a material with tunable permittivity.

2.3.2 Alignment methods

As mention before, the dielectric permittivity depends on the angle between the director $\overrightarrow{n}$ and the electric field $\overrightarrow{E}$. For that reason, it is necessary to have a mechanism for controlling the direction of $\overrightarrow{n}$, i.e., the LC molecules must be properly oriented to get a tunable dielectric material.

For illustrating the methods to align the LC molecules to achieve different states, a cell of LC formed by two parallel plates is used. The scheme is shown in Figure 2.19.

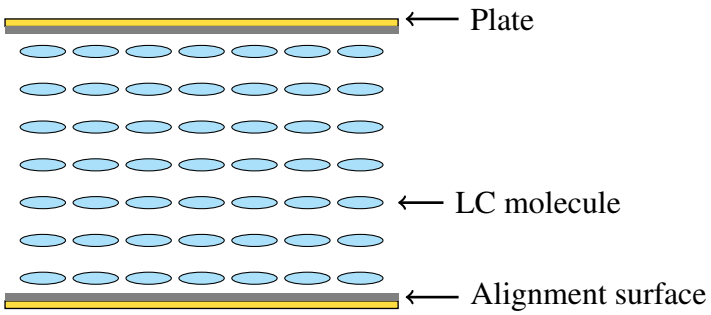

Figure 2.19: Scheme of a Liquid Crystal cell.

There are two alignment methods:

- **Alignment by surface anchoring**. The surface anchoring consists of a set of microscopic grooves performed on the inside walls of the containers of the LC bulk. If these grooves have the optimal size, distribution and direction, the LC molecules will tend to stack on these grooves to decrease their free energy, inducing an anchoring force that allows a uniform orientation throughout the entire volume of LC.

  There are two types of alignment by surface anchoring, either parallel (homogenous alignment) or orthogonal (homeotropic alignment) to the surface. The choice depends on the requeriments. In the scope of this work, the first one will be used. For the construction of this alignment layer, these grooves can be made directly on the supporting material surface (glass, plastic, copper...) rubbing with some fabric like cotton. Nevertheless, this generates an anchoring force too weak (10^{-5} J/m^2) for the handled volume [3]. Therefore, the material is usually spin coated and cured with polyimide and then, the anchoring surface is created on the polyimide by rubbing with velvet. This material is not only more resistant than the background material, but rubbing with velvet creates very effective microgrooves and the polymer chains are aligned increasing the anchoring force in two orders of magnitude [3]. The thickness of the polyimide layer is very important, since a thick layer will affect the RF signal, and a thin one will result in a low anchoring force.

- **Alignment by electromagnetic fields**. This technique consists of applying a very low frequency electric field or a static magnetic field to orient the LC molecules. These fields must be high enough to induce forces in the permanent dipole moment of the molecules for orienting them. The electric field amplitude needed for the alignment of a small volume of LC would be around 30 kV/m [23]. The magnetic field is rarely used, especially for LC devices, because of the need of heavy and bulky magnets.

These techniques only allow to orient the LC in one direction and not in a continuous set of directions to obtain reconfiguration. For this reason, a combination of both methods is usually employed. Figure 2.20 shows a typical LC cell formed by a layer of nematic LC, the molecules are represented as ellipses and they are confined between two conductive parallel plates separated by a height h. Considering that the conductive plates are perfectly covered with treated polyimide, it can be assumed that the director $\overrightarrow{n}$ is oriented in the direction of the grooves.

When applying a low frequency or static electric field to the conductive planes of the cell of Figure 2.20(a), a force is induced in the molecules to rotate them in the direction of the field. This force finds the resistance of the dipole–dipole intermolecular interactions which is strong. In other words, the local electric field on a molecule is the sum of the

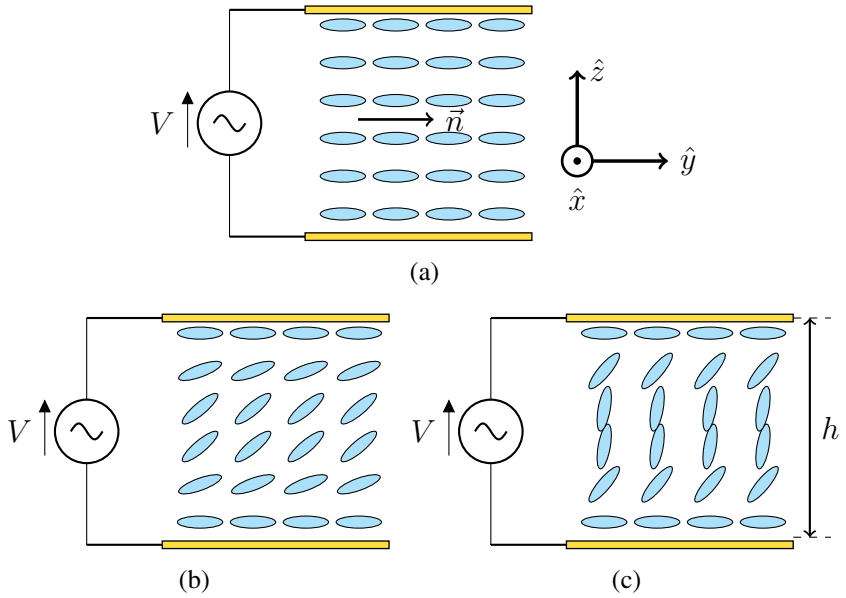

Figure 2.20: Process of alignment change with EM bias field.

externally applied electric field and the electric field produced by the dipole moments of other molecules [3]. If the applied field is not high enough, the molecules will mantain their initial position determined by the anchoring force of the alignment layer. The threshold voltage is known as the threshold voltage of Fréedericksz, and follows equation (2.2):

$$E_{th} = \frac{\pi}{h}\sqrt{\frac{K_{22}}{\varepsilon_0 \Delta\varepsilon}} \tag{2.2}$$

where h is the height of the LC cell, K_{22} is the elastic constant of Frank [71], ε_0 is the vacuum permittivity and $\Delta\varepsilon$ is the LC anisotropy.

When the applied voltage is above the threshold, the molecules start rotating in the direction of the applied voltage until the energy is minimum. When the applied bias voltage is increased, the alignment by the external field dominates and the angle between the director $\overrightarrow{n}$ and the bias voltage decreases, achieving a saturation state (molecules are parallel to the electric field).

It should be noted that the anchoring force that opposes to the electric field is not distributed uniformly throughout the cell. Nevertheless, this force is more intense the closer the molecules are to the alignment layers. This makes the orientation of the molecules of the LC not homogeneous throughout the entire height of the cell, as shown in Figure 2.20(b).

With this mechanism, an RF signal with the electric field in direction $\hat{z}$ will find, in absence of polarization voltage, the lowest permittivity value, i.e., the orthogonal permittiv-

ity $\varepsilon_{r\perp}$ (Figure 2.20(a)). When the polarization voltage increases (Figure 2.20(b)), the RF wave will find the highest permittivity, a value similar to the parallel permittivity $\varepsilon_{r\parallel}$ (Figure 2.20(c)). This feature can be used to design devices with a reconfigurable response.

For new LC mixtures, the dielectric permittivity values are not well defined in the bibliography at microwave frequencies. For this reason, a goal of the thesis is the characterization of this material for its usage in microwave devices. A review of the available methods for the dielectric characterization of materials, together with its applicability for LC materials, is done below.

2.4 Dielectric characterization methods

The dielectric permittivity is the constant that models how an electric field affects and is affected by the matter. The interaction of matter with electromagnetic fields may result in the variaton of permittivity. In the microwave range this phenomena is mainly caused by dipolar relaxation, and the absorption peaks in the infrared region and above are mainly due to atomic and electronic polarization [72]. The main mechanism of dielectric polarization at microwave frequency is dipole polarization.

Throughout this section, the main electromagnetic characterization methods of materials will be analyzed. In particular, the dielectric characterization of LC. These methods are usually organized regarding the electromagnetic structure used, thus obtaining a classification of four categories: parallel plates, coaxial probe, transmission line and methods based on resonant cavities.

The LC is an anisotropic dielectric material, thus its characterization requires to obtain, at least, its two extreme polarization states. That is, a complete dielectric characterization of this material requires the calculation of real and imaginary parts of its permittivity $\varepsilon_{r\parallel} = \varepsilon'_{r\parallel} + j\varepsilon''_{r\parallel}$ and $\varepsilon_{r\perp} = \varepsilon'_{r\perp} + j\varepsilon''_{r\perp}$. In an anisotropic crystalline solid this characterization is not a problem, since its molecules are kept oriented in a fixed direction. However, in the LC material some mechanism of alignment or polarization of its molecules must be implemented. Linearly polarized electric fields in a well-defined direction are needed to obtain the results of permittivity in both axes of the material.

2.4.1 Parallel plates method

This method, shown in Figure 2.21, is based on a capacitor formed by two parallel plates separated by the material that must be characterized (height h). The capacitor capacity (C) shows a linear dependence with the permittivity (ε_r) and the area of the its plates (A) so, to

measure the capacity and solve for the permittivity, equation (2.3) can be used.

$$\varepsilon_r = (C \cdot h)/A \tag{2.3}$$

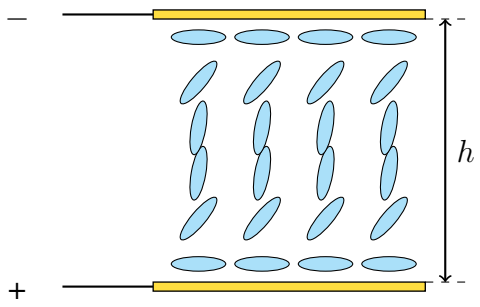

Figure 2.21: Schematic overview of parallel plates for characterizing LC permittivity.

Although this method of measurement is simple, cheap and fits perfectly to the geometry of an LC cell, it has several drawbacks. The capacity equation considers that the electric field is constant between the parallel plates. This assumption is only valid up to 1 GHz, which greatly limits its application scope. Moreover, the field used to measure the permittivity of the material is low frequency and, depending on its intensity, it could rotate the molecule in the measurement process by switching the state of the LC. This would make impossible the characterization of the dielectric anisotropy.

The simplicity of this method has led the manufacturers to use it to characterize LC at very low frequency values. Since manufacturers usually provide this value in the data-sheets, the analysis at low frequency is not necessary.

2.4.2 Coaxial probe method

This measurement method uses a coaxial cable terminated in open circuit, like an antenna that radiates a wave over the material to be characterized, as shown in Figure 2.22. The permitivity and/or permeability of the material is obtained from the analysis of the reflection experienced by the wave. This reflection is analyzed through the measurement of S_{11} parameter with a Vector Network Analyzer (VNA). The analysis bandwidth is limited to the bandwidth of the coaxial cable, which centers its operation range between 1 and 50 GHz. This makes it a good method to characterize materials in a wide bandwidth.

A solid coaxial cable can be introduced in the liquid of a container, which makes it one of the most used methods for the characterization of non-corrosive liquids. However, this method is not suitable for the measurement of materials with high or medium loss, such as

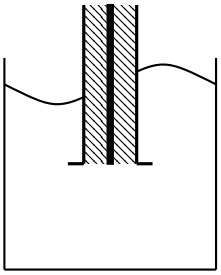

Figure 2.22: Outline of a coaxial probe used for measuring the LC permittivity.

LC, since the precision of the measurement decreases with the increment of the material loss due to the low efficiency of the coaxial cable as an antenna.

In addition, the characterization of LC with this method would require the preparation of two cells with orthogonal alignment layers to characterize the two states of polarization. An alignment layer to orientate the molecules radially to the coaxial cable, and another that orientates them perpendicularly. So that, the electric field lines and the LC molecules are arranged parallel and orthogonally, respectively. This layer of alignment is not only very difficult to implement, but any variation of the coaxial position introduces large deviations. These disadvantages advise against the use of this method for the characterization of the anisotropy of LC.

2.4.3 Transmision line method

This method uses a transmission line or a waveguide. These lines are partially or fully loaded with the material to characterize. It is possible to analyze the electromagnetic properties of the material: permittivity, permeability and losses, by studying the tranmision and/or reflection parameters measured with a VNA and knowing the materials and dimensions of the guide.

This method is one of the most used for the characterization of LC mixtures. In the bibliography, there are examples that use different types of transmission lines: planar lines, such as the inverted microstrip [73], coaxial lines [74] and some types of SIW [75].

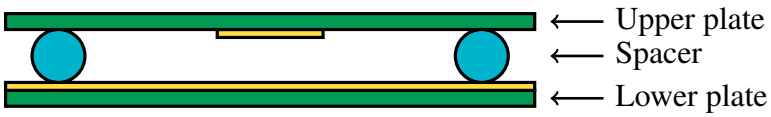

Figure 2.23: Schematic overview of an inverted microstrip. In green the supporting substrate, in yellow the conductive copper (line and ground), and in blue the spacers.

The most popular is the inverted microstrip (depicted in Figure 2.23), which is composed by an LC cell on which a conductive material has been deposited, usually copper, to shape the line and the ground of the microstrip. The supporting material is typically glass. The use of glass allows to verify optically the presence of bubbles and the correct orientation of the LC molecules created by the alignment layer. Another solution is the use of conventional substrates for microwave circuits (PCB), since they are perfectly characterized at the frequencies of interest. Nevertheless, these materials are not transparent and do not allow to observe the correct filling of the device.

An alternative line used for the characterization of LC is the circular coaxial line. However, as in the case of the coaxial probe, it presents a serious problem with its electric polarization. The parallel and perpendicular states correspond to the orientation of the molecules radially and longitudinally. This is difficult to get since the cylindrical surface makes impossible the application of an anchoring layer. For this line, toroidal magnets or coils around the coaxial line are used to induce a magnetic field high enough to polarize the LC in its two positions [24, 74].

These methods have been widely used to characterize LC materials because they can get results in a relatively large bandwidth, normally related to the mono-mode bandwidth of the line. However, the precision of the obtained results is not very high for materials with low or medium loss, since it is difficult to discern among the different sources that introduce loss (deposited metal, glass or substrate, LC loss). Moreover, in most cases, the method requires a complex design of the polarization networks (biasing), and the manufacturing of these transmission lines is not trivial, requiring a high analysis and design effort.

2.4.4 Resonant cavities method

In the methods based on resonant cavities, the material is part of a resonant structure, hence its electromagnetic properties can be characterized thanks to the resonant properties of the measured structure. The dielectric properties of the material can only be characterized at one or a few discrete frequencies, corresponding to the resonance frequency of the different modes of the structure. However, these methods are widely used due to its great accuracy and sensitivity [72].

These methods are usually classified into resonant methods and perturbational methods. In the first ones, the material is the resonator itself, or an important part of it, and the properties of the sample are determined with the resonant properties of the set. In the perturbational methods, the material is not part of the resonator, but it is introduced in some way inside it. The electromagnetic properties of the material are calculated making use of the deviations in the resonance properties of the structure.

In [76] a rectangular cavity perturbation method is proposed for characterizing a polytetrafluoroethylene (PTFE) tube filled with LC, and in [77, 78] a split-post dielectric resonator technique is used for characterizing LC mixtures in silicon cells. There are also examples of resonator methods in planar structures as in [79], which uses a patch resonator.

The great possibilities offered by these methods make them optimal for characterizing the different LC mixtures. Since for the characterization of LC mixtures the resonant cavity method is used in this work, it is explained in depth in chapter 4.

Chapter 3

Analysis and design of filters based on alternating dielectric line sections

As mentioned before, Substrate Integrated Waveguide (SIW) technology [2] and H-plane directly coupled resonant cavities topology are widely used for the implementation of filters. Their design combines resonant cavities and impedance inverters. These impedance inverters are implemented by means of coupling windows whose width values change depending on the desired impedance value [38].

Nevertheless, this is only a way to implement the resonant inverter topology. Recently, the preliminary research of a bandpass filter based on a periodically drilled SIW structure has been proposed in [80], where perforations in the dielectric substrate allow to reduce the local effective permittivity, thus creating waveguide sections below cutoff.

In this chapter an alternative solution to the previous layout is proposed. It consists of alternating waveguide sections with and without dielectric material, keeping constant the width of the whole structure. In other words, for reducing the permittivity of the sections below cutoff, they are completely emptied instead of perforating some holes. The empty line sections implement immittance inverters and the dilectric filled lines act as resonant sections. This allows to study the variation of the frequency response of a filter when it is filled with a dielectric material in alternative sections.

There are several commercial tools, like Ansys HFSS and CST Studio Suite, based on numerical methods that enable to carry out the analysis and design of these structures, but they require a very high computational time during the analysis process. This negatively affects the automated design of these devices, since the optimization process of the design requires a huge number of iterations for the analysis of the structure. In order to solve this problem, firstly, an efficient and accurate multimodal analysis method of the device has been developed. Moreover, its efficiency and accuracy have been compared with a commercial

software. Afterwards, the filter layout is depicted and the tool is used for designing a prototype that is finally manufactured and measured. Finally, the out-of-band response is analyzed in depth, and two more filters are manufactured to prove the behaviour of the rejected band for the new proposed topology.

3.1 Analysis of the filter

The developed method allows calculating the scattering parameters matrix of one filtering structure based on alternating dielectric line sections considering M modes. This multimodal scattering matrix gives, for each mode or solution of the wave equation of the electromagnetic fields, the transmission and reflection parameters of the structure, i.e. its electromagnetic behaviour.

The device under analysis is considered as a waveguide with N different sections of length $l^{(i)}$ and $N-1$ dielectric discontinuities as shown in Figure 3.1. On the one hand, the sections filled with a dielectric material, ε_r, which are the odd sections in the figure (except the first and the last one that are the input and output sections) behave as resonant cavities. On the other hand, the empty sections, ε_0, (even ones in the figure) are the coupling sections.

For the analysis, the input and output normalized electric and magnetic fields are defined for each section and mode. At each discontinuity, the continuity of electric and magnetic transverse fields is forced for the M considered modes, obtaining $2(N-1)$ equations for each mode. These equations are solved recursively obtaining the relationships between the input and output voltages of the first and last sections. The relations of these normalized voltages determine the scattering matrix (**S**) of the whole device.

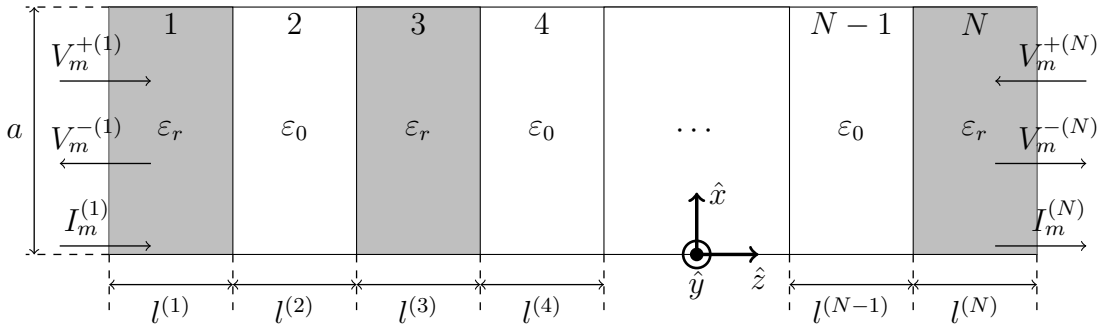

Figure 3.1: Alternating dielectric line sections waveguide filter and its reference system. In gray the dielectric filled resonant line sections. In white the empty coupling line sections.

Since both the geometry and the excitation are invariant in height (axis $\hat{y}$), for the analysis, only TE_{m0} modes are considered. Furthermore, although there are infinite modes, only the first M modes (ordered according to increasing value of each cut-off wavenumber) are selected.

The electric ($\overrightarrow{E}_t^{(i)}$) and magnetic ($\overrightarrow{H}_t^{(i)}$) transverse fields for these TE_{m0} modes of each section i of the waveguide are defined by (3.1) and (3.2), respectively [81].

$$\overrightarrow{E}_t^{(i)} = \sum_{m=1}^{M} V_m^{(i)}(z)\,\overrightarrow{e}_m^{(i)}(x) \tag{3.1}$$

$$\overrightarrow{H}_t^{(i)} = \sum_{m=1}^{M} I_m^{(i)}(z)\,\overrightarrow{h}_m^{(i)}(x) \tag{3.2}$$

where $V_m^{(i)}(z)$ and $I_m^{(i)}(z)$ are, respectively, the amplitude of the E-field and H-field components of the m-th mode of the i-th waveguide section composed by the incident ($V_m^{+(i)}$) and reflected field ($V_m^{-(i)}$). Additionally, $\overrightarrow{e}_m^{(i)}$ and $\overrightarrow{h}_m^{(i)}$ are the m-th modes in the i-th section:

$$V_m^{(i)}(z) = V_m^{+(i)} \mathrm{e}^{-\gamma_m^{(i)} z} + V_m^{-(i)} \mathrm{e}^{\gamma_m^{(i)} z} \tag{3.3}$$

$$\overrightarrow{e}_m^{(i)} = -\hat{y}\sqrt{\tfrac{2Z_{0m}^{(i)}}{a}}\sin\left(\tfrac{m\pi x}{a}\right)$$

$$I_m^{(i)}(z) = \tfrac{V_m^{+(i)}}{Z_{0m}^{(i)}} \mathrm{e}^{-\gamma_m^{(i)} z} - \tfrac{V_m^{-(i)}}{Z_{0m}^{(i)}} \mathrm{e}^{\gamma_m^{(i)} z} \tag{3.4}$$

$$\overrightarrow{h}_m^{(i)} = \hat{x}\sqrt{\tfrac{2Z_{0m}^{(i)}}{a}}\sin\left(\tfrac{m\pi x}{a}\right)$$

In these equalities:

- m and i are, respectively, the index of the correspondent guided mode and the index of the section.
- M is the number of guided modes.
- a is the width of the structure. In the structure considered in this work a is the same for all the sections i.
- $Z_{0m}^{(i)}$ is the modal characteristic impedance of the TE_{m0} mode in the i-th section.
- $\gamma_m^{(i)}$ is the propagation constant of the TE_{m0} mode in the i-th section.

These expressions are the result of the solution of the basic electromagnetism equations in a rectangular waveguide [81].

For an even section, the dielectric permittivity of the medium is that of the vacuum (ε_0), but in odd sections, there is a different dielectric (ε_r), so that:

$$Z_{0m}^{(i)} = \begin{cases} \frac{j\omega\mu}{\gamma_m^{(i)}} & \text{for even } i \\ \\ \frac{j\omega\mu}{\gamma_m^{(i)}} & \text{for odd } i \end{cases} \tag{3.5}$$

$$\gamma_m^{(i)} = \begin{cases} \frac{2\pi}{\lambda_0}\sqrt{\left(\frac{m}{2a/\lambda_0}\right)^2 - 1} & \textit{for even } i \\ \\ \frac{2\pi}{\lambda_0}\sqrt{\left(\frac{m}{2a/\lambda_0}\right)^2 - \varepsilon_r} & \textit{for odd } i \end{cases} \tag{3.6}$$

In these equalities:

– ω is the angular velocity.

– μ is the magnetic permittivity of the medium (in this case μ=μ_0).

– λ_0 is the wavelength of the electromagnetic wave in the vacuum.

After the analysis of these equalities, the next problem is obtained:

– $2N$ unknowns, since there are $V_m^{+(i)}$ and $V_m^{-(i)}$ for $i = 1, 2, \ldots N$

– $2(N-1)$ equations, since transverse fields continuity is forced, in $N-1$ discontinuities

There are $2(N-1) = 2N-2$ equations for $2N$ unknowns, so $V_m^{+(1)}$ and $V_m^{-(N)}$ have to be figured out. They are given by:

$$V_m^{(1)} = Z_m^{(1,1)} I_m^{(1)} + Z_m^{(1,N)} I_m^{(N)} \tag{3.7}$$

$$V_m^{(N)} = Z_m^{(N,1)} I_m^{(1)} + Z_m^{(N,N)} I_m^{(N)} \tag{3.8}$$

where $V_m^{(1)}$, $I_m^{(1)}$ depends on $V_m^{+(1)}$, $V_m^{-(1)}$, in addition $V_m^{(N)}$, $I_m^{(N)}$ depends on $V_m^{+(N)}$, $V_m^{-(N)}$ as seen before.

To obtain the **S** matrix, $V_m^{+(N)}$, $V_m^{-(N)}$ have to be related with $V_m^{+(1)}$, $V_m^{-(1)}$ by forcing continuity of electric and magnetic transverse fields on each discontinuity.

As $\overrightarrow{e}_m(x,y)$ and $\overrightarrow{e}_n(x,y)$, as well as $\overrightarrow{h}_m(x,y)$ and $\overrightarrow{h}_n(x,y)$, with $m \neq n$ are orthogonal, when the equalities of electric and magnetic fields are scalarly multiplied by $\overrightarrow{e}_n(x,y)$ and $\overrightarrow{h}_n(x,y)$ respectively, it is obtained:

$$V_m^{+(i)}\mathrm{e}^{-\gamma_m^{(i)}l^{(i)}} + V_m^{-(i)}\mathrm{e}^{\gamma_m^{(i)}l^{(i)}} = V_m^{+(i+1)} + V_m^{-(i+1)} \tag{3.9}$$

$$\frac{V_m^{+(i)}}{Z_{0m}^{(i)}}\mathrm{e}^{-\gamma_m^{(i)}l^{(i)}} - \frac{V_m^{-(i)}}{Z_{0m}^{(i)}}\mathrm{e}^{\gamma_m^{(i)}l^{(i)}} = \frac{V_m^{+(i+1)}}{Z_{0m}^{(i+1)}} - \frac{V_m^{-(i+1)}}{Z_{0m}^{(i+1)}} \tag{3.10}$$

Doing (3.9) + (3.10)$\cdot Z_{0m}^{(i+1)}$ and (3.9) − (3.10)$\cdot Z_{0m}^{(i+1)}$:

$$\begin{pmatrix} V_m^{+(i+1)} \\ V_m^{-(i+1)} \end{pmatrix} = \mathbf{A}_m^{(i)} \begin{pmatrix} V_m^{+(i)} \\ V_m^{-(i)} \end{pmatrix} \tag{3.11}$$

where

$$\mathbf{A}_m^{(i)} = \frac{1}{2}\left(\begin{array}{c|c} \mathrm{e}^{-\gamma_m^{(i)}l^{(i)}}\left(1+\dfrac{Z_{0m}^{(i+1)}}{Z_{0m}^{(i)}}\right) & \mathrm{e}^{\gamma_m^{(i)}l^{(i)}}\left(1-\dfrac{Z_{0m}^{(i+1)}}{Z_{0m}^{(i)}}\right) \\ \hline \mathrm{e}^{-\gamma_m^{(i)}l^{(i)}}\left(1-\dfrac{Z_{0m}^{(i+1)}}{Z_{0m}^{(i)}}\right) & \mathrm{e}^{\gamma_m^{(i)}l^{(i)}}\left(1+\dfrac{Z_{0m}^{(i+1)}}{Z_{0m}^{(i)}}\right) \end{array}\right) \tag{3.12}$$

The number of discontinuities is a multiple of 2 and N is odd, since the first and the last mediums are different from vacuum. The relation between the input and output waves in the first and last section is:

$$\begin{pmatrix} V_m^{+(N)} \\ V_m^{-(N)} \end{pmatrix} = \underbrace{\prod_{k=\frac{N-1}{2}}^{1} \mathbf{A}_m^{(2k)}\mathbf{A}_m^{(2k-1)}}_{\mathbf{A}_m} \begin{pmatrix} V_m^{+(1)} \\ V_m^{-(1)} \end{pmatrix} \tag{3.13}$$

The resulting $\mathbf{A}_m$ is a 2×2 matrix of elements a_{11}, a_{12}, a_{21} and a_{22} . As mentioned before, the scattering matrix ($\mathbf{S}$) relates the input and output voltage waves [1], considering the diagram in Figure 3.1, the values of the elements of this matrix can be expressed as:

$$\begin{aligned} V_m^{-(1)} &= s_{11}V_m^{+(1)} + s_{12}V_m^{-(N)} \\ V_m^{+(N)} &= s_{21}V_m^{+(1)} + s_{22}V_m^{-(N)} \end{aligned} \tag{3.14}$$

By operating the expression (3.13) in order to get similar equations to (3.14), it is obtained that:

$$V_m^{-(1)} = \underbrace{-a_{22}^{-1}a_{21}}_{s_{11}}V_m^{+(1)} + \underbrace{a_{22}^{-1}}_{s_{12}}V_m^{-(N)} \tag{3.15}$$

$$V_m^{+(N)} = \underbrace{a_{11} - a_{12}a_{22}^{-1}a_{21}}_{s_{21}} V_m^{+(1)} + \underbrace{a_{12}a_{22}^{-1}}_{s_{22}} V_m^{-(N)} \tag{3.16}$$

By comparing (3.15) and (3.16) with the equations in (3.14), the values of the matrix $\mathbf{S}_m$ may be determined, as indicated in the above expressions. Thus, each mode of the $\mathbf{S}$ matrix is finally expressed as follows:

$$\mathbf{S}_m = \left(\begin{array}{c|c} -a_{22}^{-1}a_{21} & a_{22}^{-1} \\ \hline a_{11} - a_{12}a_{22}^{-1}a_{21} & a_{12}a_{22}^{-1} \end{array}\right) \tag{3.17}$$

The multimodal $\mathbf{S}$ matrix can be written as:

$$\mathbf{S} = \left(\begin{array}{cccc|cccc} s_1^{(1,1)} & 0 & \cdots & 0 & s_1^{(1,2)} & 0 & \cdots & 0 \\ 0 & s_2^{(1,1)} & \cdots & 0 & 0 & s_2^{(1,2)} & \cdots & 0 \\ \vdots & \ddots & & \vdots & | & \ddots & & \vdots \\ 0 & \cdots & s_{M-1}^{(1,1)} & 0 & 0 & \cdots & s_{M-1}^{(1,2)} & 0 \\ 0 & \cdots & 0 & s_M^{(1,1)} & 0 & \cdots & 0 & s_M^{(1,2)} \\ \hline s_1^{(2,1)} & 0 & \cdots & 0 & s_1^{(2,2)} & 0 & \cdots & 0 \\ 0 & s_2^{(2,1)} & \cdots & 0 & 0 & s_2^{(2,2)} & \cdots & 0 \\ \vdots & \ddots & & \vdots & \vdots & \ddots & & \vdots \\ 0 & \cdots & s_{M-1}^{(2,1)} & 0 & 0 & \cdots & s_{M-1}^{(2,2)} & 0 \\ 0 & \cdots & 0 & s_M^{(2,1)} & 0 & \cdots & 0 & s_M^{(2,2)} \end{array}\right) \tag{3.18}$$

This matrix is $2M \times 2M$, since each block is composed by one $M \times M$ matrix. Moreover, they are diagonal matrices, so $\mathbf{S}$ is a tri-diagonal matrix (composed of 4 diagonal matrix blocks).

3.2 Design method

In this section the design process is described in detail. The filter is designed forcing the structure to match the behaviour of an ideal network composed by resonating sections (of half-wavelength length) plus inverters (or coupling sections), as shown in Figure 3.2.

This is a classical representation of an ideal filter prototype, as it is detailed in [53], where the expressions for computing the values of all the involved network elements (in order to implement, in this case, a standard Chebyshev response with constant ripple in the pass-band) can be found.

In the proposed structure, the function of the ideal impedance inverters is accomplished

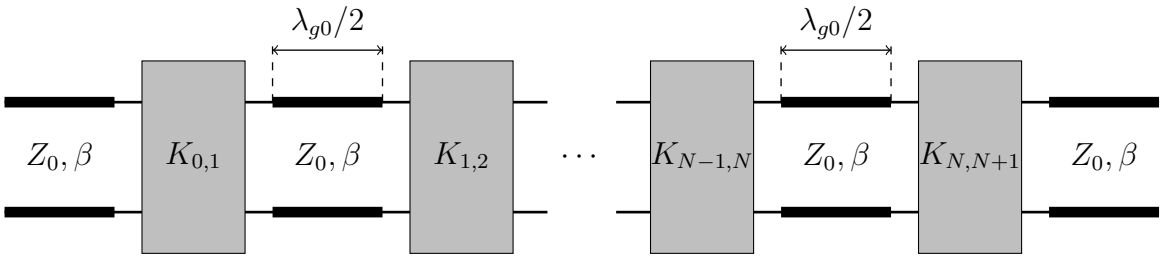

Figure 3.2: Ideal network of a filter based on resonators and inverters.

by the line sections without dielectric accessed with lines filled with dielectric (see Figure 3.1). The length of each one of these empty sections is optimized, so that the amplitude of the refection coefficient matches that of the corresponding ideal inverter that the empty line section has to implement. It is important to note that the empty line sections are simulated here with ports of line sections filled with dielectric. That is, the steps from filled to empty line are included in the simulation.

The previous optimization goal is done by seeking the zero of the equation (3.19):

$$\frac{1-|S_{11}|}{1+|S_{11}|} - (\overline{K_{l,l+1}})^2 = 0 \tag{3.19}$$

where $|S_{11}|$ is the reflection coefficient of the empty line section with ports of line sections filled with dielectric, and $\overline{K_{l,l+1}}$ is the normalized constant of the corresponding ideal impedance inverter.

Once the length of the empty line section is fixed, this section provides the same amplitude of the reflection coefficient as that of the corresponding ideal inverter. But the phase is not yet the same. So, additional sections of lines of length l_i, filled with dielectric, have to be added, before and after the empty line section, in order to recover the ideal inverter behaviour, in terms of both the amplitude and the phase of the reflection coefficient.

The phase of the refection coefficient of an ideal inverter is π, so the length l_i of the lines added before and after the empty line section can be obtained with equation (3.20).

$$\measuredangle|S_{11}| - 2\beta l_i = \pi \tag{3.20}$$

This gives:

$$l_i = \frac{\measuredangle|S_{11}| - \pi}{2\beta} \tag{3.21}$$

Once the additional lengths required by each empty line section to behave like an ideal

impedance inverter are determined, these lengths have to be added to the lengths of the resonators placed at both sides of the empty line section. Initially, each resonator length was $\lambda_{g0}/2$. After the addition of these extra lengths corresponding to the preceding and subsequent empty line sections (acting as inverters), the length of each resonator i-th will be:

$$l_{Res}^{(i)} = \frac{\lambda_{g0}}{2} + l_i + l_{i+1} \tag{3.22}$$

In practice, the lengths l_i and l_{i+1} are negative, which means that the lengths of the resonators are shortened. This explains why the line sections with dielectric material are shorter than half-wavelength, although they act as resonators. In this case, the final lengths of the line sections acting as resonators are even shorter than those of the conventional designs based on classical half-wavelength SIW resonators, due to the different values obtained for the additional lengths to be placed before and after each section that acts as inverter. This is better illustrated in the following section with details of the dimensions obtained in different phases of the design of the filter presented in this work. Therefore, using a different practical implementation of the inverter in the proposed filter (empty line section between two dielectric-loaded lines), provides different length corrections to the resonator line sections than in the conventional SIW filter (where inductive coupling iris between adjacent cavities act as inverters).

3.3 Validation of the tool

The analysis and design theories are implemented in MatLab and fully integrated into a Computer Aided Design (CAD) tool, in order to have a software able to calculate the dimensions of a filter given certain specifications as central frequency, bandwidth, ripple, number of cavities, permittivity values and so on.

The design process is carried out in four stages:

- **Theoretical synthesis**. The first step is the theoretical synthesis of a starting point based on the ideal network, in order to extract the values of the inverters and resonators for the Chebyshev prototype. This is a well known theoretical process [53].

- **Initial value**. Once the values of the ideal network have been obtained, these are used to calculate an initial point of the physical parameters of the structure, i.e. the lengths of the resonant line sections and the coupling line sections. The mode-matching method has been used to simulate the reflection coefficient of the empty line sections, in order to find the optimum length of these sections that provide the same amplitude and phase of the reflection coefficient of the corresponding ideal inverter [38].

- **Modal optimization**. When the previous procedure is complete, and initial values are obtained for all the dimensions of the structure, a fine-tuning optimization of these design dimensions is done to get a frequency response as much similar as possible to the ideal response. The optimization process is based on several iterations of the analysis of the structure. In each iteration, the analysis tool calculates the electromagnetic response of the structure. Then it is compared to the desired response; if the difference between them does not reach a predefined minimum, the structure parameters are slightly changed and the process is repeated. Obviously, the strategy for changing these physical dimensions is not random, but a set of optimization algorithms are used [25]. The whole process is described in [42], where its efficiency and robustness are improved by using the adequate combination of algorithms, i.e. the hybridization of Direct Search with Coordinate Rotation [82], Downhill Simplex Method [26] and Broyden Fletcher Goldfarb Shanno (BFGS) [83] methods.

- **Realistic optimization**. Finally, a design of the realistic filter is done. The employed mode-matching method assumes that the lateral walls are solid, but in the proposed structure, the walls of the dielectric-filled sections are rows of metallized vias. Thus, the mode-matching model is not enough accurate for these sections, so the CST full-wave simulator is used during this last optimization process, thus ensuring that the final design is fully accurate. Moreover, all other technological issues concerning manufacturing of a real filter have been taken into account in this stage: transition to microstrip access lines and height of soldering layers.

In order to test the validity of the proposed structure as a filter, and to establish a consistent design procedure, a simple filter with only one resonator is first designed using the standard procedure of [53], which uses an equivalent ideal network composed of ideal inverters and resonators as a reference. In Figure 3.3 the equivalent network for this 1-pole filter is shown, designed for providing a Chebyshev response with the following specifications:

– Number of cavities: N = 1 cavity.

– Central frequency: f_0 = 11 GHz.

– Bandwidth: 300 MHz.

– Dielectric permittivity: ε_r = 6.

– Cavities width: a = 8 mm.

The input and output lines of the resonator are lines filled with dielectric. The desired response is achieved with the ideal equivalent network when the inverters have normalized inversion constants $\overline{K}_{0,1} = \overline{K}_{1,2} = 0.3529$ (first stage).

Considering the topology described above (Figure 3.1 with $N = 1$), the resulting resonator layout is shown in Figure 3.3. The ideal inverter of the resonator will be implemented with an empty line section of length $l_{Win}^{(1)}$. So, an empty line section below cut-off of width $a = 8$ mm, accessed with filled lines, is simulated using the fast mode-matching method described before, which considers the filled line sections as closed rectangular waveguides filled with dielectric. The length $l_{Win}^{(1)}$ is optimized until the amplitude of the refection coefficient is the same than that of the ideal inverter, which happens when $l_{Win}^{(1)} = 3.204$ mm. The next step is to find out where the reference planes have to be placed along the filled accessing lines, in order to have the same phase of the reflection coefficient than that of an ideal inverter (i.e. phase π). This happens when $l_{corr}^{(1)} = -2.1661$ mm. So, the empty line section together with two accessing lines filled with dielectric of lengths $l_{corr}^{(1)}$ behaves as an ideal inverter. When both adjacent inverters are connected to the resonator (a filled line section of length $\lambda_{g_0}/2$), the total length of the filled line between the two empty sections is $l_{Res}^{(1)} = \lambda_{g_0}/2 + 2 \cdot l_{corr}^{(1)} = 7.7414 - 2 \cdot 2.1661 = 3.4092$ mm. These values of $l_{Win}^{(1)}$ and $l_{Res}^{(1)}$ are used as an initial point (second stage), and are fine optimized with the developed mode-matching method to have a frequency response as much similar as possible to the ideal one (third stage).

Figure 3.4 shows the relation between the dimensions of the filled line sections and the air filled sections with the resonance frequency and the coupling coefficient, respectively.

Figure 3.5 shows the reflection and transmission coefficients of the single resonator filter with the values of $l_{Win}^{(1)}$ and $l_{Res}^{(1)}$ obtained with this procedure. These parameters are compared with those of the ideal network, and a very good agreement can be observed.

The electric field distribution inside the single resonator filter is also included in Figure 3.6. It can be observed that the electromagnetic field is concentrated in the line sections filled with dielectric, which validates the idea that it behaves as a resonator, and that its short length is consequence of the negative lengths that have been added in order to implement the ideal inverter with the empty line section. The field distribution also proves that the empty line sections behave as the filter coupling elements.

This structure can be repeated for filters with any arbitrary number of resonators (N), with the exception that, in the optimization processes, the segmentation technique described in [42] is used in order to speed up the overall process, optimizing only a small amount of design parameters in each step of the segmentation.

The results show that the procedure used for the synthesis and design of a traditional H-

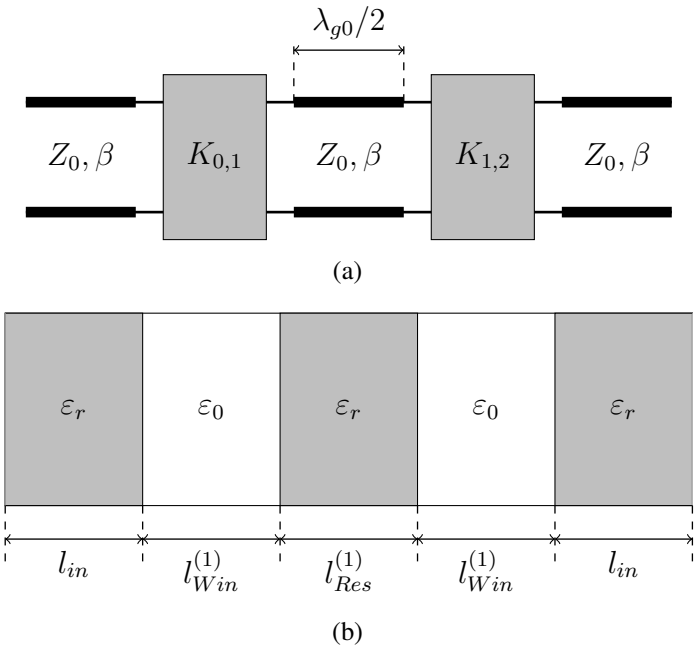

Figure 3.3: Network of a resonator. (a) Ideal network based on resonators plus inverters. (b) Ideal network based on filled and empty line sections.

plane directly coupled cavities waveguide filter can also be used to synthesize and design the alternating dielectric line sections filter presented in this work, stating that the filled dielectric sections act as the resonators and the air-filled sections act as inverters.

Finally, the resulting optimized values with the mode-matching method are then used as an initial point for a new optimization with the commercial electromagnetic software (CST Studio Suite). It simulates a realistic and manufacturable prototype, and adjusts the response to that of the ideal network as much as possible (fourth stage). This is explained in detail in the following section.

Furthermore, in order to evaluate the efficiency (computational time) and the accuracy (frequency response) of the analysis tool, several filters with different number of cavities (2, 4, 6, 8, and 10 cavities) have been designed. The number of modes used in the analysis tool for all design cases is M = 11. This value is a trade-off, and it was selected after some research concerning its impact on two parameters: the computational time and the accuracy of the response. More information about the maximum number of modes used in modal analysis can be found in [50]. The specifications of these filters are detailed below, being the same for all the number of cavities. The dimensions (see Table 3.1) and the frequency responses of three of them are presented.

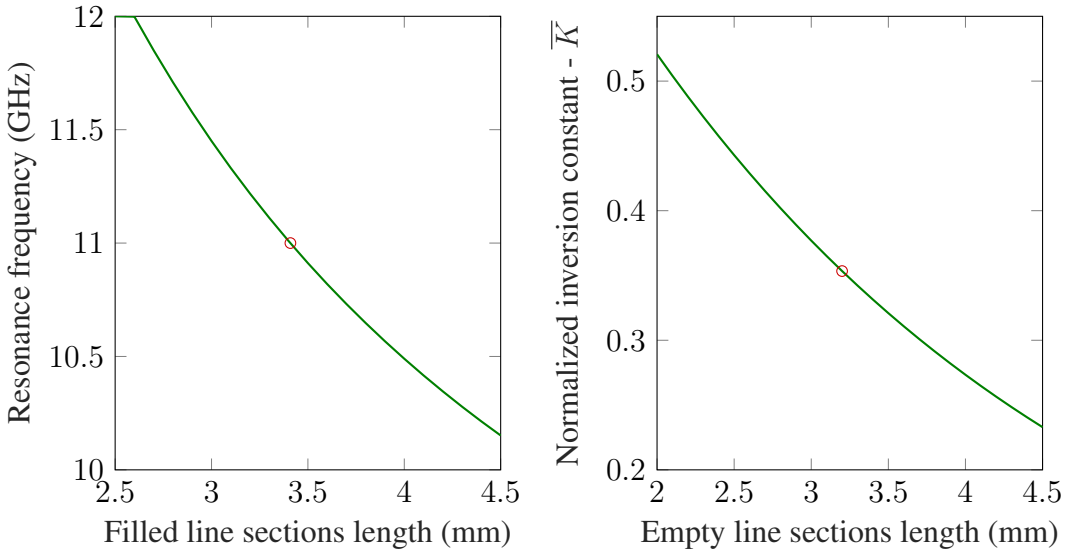

Figure 3.4: (a) Relation between dielectric filled line sections length and the resonance frequency. (b) Relation between empty line sections length and the normalized inversion constant.

- Number of cavities: N = 2, 4, 6, 8, and 10 resonant sections.
- Central frequency: f_0 = 11 GHz.
- Bandwidth: 300 MHz.
- Ripple: 0.01 dB.
- Return loss: 25 dB.
- Dielectric permittivity: ε_r = 9.2.
- Cavities width: a = 6.25 mm.
- Filter height: h = 1.27 mm.

Figure 3.7 shows the frequency response of a filter of two cavities, when it is analyzed with the developed modal tool, versus a commercial software (CST Studio Suite). Both modal and numerical analysis are compared to the ideal frequency response of a two cavities Chebysev filter. It is observed that there is a very good agreement between all of them. It means that the developed analysis tool is accurate enough.

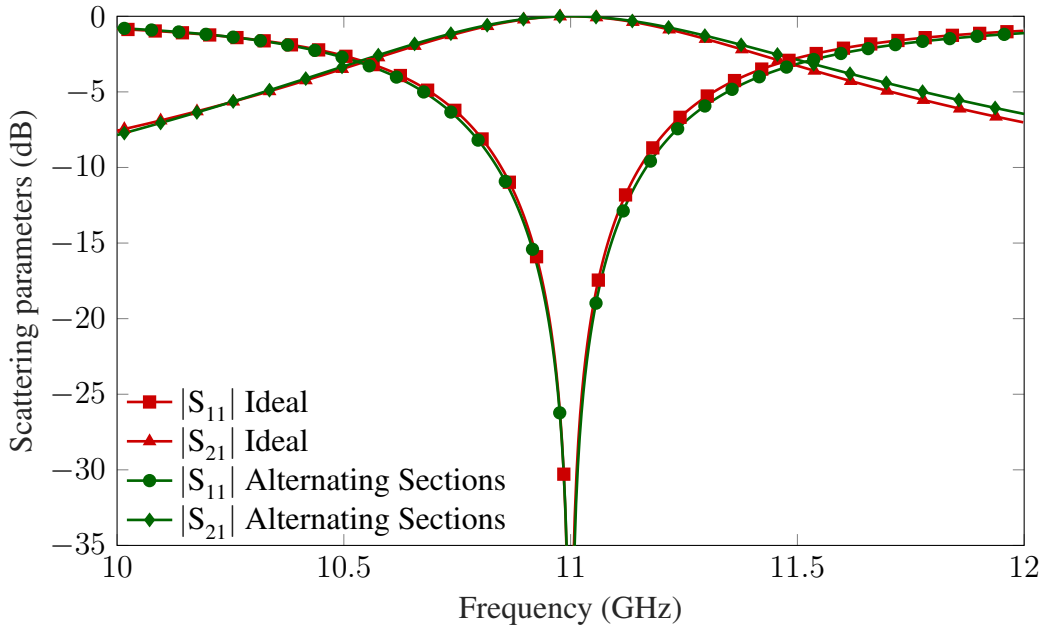

Figure 3.5: Frequency response comparison for 1-pole basic filter.

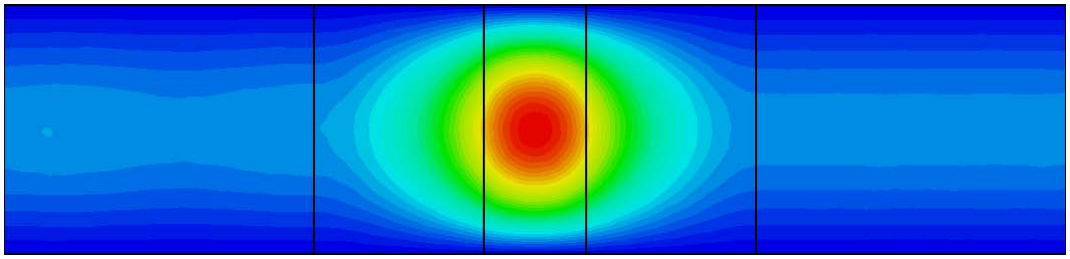

Figure 3.6: Electric field distribution at 11 GHz for 1-pole basic filter.

Figure 3.8 and Figure 3.9 show the same comparison that the previous figure but for a filter of four cavities and ten cavities, respectively. In these cases, it is also observed the very good agreement between all the frequency responses. The analysis tool can be used for filters of any order value.

Once the accuracy of the tool is checked, the efficiency is also tested. The computational time for the analysis of filters from two to ten cavities is shown in Table 3.2 for the modal method and CST commercial software. This time is calculated under the same conditions for both tools: computing processor, start and stop frequencies and number of sample points. All the materials used in CST are loss free, since the modal method does not take into account the loss. Moreover, the simulation boundary conditions have been applied as electric (E_t =

Filter 2 cavities		Filter 4 cavities		Filter 10 cavities	
$l^{(1)}$, $l^{(7)}$	10.000 mm	$l^{(1)}$, $l^{(11)}$	10.000 mm	$l^{(1)}$, $l^{(23)}$	10.000 mm
$l^{(2)}$, $l^{(6)}$	3.3621 mm	$l^{(2)}$, $l^{(10)}$	3.8364 mm	$l^{(2)}$, $l^{(22)}$	2.7824 mm
$l^{(3)}$, $l^{(5)}$	3.0673 mm	$l^{(3)}$, $l^{(9)}$	3.0628 mm	$l^{(3)}$, $l^{(21)}$	3.0766 mm
$l^{(4)}$	6.6046 mm	$l^{(4)}$, $l^{(8)}$	8.2163 mm	$l^{(4)}$, $l^{(20)}$	6.1136 mm
		$l^{(5)}$, $l^{(7)}$	3.0576 mm	$l^{(5)}$, $l^{(19)}$	3.0610 mm
		$l^{(6)}$	8.8717 mm	$l^{(6)}$, $l^{(18)}$	6.9589 mm
				$l^{(7)}$, $l^{(17)}$	3.0581 mm
				$l^{(8)}$, $l^{(16)}$	7.1551 mm
				$l^{(9)}$, $l^{(15)}$	3.0582 mm
				$l^{(10)}$, $l^{(14)}$	7.2139 mm
				$l^{(11)}$, $l^{(13)}$	3.0590 mm
				$l^{(12)}$	7.2225 mm

Table 3.1: Dimensions of the line sections of filters of 2, 4, and 10 cavities, according to Figure 3.1.

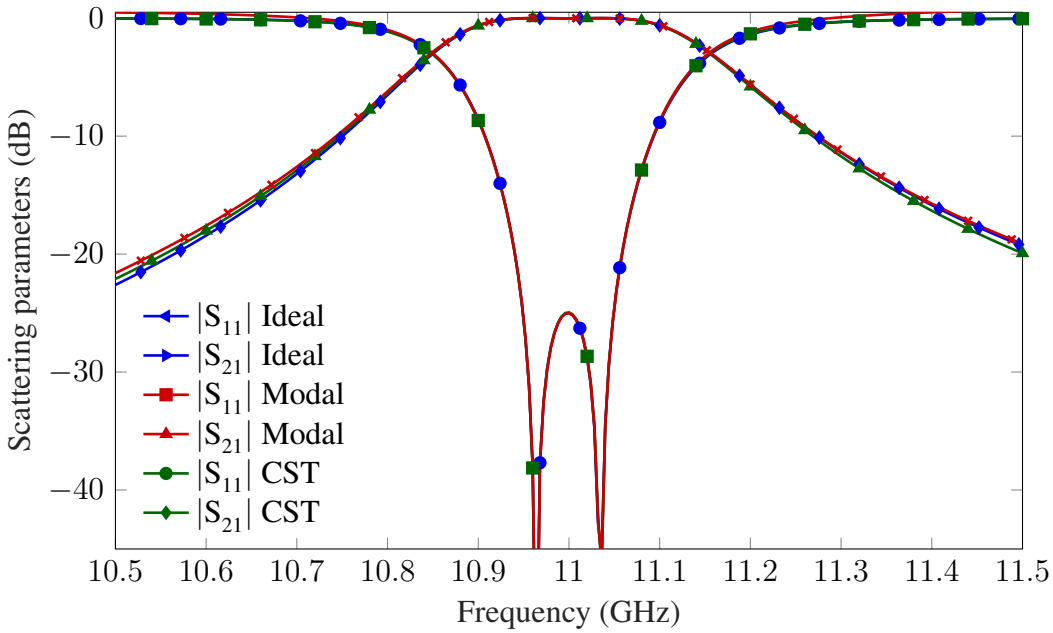

Figure 3.7: Comparison of frequency responses for a filter of two poles.

0) in all directions and the background properties as PEC, in order to have the most similar analysis conditions between both tools. The obtained times are plotted in Figure 3.10. It is observed that the computational time of the commercial software based on numerical methods increases linearly with a sharp slope when the number of cavities increases. However, in the case of the developed modal method, the time increases very slowly. It shows the advan-

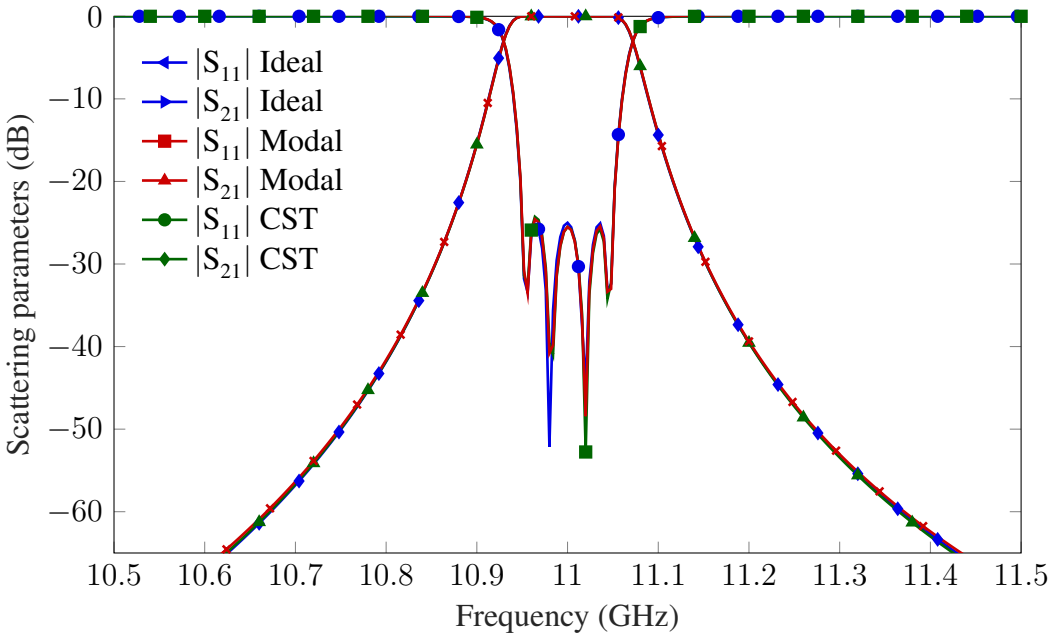

Figure 3.8: Comparison of frequency responses for a filter of four poles.

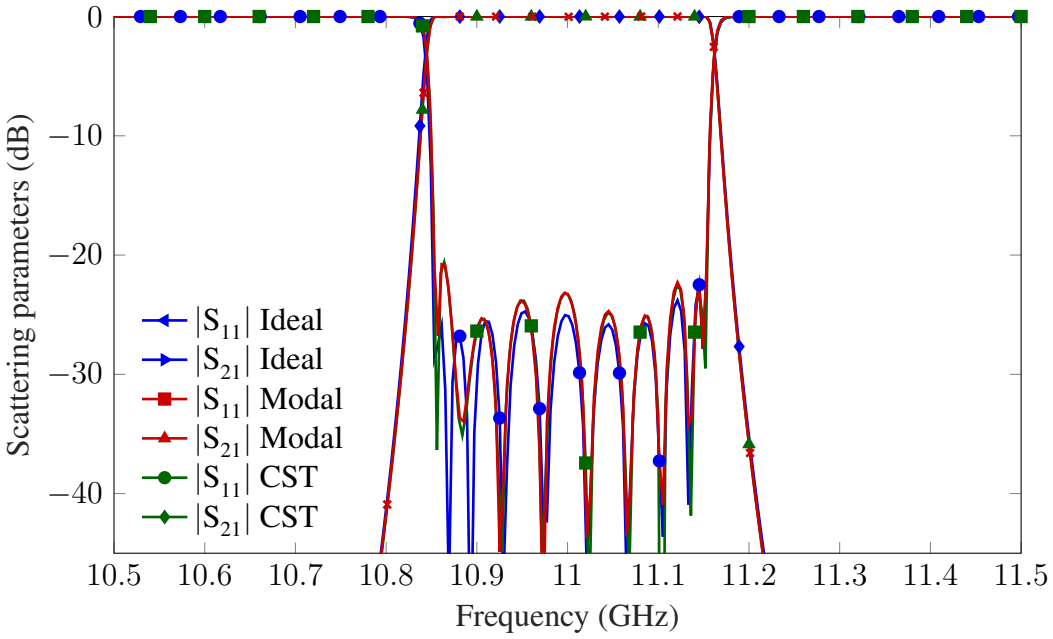

Figure 3.9: Comparison of frequency responses for a filter of ten poles.

tage of the new method versus the commercial one, which proves the convenience of using the modal analysis tool in the first stages of the design process.

Cavities	Modal Method	CST
2	2.70 s	40.00 s
4	4.28 s	80.00 s
6	5.79 s	130.00 s
8	7.15 s	160.00 s
10	8.85 s	194.00 s

Table 3.2: Computational time for the analysis of the filter.

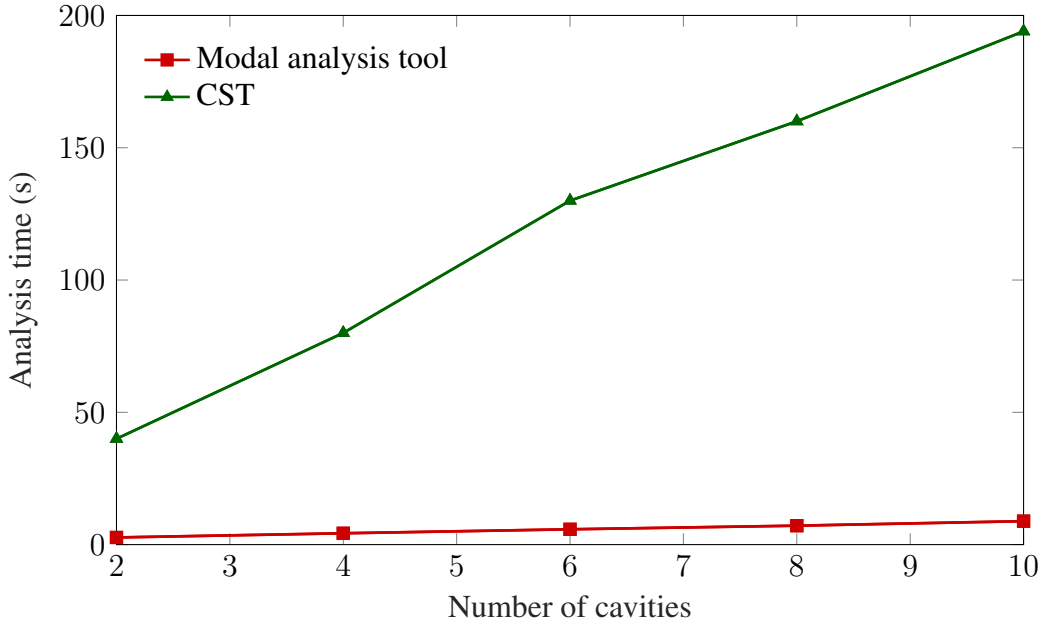

Figure 3.10: Computational time comparison between both methods.

3.4 Filter topology and design

Once the efficiency and accuracy of the developed modal method has been assessed, and an equivalent waveguide filter is obtained, a manufacturable real prototype can be designed and fabricated.

The strucutre is based on a combination of SIW [2] and ESIW [5] technologies. The line is developed into three different layers, two of them are the top and bottom covers of the line, and the other is the body of the transmission line. The top and bottom covers are just two metallic layers, and the body of the line contains the microstrip access line, the filter itself and the transition between microstrip and SIW.

The layout of the central layer is shown in Figure 3.11, where it can be seen the succession of substrate integrated line sections with and without dielectric. In the empty line sections,

the field is confined laterally using metallized walls. And in the dielectric filled line sections, metallized via holes, as in the traditional SIW, are used. As in the ESIW case, metallic top and bottom layers are finally added for confining the field in the empty line sections vertically. For a filter of order N, with N reflection zeros, N line sections with dielectric of lengths $l_{Res}^{(i)}$ ($i \in 1 \cdots N$) are used, acting as resonators. The empty line sections, where the fundamental mode is below cut-off, act as inverters, implementing the coupling between resonators and with the input and output lines. This gives $N + 1$ empty lines sections of length $l_{Win}^{(i)}$ ($i \in 1 \cdots N + 1$).

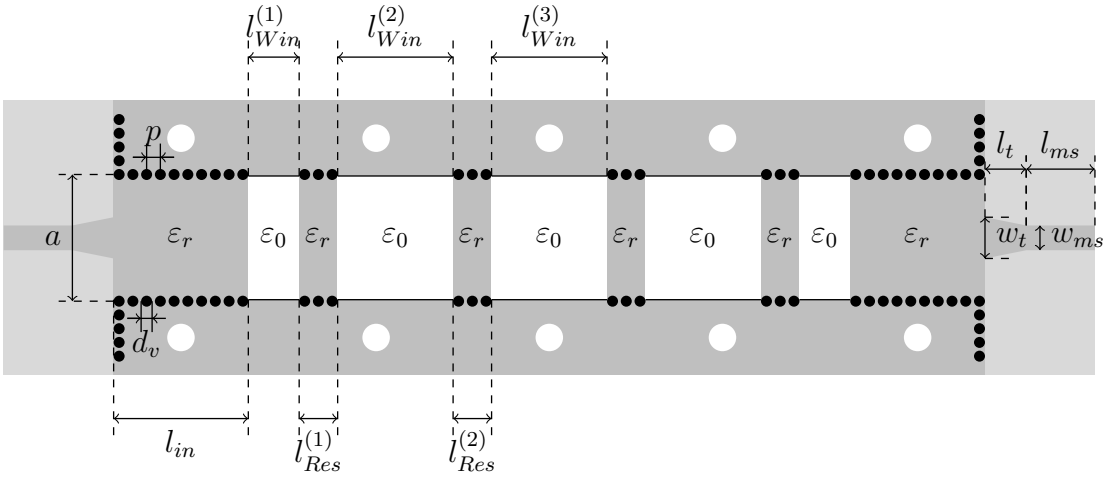

Figure 3.11: Layout of the central substrate of the filter based on alternating dielectric line sections (with $N = 4$). In black the metallized vias and the border copper metallization, in dark gray the copper metallization on top of the layer, in light gray the dielectric substrate, and in white the air-filled sections and the fastening screw holes. To close the air-filled sections, top and bottom copper covers are used.

Following the procedure described in the previous section, a Chebyshev response band-pass filter with the following specifications is designed:

- Number of cavities: N = 4 resonant sections.
- Central frequency: f_0 = 11 GHz.
- Bandwidth: 300 MHz.
- Ripple: 0.01 dB.
- Return loss: 25 dB.

– Dielectric permittivity: ε_r = 6.

– Cavities width: a = 8 mm.

– Filter height: h = 1.27 mm.

As mentioned before, this prototype of the proposed filtering device must be re-optimized in CST Studio Suite considering all the fabrication aspects, obtaining the resulting dimensions (considering the symmetry) shown in Table 3.3.

Parameter	Dimension
l_{in}	10.000 mm
$l_{Win}^{(1)}$	3.708 mm
$l_{Win}^{(2)}$	8.366 mm
$l_{Win}^{(3)}$	9.283 mm
$l_{Res}^{(1)}$	3.011 mm
$l_{Res}^{(2)}$	2.943 mm

Table 3.3: Dimensions of the bandpass filter.

On the other hand, a detailed view of the tapered transition from microstrip to SIW is shown in Figure 3.12. It has been synthesized as proposed in [84], where the transition is divided into two sections: the tapered microstrip line and the step between the microstrip and the rectangular waveguide (see Figure 3.12). The combination of these two parts provides a good matching over the complete SIW bandwidth, since microstrip matches very well the field distribution of the fundamental mode TE_{10} in the SIW. The obtaining dimensions (as shown in Figure 3.11) are depicted in Table 3.4, and the simulated frequency response is shown in Figure 3.13.

Parameter	Dimensions
w_t	3.084 mm
w_{ms}	1.800 mm
l_t	2.201 mm
l_{ms}	5.000 mm

Table 3.4: Dimensions of the tapered transition.

Finally, both the filter layout and the transition are simulated together and its frequency response is shown in Figure 3.14. The simulation only considers the bandpass, whereas an analysis of the out-of-band behaviour is done in the following section.

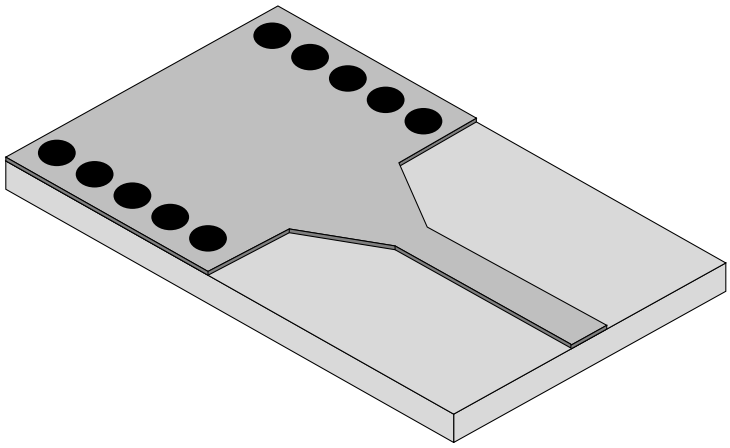

Figure 3.12: Layout of the tapered transition from microstrip to SIW.

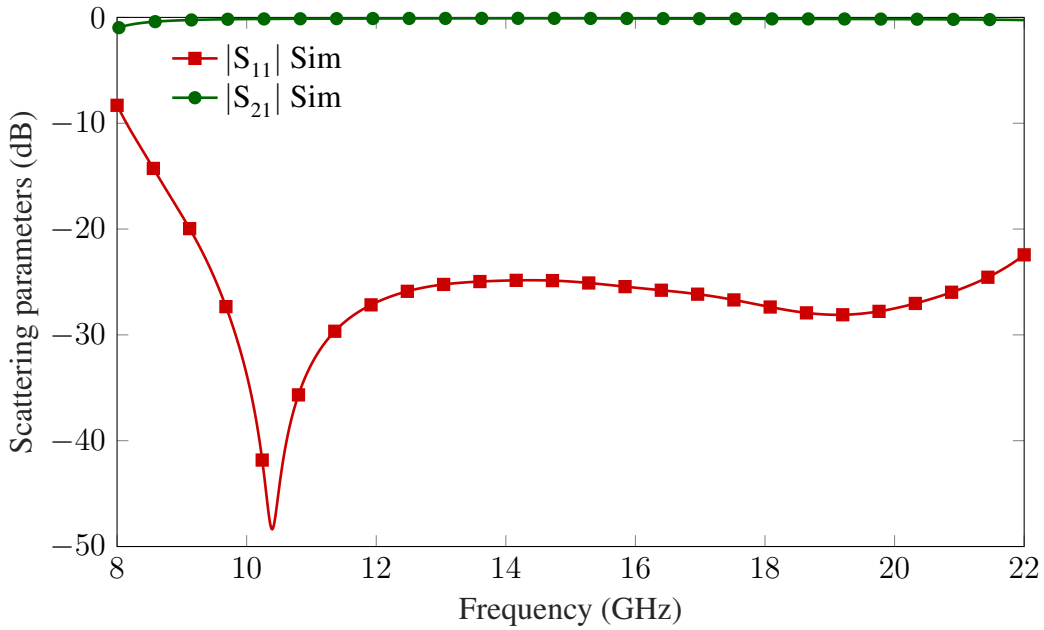

Figure 3.13: Simulated frequency response of the transition from microstrip to SIW.

3.5 Study of the out of band response

The out-of-band frequency response of microwave bandpass filters is degraded by the excitation of higher order modes in the resonators. Also, for most of the filters, the first spurious band due to the excitation of the second mode is relatively close to the frequency of the interest region. These undesired responses degrade the filter performance and may be critical in some applications, where high rejection and spurious-free out-band response are

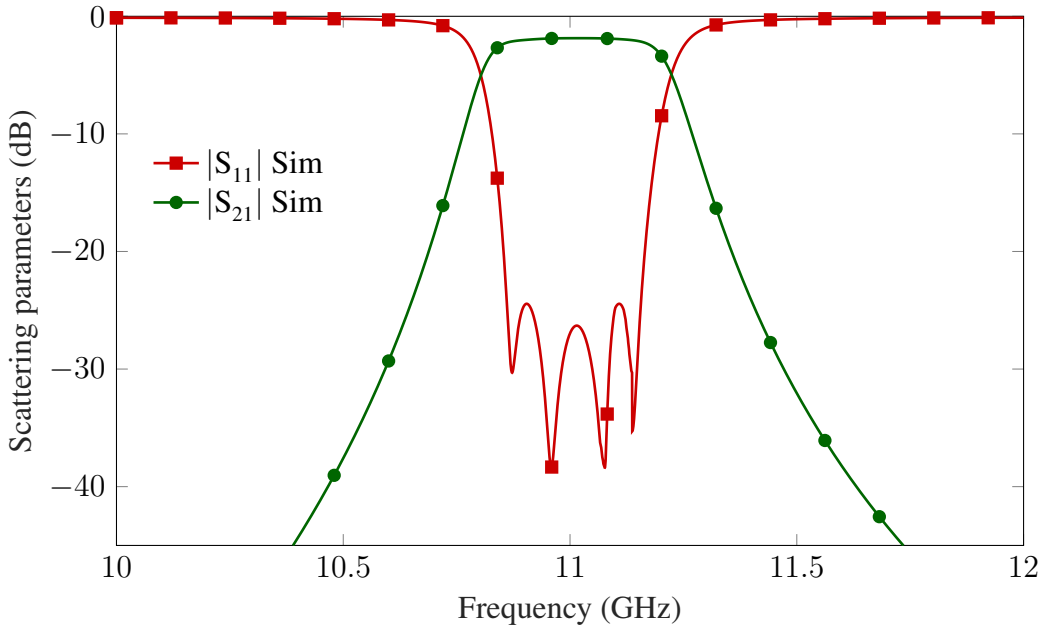

Figure 3.14: Simulated frequency response of the filter with transition from microstrip to SIW.

required. A study of the out-of-band behaviour is performed considering two parameters: the width and the depth of the rejected band.

3.5.1 Depth of the rejected band

The depth of the rejected band is related to the order of the filter, as stated in the study performed in [85]. By increasing the number of the filter sections, the value of the cited parameter can be increased. Figure 3.15 shows the depth of the rejected band for a filter with the same specifications than the previous one, i.e. centred at 11 GHz, with 300 MHz bandwidth, 0.01 dB ripple in the passband, and the same substrate with permittivity value ε_r = 6.

In this case, it has been designed with 2, 3, 4, 5 and 6 resonant sections. As it can be seen, the rejection band is deeper for the higher order filters. It is noticeable that the width of the rejected band is not related to the order of the filter, but to the permittivity value of the substrate (as it will be studied next). With the considered substrate, the second spurious is at $1.5 f_0$, no matter the number of resonant sections.

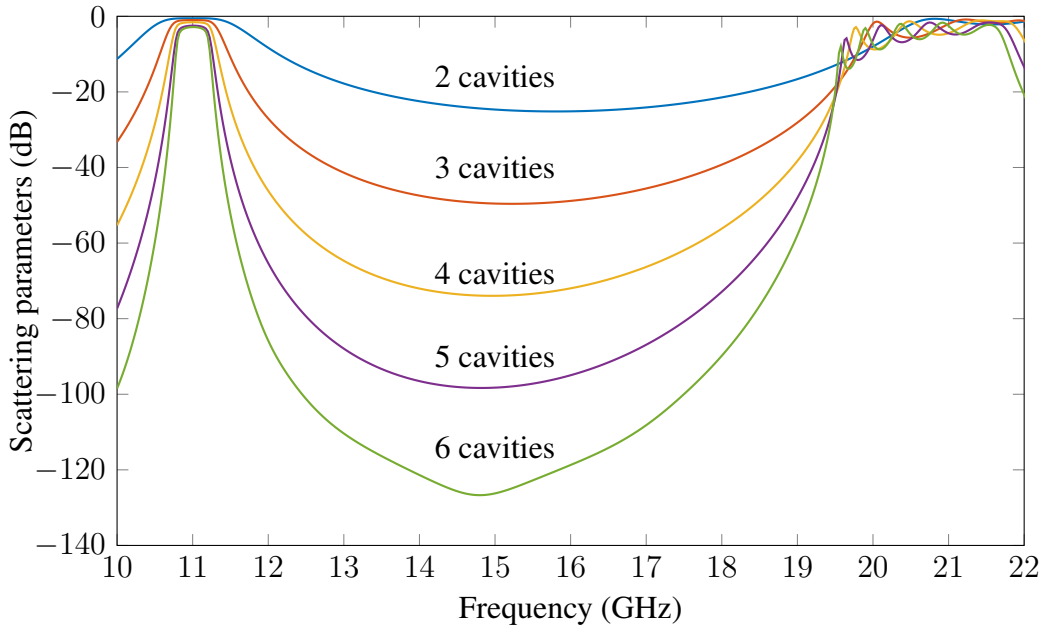

Figure 3.15: Impact of the filter order on the depth of the rejected band.

3.5.2 Width of the rejected band

Different substrates have been used for designing a filter with four resonant sections and the same specifications as in the previous one (centred at 11 GHz, with 300 MHz bandwidth, and 0.01 dB ripple in the passband). The dielectric permittivity and, consequently the cavity width (a) are the parameters to be changed. The values used for the different designs and the dimensions of the filter obtained with those specifications are shown in Table 3.5. It can be seen that the higher the permittivity value, the smaller the size, where the reduction of filter footprint between the biggest and the smallest filters is about 80% (see Figure 3.16).

Substrate	ε_r	Width (a)	Total length (l)	Thickness (h)
RT/duroid 5880	2.20	12.50 mm ($0.5\lambda_0$)	98.497 mm ($3.6\lambda_0$)	0.787 mm
RO4003C	3.55	10.50 mm ($0.4\lambda_0$)	68.379 mm ($2.5\lambda_0$)	0.813 mm
TMM6	6.00	8.00 mm ($0.3\lambda_0$)	47.170 mm ($1.7\lambda_0$)	1.270 mm
TMM10i	9.80	6.00 mm ($0.2\lambda_0$)	34.352 mm ($1.3\lambda_0$)	1.270 mm

Table 3.5: Dimensions of the bandpass filters for the different substrates.

The frequency responses of these filters have been analyzed. The first maximum (circle 1) in all the frequency responses is the desired response of the filter, its passband (see Figures 3.17, 3.18, 3.19, 3.20). The electric field at this frequency is shown in Figures 3.21(a), 3.22(a), 3.23(a), and 3.24(a).

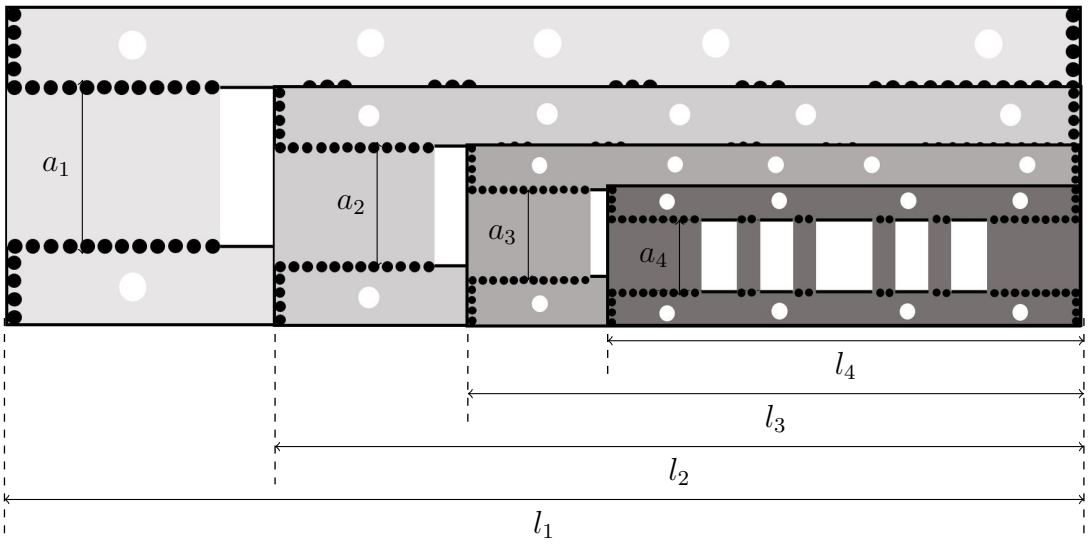

Figure 3.16: Scaled size comparison for ADLS filters with different substrates. Black are the metallized via holes of the filled sections and the border copper metallization to implement empty sections, gray is the copper metallization on top layer, and white are the empty sections (also metallized on top) and the fastening screws holes. (1) ε_r = 2.2, (2) ε_r = 3.55, (3) ε_r = 6, (4) ε_r = 9.8.

Even when the passband of all these realizations is the same, the out of band rejection is different depending on the selected permittivity. The increment of the dielectric permittivity allows to control the width of the rejection band. In the responses, some different local maxima of the transmission parameter are presented. For that, an analysis of the electric field inside the filters at each frequency peak can give a clearer idea of the working principle of the out-of-band behaviour (see Figures 3.21, 3.22, 3.23, 3.24).

On the one hand, for substrates with a dielectric permittivity value of ε_r = 6 and ε_r = 9.8, the cut-off frequency of the spurious band appears at the second resonance of the resonators, whose mode is TE_{102}. The frequency of this mode depends on the resonator length, permittivity and width. In these particular realizations the length of the resonators is very short, as explained in the design section, thus increasing the cut-off frequency of this spurious band at $2f_0$. This behaviour can be appreciated in Figures 3.19 and 3.20, with circle number 2, around 20 GHz. Furthermore, the electric fields of this mode are shown in Figures 3.23, where the second resonant mode appears in the filled sections showing two maxima of electrical field inside each resonator.

Nevertheless, there is another spurious in the rejection band. In this case, the electric field indicates a different working principle: the empty line sections propagate at those higher

frequencies and concentrate the electrical field; they do not behave as inverters but as resonant sections of mode TE_{101}. This is shown in Figure 3.24, where the maxima of the electric field are placed in the empty sections. This mode is represented by circle 3 in all the frequency responses.

On the other hand, for substrates with a dielectric permittivity value of ε_r = 2.2 and ε_r = 3.55, the spurious band behaviour is alternated: the first spurious is related to the second and higher order modes of the empty line sections, and the second mode of the filled line sections remains fixed at $2f_0$, around 20 GHz.

As it can be seen, the resonance of the empty line sections is achieved at different frequencies depending on the filter width, which is conditioned by the substrate permittivity value. The cut-off frequency of the empty sections is shown in Table 3.6 together with the permittivity values and the width of the filters. The lower the permittivity value, the wider the filter, and consequently the lower the spurious frequency.

ε_r	Cavity width	f_c
2.20	12.50 mm	12.00 GHz
3.55	10.50 mm	14.29 GHz
6.00	8.00 mm	18.75 GHz
9.80	6.00 mm	25.00 GHz

Table 3.6: Cut-off frequency for the TE_{101} mode of the empty line sections.

Therefore, it is noticed that the width of the rejected band is is not related to the order of the filter, but to the permittivity value of the substrate. Additionally, the spurious band is a combination of the two aforementioned effects, and both can be properly tuned by the permittivity of the substrate to ensure the out of band behaviour of the filter, reaching values up to $2f_0$, instead of $1.5f_0$ of conventional SIW realizations [57]. The tuning of the rejection band is limited by two reasons. On the one hand, the change of permittivity cannot modify the position of the second mode of the dielectric filled sections beyond $2f_0$ and, on the other hand, the values of dielectric permittivity are conditioned to the available substrates.

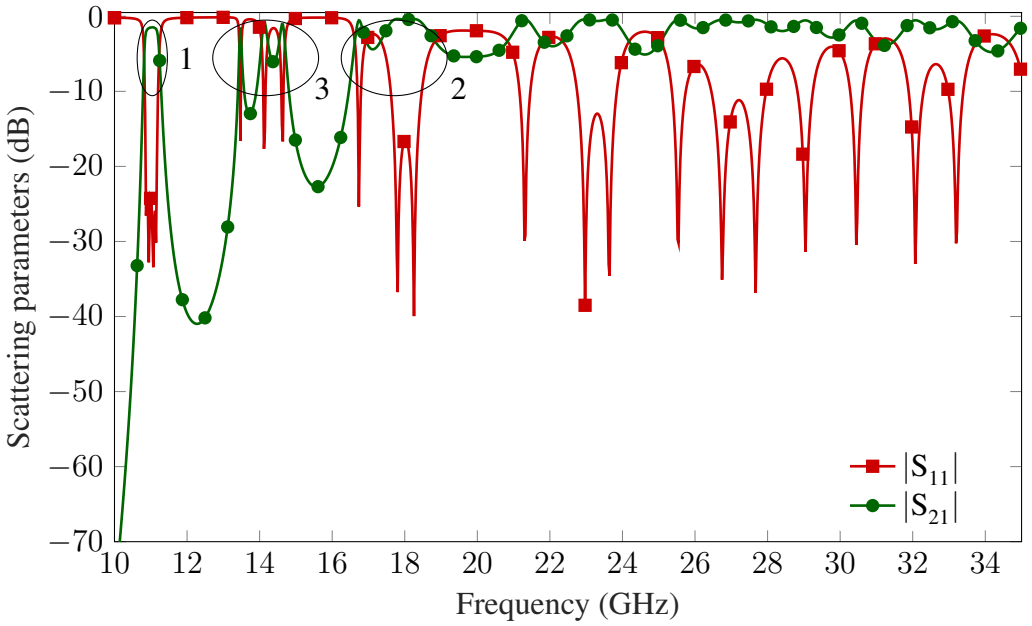

Figure 3.17: Out of band response for the filter with substrate RT/duroid with ε_r = 2.2.

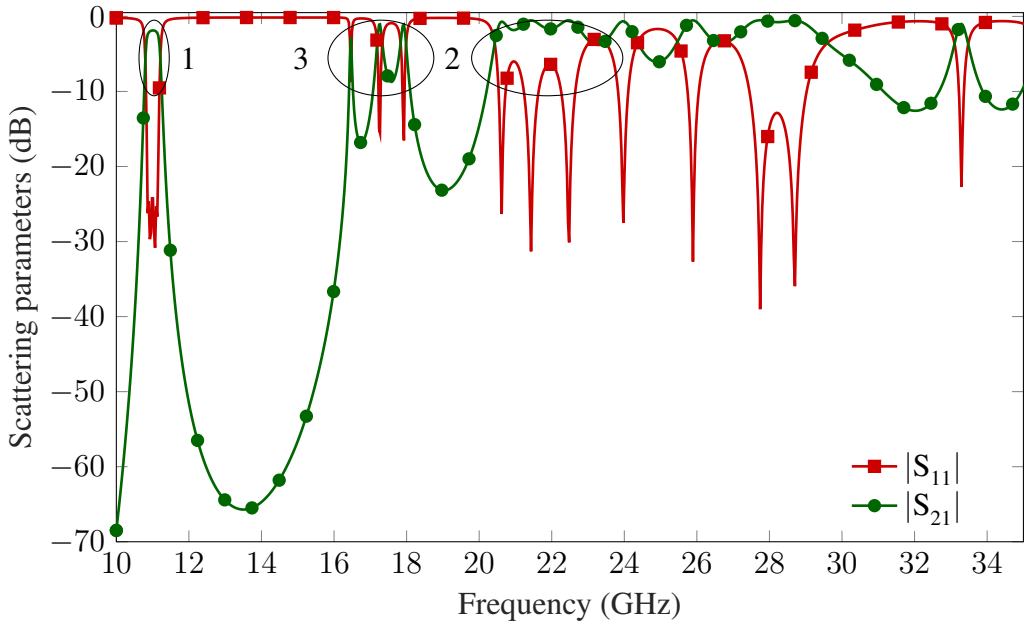

Figure 3.18: Out of band response for the filter with substrate RO4003C with ε_r=3.55.

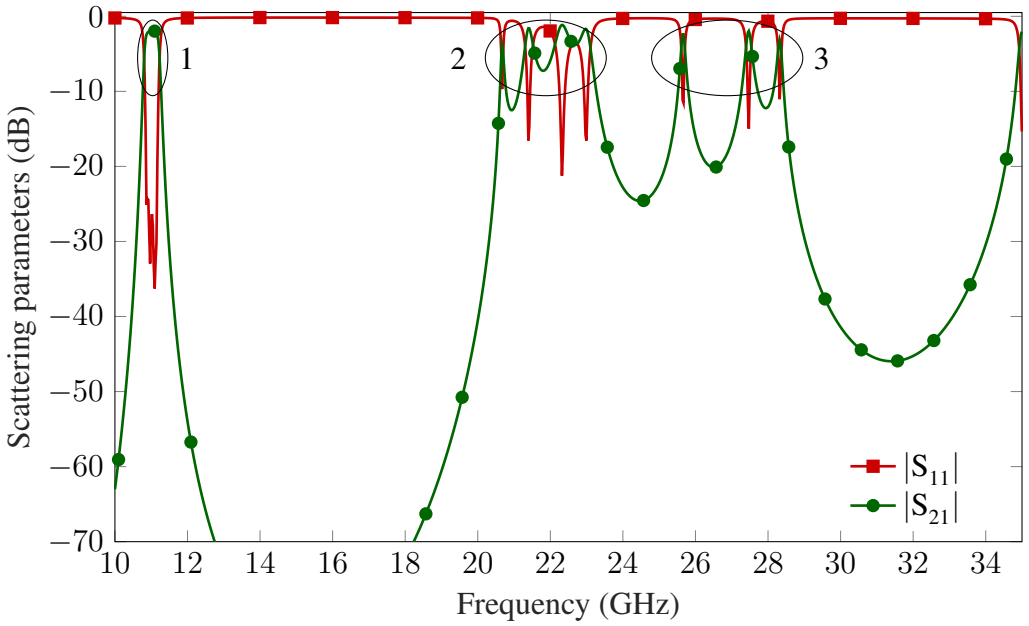

Figure 3.19: Out of band response for the filter with substrate TMM6 with ε_r=6.

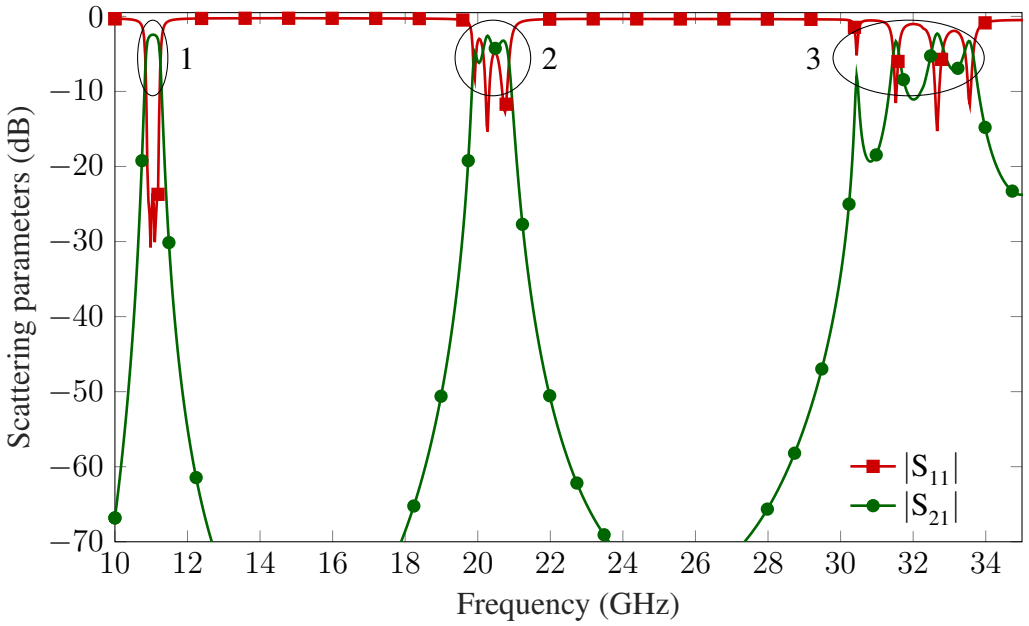

Figure 3.20: Out of band response for the filter with substrate TMM10i with ε_r=9.8.

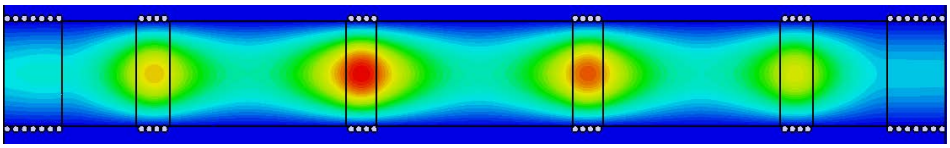

(a) f=11 GHz. TE_{101} in the dielectric filled line sections (passband).

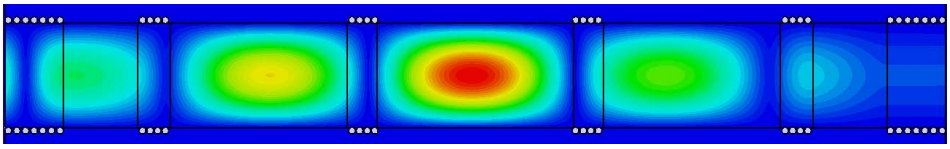

(b) f=13.42 GHz. TE_{101} in the empty line sections.

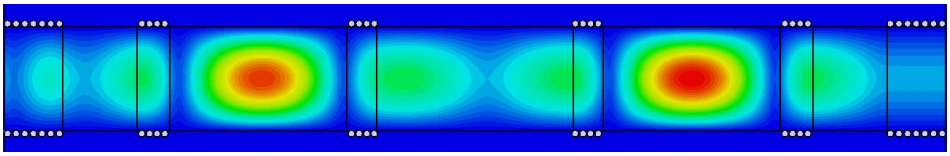

(c) f=14.16 GHz. TE_{101} in the empty line sections.

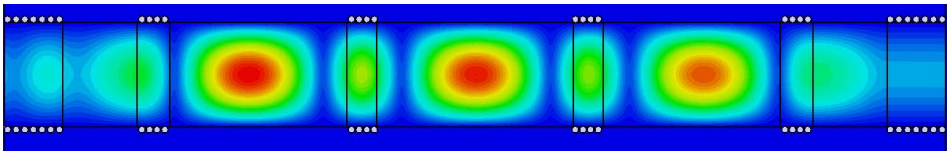

(d) f=14.65 GHz. TE_{101} in the empty line sections.

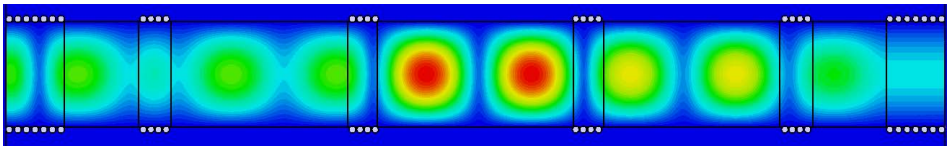

(e) f=16.87 GHz. TE_{102} in the empty line sections.

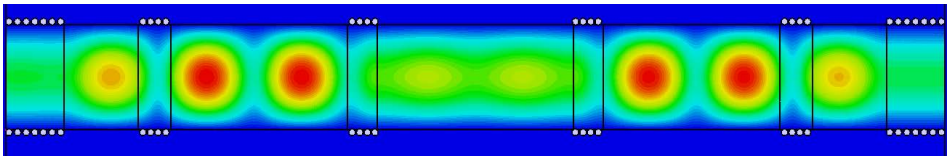

(f) f=17.80 GHz. TE_{102} in the empty line sections.

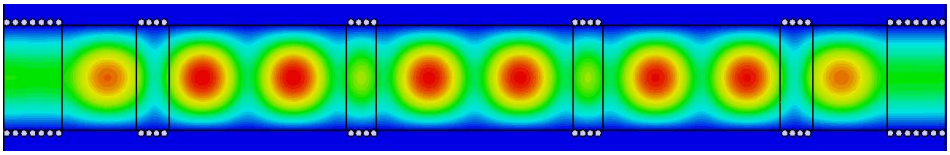

(g) f=18.25 GHz. TE_{102} in the empty line sections.

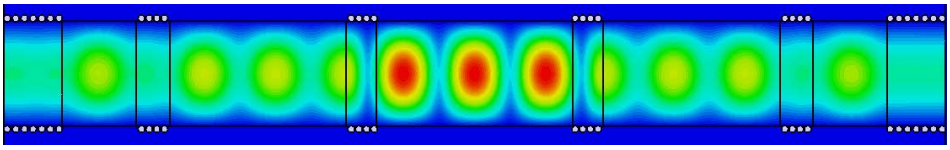

(h) f=21.31 GHz. TE_{102} in the dielectric filled line sections and TE_{103} in the empty line sections.

Figure 3.21: Electric field for the filter with substrate RT/duroid 5880 with ε_r = 2.20.

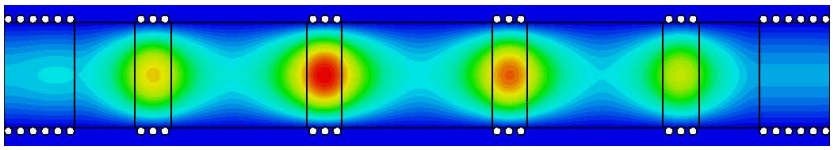

(a) f=11 GHz. TE_{101} in the dielectric filled line sections (passband).

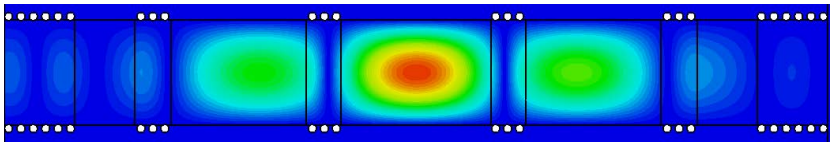

(b) f=16.47 GHz. TE_{101} in the central empty line sections.

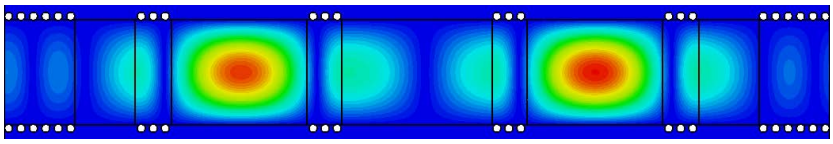

(c) f=17.27 GHz. TE_{101} in the central empty line sections.

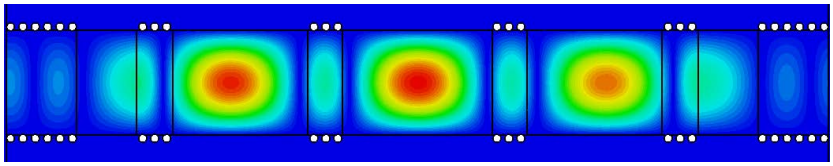

(d) f=17.93 GHz. TE_{101} in the central empty line sections.

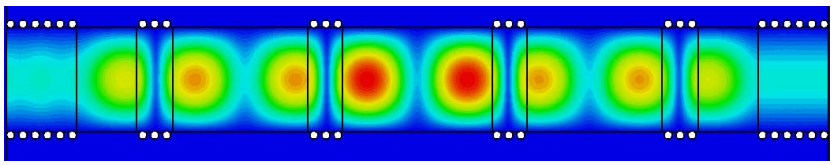

(e) f=20.62 GHz. TE_{102} in the dielectric filled line sections.

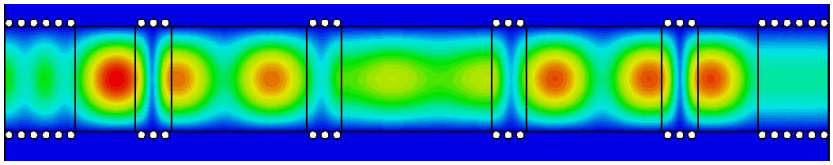

(f) f=21.32 GHz. TE_{102} in the dielectric filled line sections.

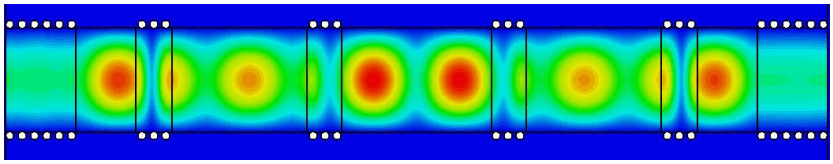

(g) f=22.47 GHz. TE_{102} in the dielectric filled line sections.

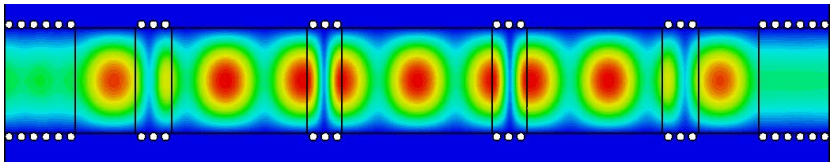

(h) f=23.97 GHz. TE_{102} in the dielectric filled line sections.

Figure 3.22: Electric field for the filter with substrate RO4003C with ε_r=3.55.

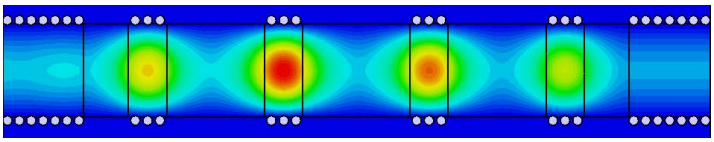

(a) f=11 GHz. TE_{101} in the dielectric filled line sections (pass-band).

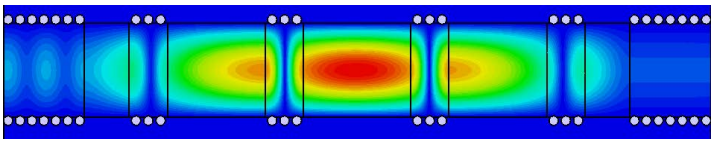

(b) f=20.69 GHz. TE_{102} in the dielectric filled line sections.

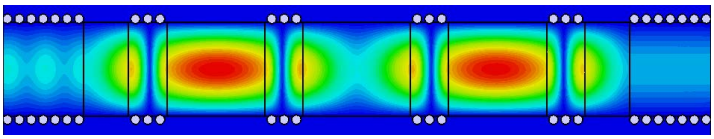

(c) f=21.40 GHz. TE_{102} in the dielectric filled line sections.

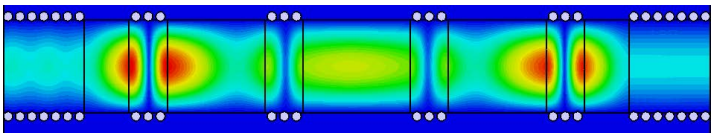

(d) f=22.32 GHz. TE_{102} in the dielectric filled line sections.

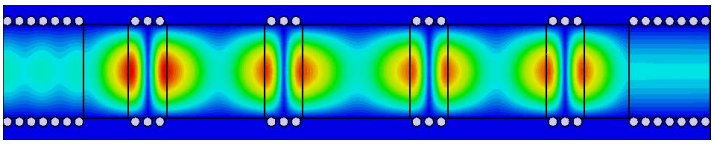

(e) f=22.99 GHz. TE_{102} in the dielectric filled line sections.

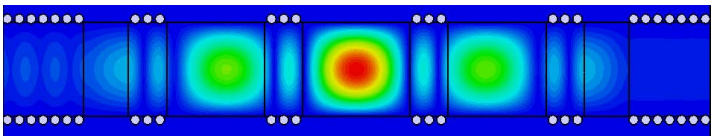

(f) f=25.67 GHz. TE_{101} in the empty line sections.

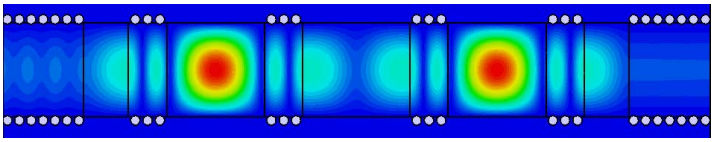

(g) f=27.46 GHz. TE_{101} in the empty line sections.

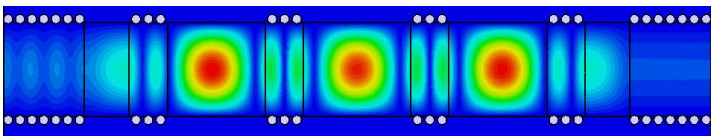

(h) f=28.32 GHz. TE_{101} in the empty line sections.

Figure 3.23: Electric field for the filter with substrate TMM6 with ε_r=6.

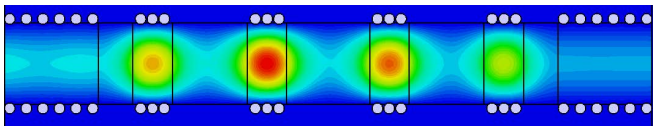

(a) f=11 GHz. TE_{101} in the dielectric filled line sections (passband).

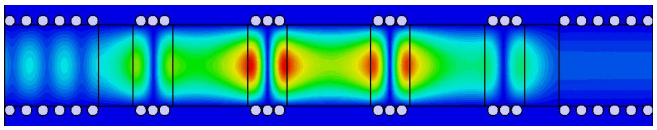

(b) f=19.90 GHz. TE_{102} in the dielectric line sections.

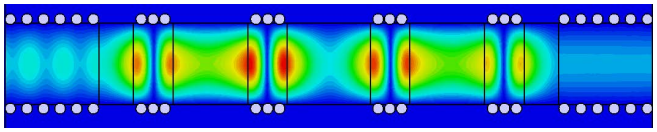

(c) f=20.27 GHz. TE_{102} in the dielectric line sections.

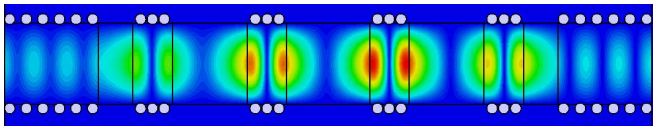

(d) f=20.76 GHz. TE_{102} in the dielectric line sections.

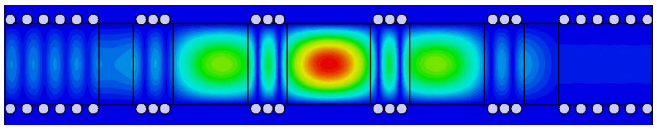

(e) f=30.45 GHz. TE_{101} in the empty line sections.

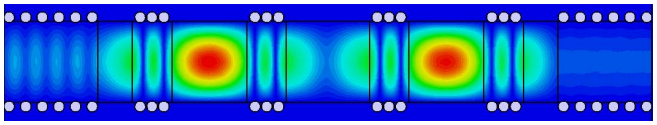

(f) f=31.51 GHz. TE_{101} in the empty line sections.

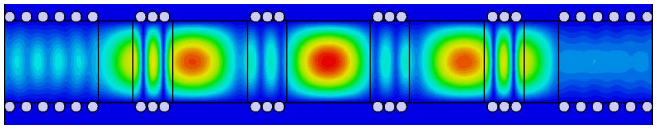

(g) f=32.67 GHz. TE_{101} in the empty line sections.

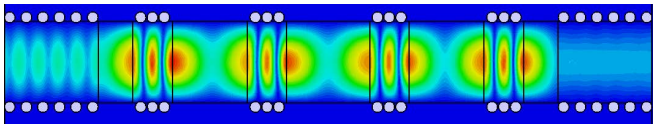

(h) f=33.55 GHz. TE_{103} in the dielectric filled line sections.

Figure 3.24: Electric field for the filter with substrate TMM10i with ε_r=9.8.

For a deeper analysis, a filter of higher order and with a different central frequency has been designed. The purpose of this design is to ensure the previous statements about the out-of-band behaviour (the variation of the depth and the width of the rejected band). In this case, the specifications are:

- Number of cavities: N = 5 resonant sections.
- Central frequency: f_0 = 13 GHz.
- Bandwidth: 300 MHz.
- Ripple: 0.01 dB.
- Return loss: 25 dB.
- Dielectric permittivity: ε_r = 3.55.
- Cavities width: a = 8 mm.
- Filter height: h = 0.813 mm.

The specifications have been chosen for different reasons: the increase of the number of resonant sections will test the improvement of the depth of the out-of-band response, and a different central frequency will prove that the width of the stopband is achieved at any frequency band. Following the same design procedure, the resulting dimensions of the filter are depicted in Table 3.7 and the frequency response is plotted in Figure 3.25.

Parameter	Dimensions
l_{in}	10.000 mm
$l_{Win}^{(1)}$	4.878 mm
$l_{Win}^{(2)}$	10.655 mm
$l_{Win}^{(3)}$	12.059 mm
$l_{Res}^{(1)}$	3.181 mm
$l_{Res}^{(2)}$	3.104 mm
$l_{Res}^{(2)}$	3.099 mm

Table 3.7: Dimensions of the bandpass filter centred at 13 GHz.

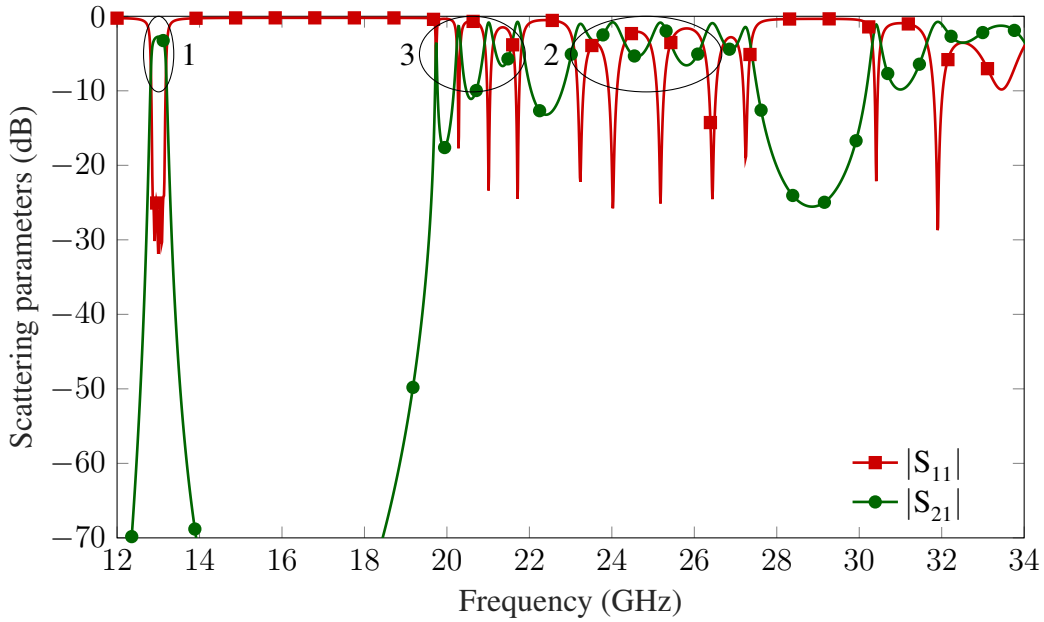

Figure 3.25: Out of band response for the 5-pole filter with substrate RO4003C with ε_r=3.55.

3.6 Results

In order to verify all the simulations carried out, different filters have been manufactured. A prototype of the 4-pole bandpass filter has been manufactured using Rogers TMM6 substrate with a thickness of 1.27 mm and a copper cladding of 17.5 μm, as shown in Figure 3.26. The fabrication process for producing the body consists on drilling the vias in the filled sections, and cutting the walls in the empty ones. Then, the substrate is metallized, and the top metallic layer is milled to form the transition and the microstrip line. The top and bottom covers are just two metallic layers with alignment holes and fastening screws. Finally, the device is cut and separated from the substrate sheet, and layers are duly fastened and welded in order to ensure electric continuity.

Figure 3.27 shows also a detailed view of the alternating dielectric sections, the metallized sidewalls of the empty sections, as well as the arrays of metallized via holes of the filled sections. It can also be checked that the front walls of the empty sections are not metallized.

In Figure 3.30, the measured frequency response of the manufactured prototype is compared with the simulation data obtained with CST.

In order to fairly compare the proposed topology with other available SIW realizations, the parameters of similar filter implementations are shown in Table 3.8. The same filter specifications and substrate are used in all of them: 11 GHz of central frequency, 2.7% of

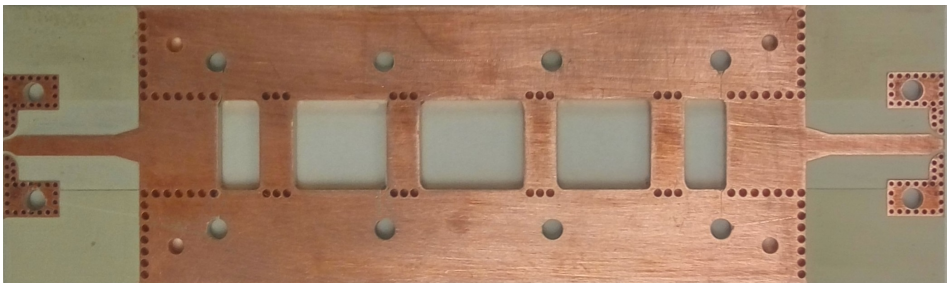

Figure 3.26: Central layer of the 4-poles manufactured filter on substrate TMM6.

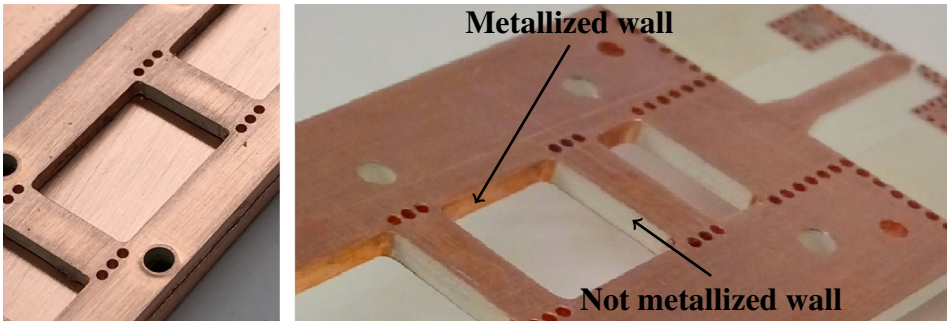

Figure 3.27: Detailed views of the manufactured filter (on the left with bottom cover) showing the discontinuities between sections and the side wall conductors

relative bandwidth, and dielectric substrate TMM6 (ε_r = 6, $tan\delta$ = 0.0023), except for the case of ESIW, which is empty. The Q-factor has been estimated applying the formula (3.23) in [38].

$$Q = \frac{4.343 f_0}{IL(f_H - f_L)} \sum_{r=1}^{N} g_r \tag{3.23}$$

where f_0 is the center resonant frequency, $f_H - f_L$ is the filter bandwidth, IL is the insertion loss at f_0, and g_r are the element values for the low-pass filter Chebysev prototype.

In order to verify the study of the out-of-band response, the measured rejected band is compared with the simulation in Figure 3.31. Additionally, 4-pole filter has been manufactured using Rogers TMM10i substrate with a thickness of 1.524 mm and a copper cladding of 35 μm, as shown in Figure 3.28. The manufacturing process is the same one. In Figure 3.32, the measured frequency response in the passband and stopband of the manufactured prototype is compared with the simulation data obtained with CST. Additionally, it is presented the frequency response of an equivalent filter in conventional SIW technology with the same characteristics.

Figure 3.28: Central layer of the 4-pole manufactured filter on substrate TMM10i.

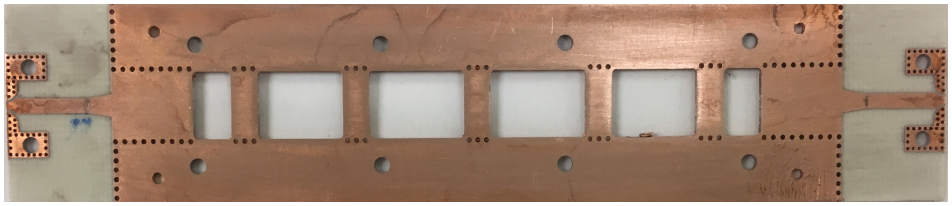

Figure 3.29: Central layer of the 5-pole manufactured filter on substrate RO4003C.

	ADLS	SIW	ESIW
Q-factor	350	273	1226
1^{st} spurious frequency	$2f_0$	$1.5f_0$	$1.5f_0$
Width	8.65 mm	8.65 mm	19.05 mm
Length	45 mm	30 mm	77 mm
Number of layers	3	1	3

Table 3.8: Comparison between the filter based on Alternating Dielectric Line Sections (ADLS) and SIW filters.

Moreover, the 5-pole filter has also been manufactured using Rogers 4003C substrate with a thickness of 0.813 mm and a copper cladding of 17.5 μm, as shown in Figure 3.29. Figure 3.33 shows the measured frequency response and the simulation data, compared to an equivalent SIW filter with the same features.

In both cases, the simulated and measured results show a good agreement. The comparison with the equivalent SIW filter confirms the expected results for the out-of-band behaviour. The measured insertion loss is higher due to the effect of transitions and connectors. The 13 GHz filter has insertion and return loss of values equal to 4 dB and 25 dB, respectively. In the 11 GHz case, the insertion loss is around 3 dB due to the substrate features and reduced center frequency. However, a misalignment between simulated and measured return loss, of 30 dB and 10 dB respectively, can be observed for the 11 GHz filter. This is caused by the type of employed connectors. The 13 GHz filter uses screwed End-Launch with enhanced performance, while in the case of 11 GHz filter the height of the substrate forced to employ

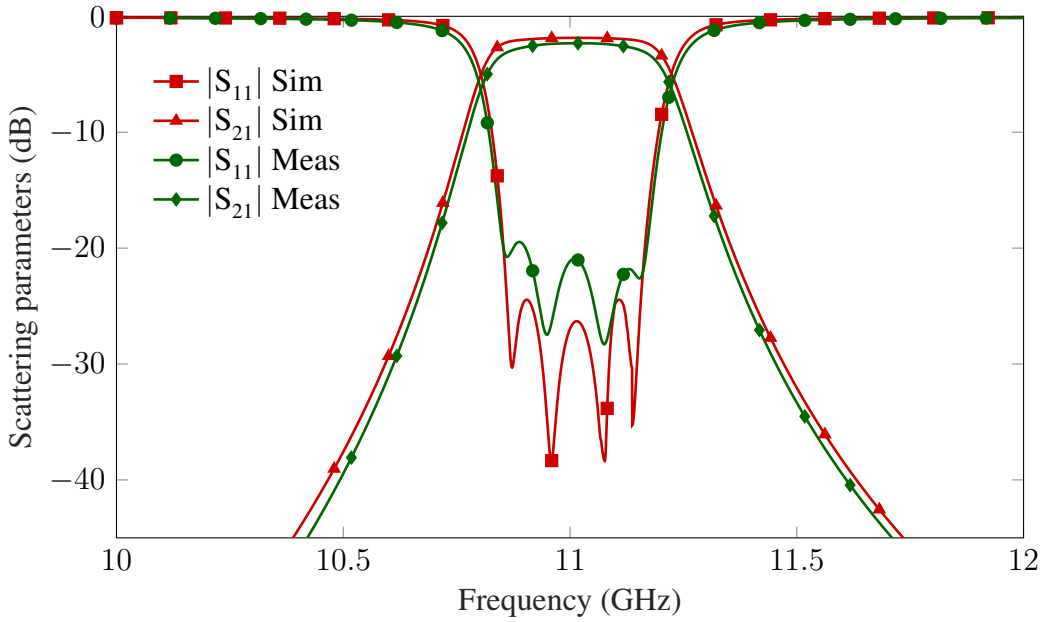

Figure 3.30: Comparison between simulated and measured frequency responses for the 4-pole filter on substrate TMM6.

typical welded SMA (see the footprint of both filters in Figures 3.28 and 3.29).

The proposed structure presents several advantages: its associated Q-factor is better than other SIW filters, it is easy to design and simple to manufacture, and their inverters can be done more accurately (since the use of vias for implementing narrower SIW widths is avoided). Obviously, ESIW presents higher Q-factor due to the absence of dielectric substrate in the whole structure, but the ESIW filter is bigger than the proposed one and requires a more complex transition [5]. Furthermore, the out-of-band response presents better behaviour than conventional filters.

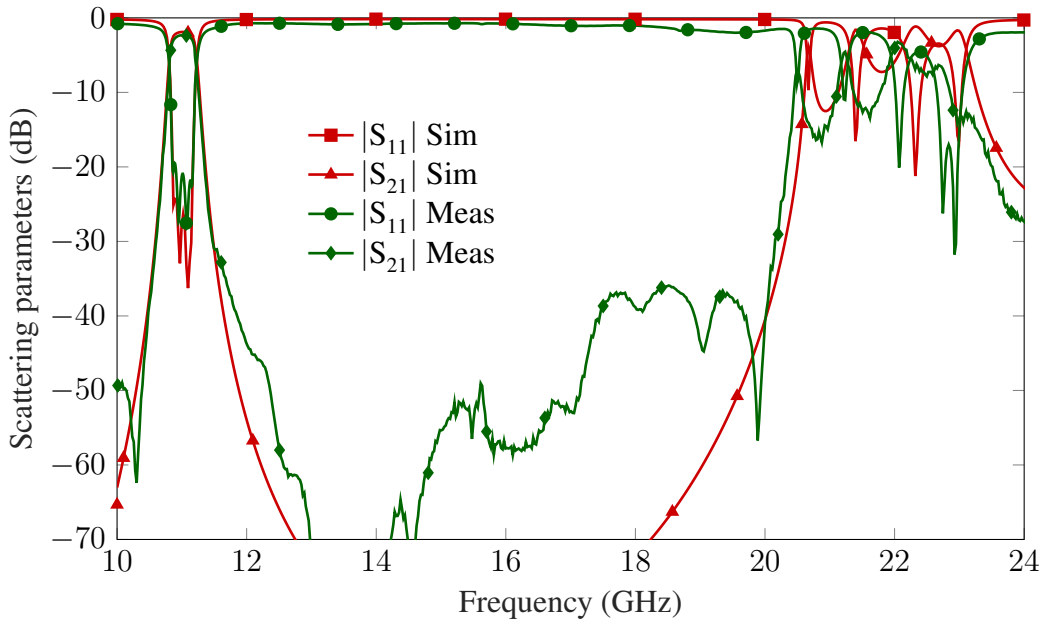

Figure 3.31: Comparison between simulated and measured frequency responses for the 4-pole filter on substrate TMM6.

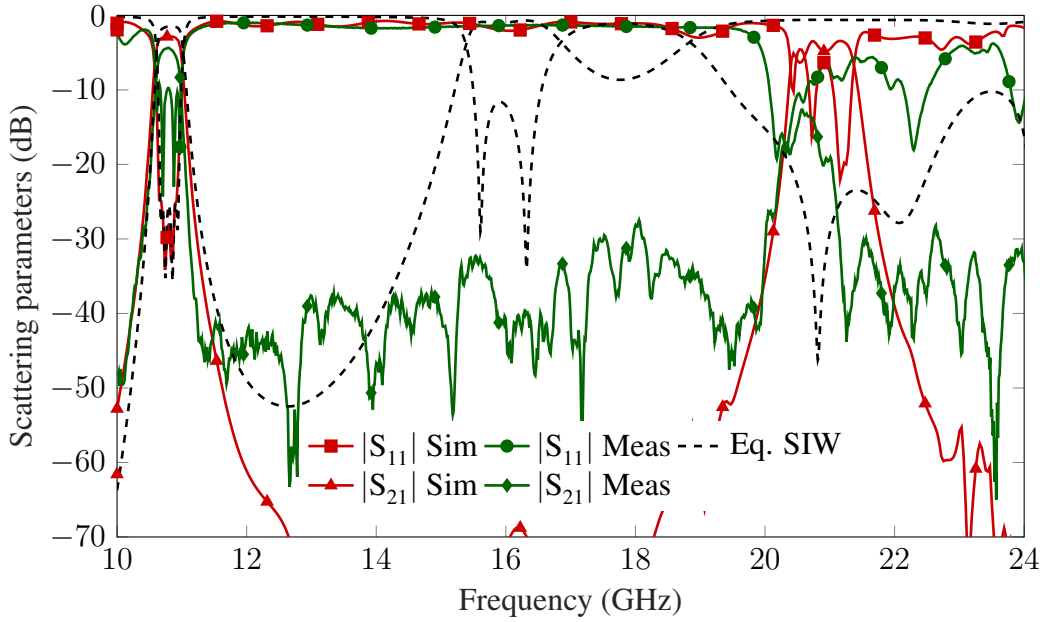

Figure 3.32: Comparison between simulated and measured frequency responses for the 4-pole filter on substrate TMM10i.

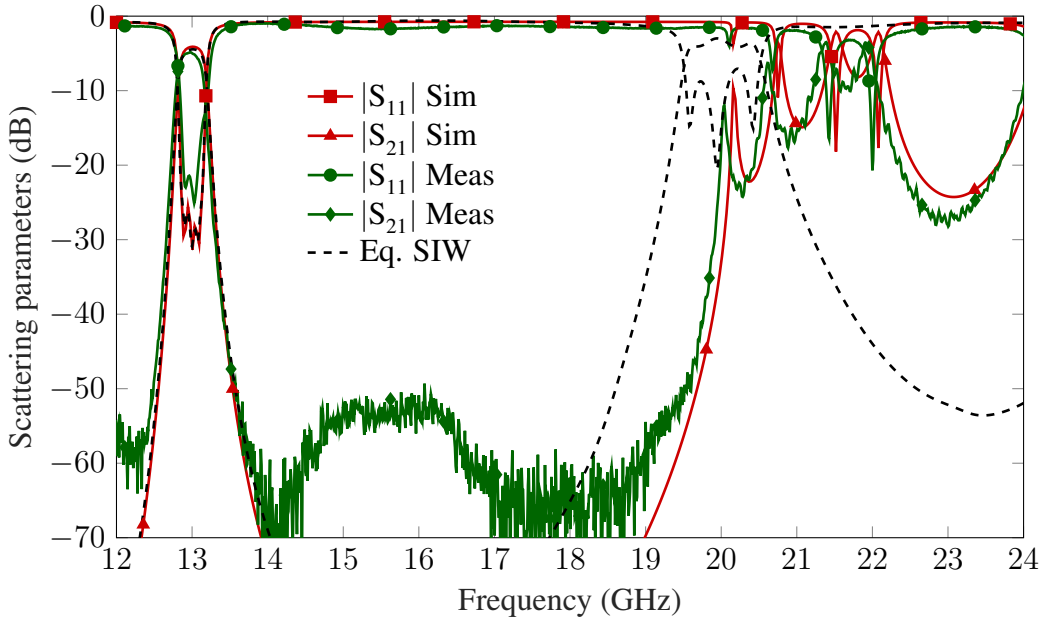

Figure 3.33: Comparison between simulated and measured frequency responses for the 5-pole filter on substrate RO4003C.

Chapter 4

Liquid Crystal characterization

This chapter exposes the theoretical knowledge needed to understand the dielectric characteristics of the LC, and a brief description of the methods of dielectric characterization. This knowledge will be used and applied to characterize the dielectric anisotropy of four commercial mixtures of LCs.

On the one hand, an LC widely studied in the bibliography will be characterized: GT3-23002 from Merck KGaA. Since, both the company and the LC mixture are a reference in the subject under study, this LC can be taken as a validator of the results obtained by the characterization method developed in this work.

On the other hand, it was decided to characterize three other LC mixtures of a less known company, Qingdao QY Liquid Crystal Co, which although presumes to have LC mixtures similar to those of Merck KGaA at lower prices, has a poorer characterization of their properties. The chosen mixtures are QYPDLC-142, QYPDLC-36 and QYPDLC-193.

The most suitable characterization method for the purpose of this work is the split-cylinder, a method based on resonant cavities. For the characterization, three resonators have been designed and manufactured for operation at 3 different frequencies: 5 GHz, 9.5 GHz, and 11 GHz, representing the bandwidth of the microwave applications considered in this Thesis work.

This method of characterization is applied to flat thin solids, so for the characterization of the LC, glass cells are used. A glass cell is a container made of two thin glasses separated by spacers, inside this cell the layer of LC is placed, as depicted in Figure 4.1(c). As explained later, the choice for this method of dielectric characterization, together with the anchoring properties of the LC cells used, allows obtaining the dielectric permittivity values of the two extreme states ($\varepsilon_{r\parallel}$ and $\varepsilon_{r\perp}$) without the need to apply a polarization electric field. This has the advantage that the cells do not need to be doped or coated with any conductive material, no biasing networks are needed, and the orientation of the molecules of the LC is much more

accurate than that obtained with switching methods.

4.1 Split-cylinder resonator method

4.1.1 Procedure description

This method of measurement is suitable for the characterization of thin and flat material samples, the main reason why it has been selected as a method for the characterization of LC cells. In this method a cylindrical resonant cavity is used, which is divided into two parts across an orthogonal plane to the axis of the cylinder as can be seen in Figure 4.1. The material under analysis (in this case the LC cell) is located between these two parts where, according to the resonant mode used, its electrical properties (dielectric permittivity) or its magnetic properties (magnetic permeability) are measured.

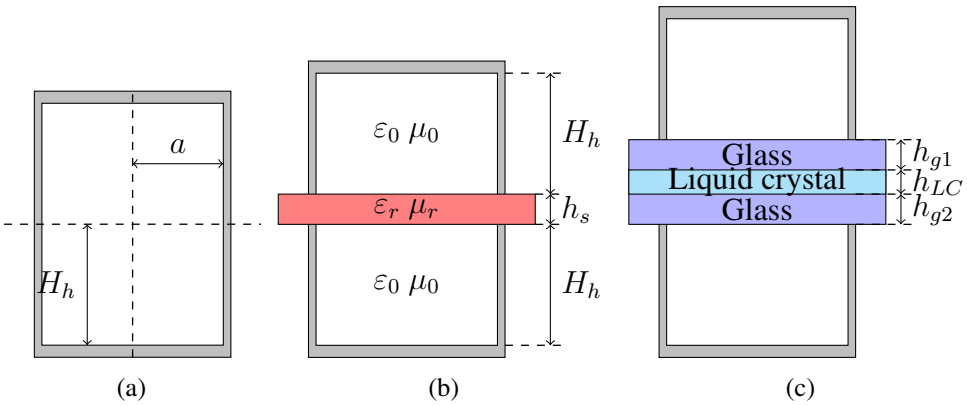

Figure 4.1: Transverse section of a split-cylinder cavity: (a) Without dielectric. (b) Cavity with uniform dielectric material. (c) Cavity with a liquid crystal cell.

In the characterization of isotropic materials, the transverse variation of the electric field in the cavity is indifferent. However, in the specific case of the characterization of a dielectrically anisotropic material this variation is very important, since the molecules of the material must be oriented in a specific way with respect to the electric field.

For this reason it is necessary to study the distribution of the transverse field in the cavity. For this purpose, the model is simplified assuming that the cavity does not present any division, obtaining a regular cylindrical cavity of length $L = 2H_h$ and radius a, as shown in Figure 4.1(a).

In this case, the transverse variation of its fields can be obtained by solving the Maxwell Equations. The solution is separated into transverse electric (TE) and transverse magnetic

(TM) modes, applying the boundary conditions of the problem (tangential electric field must be zero in the conductive walls) [1, 72].

For TE_{nm} modes:

$$\begin{aligned} H_\rho &= -j\tfrac{\beta}{k_c} J_n(k_c\rho)' \left[A\sin(n\phi) + B\cos(n\phi)\right] \\ H_\phi &= -j\tfrac{\beta n}{{k_c}^2\rho} J_n(k_c\rho) \left[A\cos(n\phi) - B\sin(n\phi)\right] \end{aligned} \tag{4.1}$$

$$\begin{aligned} E_\rho &= Z_{TE} H_\phi \\ E_\phi &= Z_{TE} H_\rho \end{aligned} \tag{4.2}$$

$$f_c = \frac{\chi'_{nm}}{2\pi a\sqrt{\mu\varepsilon}} \tag{4.3}$$

For TM_{nm} modes:

$$\begin{aligned} E_\rho &= -j\tfrac{\beta}{k_c} J_n(k_c\rho)' \left[A\cos(n\phi) + B\sin(n\phi)\right] \\ E_\phi &= -j\tfrac{\beta}{{k_c}^2}\tfrac{n}{\rho} J_n(k_c\rho) \left[-A\cos(n\phi) + B\sin(n\phi)\right] \end{aligned} \tag{4.4}$$

$$\begin{aligned} H_\rho &= \tfrac{-E_\phi}{Z_{TM}} \\ H_\phi &= \tfrac{E_\rho}{Z_{TM}} \end{aligned} \tag{4.5}$$

$$f_c = \frac{\chi_{nm}}{2\pi a\sqrt{\mu\varepsilon}} \tag{4.6}$$

Equations from (4.1) to (4.6) describe the behaviour of electric (E) and magnetic (H) fields in their different spatial components. In these equations:

- β is the mode propagation constant.
- k_c is the mode cut-off wavenumber.
- $J_n(x)$ is the Bessel functions of order n.
- χ_{nm} is the m-th root of the Bessel function of order n.
- χ'_{nm} is the m-th root of the first derivative of the Bessel function of order n.
- Z_{TE} is the modal impedance of the TE mode.
- Z_{TM} is the modal impedance of the TM mode.

Using these equations the distributions of the most representative modes of a circular waveguide can be represented, as shown in Figure 4.2.

The TE_{01} mode is traditionally used by Kent and Janezic [27, 86] for the characterization of materials by the split-cylinder resonator method. Nevertheless, in the case of the characterization of an anisotropic material, as the LC used in this work, the transverse electric field must present a linear polarization, something almost impossible. However, it can be seen that the field distribution that better fits for the solution of the problem is the TE_{11} mode, since it has quite straight field lines in the center of the cavity. In addition, it has the advantage of being the fundamental mode, i.e. it is excited at the lowest frequency, as it is depicted in Figure 4.3.

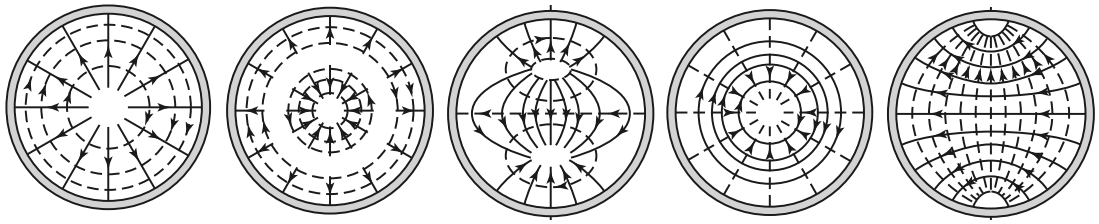

(a) TM_{01} (b) TM_{02} (c) TM_{11} (d) TE_{01} (e) TE_{11}

Figure 4.2: Field lines for some of the lower order modes of a circular waveguide [1].

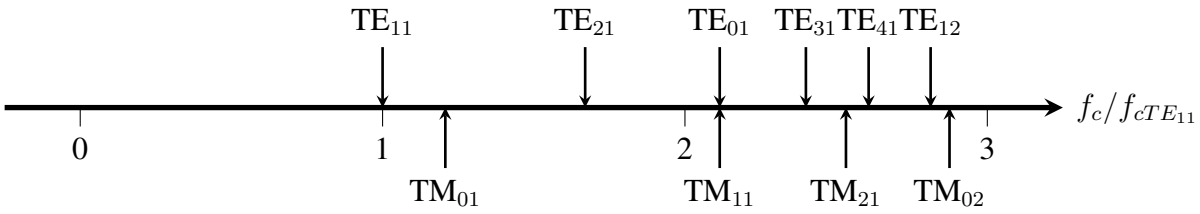

Figure 4.3: Cutoff frequencies of the first TE and TM modes of a circular waveguide, relative to the cutoff frequency of the dominant TE_{11} mode.

The main advantage of this method is that, depending on the position of the cells, the two extreme polarization states of the LC can be characterized. Neither an electric nor magnetic field are needed for polarization. This avoids the use of decoupled structures or magnets outside the cylinder. The cell can be inserted with the molecules placed orthogonally to the electric field, thus measuring the perpendicular permittivity ($\varepsilon_{r\perp}$). Furthermore, just rotating the cell 90°, the molecules are placed parallely to the electric field, thus measuring the parallel permittivity ($\varepsilon_{r\parallel}$).

Although the equations of the fields in a circular waveguide have been solved, the resonance conditions must be studied. This will determine the necessary length of the cavity to place a maximum of the electric field in the sample area, which is required to characterize the dielectric permittivity. For this reason, the longitudinal distribution of the field inside the cavity has to be analyzed starting from the wave equations.

For TE modes:

$$\begin{aligned} E_\rho &= f^{TE}_{1(\rho,\phi)} \left[A^+ e^{-j\beta z} + A^- e^{j\beta z}\right] \\ E_\phi &= f^{TE}_{2(\rho,\phi)} \left[A^+ e^{-j\beta z} + A^- e^{j\beta z}\right] \end{aligned} \tag{4.7}$$

$$\begin{aligned} H_\rho &= f^{TE}_{3(\rho,\phi)} \left[A^+ e^{-j\beta z} - A^- e^{j\beta z}\right] \\ H_\phi &= f^{TE}_{4(\rho,\phi)} \left[A^+ e^{-j\beta z} - A^- e^{j\beta z}\right] \end{aligned} \tag{4.8}$$

For TM modes, the modal functions and amplitudes change:

$$\begin{aligned} E_\rho &= f^{TM}_{1(\rho,\phi)} \left[B^+ e^{-j\beta z} - B^- e^{j\beta z}\right] \\ E_\phi &= f^{TM}_{2(\rho,\phi)} \left[B^+ e^{-j\beta z} - B^- e^{j\beta z}\right] \end{aligned} \tag{4.9}$$

$$\begin{aligned} H_\rho &= f^{TM}_{3(\rho,\phi)} \left[B^+ e^{-j\beta z} + B^- e^{j\beta z}\right] \\ H_\phi &= f^{TM}_{4(\rho,\phi)} \left[B^+ e^{-j\beta z} + B^- e^{j\beta z}\right] \end{aligned} \tag{4.10}$$

Applying the first resonance condition to these equations (short circuit located at $z = 0$, that is, $E_{(\rho,\phi),z=0} = 0$) the following field distributions are obtained for TE_{nmp} modes:

$$\begin{aligned} E_\rho &= f^{TE}_{1(\rho,\phi)} sen(\beta z) \\ E_\phi &= f^{TE}_{2(\rho,\phi)} sen(\beta z) \end{aligned} \tag{4.11}$$

$$\begin{aligned} H_\rho &= f^{TE}_{3(\rho,\phi)} cos(\beta z) \\ H_\phi &= f^{TE}_{4(\rho,\phi)} cos(\beta z) \end{aligned} \tag{4.12}$$

For TM_{nmp} modes, it is calculated in the same way.

Considering these equations, it can be observed that the electric field maxima occur in position with magnetic minima and vice versa, which allows to characterize either the dielectric

permittivity or the magnetic permeability of the material varying the resonant mode.

To obtain the relation of the propagation constant β with the length of the cavity, the boundary condition is forced in the cover located at $z = L = 2H_h$, obtaining:

$$\beta_{nm} 2H_h = p\pi \quad \text{for } p = 1, 2, 3, ... \tag{4.13}$$

This implies that the cavity length must be an integer of half-guide wavelengths. Thus, the resonant frequency of the TE_{nmp} mode is detailed in (4.14) and the resonant frequency of the TM_{nmp} mode is detailed in (4.15) as follows:

$$f_r^{TE}{}_{nmp} = \frac{1}{2\pi\sqrt{\mu\varepsilon}} \sqrt{\left(\frac{\chi'_{nm}}{a}\right)^2 + \left(\frac{p\pi}{2H_h}\right)^2} \tag{4.14}$$

$$f_r^{TM}{}_{nmp} = \frac{1}{2\pi\sqrt{\mu\varepsilon}} \sqrt{\left(\frac{\chi_{nm}}{a}\right)^2 + \left(\frac{p\pi}{2H_h}\right)^2} \tag{4.15}$$

From these equations, it can be concluded that the modes that are useful for the characterization of the LC cells are the TE_{11p} modes with an odd p. They present a maximum of the electric field in the middle of the resonator where the material is placed.

4.1.2 Design and manufacturing of split-cylinder resonators

For achieving the proposed objectives, two split-cylinder resonators have been designed and manufactured, whereas a previously fabricated split-cylinder has been also used. The aim is to have three measurement points in the frequency range from 0 GHz to 20 GHz. The resonators have been designed for presenting the resonance of the mode of interest TE_{111} at 5 GHz, 9.5 GHz, and 11 GHz. As mentioned before, these frequency points have been chosen since the manufactured devices are operating in this frequency band.

Equations of the previous section give a relation between the resonance frequency of the mode (TE_{111}), cylinder radius (a), and cylinder length ($2H_h$). While there are infinite combinations that meet this equation, not all are equally stable in the presence of small variations of the dimensions caused by the manufacturing tolerances. Through a small analysis of the relation between radius and length of a cavity that are needed to obtain the resonance frequencies of interest for the TE_{111} mode, the most stable combinations can be observed.

Looking at Figure 4.4 a large peak can be observed in the curves that relate both parameters, radius and length of the cavitiy. The most stable combinations are those that are found as far away as possible from the peaks. The devices that have the peaks inside the stability ranges have a lower sensitivity to manufacturing tolerances. In Figure 4.4 the chosen values

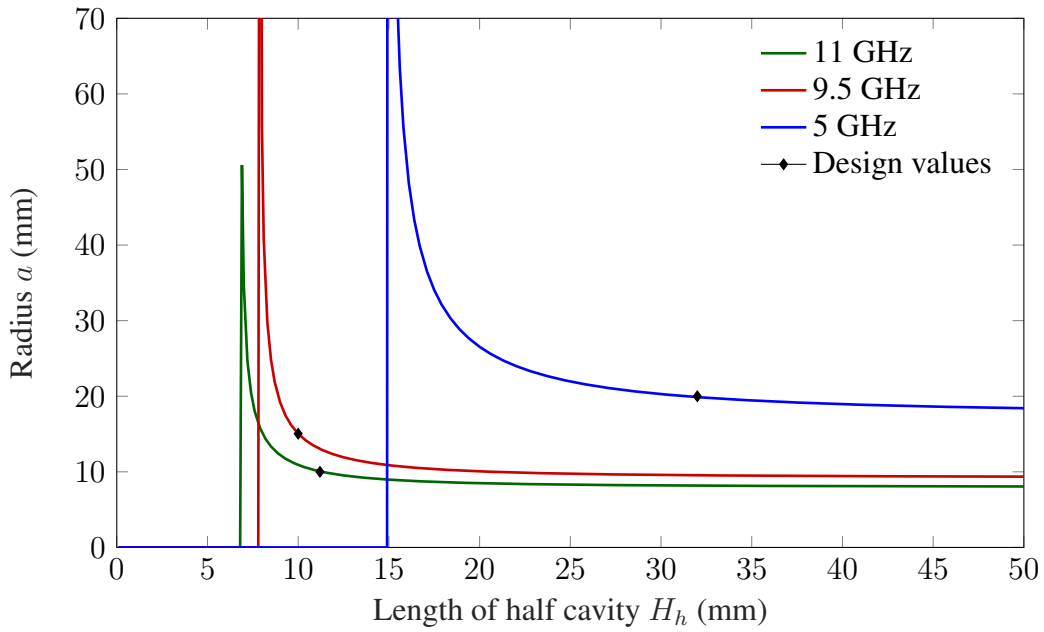

Figure 4.4: Comparison between radius and cavity length to excite TE_{111} mode at the indicated frequencies.

detailed in Table 4.1 are also plotted. It can be seen how the resonator designed for 9.5 GHz is inside an area of low stability. This is because the resonator was manufactured before the project begins and was designed for operating in a different mode. However, it has been used to obtain an intermediate measurement point between the other two designed resonators.

Resonance frequency TE_{111} mode (GHz)	Radius a (mm)	Height H_h (mm)
5	20.00	32.00
9.5	15.04	10.00
11	10.00	11.20

Table 4.1: Dimensions of the split-cylinder resonators.

Another parameter to be taken into account is the feeding network of the split-cylinder resonator. In this case, it has been decided to place two coaxial cables in the same plane with a feeding loop. The loop is oriented to excite the longitudinal magnetic field of the cavity, as shown in Figure 4.5. It has been decided to implement these two feeding networks to analyze the transmission parameters (S_{12} and S_{21}) and the reflection ones (S_{11} and S_{22}). Furthermore, the position of the loop inside the cavity can be changed, which allows to adjust the coupling level of the feeding network depending on the measurement requirements.

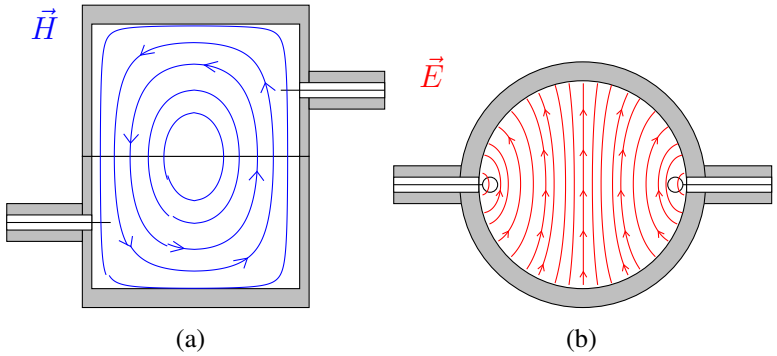

Figure 4.5: Feeding model of the split-cylinder resonator. (a) Longitudinal section with magnetic field (b) Transverse section with electric field.

Moreover, the structure needs to keep the two halves perfectly aligned. For this reason, aluminium guide rails have been built to ensure their alignment allowing their movement to introduce the material. A manufactured design is shown in Figure 4.6. The resonators have been manufactured on brass and the cylinder guides on aluminium. All parts have been manufactured with mechanical milling in the workshop of the Technical University of Cologne.

Figure 4.6: Manufactured split-cylinder resonator.

4.1.3 Analysis methods

Three methods of analysis of the electromagnetic response have been used for calculating the permittivity of the different materials. These methods have been combined or used in different stages of the process in order to obtain coherent results.

All of them use a calibration prior to the measurement of the resonators with the sample. This calibration consists on measuring the resonator without the sample of dielectric material to adjust the coupling of the feeding loop, and to measure the real dimensions, characteristics and configuration of the resonator (radius, height, and conductivity of the walls). This is the starting point for all the measurements.

- **Kent method**. This method is described in [27, 86, 87]. It assumes a homogeneous and planar sample, hence it is only used for the characterization of the glasses of the LC cell.

  First, when the split-cylinder resonator is empty, the resonance frequency, the insertion loss at the resonance, and the 3 dB bandwidth of the transmission spectrum are measured. These measurements are used to calculate the effective radius of the cavity (a) and the conductivity of the brass (σ) using equations (4.16) and (4.17), respectively.

$$f_r^{TE}{}_{nmp} = \frac{1}{2\pi\sqrt{\mu\varepsilon}}\sqrt{\left(\frac{\chi'_{nm}}{a}\right)^2 + \left(\frac{p\pi}{H_h}\right)^2} \tag{4.16}$$

$$\sigma = \frac{2\pi f \mu_0}{2R_s^2} \tag{4.17}$$

  where R_s is the surface resistance, BW is the 3 dB fractional bandwidth, f_0 is the resonance frequency and Δf is the 3 dB bandwidth [1]:

$$R_s = \frac{(ka)^3 2H_h}{4\left(\chi'_{11}\right)^2 Q_0} \frac{1 - \left(\frac{1}{(\chi'_{11})^2}\right)^2}{aH_h\left[1 + \left(\frac{a\pi}{2H_h(\chi'_{11})^2}\right)\right] + \left(\frac{\pi a^2}{2H_h\chi'_{11}}\right)^2\left(1 - \frac{1}{(\chi'_{11})^2}\right)} \tag{4.18}$$

$$Q_0 = \frac{Q_L}{1 - 10^{S_{21}(dB)/20}} \tag{4.19}$$

$$Q_L = \frac{1}{BW} = \frac{f_0}{\Delta f} \tag{4.20}$$

  After the calibration of the resonator properties, the dielectric material layer (in this case the glass) is inserted in the middle of the cavity. This means that there are three

regions, two of them are filled with air and the other is the region where the dielectric layer is inserted, as shown in Figure 4.1(b). The propagation constant in each medium is different, as shown in the following equations:

$$\beta = \sqrt{\omega^2 \varepsilon_r \varepsilon_0 \mu_0 - \left(\frac{\chi'_{nm}}{a}\right)} \tag{4.21}$$

$$\beta_0 = \sqrt{\omega^2 \varepsilon_0 \mu_0 - \left(\frac{\chi'_{nm}}{a}\right)} \tag{4.22}$$

The phase shift of the air and the dielectric layer is $\theta_0 = \beta_0 H_h$ and $\theta = \beta h_s/2$, respectively. Then, continuity of electromagnetic field must be forced in the boundary. These boundary conditions at the surface of the dielectric require an eigenvalue, θ, that satisfies the equation (4.23) where ε_r is the variable to find out.

$$\theta \tan\theta = (h_s/2) H_h \theta_0 \cot\theta_0 \tag{4.23}$$

This procedure for the calculation of the permittivity is an approximation, because the layer is assumed to be enclosed inside of the cylinder by a conducting ring at the cavity diameter, thus, loss in the gap region and radiation outside the cavity are neglected [86].

For calculating the loss tangent, the quality factor, Q_L, must be analyzed. Q_L is defined as the relation between the stored average energy and the dissipated average power. In the resonant structure under analysis, Q_L can be calculated with the expression in (4.20).

The insertion loss at the resonance frequency is also needed to calculate Q_0 as detailed in (4.19). To separate resonator loss from dielectric ones, two functions are defined. Equation (4.24) calculates the loss tangent of the measured sample. In this equation, U is the ratio of the electric energy in the cavity outside the sample to the electric energy in the sample, W is the ratio of end-wall to side-wall loss, and S is the conductor loss [86]. They are defined in (4.25), (4.26), and (4.27), respectively.

$$tan\delta = \frac{1+U}{Q_0} - SU\,(1+W) \tag{4.24}$$

$$U = \frac{1}{\varepsilon_r} \frac{\cos^3\theta}{(\theta + \sin\theta\cos\theta)\sin\theta} \frac{\cos\theta_0(\theta_0 - \sin\theta_0\cos\theta_0)}{\sin^3\theta_0} \tag{4.25}$$

$$W = \frac{\chi'_{nm}\left(\frac{\theta_0}{\theta_c}\right)^3}{1-\sin\theta_0\cos\theta_0} \tag{4.26}$$

$$S = \frac{1.0422}{\sqrt{a\sigma\eta_0(f/f_c)^3}} \tag{4.27}$$

where:

- η_0 is the free-space wave impedance.
- $\theta_c = \chi'_{nm}\left(\frac{H_h}{a}\right)$

- **Modal method**. For the characterization of the LC, the method described in [88] is employed. It implements a full-wave circuit analysis of the structure (split-cylinder). It is an analytic method, thereby it is much more accurate and requires a lower computational cost than a numerical method (based on FDTD or FEM), but requires the resolution of the full analytical problem of each structure in particular. This method allows to study materials of non-homogeneous construction like the LC cells, although it is necessary to previously know the permittivity, the loss, and the thickness of the glasses of these cells, and thickness of each LC sample cell.

  The method is based on segmenting the whole structure in canonical circuital elements that can be solved in a simpler way to obtain the Generalized Admittance Matrix (GAM) of each element [89]. An equivalent microwave network is obtained, which represents all the possible modes that can be excited in these elements. Afterwards, all of them are recursively joined by pairs to obtain one equivalent multimodal network of two ports of the whole structure. At this point, the complex permittivity ($\varepsilon_r = \varepsilon'_r - j\varepsilon''_r$) can be obtained [90].

  As can be seen in Figure 4.7(a), the split-cylinder resonator with an LC cell has been split in 5 zones in the vertical direction. In this structure, the upper and lower zones model the air filled resonator sections (each one is a 3-port network), the second and the fourth zones model the glass of the cell (two 3-port networks for each one), and the central region models the LC sample (two 3-port networks). All the dimensions and two permittivities are known (air and glass) and one is unknown (the complex permittivity of the LC sample).

  Once the structure has been split, each circuit is electromagnetically characterized by its GAM which is computed by using the mode matching method. With this modal method, the electromagnetic fields of each port network are approximated by the series

expansion of equation (4.28). Since the proposed method is a full-wave circuit analysis, every possible electromagnetic modes inside the structure has been taken into account, i.e. TE_{nm} and TM_{nm}.

$$\vec{E}_{port} = \sum_n e_n \cdot \vec{E_n} \quad \vec{H}_{port} = \sum_n h_n \cdot \vec{H}_n \tag{4.28}$$

where:

- $\vec{E}_{port}$ and $\vec{H}_{port}$ are the electric and magnetic fields in the port surface.
- e_n and h_n are the amplitudes of each base function.
- $\vec{E}_n$ and $\vec{H}_n$ are the base functions for the electric and magnetic fields.

According to equation (4.28), the relation between electric and magnetic fields can be established by the general GAM matrix for an N-port network represented in equation (4.29).

$$\mathbf{h} = \begin{pmatrix} h_1 \\ h_2 \\ \dots \\ h_N \end{pmatrix} = \begin{pmatrix} \mathbf{Y_{11}} & \mathbf{Y_{12}} & \dots & \mathbf{Y_{1N}} \\ \mathbf{Y_{21}} & \mathbf{Y_{22}} & \dots & \mathbf{Y_{2N}} \\ \dots & \dots & \dots & \dots \\ \mathbf{Y_{N1}} & \mathbf{Y_{N2}} & \dots & \mathbf{Y_{NN}} \end{pmatrix} \begin{pmatrix} e_1 \\ e_2 \\ \dots \\ e_N \end{pmatrix} = \mathbf{Y} \cdot \mathbf{e} \tag{4.29}$$

In the GAM matrix, each h_n and e_n element is a vector with the coefficient of the series expansion shown in equation (4.28). Consequently, each element $\mathbf{Y_{ij}}$ is not a scalar value but a matrix. Thus, any $\mathbf{Y_{ij}}$ element of each network can be calculated by forcing the boundary conditions of the particular network and a short circuit condition in the other ports for every considered base function.

Once every GAM network is calculated, the networks are connected to each other enforcing the boundary conditions. A recursive method by pairs is used to obtain the GAM of the whole structure [89]. This new GAM is obtained for only one port (port 1 of Figure 4.7(c)). This port is then connected to ground (port 2 of Figure 4.7(c)) to force the resonance condition, which leads to solve equation (4.30).

$$|\det\left(\mathbf{Z_R}(dim, \varepsilon, \mu, f) + \mathbf{Z_L}(dim, \varepsilon, \mu, f)\right)| = 0 \tag{4.30}$$

where:

- $\mathbf{Z_R}$ and $\mathbf{Z_L}$ are the Generalized Impedance Matrices, defined as the inverse of the GAM, of each 1-port network (see Figure 4.7(c)).

– dim contains the dimensions of the resonator and LC cells.

– ε is the LC permittivity.

– μ is the LC permeability.

– f is the resonance frequency when the LC cell is placed in the resonator.

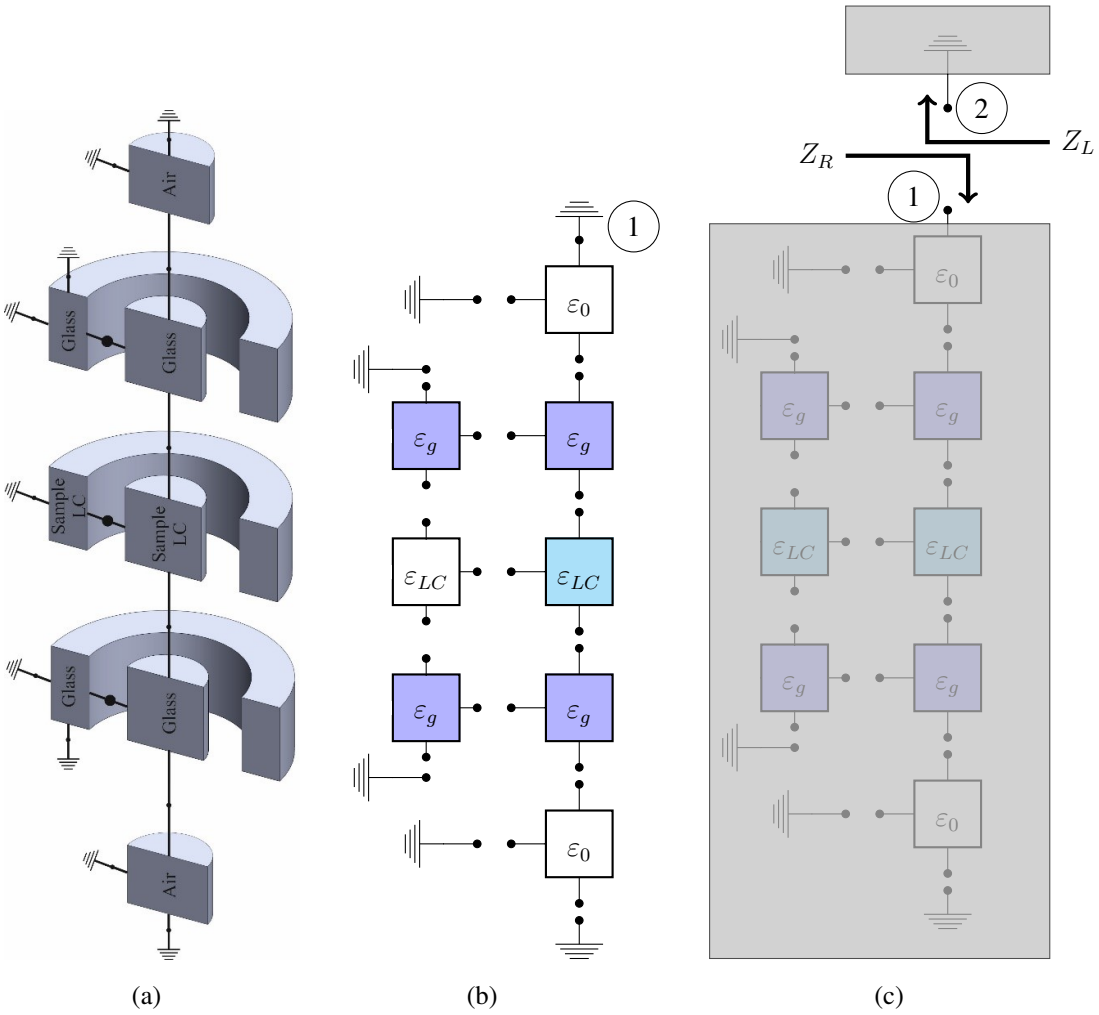

Figure 4.7: (a) Transverse section of a split-cylinder resonator loaded with a LC cell. (b) Circuital model of the resonant cavity and LC cell segmented into 8 simple circuits.

As can be seen in equation (4.30), every GAM network is a function of the dimensions of the structure, its electromagnetic properties (permeability and permittivity) and frequency. All these variables are known except the LC complex permittivity, which can be obtained by forcing this resonance condition [91].

As in the previous method, a calibration is also done with this method. This calibration consists on modelling the resonant cavity (without dielectric material) applying the same analysis method interconnection, in order to adjust the values of the feeding network, the radius of the resonator and the brass loss that form the structure.

- **Numerical method**. To validate the results obtained with the modal method and analyze its accuracy, a third method of numerical analysis is applied. Once the glass permittivity and dimensions of the LC cells and the measurement set-up (split-cylinder resonator and connectors) are known, an electrical model is simulated in a numerical electromagnetic simulation software: CST Studio Suite, as shown in Figure 4.8. With this method, the electromagnetic fields inside the structure will be iteratively simulated, as a function of the permittivity and the loss tangent of the LC or the material to characterize, to get a simulated resonance frequency and quality factor as much similar as possible to the measured ones in the real resonator. To adjust these values, a hybridization of different optimization algorithms is used to select the most suitable in each case. The process starts with 50 evaluations of a genetic algorithm. Then, the best values are used as the starting point of a Simplex or Trust Region algorithm. When the error of the resonance frequency and the quality factor is below 1 MHz and 5 respectively, the optimization algorithm is finally changed to a Quasi Newton method.

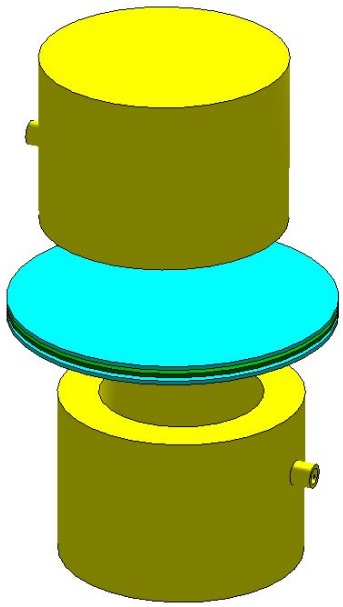

Figure 4.8: Model of the split-cylinder resonator for the numerical method.

4.1.4 Final adjustment

All these methods allow to extract values of the dielectric permittivity and the loss tangent. For that, taking into account the field distribution of the mode TE_{111} shown in Figure. 4.5(b), the cell is placed into the resonator with the molecules aligned in the same direction of the E-field, i.e. parallel to the major field distribution to measure ε_{rpos1}. Then, it is placed in the opposite direction (turned 90°), it means, perpendicular to the major field distribution, to measure ε_{rpos2}. This can be seen, respectively, in Figure 4.25(a) and 4.25(b) of section 4.3, where the whole process is explained in detail.

Since the E-field vector direction is not ideal for the TE_{111} mode, the ε_{rpos1} and ε_{rpos2} do not correspond to $\varepsilon_{r\parallel}$ and $\varepsilon_{r\perp}$, so the field distribution inside the cell should be considered in order to extract the precise values, as stated in equation (4.31).

$$\begin{aligned} \varepsilon_{rpos1} \iint |\overrightarrow{E}| dS &= \varepsilon_{r\perp} \iint E_{\perp} dS + \varepsilon_{r\parallel} \iint E_{\parallel} dS \\ \varepsilon_{rpos2} \iint |\overrightarrow{E}| dS &= \varepsilon_{r\parallel} \iint E_{\perp} dS + \varepsilon_{r\perp} \iint E_{\parallel} dS \end{aligned} \tag{4.31}$$

where:

- ε_{rpos1} and ε_{rpos2} are the measured complex permittivities with the cells in position 1 and 2 respectively, assuming an ideal (lineal polarization) E field .
- $|\overrightarrow{E}|$ is the module of the electric field calculated in each point of the cell, with the real polarization shown in Figure 4.5 (b).
- $E_{\parallel}$ is the component of the electric field in the parallel direction, see Figure 4.9 (a).
- $E_{\perp}$ is the component of the electric field in the normal direction, see Figure 4.9 (b).

Furthermore, all the methods consider the fields in the sample, including the portion of sample that is located close to the fringing fields. The use of TE_{nmp} modes implies that there is no propagation beyond the diameter of the upper and lower parts of the cavity. Then, as explained in classical publications [27, 86, 92], an electric wall is forced in the radius $r = b$, where b is the radius of the fringing area ($b = a + \Delta$, with Δ being the estimated fringing length, that usually is about $\Delta = 2$ cm).

Since it is clear that the actual cavity does not have a perfect wall in $r = b$, then it is important to validate that the fringing fields vanish in this area. This has been confirmed in several previous works [27, 93]. Additionally, works [94–97] also validate that the fringing fields vanish really fast, thus proving that the influence of power leakage onto loss calculations are practically negligible.

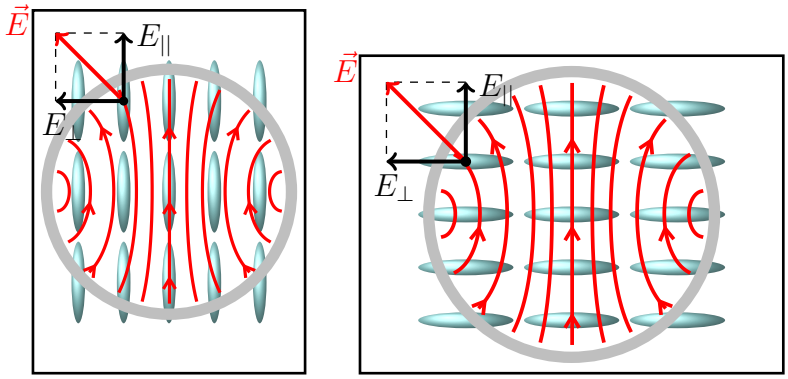

(a) (b)

Figure 4.9: (a) E-field and LC molecules in position 1. (b) E-field and LC molecules in position 2.

4.2 Liquid crystal cells

The development of LC cells requires a depth study with the aim of getting structures that allow the characterization of the dielectric properties of different LC samples as accurate as possible. The processes employed in the construction of the LC cell are not used in the microwave field and, in addition, minimal errors have hight impact in the results.

The materials used to form the cells are: glasses of 0.410 mm thickness whose dielectric properties must be characterized, Mylar spacers of 0.100 mm, and optical glue Norland UV Sealant 91 specially designed for the sealing of LC devices. They are shown in Figure 4.10

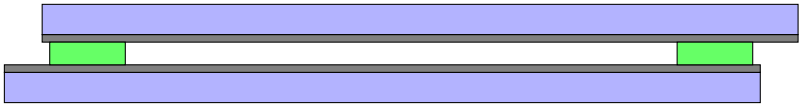

Figure 4.10: Outline of the LC cell. In blue the glasses that forms the covers, in gray the alignment layers, in green the spacers, and in white the hole intended to keep the LC sample.

The process for the construction of the cells is described below:

- **Glass cleaning**. The glass should be as clean as possible, for which a meticulous cleaning process is done in two stages:
  - Firstly, the glass is rubbed with a disposable cellulose cloth soaked in organic solvent (isopropyl alcohol and/or acetone). In this process the fat and larger particles are removed. The glass may seem clean, although it actually has a lot of

microscopic particles that could damage the homogeneity of the alignment layer and even the separation between glasses of the cell.

– Next, a second washing step is carried out in an ultrasound tank. In this process the glasses are immersed in a special detergent solution for ultrasonic cleaning (Nahita), and left into an ultrasound tank (Branson 1510) for at least 15 minutes (Figure 4.11). After this cleaning process the glasses are dried and stored in hermetic containers to avoid possible contamination.

Figure 4.11: Ultrasonic bath for cleaning the glasses.

- **Alignment surface**. To characterize the value of the dielectric anisotropy of the LC, its molecules must present a well defined orientation. For that, an alignment surface is created in one side of each glass of the cell. The creation of this alignment by anchoring surface is carried out in three main steps: the deposition of polyimide, the curing of this polymer and the realization of the microscopic grooves.

  – The deposition of the polyimide is done with a centrifuge mechanism: the glass is deposited on a spinner on which it is maintained by suction, covered with polyimide and centrifuged for 10 seconds at 16 revolutions per second, and then at 66 revolutions per second for 60 seconds to get a uniform surface of approximately 100 nm (see Figure 4.12). This thickness is an average value measured with a contact profilometer.

Figure 4.12: Spinner coater used for deposition of polyimide.

– After the deposition, the samples are cured at high temperature (90°C) to get the polymerization of the polyimide, thus, the material is hardened.

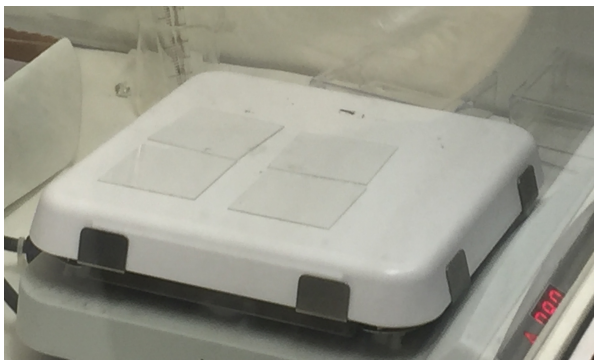

Figure 4.13: Curing of the polyimide on a laboratory heating plate.

– Finally, the samples are ready to make the microgrooves that will mark the orientation of the LC molecules. This is done by a rubbing process on a natural silk velvet, which leaves no residue. In this process the polyimide-covered face of the glass is rubbed repeatedly (at least 20 times) on a velvet strip. It is very important to perform rubbing in a unique way, since this will determine the initial inclination of the molecules. To achieve an homogeneous alignment direction, the velvet is fastened to a straight tray on which one of the faces of the glass can rest and move in a specific direction, as shown in Figure 4.14.

The microgrooves created on the alignment layer are of a few cents of nanometers. The Atomic Force Microscopy (AFM) measurements (see Figure 4.15) show grooves widths from 150 – 300 nm, similar to values reported in the literature [98]. On these

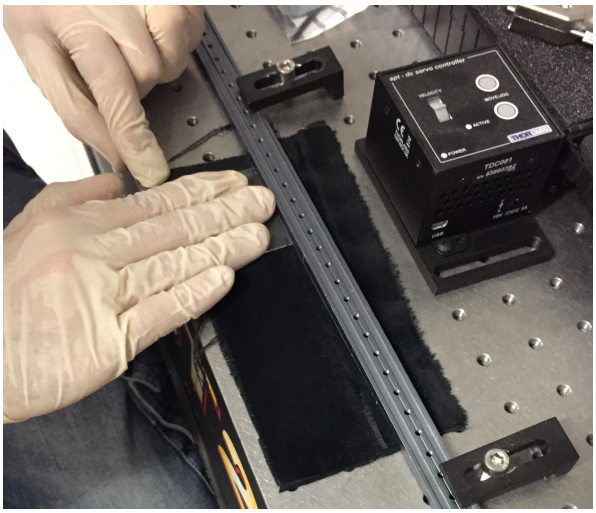

Figure 4.14: Set up for velvet rubbing.

microgrooves, the LC molecules lay down creating a perfect alignment of the material. It should be mentioned that rubbing process creates, besides unidirectional groove structures, the ordering of polymer chains. It is described that both effects contribute to LC preferential orientation [3].

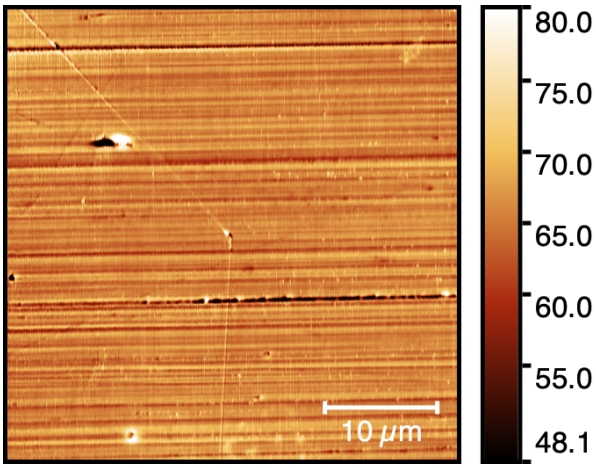

Figure 4.15: Microscopic view of the microgrooves on the polyimide layer of the glass.

- **Cells assembly** To form the LC cell, 4 Mylar separators are adhered near the corners of one glass with Norland glue, which is a harmless material for LC, not interacting with it. This will achieve to separate homogeneously the two glasses that make up the cell. Another glass is superimposed over the separators, both glasses have the same

alignment layer direction. A separation between both glasses, acting as a “bed", has to be left for the filling process, as shown in Figure 4.16. Next, pressure should be applied on the points of the adhesive to consolidate the structure and minimize the thickness added by the glue. Finally, the curing is carried out using an ultraviolet light oven following the indications pointed by the manufacturer.

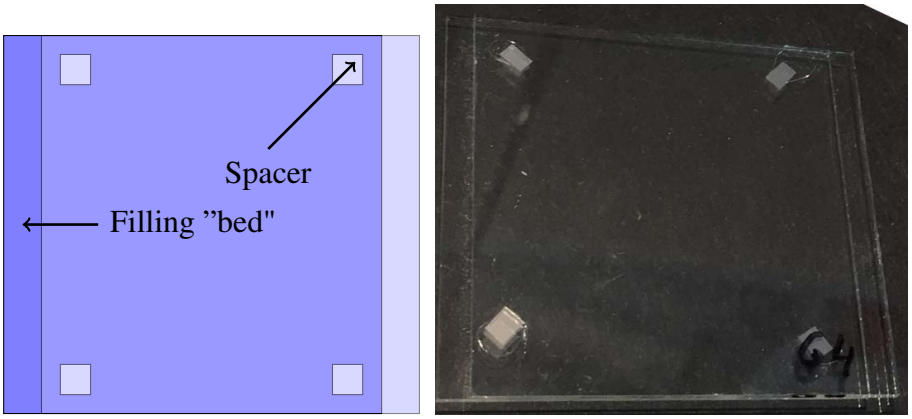

(a) (b)

Figure 4.16: (a) Layout of an LC cell. (b) Real LC cell assembled

As mentioned before, the thickness of the materials used in the characterization presents a great importance in the obtained results. For that reason, the thickness of the glasses of each cell has been measured in 8 different points before assembling the cells. To do the measurement a micrometer screw (Mitutoyo) with an accuracy of ± 2 μm has been used. For each glass of the four cells, the average thickness is detailed in Table 4.2.

Cell	Glass 1 (mm)	Glass 2 (mm)
TH1	0.410	0.410
TH2	0.404	0.410
TH3	0.410	0.410
TH4	0.409	0.409

Table 4.2: Average thickness of the glasses of the four LC cells.

The thickness of the cavity created between the two glasses of the cell has been measured by using of a spectrophotometer (Cary 5000 UV-Vis-NIR from Agilent). The measurement of the gap has been made taking advantage of the Fabry-Pérot resonance that occurs in the glass-air-glass interface of the LC cell.

The optical transmission spectrum of each empty cell, recorded as a function of the wavelength, shows a series of maxima and minima due to the interference phenomena originated by multiple reflections at the glass-air-glass interfaces. The frequency difference between consecutive maxima is related to the air gap thickness (h_g), according to the expression (4.32).

$$\Delta f = \frac{c}{2hn} \tag{4.32}$$

where

- Δf is the frequency space between two consecutive maximums.
- c is the speed light in the vacuum. c = 299792458 m/s.
- h is the separation between glasses.
- n is the refraction index of the medium (in this case the air: n = 1).

The smaller the spacing, the greater the frequency separation will be, so it will be easier to distinguish the maxima or minima. For this reason, this method is used for measuring very small values of thickness (thin samples). The thickness measurements with spectrophotometer are easier to perform in empty cells than in filled cells, because the maxima and minima are more pronounced, since the difference in refractive indexes between glass and LC is much smaller than the difference between glass and air refractive indexes.

Taking into account this phenomenon, it can be obtained a relationship between the separation of the glasses h_g and the number m of minima (or maxima) in a bandwidth. This bandwidth is defined by two non-consecutive maxima (or minima) located at the wavelengths λ_1 and λ_2.

$$h_g = \frac{m\lambda_1\lambda_2}{2n|\lambda_2 - \lambda_1|} \tag{4.33}$$

Figure 4.17 shows the interferometric measurement of the four cells. The thickness of the gaps has been measured using the method described above. Furthermore, to confirm these results the total thickness of the cells has been measured with a micrometer screw over the spacers (to prevent warping of the glasses), thereby subtracting the thickness of the glasses of Table 4.2, the separation of the glasses can be obtained. Both measurement results are shown in Table 4.3.

After obtaining the measurements of both glasses and the separation between them, the LC cells can be filled in. They are filled by depositing the material on the “bed" with a pipette and, this, by capillarity, extends for the whole cell as shown in Figure 4.18. Then, the cells are sealed with optical glue to avoid emptied during the measurement process.

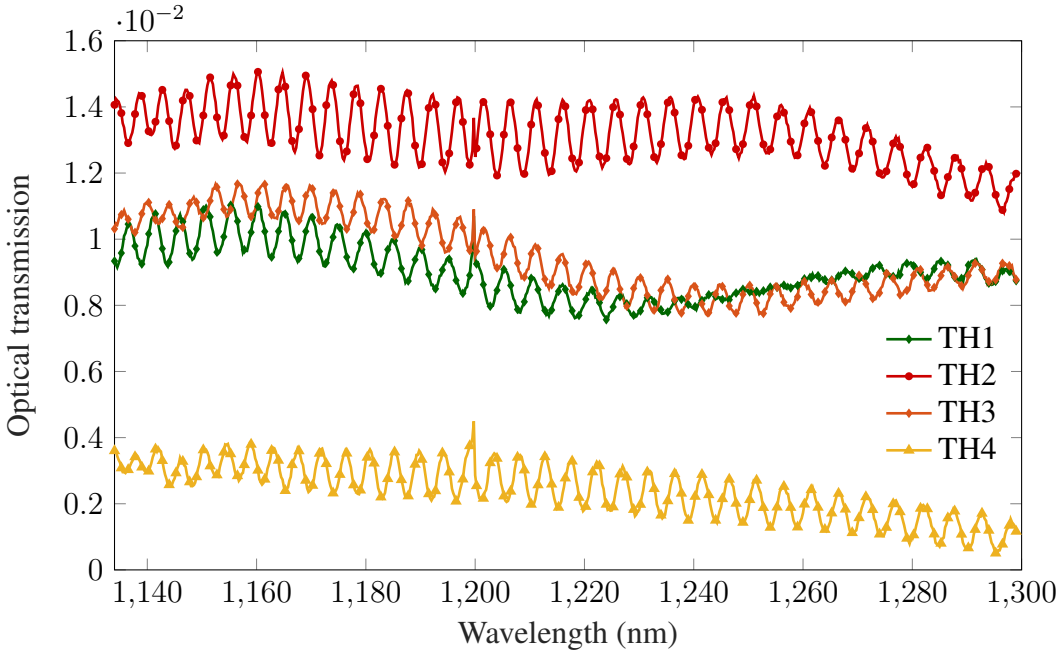

Figure 4.17: Optical transmission spectrum for the different cells.

Cell	Interferometric measurement (μm)	Micrometer screw measurement (μm)
TH1	156	155
TH2	151	150
TH3	151	151
TH4	144	145

Table 4.3: Average thickness of the space between glasses of the four LC cells.

One of the great advantages of using LC cells formed by transparent glasses is the possibility to check the correct alignment of the molecules. The asymmetry of the molecules of LC and its orientation, parallel to the polyimide rubbing, give the property of birefringence. When an isotropic medium is placed between two linear polarizers that stand orthogonally (crossed polarizers) over a source of white light, the light transmission is blocked. This happens because the polarization induced by the first polarizer is essentially maintained through the isotropic medium and so, it is totally filtered by the orthogonal second polarizer.

Now, an LC cell (with its axis rotated 45° with respect to the linear polarizers) is introduced between the two crossed polarizers. In this case, the light with linear polarization that goes through the first polarizer can be decomposed in the axes of the LC molecules into two orthogonal polarizations that, crossing the same medium, present different refractive indexes (different permittivity). This makes that the components travel at different speeds and, there-

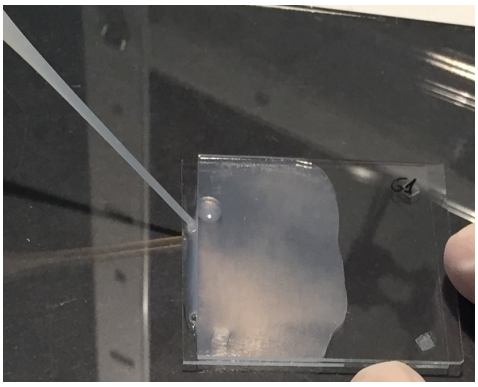

Figure 4.18: Filling process of an LC cell by capillarity.

fore, a phase shift between them is introduced. The result is a change in the polarization of light from linear to elliptical, therefore, when the light crosses the material and reaches the second polarizer, part of it passes through. This effect can be clearly seen in Figure 4.19, where the cell appears brighter when the rubbing direction forms 45° to the polarizers than when it is aligned either parallel or perpendicular to the incident polarization.

LC cells prepared in a similar way, but without any aligning layer, do not behave as described above. When they are inserted between the crossed polarizers they show similar light transmission, independently of the orientation relative to the polarization of the incident light.

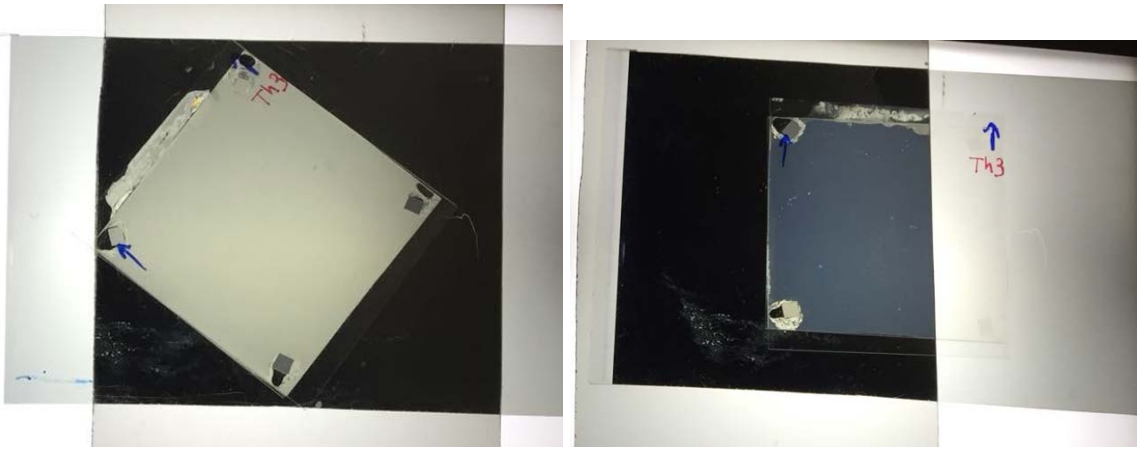

(a) (b)

Figure 4.19: (a) LC cell axis rotated 45° with respect to one of the crossed polarizers. (b) LC cell axis parallel to one of the crossed polarizers.

The polarizing optical microscopy images in Figure 4.20(a) and (b) correspond to an

oriented cell with the rubbing direction forming 45° and 0° to the polarizer, respectively.

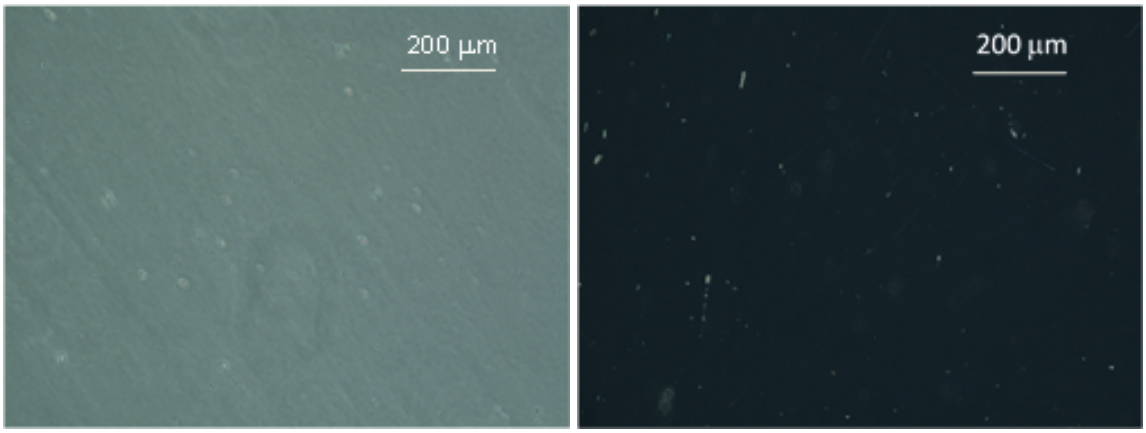

(a) (b)

Figure 4.20: Microscopic view of a filled LC cell with alignment surface. (a) LC cell axis rotated 45° with respect to one of the crossed polarizers. (b) LC cell axis parallel to one of the crossed polarizers.

For non-oriented LC cells, i.e. without polyimide alignment layer (see Figure 4.21), similar polarizing optical images are obtained for any sample orientation.

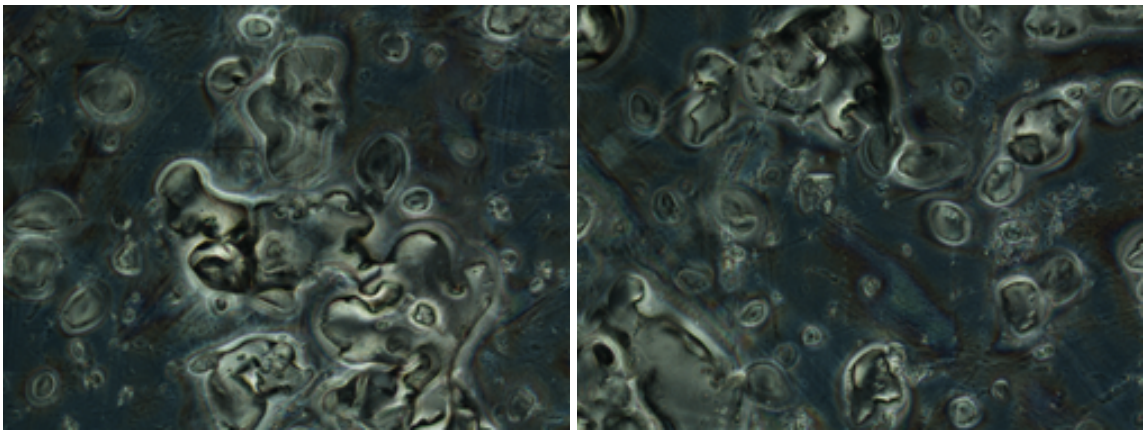

(a) (b)

Figure 4.21: Microscopic view of a filled LC cell without alignment surface. (a) LC cell axis rotated 45° with respect to one of the crossed polarizers. (b) LC cell axis parallel to one of the crossed polarizers.

4.3 Measurements

In this section the permittivity results are shown, together with some measurements and simulations of the scattering parameters obtained by applying the techniques described in the previous sections.

The analysis of the permittivity is performed with the TE_{111} mode in 3 split-cylinder resonators with the central frequencies in vacuum at 5 GHz, 9.5 GHz, and 11 GHz. Their dimensions and design process are described in section 4.1. With these resonators, the dielectric permittivity and loss tangent of four LC samples will be obtained in their two extreme polarization states.

The acquisition of the scattering parameters response (S-parameters) of the resonators, both in vacuum and with cells or glass, is perfomed using a VNA. The parameters to be analyzed are the variation of the resonance frequency of the resonator without any sample (f_0) versus the one of the resonator with some sample (f_s). In the same way, the quality factor must be calculated for the empty case (Q_0) and for the resonator with sample (Q_s).

With the objective of removing the systematic uncertainty, both in amplitude and phase, the VNA is calibrated using a SOLT (Short, Open, Load and Through) calibration set [99, 100]. The VNA has been configured to obtain measurements with the highest signal-to-noise ratio in order to have precise results for the permittivity values. An output power of 10 dBm is used, a central frequency and a bandwidth large enough to correctly display the response of each measurement. Moreover, a bandwidth of the intermediate frequency filter of 1 kHz is used to increase the accuracy.

In this work, four LC cells have been manufactured, whose dimensions are specified in section 4.2. The LC mixtures used for filling each cell are detailed in Table 4.4. In this Table the characteristics and specifications provided by the manufacturers of the LC are also shown. It is detailed the refractive indexes and the corresponding dielectric permittivity of each one for its two extreme states (parallel and perpendicular $n_\perp$, $n_\parallel$, $\varepsilon_{r\perp}$, and $\varepsilon_{r\parallel}$) provided in the data sheet of manufacturers. These parameters have been measured at a wavelength of 589 nm, thus about 509 THz.

Cell	Liquid Crystal	λ_{meas} (nm)	$n_\perp$	$\varepsilon_\perp$	$n_\parallel$	$\varepsilon_\parallel$
TH1	QYPDLC-036	589	1.5210	2.3134	1.7710	3.1364
TH2	QYPDLC-142	589	1.5235	2.3211	1.7745	3.1488
TH3	QYPDLC-193	589	1.5250	2.3256	1.7770	3.1577
TH4	GT3-23002	589	1.5094	2.2783	1.7986	3.2350

Table 4.4: Summary of the most important characteristics of the considered LC samples.

4.3.1 Calibration of the resonators

The characterization process begins with the measurement of the electromagnetic response of the resonators without any sample. This measurement is used to adjust the theoretical model of the resonators, thus helping to fix the effective radius, the feeding coupling and the loss for the metal of both measurements and model. This measurement of the resonator must be performed in the same conditions so that, it can be eliminated the effect of the feeding network and the losses of the metal over the resonance parameters used to calculate the electromagnetic properties of the materials. Since the structure does not have a prearranged feeding, but the penetration of the power loop can be modified according any specific need, the resonator should be calibrated each time this parameter is changed.

5 GHz resonator

All the measurements at 5 GHz have been made at the same time without modifications in the measurement conditions, therefore, only one calibration has been carried out. The frequency response of the resonator without any sample and the adjustment of the numerical method can be seen in Figure 4.22.

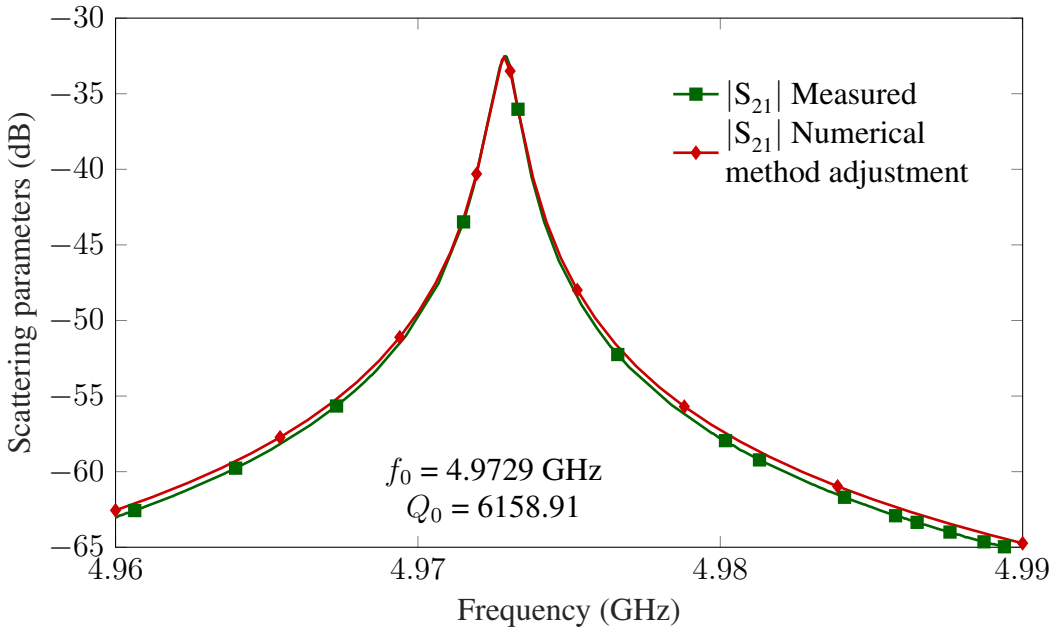

Figure 4.22: Comparison between the measurement of the 5 GHz resonator without sample and the adjustment of the numerical method (CST).

Once the measurement of the electromagnetic response of the unloaded resonator is made, the dimensions and theoretical characteristics of the resonators are adjusted to obtain the same

conditions of resonance frequency and quality factor (Q_0). The parameters can be adapted depending on the method used and can be consulted, together with the values obtained for each model, in Table 4.5, where a_{eff} is the effective radius of the resonator, σ_{brass} is the effective conductivity of the brass of the walls of the resonator, and fl is the insertion length of the feeding loop.

Kent		Numerical		Modal	
a_{eff}	20.0177 mm	a_{eff}	20.0157 mm	a_{eff}	20.0257 mm
σ_{brass}	$8.5730 \cdot 10^6$ S/m	σ_{brass}	$8.5530 \cdot 10^6$ S/m	σ_{brass}	$8.5920 \cdot 10^6$ S/m
		fl	0.0370 mm		

Table 4.5: Parameters of the 5 GHz resonator adjusted according to the method used.

As can be observed in Figure 4.22, when applying the values obtained in the calibration, the electromagnetic response of the model of the simulated resonator with the numerical method (CST Studio Suite) fits very well to the real measurement. The same process is carried out with the rest of the resonators.

9.5 GHz resonator

In this case, all the measurements have been also made without modifications in the configuration of the resonator, with a single calibration of the resonator parameters. The frequency response of the empty resonator and the adjustment of the numerical method can be seen in Figure 4.23, and the corresponding calculated parameters of the resonators for all the methods are detailed in Table 4.6.

Kent		Numerical		Modal	
a_{eff}	15.1014 mm	a_{eff}	15.0457 mm	a_{eff}	15.0572 mm
σ_{brass}	$7.7437 \cdot 10^6$ S/m	σ_{brass}	$7 \cdot 10^6$ S/m	σ_{brass}	$6.7749 \cdot 10^6$ S/m
		fl	0.3000 mm		

Table 4.6: Parameters of the 9.5 GHz resonator adjusted according to the method used.

11 GHz resonator

In this case, all the measurements have not been made at the same time, forcing to perform 5 different calibrations: one for the measurement of the glasses and the others for the measurement of each LC cell. The frequency response of the empty resonator and the adjustment of the numerical method for one calibration can be seen in Figure 4.24. Only one calibration is presented, since the others are very similar. As can be observed in Table 4.7, the

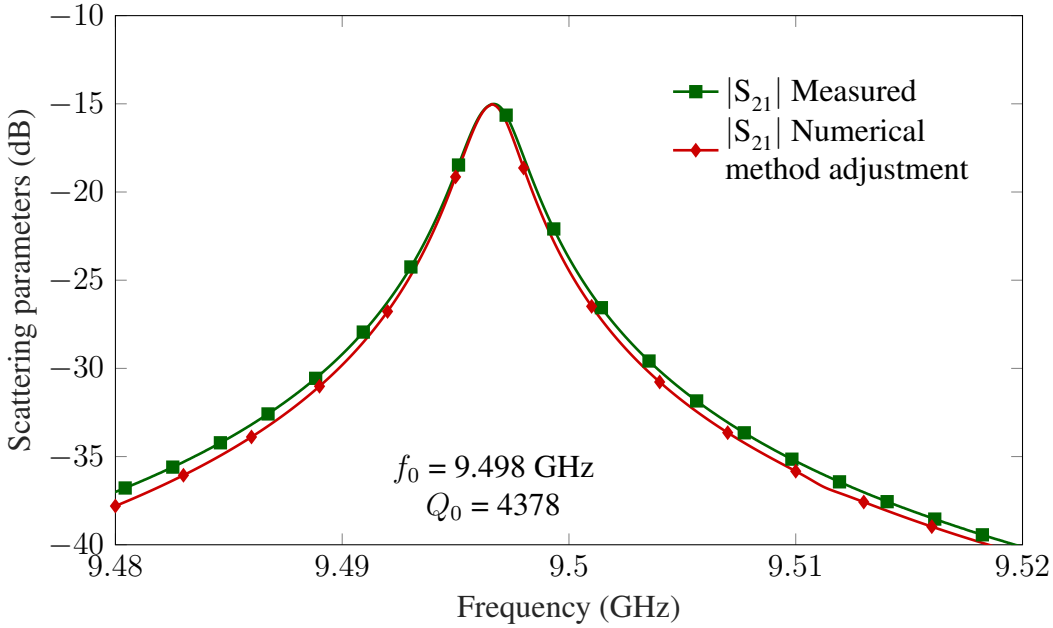

Figure 4.23: Comparison between the measurement of the 9.5 GHz resonator without sample and the adjustment of the numerical method.

resonance frequencies and the quality factors of the resonator without any sample for each calibration present a small variation. These variations between all the measurements without sample are mainly due to changes in the coupling of the feeding loop. The resulting parameters of the resonators, after applying all the three considered methods, are detailed in Table 4.8 and Table 4.9 for the calibration performed for the measurements of the glass and of the different LC cells, respectively.

Calibration	f_0 (GHz)	Q_0
1	11.041	4380.250
2	11.031	3626.850
3	11.035	4042.300
4	11.041	4380.250
5	11.040	3696.840

Table 4.7: Resonance frequency and quality factor of the 11 GHz resonator without samples for the different performed calibrations.

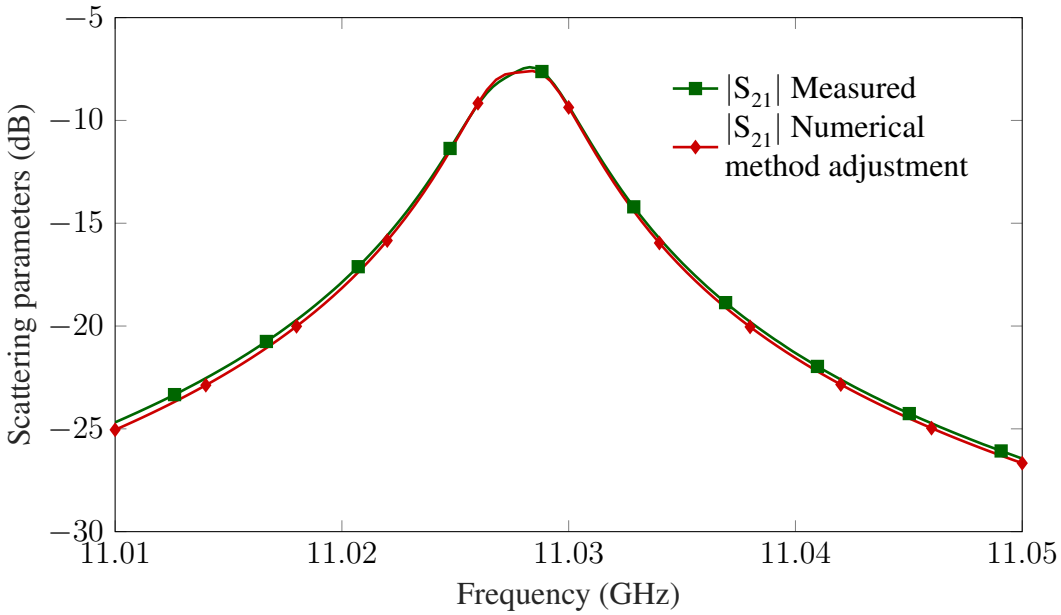

Figure 4.24: Comparison between the measurement of the 11 GHz resonator without sample and the adjustment of the numerical method.

Calibration	Kent		Numerical		Modal	
1	a_{eff}	10.0023 mm	a_{eff}	9.9989 mm	a_{eff}	10.0033 mm
	σ_{brass}	$8.4307 \cdot 10^6$ S/m	σ_{brass}	$10 \cdot 10^6$ S/m	σ_{brass}	$8.3671 \cdot 10^6$ S/m
			fl	0.3000 mm		

Table 4.8: Parameters of the 11 GHz resonator adjusted according to the method used for calibration related to glass measurements.

4.3.2 Measurement procedure

Once the configuration of the resonator and of the VNA are performed, the measurement of the empty resonator parameters is carried out. This measurement is used for the subsequent calibration of the aforementioned resonator variables. Then, the LC cells can be measured and analyzed for the calculation of their dielectric permittivity (real and imaginary part). This section describes the measurement process carried out.

Once the LC cell is built, filled with the LC mixture and sealed, it is introduced into the resonator, orienting its molecules parallel to the electromagnetic field in the mode TE_{111} (Figure 4.25(a)) and a measurement of the S-parameters of the resonator is carried out (position 1). Later on, the cell is rotated 90° by positioning its molecules perpendicular to the electric field (Figure 4.25(b)) and another measurement is acquired (position 2). This process is repeated several times obtaining several realizations in its two positions. In this way, the

Calibration	Numerical		Modal	
2	a_{eff}	10.0130 mm	a_{eff}	10.0177 mm
	σ_{brass}	$9 \cdot 10^6$ S/m	σ_{brass}	$5.7285 \cdot 10^6$ S/m
	fl	0.3090 mm		
3	a_{eff}	9.9970 mm	a_{eff}	10.0119 mm
	σ_{brass}	$10 \cdot 10^6$ S/m	σ_{brass}	$7.1199 \cdot 10^6$ S/m
	fl	0.3000 mm		
4	a_{eff}	9.9980 mm	a_{eff}	10.0033 mm
	σ_{brass}	$10 \cdot 10^6$ S/m	σ_{brass}	$8.3671 \cdot 10^6$ S/m
	fl	0.29000 mm		
5	a_{eff}	9.9970 mm	a_{eff}	10.0119 mm
	σ_{brass}	$10 \cdot 10^6$ S/m	σ_{brass}	$7.1199 \cdot 10^6$ S/m
	fl	0.3000 mm		

Table 4.9: Parameters of the 11 GHz resonator adjusted according to the method used for calibrations related to the cell measurements.

accuracy and repeatability of the measurement process can be studied.

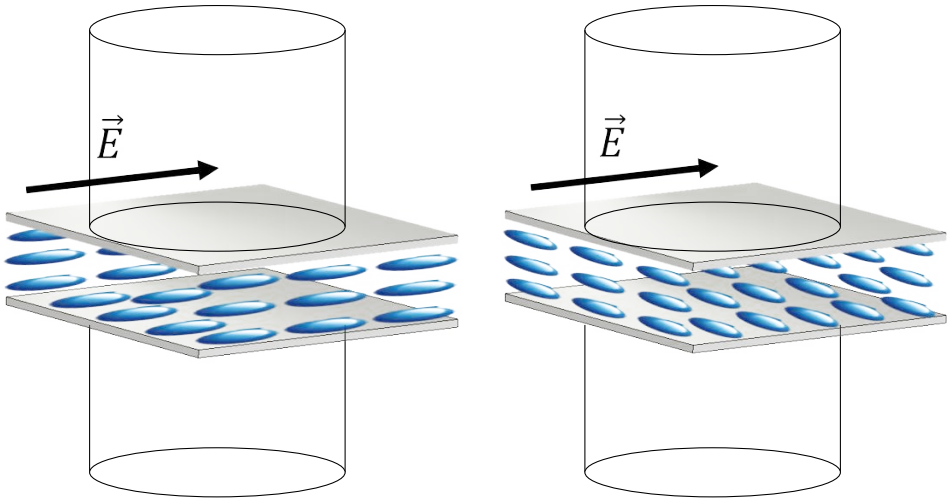

Figure 4.25: Positions of the cell samples: (a) Position 1. (b) Position 2.

The introduction of the sample in any of its positions involves a change in the boundary conditions of the resonator, which causes consequently a change in its resonance frequency and quality factor. The changes produced when introducing the sample and even when changing its position are clearly observed.

The next step is to calculate the resonance frequency and the quality factor of each situation, and analyze them with the proposed methods to obtain the permittivity values of the

material under analysis.

4.3.3 Characterization of the glasses

To analyze the permittivity of the glasses, the three analysis methods described in section 4.1.2 have been applied. In this case, as crystalline solids like glass might present a dielectric anisotropy, it has been decided to perform more than one measurement modifying the orientation of the glass respect the electric field, in a similar way to the proposed procedure for the measurement of the anisotropy of the LC illustrated in Figure 4.25.

To cover a wider range of results, it has been decided to measure two different samples of the same glass used to make the LC cells. In this case, they have been denominated G_1 and G_2 with thicknesses equal to 0.394 mm and 0.403 mm, respectively. The following sections will show the results obtained after the analysis with the three resonators used.

11 GHz resonator

The glasses have been introduced into the resonator several times and in different positions, obtaining a representative set of measurements, as can be observed in the measurements related to the sample G_1 of Figure 4.26.

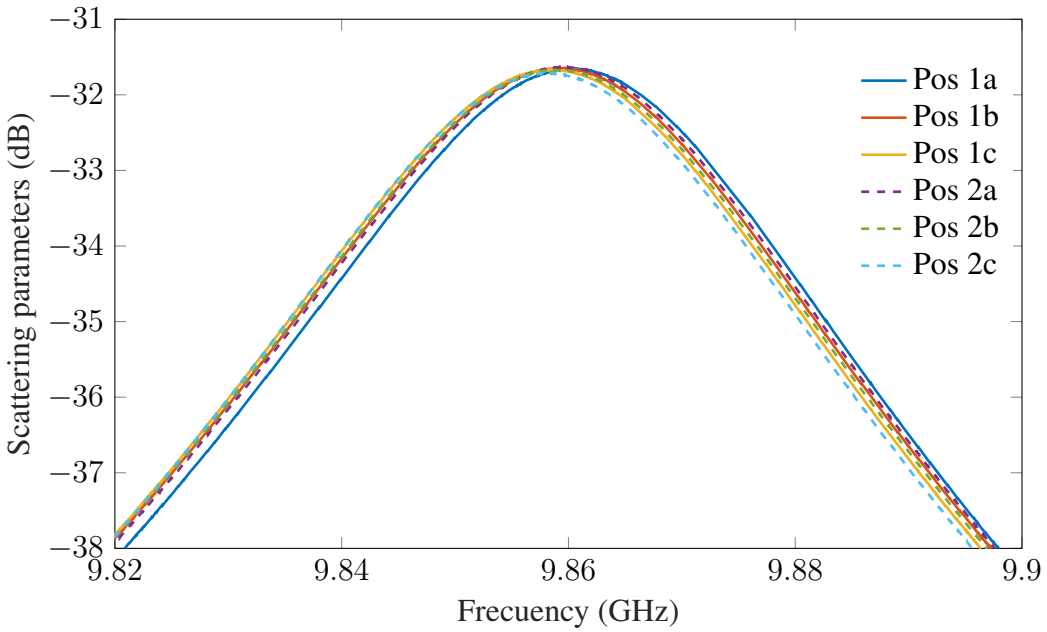

Figure 4.26: Measurements of the 11 GHz resonator with the glass G_1 at different positions.

The parameters of the resonator when the glasses are placed in different positions are

shown in Table 4.10. The number of position indicates when one of the axis of the glass is parallel (1) or perpendicular (2) to the major electric field of the resonator and the letter indicates different realizations of the same measurement, same glass and position. These values have been analyzed with all the methods described to obtain the permittivity values shown in Table 4.11.

Position	Resonance frequency	Q_s-factor	Average f_s	Average Q_s
1a	9.8604 GHz	239.00		
1b	9.8595 GHz	237.70	9.8593 GHz	237.27
1c	9.8582 GHz	238.11		
2a	9.8595 GHz	238.00		
2b	9.8589 GHz	237.33	9.8588 GHz	237.92
2c	9.8581 GHz	238.45		

Table 4.10: Resonance frequency and Q-factor of the 11 GHz resonator with glass G_1.

	Kent		Numerical		Modal	
Position	ε_r	$tan\delta$	ε_r	$tan\delta$	ε_r	$tan\delta$
1	7.148	0.0166	7.13	0.0164	7.13	0.0168
2	7.152	0.0166	7.13	0.0168	7.14	0.0168

Table 4.11: Calculated permittivity values and loss tangent of glass G_1 for 11 GHz.

From these data it can be concluded that the glasses are isotropic dielectric materials. In the same way, the great repeatability of the results in each measurement demonstrates that it is not necessary to measure several implementations with sample G_2. However, its dielectric properties will be characterized in order to check whether all the glasses present homogeneous dielectric characteristics. As in the previous case, the resonance frequency and the Q-factor are measured (Table 4.12), and the obtained permittivity values and loss tangent are shown in Table 4.13. Since the error margin of the glass measurements is below 0.1% and 0.001% in terms of permittivity and loss tangent respectively, its effect has been neglected due to the small influence in the final LC results.

Sample	Resonance frequency	Q-factor
G_2	9.861 GHz	237

Table 4.12: Resonance frequency and Q-factor of the 11 GHz resonator with glass G_1.

Kent		Numerical		Modal	
ε_r	$tan\delta$	ε_r	$tan\delta$	ε_r	$tan\delta$
7.1202	0.0164	7.1095	0.0164	6.97	0.0172

Table 4.13: Calculated permittivity values and loss tangent of glass G_2 for 11 GHz.

5 GHz resonator

The procedure is exactly the same followed with the 11 GHz resonator; however, in this case only one measurement of each of the two orthogonal positions of the glasses G_1 and G_2 has been made (see Table 4.14), obtaining the results of the Table 4.15.

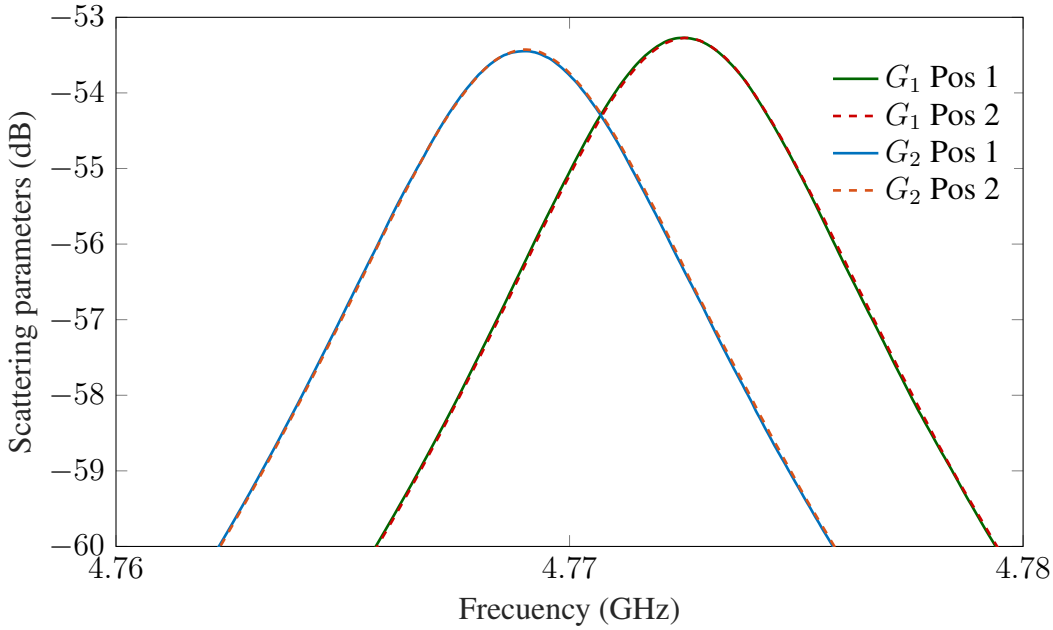

Figure 4.27: Measurements of the 5 GHz resonator with G_1 and G_2 at different positions.

Sample	Position	Resonance frequency	Q-factor
G_1	1	4.7725 GHz	677.34
G_1	2	4.7726 GHz	674.75
G_2	1	4.7689 GHz	667.11
G_2	2	4.7690 GHz	670.11

Table 4.14: Resonance frequency and Q-factor of the 5 GHz resonator with G_1 and G_2.

In this case, a smaller deviation is observed between the electromagnetic characteristics measured in the two orthogonal positions of the glasses. Therefore, this variation allows to assume that it is an isotropic material. In the same way, the error margin is negligible.

Sample	Kent		Numerical		Modal	
	ε_r	$tan\delta$	ε_r	$tan\delta$	ε_r	$tan\delta$
G_1	7.287	0.0144	7.247	0.0138	7.219	0.0155
G_2	7.254	0.0144	7.220	0.0140	7.200	0.0154

Table 4.15: Calculated permittivity values and loss tangent of G_1 and G_2 for 5 GHz.

9.5 GHz resonator

As in the previous cases, one measurement for each position of each glass is carried out. The measured parameters are indicated in Table 4.16, and applying the three methods, the permittivity values and loss tangent are those indicated in Table 4.17.

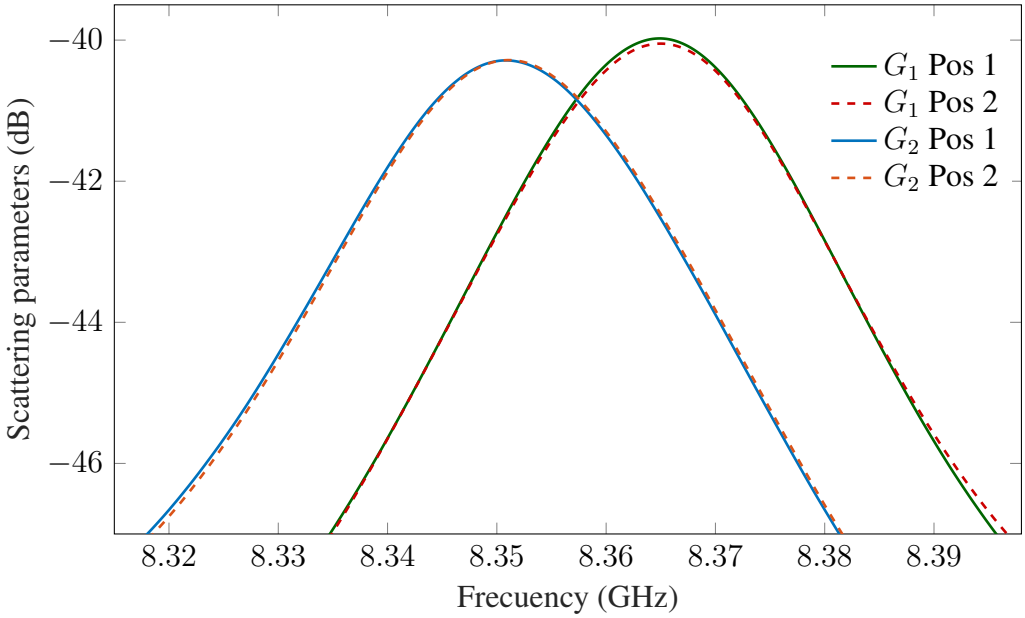

Figure 4.28: Measurements of the 9.5 GHz resonator with G_1 and G_2 at different positions.

Sample	Position	Resonance frequency	Q-factor
G_1	1	8.3635 GHz	269.92
G_1	2	8.3640 GHz	266.66
G_2	1	8.3510 GHz	252.40
G_2	2	8.3510 GHz	252.90

Table 4.16: Resonance frequency and Q-factor of 9.5 GHz resonator with G_1 and G_2.

Analyzing these results, it can be affirmed that the glasses have an isotropic and homogeneous permittivity. This permittivity value will be considered for the calculation of the

	Kent		Numerical		Modal	
Sample	ε_r	$tan\delta$	ε_r	$tan\delta$	ε_r	$tan\delta$
G_1	7.163	0.0142	7.24	0.0152	7.2213	0.0146
G_2	7.090	0.0149	7.20	0.0153	7.1504	0.0154

Table 4.17: Calculated permittivity values and loss tangent of G_1 and G_2 for 9.5 GHz.

permittivity of the LC mixtures.

4.3.4 Liquid Crystal characterization

Now, the measurement of the electromagnetic response of the three resonators with the LC cells can be performed, in order to obtain the dielectric permittivity and loss tangent values after their analysis.

The cells are formed by layers of different materials (the two glasses and the LC between them), thereby the Kent method can not be applied. In this case the measurements have been only analyzed with two methods: the numerical method and the modal one.

For the analysis of the permittivity it is needed to know: the thickness of the glass and LC samples measured before, the average values of the dielectric permittivity of the glasses that form the cell, and the resonator configuration.

There are many error sources that affect the extraction of the complex permittivity: the features of the cylinder (dimensions a and L, conductivity, feeding loops), the measured EM response (f_{us} and Q_{us}), the thickness of the glasses (h_{g1} and h_{g2}) and the thickness of liquid crystal (h_{LC}). The impact of the cylinder dimensions and elements (a and L) is calibrated and compensated with a first measurement of the empty cylinder. However, the tolerance in the measurement of the other parameters is translated into a set of uncertainties (σ_i), and their error contributions to the complex permittivity results are quantified as $\frac{\partial \varepsilon}{\partial i}$. Then, if the error contribution of these parameters is independent and known, the total uncertainty of the complex dielectric permittivity can be expressed as the quadrature sum [101] described in equation (4.34). Finally, once the uncertainty of the complex permittivity is calculated, the error can be easily propagated to obtain the uncertainty of the real and imaginary parts (as well as of the loss tangent):

$$\sigma_\varepsilon = \sqrt{\left(\left|\frac{\partial \varepsilon}{\partial f}\right|^2 \sigma_f^2 + \left|\frac{\partial \varepsilon}{\partial Q}\right|^2 \sigma_Q^2 + \left|\frac{\partial \varepsilon}{\partial h_{g1}}\right|^2 \sigma_{h_{g1}}^2 + \left|\frac{\partial \varepsilon}{\partial h_{g2}}\right|^2 \sigma_{h_{g2}}^2 + \left|\frac{\partial \varepsilon}{\partial h_{LC}}\right|^2 \sigma_{h_{LC}}^2 \right)} \quad (4.34)$$

11 GHz resonator

Several measurements of each cell and position have been repeated. Figures 4.29, 4.30, 4.31, and 4.32 show the frequency response of the 11 GHz resonator when the cell TH1, TH2, TH3, and TH4 are placed, respectively, in the center of the resonator.

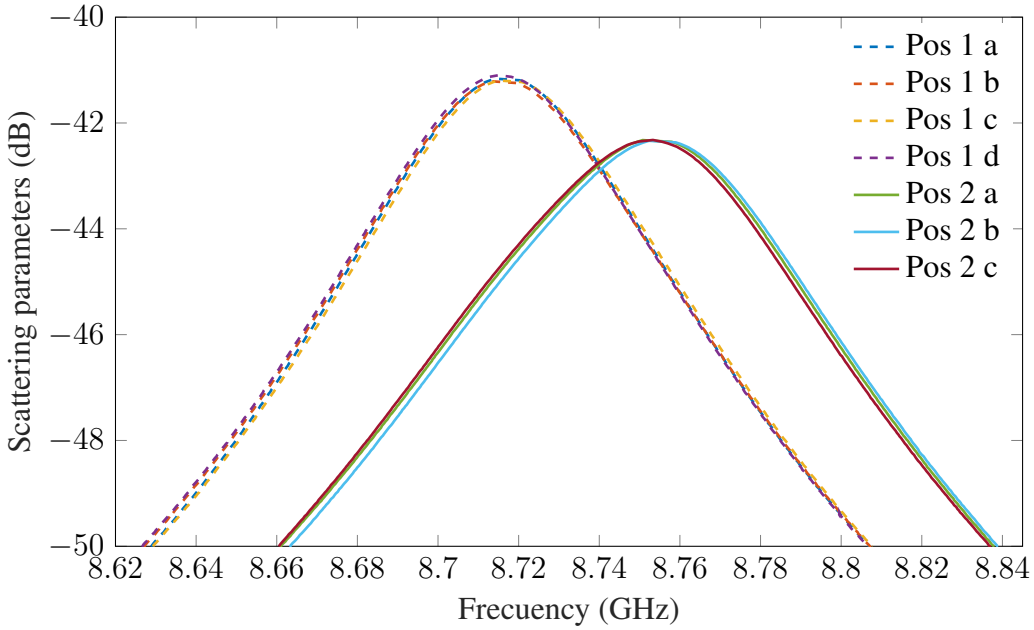

Figure 4.29: Measurement of the 11 GHz resonator with cell TH1.

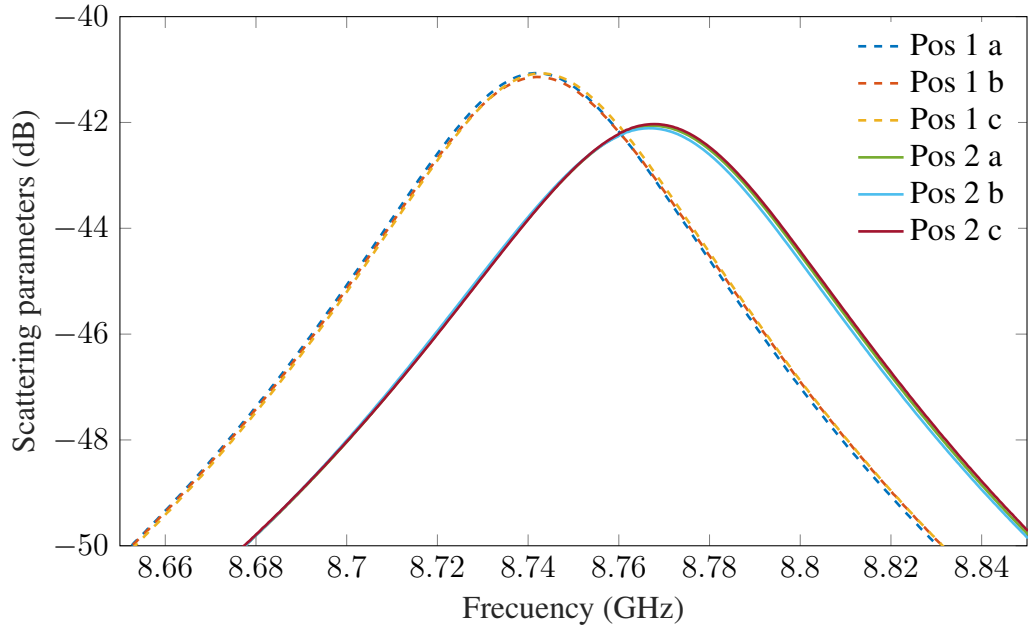

Figure 4.30: Measurement of the 11 GHz resonator with cell TH2.

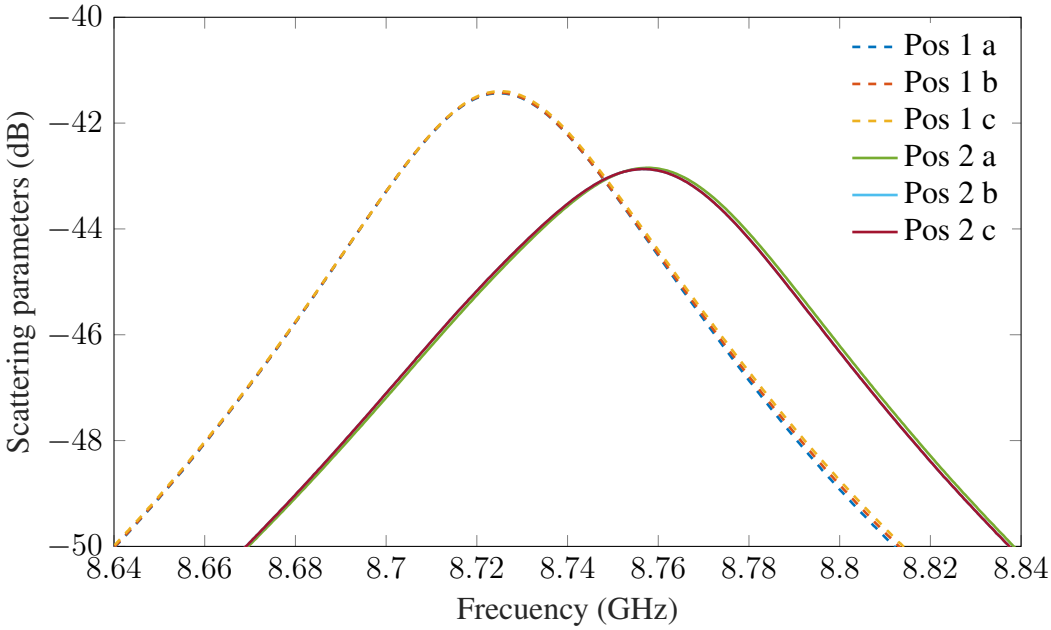

Figure 4.31: Measurement of the 11 GHz resonator with cell TH3.

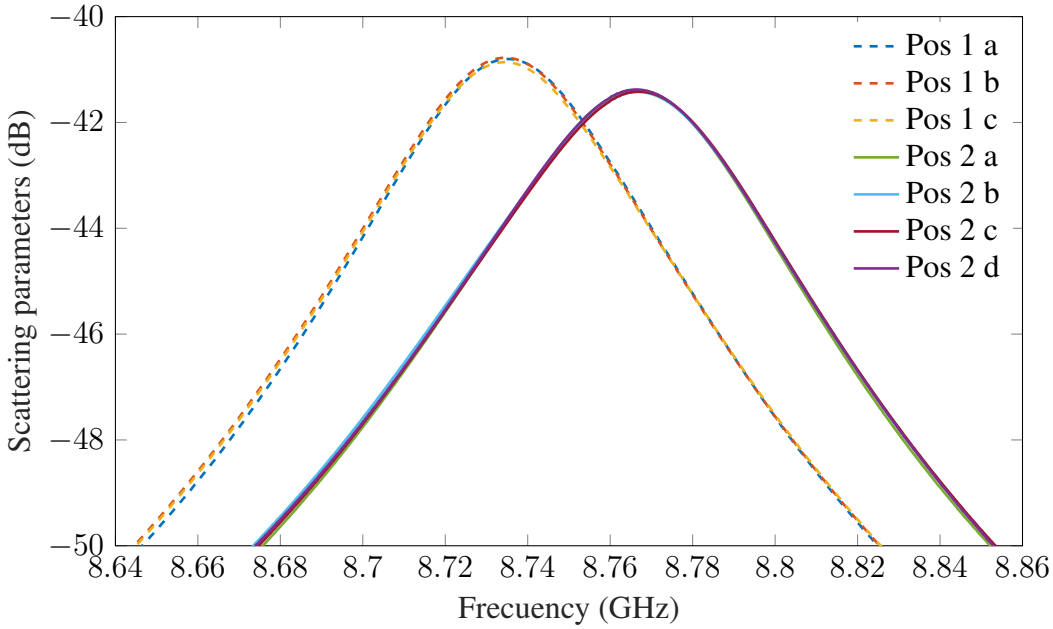

Figure 4.32: Measurement of the 11 GHz resonator with cell TH4.

In these cases, it can be seen at least three repetitions of position 1 and three repetitions of the cell rotated 90°, position 2. Both positions are used together for extracting the parallel permittivity value ($\varepsilon_{r\parallel}$) and the perpendicular permittivity value ($\varepsilon_{r\perp}$). The data presented in Table 4.18 shows the resonance frequency (related to dielectric anisotropy) and quality factor (related to the loss tangent anisotropy).

	Position 1		Position 2	
Liquid Crystal	f_{us} (GHz)	Q-factor	f_{us} (GHz)	Q-factor
QYPDLC-036	8.7165 ± 0.00058	127.54 ± 1.02	8.7539 ± 0.00042	108.75 ± 0.58
QYPDLC-142	8.7425 ± 0.00055	129.24 ± 1.02	8.7675 ± 0.00096	115.78 ± 0.78
QYPDLC-193	8.7249 ± 0.00035	128.15 ± 0.22	8.7566 ± 0.00016	106.19 ± 0.18
GT3-23002	8.7350 ± 0.00061	133.02 ± 1.26	8.7667 ± 0.00032	124.82 ± 1.59

Table 4.18: Resonance frequency and Q-factor of 11 GHz resonator with LC cells.

The resulting data from the analysis of the resonance frequency and the quality factor with the two proposed methods, the modal and the numerical, can be observed in Table 4.19 and Table 4.21 for position 1 and position 2. When these values are corrected with equation (4.31), based on the non-ideality of the electric field distribution, the resultant values are shown in Tables 4.20 and 4.22. Moreover, these tables include the uncertainty of the dielectric permittivity and the loss tangent, calculated as expressed in (4.34).

Some conclusions can be drawn from the obtained results: there is a good agreement in

	Position 1		Position 2	
Liquid Crystal	ε_r	$tan\delta$	ε_r	$tan\delta$
QYPDLC-036	3.500	0.0139	2.763	0.0579
QYPDLC-142	3.359	0.0128	2.857	0.0416
QYPDLC-193	3.563	0.0130	2.920	0.0634
GT3-23002	3.548	0.0063	2.879	0.0224

Table 4.19: Calculated position 1 and 2 permittivity values and loss tangent of LC cells for 11 GHz resonator with the modal method.

Liquid Crystal	$\varepsilon_{r\parallel}$	$tan\delta_{\parallel} \times 1000$	$\varepsilon_{r\perp}$	$tan\delta_{\perp} \times 1000$
QYPDLC-036	3.22 ± 0.19	3.95 ± 0.67	2.24 ± 0.15	57.51 ± 6.8
QYPDLC-142	3.05 ± 0.18	5.80 ± 1.06	2.36 ± 0.16	40.88 ± 4.92
QYPDLC-193	3.26 ± 0.20	1.97 ± 0.11	2.40 ± 0.17	63.31 ± 4.40
GT3-23002	3.25 ± 0.21	2.50 ± 0.83	2.35 ± 0.17	22.05 ± 3.81

Table 4.20: Adjusted parallel and perpendicular permittivity values and loss tangent of LC cells for 11 GHz resonator with the modal method.

	Position 1		Position 2	
Liquid Crystal	ε_r	$tan\delta$	ε_r	$tan\delta$
QYPDLC-036	3.505	0.044	2.745	0.160
QYPDLC-142	3.390	0.031	2.823	0.103
QYPDLC-193	3.550	0.036	2.870	0.142
GT3-23002	3.559	0.014	2.858	0.048

Table 4.21: Calculated position 1 and 2 permittivity values and loss tangent of LC cells for 11 GHz resonator with the numerical method.

Liquid Crystal	$\varepsilon_{r\parallel}$	$tan\delta_{\parallel} \times 1000$	$\varepsilon_{r\perp}$	$tan\delta_{\perp} \times 1000$
QYPDLC-036	3.22 ± 0.20	3.47 ± 0.80	2.23 ± 0.19	71.38 ± 18.57
QYPDLC-142	3.09 ± 0.21	6.63 ± 1.76	2.33 ± 0.15	43.05 ± 3.77
QYPDLC-193	3.26 ± 0.16	3.58 ± 0.54	2.34 ± 0.17	60.43 ± 4.75
GT3-23002	3.32 ± 0.20	3.70 ± 1.00	2.32 ± 0.16	19.92 ± 5.20

Table 4.22: Adjusted parallel and perpendicular permittivity values and loss tangent of LC cells for 11 GHz resonator with the numerical method.

the results of both methods. Moreover, the error of the results is small enough to consider the results consistent and valid.

5 GHz resonator

As in the previous case, the frequency responses of the different cells are shown in Figures 4.33, 4.34, 4.35, and 4.36 for TH1, TH2, TH3, and TH4, respectively. In the same mode, the measured values of resonance frequency and Q-factor are shown in Table 4.23.

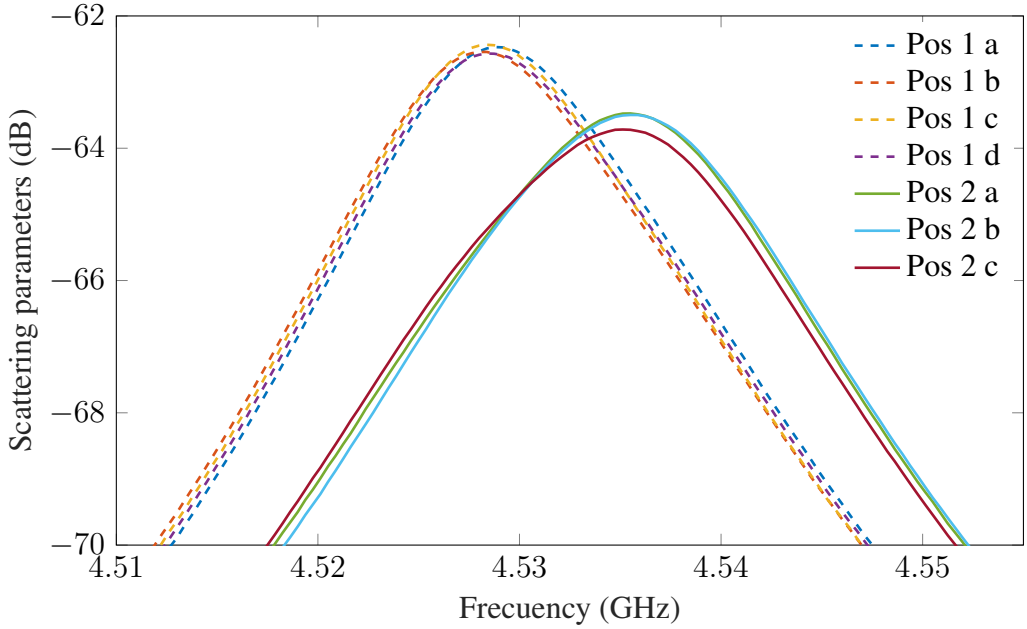

Figure 4.33: Measurement of the 5 GHz resonator with cell TH1.

	Position 1		Position 2	
Liquid Crystal	f_{us} (GHz)	Q-factor	f_{us} (GHz)	Q-factor
QYPDLC-036	4.5283 ± 0.13	281.61 ± 1.5	4.5355 ± 0.28	245.30 ± 0.51
QYPDLC-142	4.5363 ± 0.07	298.94 ± 1.49	4.5400 ± 0.07	255.60 ± 0.21
QYPDLC-193	4.5299 ± 0.18	292.99 ± 2.11	4.5370 ± 0.09	238.94 ± 3.30
GT3-23002	4.5375 ± 0.07	308.51 ± 3.76	4.5429 ± 0.09	286.05 ± 4.02

Table 4.23: Resonance frequency and Q-factor of 5 GHz resonator with LC cells.

The difference in resonance frequencies between both positions may seem smaller than in the previous case (resonator with central frequency at 11 GHz), although the relative change remains almost the same. It is only an effect caused by the frequency dropping, since the obtained results demonstrate a similar anisotropy as shown in Table 4.24 and Table 4.26 for position 1 and position 2. Tables 4.25 and 4.27 show the corrected values of dielectric permittivity and loss tangent together with their uncertainties calculated as in the previous case.

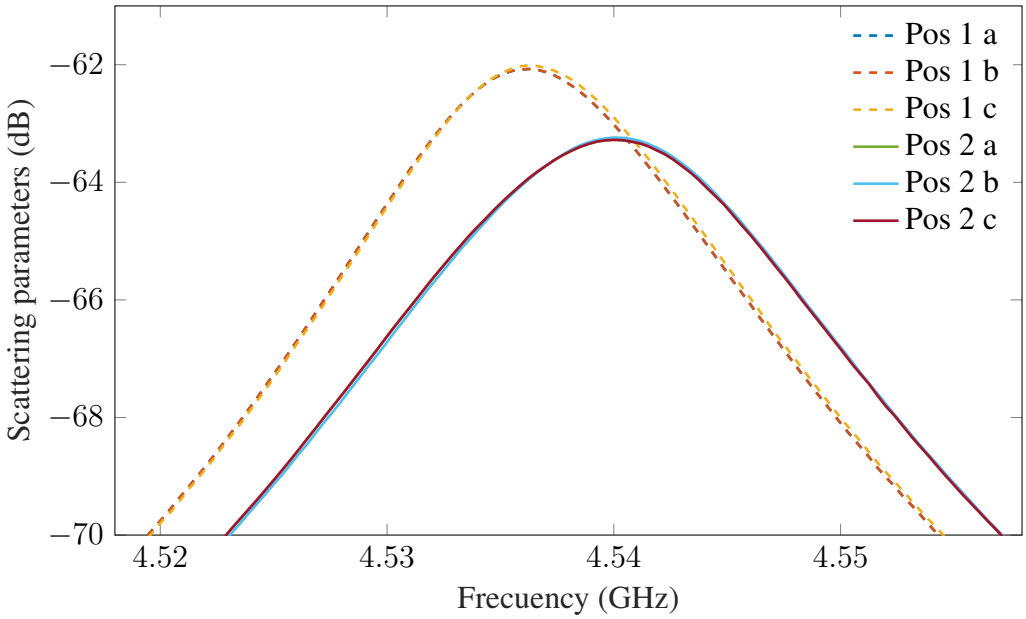

Figure 4.34: Measurement of the 5 GHz resonator with cell TH2.

	Position 1		Position 2	
Liquid Crystal	ε_r	$tan\delta$	ε_r	$tan\delta$
QYPDLC-036	3.3675	0.0239	2.7715	0.0648
QYPDLC-142	3.0181	0.0148	2.7020	0.0585
QYPDLC-193	3.3132	0.0171	2.7062	0.0763
GT3-23002	2.8389	0.0092	2.3555	0.0331

Table 4.24: Calculated position 1 and 2 permittivity values and loss tangent of LC cells for 5 GHz resonator with the modal method.

Liquid Crystal	$\varepsilon_{r\parallel}$	$tan\delta_{\parallel} \times 1000$	$\varepsilon_{r\perp}$	$tan\delta_{\perp} \times 1000$
QYPDLC-036	3.08 ± 0.19	17.06 ± 2.08	2.28 ± 0.15	75.45 ± 7.89
QYPDLC-142	2.72 ± 0.17	7.95 ± 1.09	2.27 ± 0.16	58.51 ± 7.20
QYPDLC-193	3.03 ± 0.19	7.14 ± 0.97	2.22 ± 0.15	91.90 ± 7.55
GT3-23002	2.59 ± 0.15	5.13 ± 1.79	1.94 ± 0.14	39.33 ± 10.90

Table 4.25: Adjusted parallel and perpendicular permittivity values and loss tangent of LC cells for 5 GHz resonator with the modal method.

As in the results obtained with the 11 GHz resonator, the results of the average permittivity values obtained with the two methods are very similar.

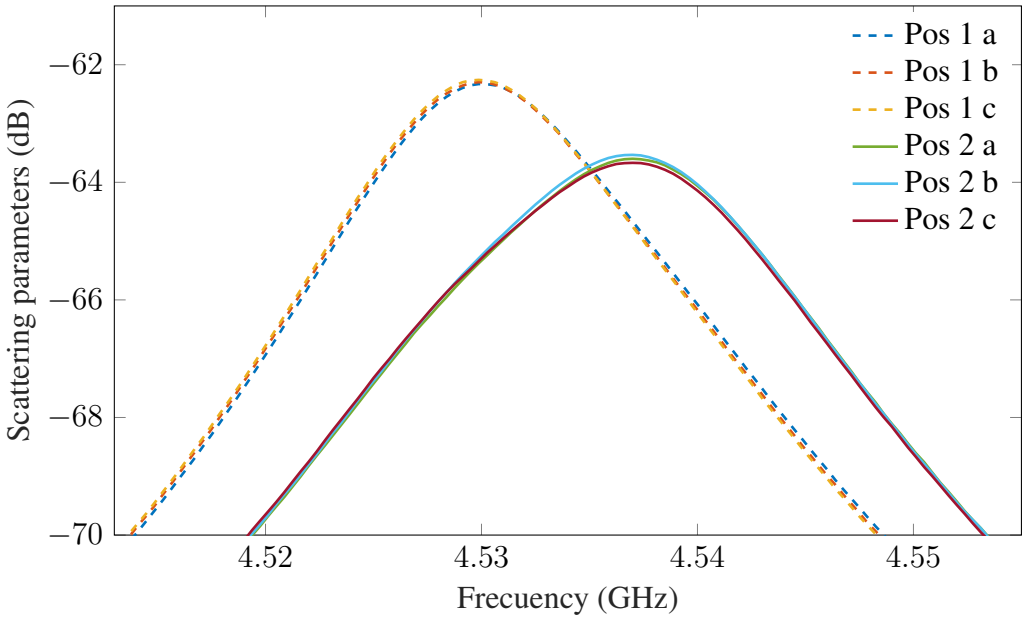

Figure 4.35: Measurement of the 5 GHz resonator with cell TH3.

	Position 1		Position 2	
Liquid Crystal	ε_r	$tan\delta$	ε_r	$tan\delta$
QYPDLC-036	3.420	0.083	2.795	0.183
QYPDLC-142	3.032	0.048	2.704	0.152
QYPDLC-193	3.346	0.061	2.718	0.213
GT3-23002	2.856	0.025	2.390	0.079

Table 4.26: Calculated position 1 and 2 permittivity values and loss tangent of LC cells for 5 GHz resonator with the numerical method.

Liquid Crystal	$\varepsilon_{r\parallel}$	$tan\delta_{\parallel} \times 1000$	$\varepsilon_{r\perp}$	$tan\delta_{\perp} \times 1000$
QYPDLC-036	3.11 ± 0.22	17.01 ± 2.67	2.29 ± 0.19	75.61 ± 9.45
QYPDLC-142	2.74 ± 0.15	8.73 ± 2.03	2.26 ± 0.13	65.97 ± 6.70
QYPDLC-193	3.07 ± 0.10	6.64 ± 0.70	2.22 ± 0.13	94.82 ± 14.51
GT3-23002	2.63 ± 0.16	4.81 ± 2.27	1.97 ± 0.17	39.14 ± 11.81

Table 4.27: Adjusted parallel and perpendicular permittivity values and loss tangent of LC cells for 5 GHz resonator with the numerical method.

9.5 GHz resonator

The measured frequency responses are shown in Figures 4.37, 4.38, 4.39, and 4.40, and the experimental results of resonance frequency and Q-factor can be seen in Table 4.28. As in other frequencies, these data have been analyzed obtaining the dielectric features of Table

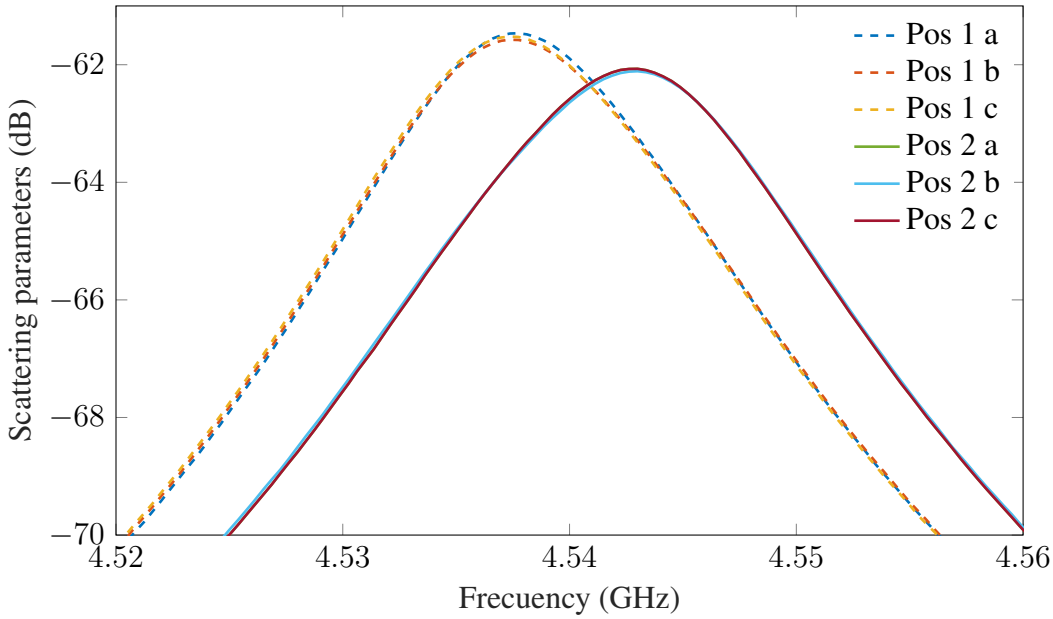

Figure 4.36: Measurement of the 5 GHz resonator with cell TH4.

4.29.

The values could only be extracted with the modal method, since the numerical method does not converge to any realistic value. This is caused by several reasons. First, the permittivity obtained for the cells oriented in position 1 is smaller than for position 2, which is contradictory to the expected results. On the other hand, the loss tangent presents, in some measurements, not consistent values, even reaching negative values (gain), which is impossible. It is obvious that the results obtained using the 9.5 GHz resonator are not valid. The source of error must have been systematic and possibly due to the radius and height configuration chosen for this resonator, since the selected working region (Figure 4.4) is very close to a conflictive point. For this reason, the values for position 1 and 2 are not corrected to obtain the correspondent perpendicular and parallel values.

	Position 1		Position 2	
Liquid Crystal	f_{us} (GHz)	Q-factor	f_{us} (GHz)	Q-factor
QYPDLC-036	7.3490 ± 0.26	150.70 ± 0.46	7.3386 ± 0.60	167.32 ± 0.34
QYPDLC-142	7.3700 ± 0.15	161.92 ± 1.17	7.3572 ± 0.20	182.37 ± 0.40
QYPDLC-193	7.3255 ± 0.24	151.06 ± 0.51	7.3177 ± 1.00	159.62 ± 1.30
GT3-23002	7.3710 ± 0.40	160.30 ± 1.11	7.3606 ± 0.18	180.66 ± 1.59

Table 4.28: Resonance frequency and Q-factor of 5 GHz resonator with LC cells.

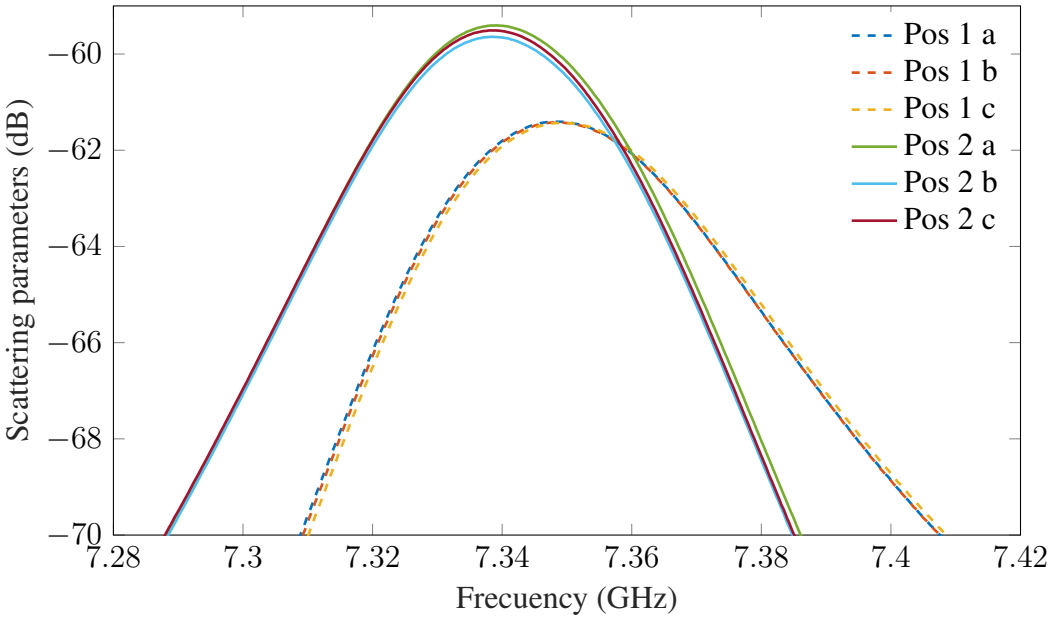

Figure 4.37: Measurement of the 9.5 GHz resonator with cell TH1.

	Position 1		Position 2	
Liquid Crystal	ε_r	$tan\delta$	ε_r	$tan\delta$
QYPDLC-036	2.8725	0.0062	3.1203	-0.0123
QYPDLC-142	2.6170	-0.0098	3.0104	-0.0273
QYPDLC-193	3.5268	0.0055	3.7201	-0.0031
GT3-23002	2.592	-0.0076	2.8579	-0.0297

Table 4.29: Calculated position 1 and 2 permittivity values and loss tangent of LC cells for 5 GHz resonator with the modal method.

As summary, after the evaluation of the characteristics of the LC mixtures measured at 11 GHz and 5 GHz, the highest values of the dielectric anisotropy are presented for the samples QYPDLC-036 and QYPDLC-193, together with the highest values of the corresponding loss tangent parameters. Furthermore, it is observed for all the LCs that the loss tangent decreases and the dielectric anisotropy increases at higher frequencies, which must be taken into account in the development of reconfigurable microwave devices.

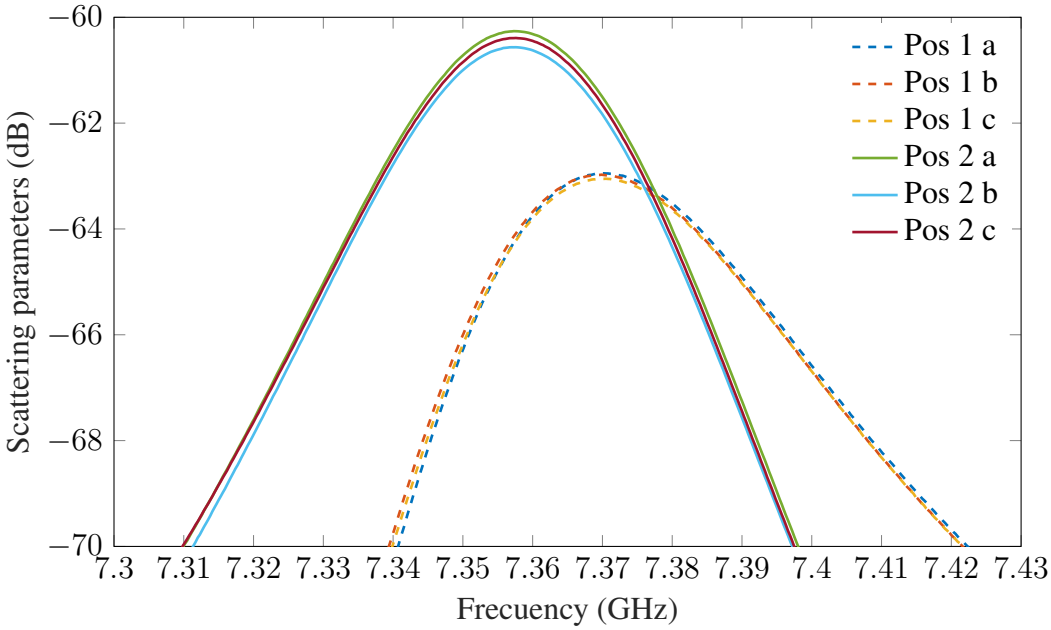

Figure 4.38: Measurement of the 9.5 GHz resonator with cell TH2.

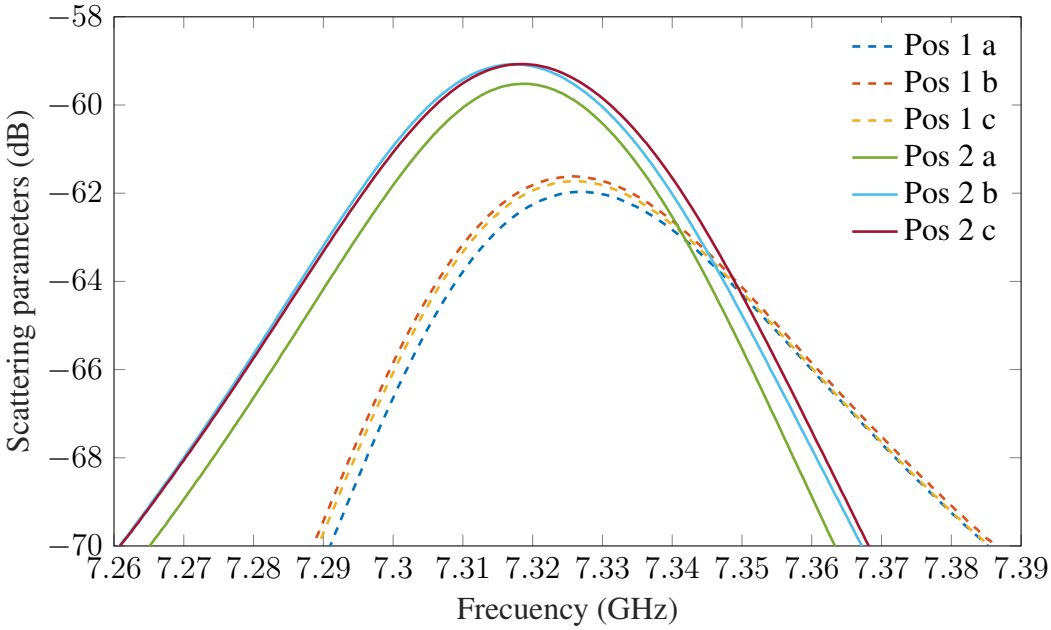

Figure 4.39: Measurement of the 9.5 GHz resonator with cell TH3.

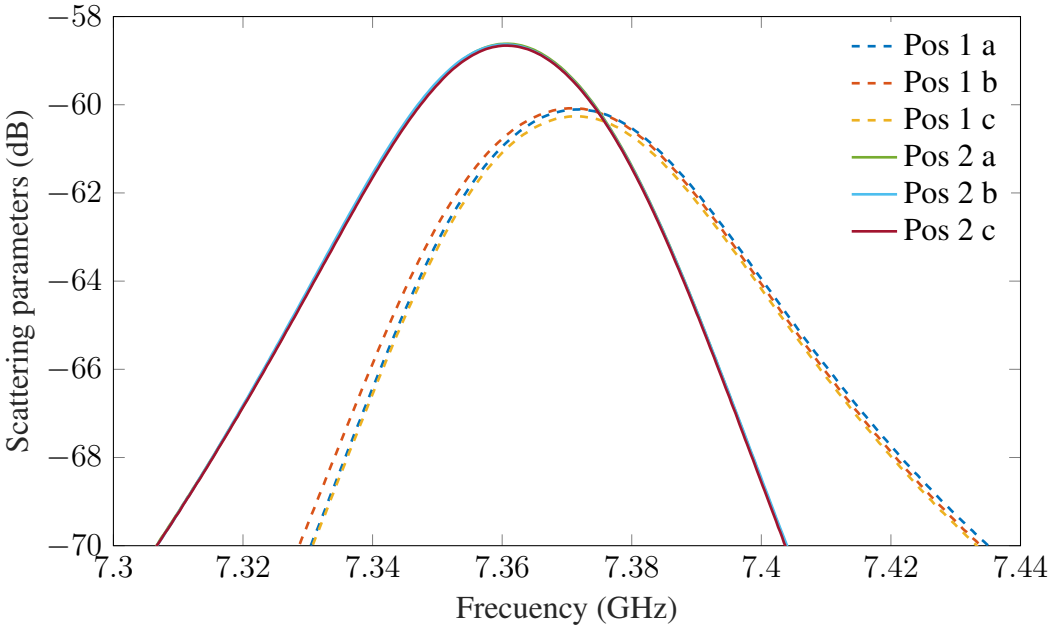

Figure 4.40: Measurement of the 9.5 GHz resonator with cell TH4.

Chapter 5

Decoupled Empty Substrate Integrated Waveguide

As described in chapter 2, the reconfiguration of microwave devices is one of the challenges in the current state-of-the-art of microwave technology. Furthermore, the ESIW is a promising structure that combines the properties of the waveguide devices and the compact size of the planar structures. It is a three layered structure (central body and two covers) of very low height, perfectly integrated in a substrate circuit, and presenting better performance in terms of dispersion and loss than planar lines and SIWs. However, the ESIW is a single conductor structure, i.e. a closed non-radiative transmission line, which has obvious advantages but also one disadvantage concerning reconfiguration: this structure is not AC/DC decoupled, thus it cannot be used to integrate elements that need a bias voltage to be operated. These elements are of great practical interest, since they can provide a certain reconfiguration range to the devices where they are inserted.

The need of reconfigurable devices has also led to different strategies. Many of them include the possibility of introducing a DC bias voltage in the device, acting on an additional element that is capable of modifying its response as explained in detail in section 2.2. Obviously, this involves that the structure must be composed of more than one single conductor. This is not the case of the ESIW structure, which is completely closed on itself with a single conductor.

The decoupling of waveguides has been tried in several ways. The Corrugated Substrate Integrated Waveguide (CSIW) [20] is a SIW structure where the metallized vias are replaced by open-circuit quarter-wavelength microstrip stubs to form the sidewalls of the waveguide [102]. This structure can support the TE_{10} mode. It can be connected to the SIW with interdigital capacitors [103] resulting in a structure completely DC isolated from the ground plane, which allows shunt connection of biased active devices. This simple structure provides

worse results than the standard SIW case in terms of return loss. Furthermore, both are supported on a dielectric substrate, thus both have similar levels of insertion loss.

Another alternative in SIW technology is achieve by the structures based on Stop-Band Response Frequency Selective Surfaces (SBFSS-SIW) [104]. They consist of a conventional SIW where the side walls are defined by metallized via holes, moreover periodic isolated pads are made over the top and/or bottom sides of the substrate. This getss AC/DC decoupling but preserves the propagation properties and dimensions of the traditional SIW [105].

All of these structures make possible the integration of biased active and passive devices for reconfiguration [6]. However, the presence of dielectric substrate make impossible the use of reconfigurable material, as the LC. For avoiding this issue, in this chapter a modification of ESIW transmission line is proposed in order to get its decoupling and transform it in a potential alternative to previous solutions, i.e. the Decoupled Empty Substrate Integrated Waveguide (DESIW).

5.1 Topology and design

The basic idea of the DESIW line is to maintain the three layered structure of the ESIW techonology, but decoupling one of the metallic covers. For the fundamental mode of the waveguide, the RF electric field currents flow on the surface of the structure. If DC decoupling is pursued, the continuity of these high frequency surface currents should be granted. To avoid cutting the currents and inducing radiation, a square pattern grid is craved on the surface of the top cover, i.e. a cover divided in several isolated metal squares. Thus, RF currents can flow through the grid created between the squares, preventing interruption by the discontinuity as shown in Figure 5.1.

The design of this square grid surface, also called Frequency Selective Surface (FSS) [106] cannot be random. FSSs have a passband response in a frequency range, so this behaviour must be far from the working frequency band of the transmission line. This will assure the transmission together with an AC/DC decoupling.

Munk [106] states that the resonance frequency of a FSS (formed by loaded square apertures with a solid plate inside as in this case), has its resonance frequency at $f_r = c/\lambda_r$, being c the speed of the light and $\lambda_r/4$ the lateral size of the aperture. The apertures must be designed small enough to have the resonance frequency out of the desired working band. Therefore, the cover with the FSS cells will have a reflection parameter high enough to ensure that the entire structure behaves like a conventional ESIW.

The voltage can be applied between each small inner square and the rest of the structure. It is expected that this solution, even considering some low radiation loss, has a proper per-

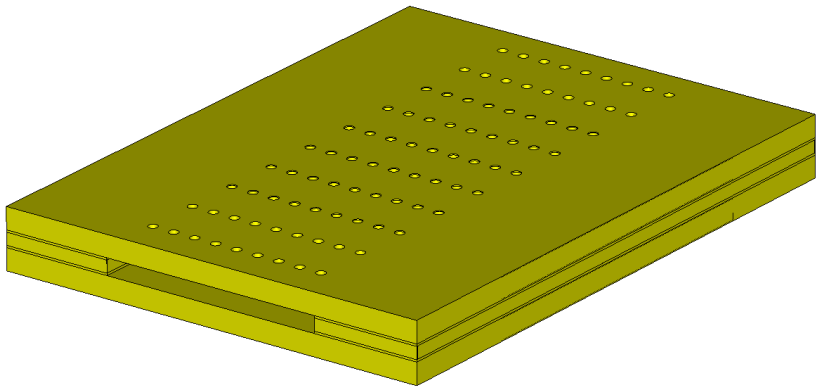

(a)

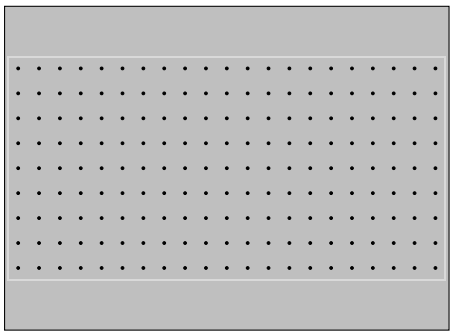

(b)

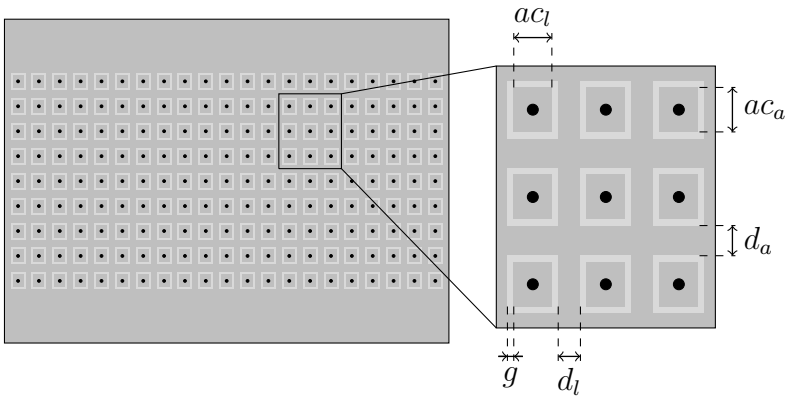

(c)

Figure 5.1: Layout of a DESIW with the top cover cut in small squares. In black the metallized vias and the border copper metallization, in dark gray the copper metallization on top of the layer, in light gray the dielectric substrate, and in white the air-filled sections. (a) 3D view of the DESIW line. (b) Top view of the top cover. (c) Bottom view of the top cover with detail of the squares.

formance. In order to have access to the decoupled conductors from outside of the structure, it is needed to drill a set of metallized vias in the center of each square, between the bottom and top sides of the upper cover of the DESIW. In this way, the bias voltage can be applied to the top surface of the waveguide. Moreover, different bias voltages could be applied to different sections of the waveguide, since the squares are accessible separately.

For calculating the dimensions of squares patches, firstly, an initial point is obtained, following the strategy described by Munk in [106], as explained in detail in section 5.2. Then, in order to maximize return loss, the dimensions (ac_l, ac_a, d_a, d_l, and g) are optimized in CST Studio Suite using Genetic Algorithms in a first approach, and with the Simplex Algorithm in a refinement stage. Furthermore, the placement of the square patches is carefully designed for avoiding short circuit between the transition and the isolated squares. For that, when a transition from microstrip to DESIW is chosen, the squares are placed properly.

Finally, to show that DESIW has similar propagation characteristics than ESIW, a comparison of the E-field distribution for the dominant mode is presented in Figure 5.2. The dominant mode behaviour of the DESIW line is equal to that of the conventional ESIW, so the common E-field distribution is not internally modified by the FSS topology. Even though the DESIW looks like a radiative structure, while it is operating in the FSS stop-band frequency no radiation exists as it happens in the reference ESIW. However, in the FSS pass-band frequency range the structure becomes radiative.

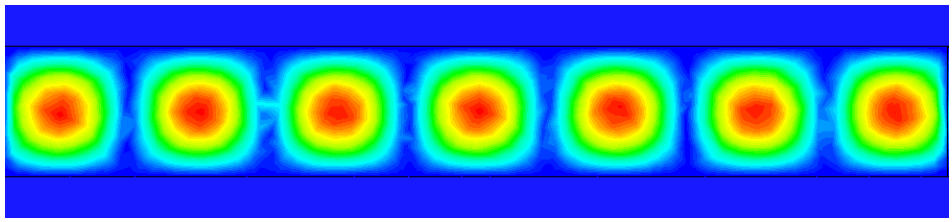

(a)

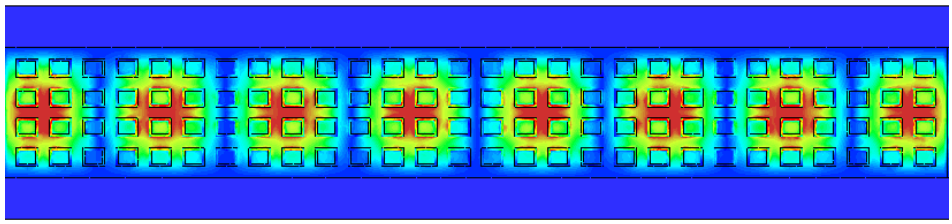

(b)

Figure 5.2: Electric field distribution of the dominant mode at 11 GHz. (a) ESIW line. (b) DESIW line.

5.1.1 Transitions

Two transitions are studied in order to know which one presents better performance in terms of return and insertion loss.

Linearly tapered transition

To interconnect the microstrip with the DESIW line, a linearly tapered transition is proposed in [107]. This transition is illustrated in Figure 5.3.

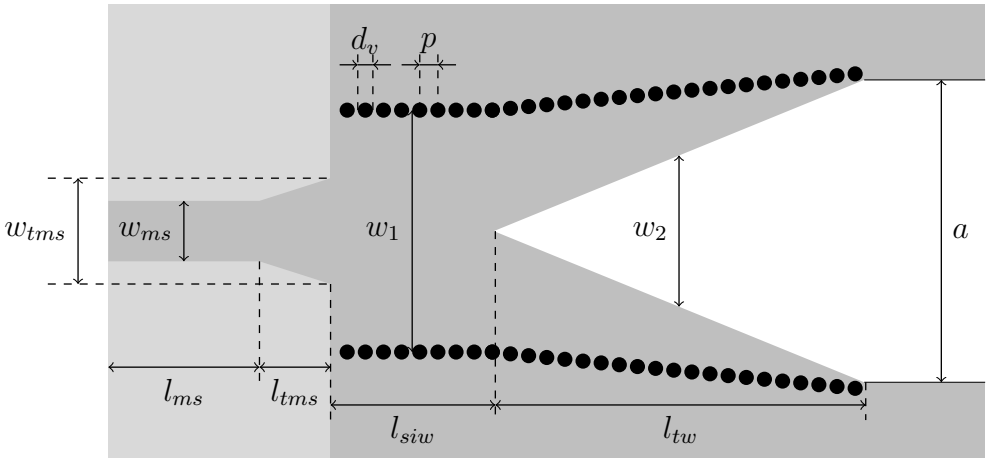

Figure 5.3: Layout of the linearly tapered transition. In black the metallized vias and the border copper metallization, in dark gray the copper metallization on top of the layer, in light gray the dielectric substrate, and in white the air-filled sections.

The transition is composed by a SIW line section fed by a linear taper from the width of the microstrip line (w_{ms}) to the width of a microstrip (w_{tms}) whose impedance is similar to the waveguide impedance. This is followed by a taper where the air penetrates into the dielectric substrate. The equivalent width of the SIW line (w_1) and the width of the empty transition region (w_2) are progressively increased along the transition, until the equivalent width of the empty waveguide (a) is obtained. The longer the transition, the better the matching. This leads to a tradeoff between total transition length l_{tw} and return loss. The electric walls of the taper are formed by metallized via holes of diameter d_v and pitch p. However, in the empty waveguide the walls are fully metallized to get better performance.

The initial point for the dimension of this transition can be obtained using the expressions given in equation (5.1). The initial equivalent width of the SIW section ($w_1(z = 0)$), and the width of the ESIW (a) are selected so that both lines have the same cutoff frequency, so they

are related by the dielectric permittivity of the substrate ε_r. In the case of w_2, it starts as 0 mm or the minimum manufacturable value.

An initial estimation of all these dimensions has been calculated with these expressions for having a cutoff frequency of 8 GHz. Afterwards, those values have been optimized in CST Studio Suite for maximizing return loss. The obtained dimensions are depicted in Table 5.1. These dimensions have been calculated for a substrate RO4003C with ε_r = 3.55, a height of 0.508 mm, and a copper cladding of 17.5 μm.

$$\begin{aligned} l_{tms} &= \tfrac{\lambda_{ms}(f_0)}{4}, \\ w_{tms} &= \tfrac{2w_{ms}}{3}, \\ w_1(z=0) &= a/\sqrt{\varepsilon_r}, \\ l_{tw} &\geq \lambda_0. \end{aligned} \tag{5.1}$$

Parameter	Dimension
a	19.050 mm
w_{ms}	1.100 mm
l_{ms}	10.000 mm
w_{tms}	2.280 mm
l_{tms}	3.640 mm
d_v	0.700 mm
p	1.170 mm
w_1	8.800 mm
l_{siw}	6.750 mm
l_{tw}	30.000 mm

Table 5.1: Dimensions of the linearly tapered transition from microstrip to DESIW.

The obtained reflection coefficient is shown in Figure 5.4, where it can be seen that return loss are greater than 20 dB, and insertion loss are low (around 0.5 dB).

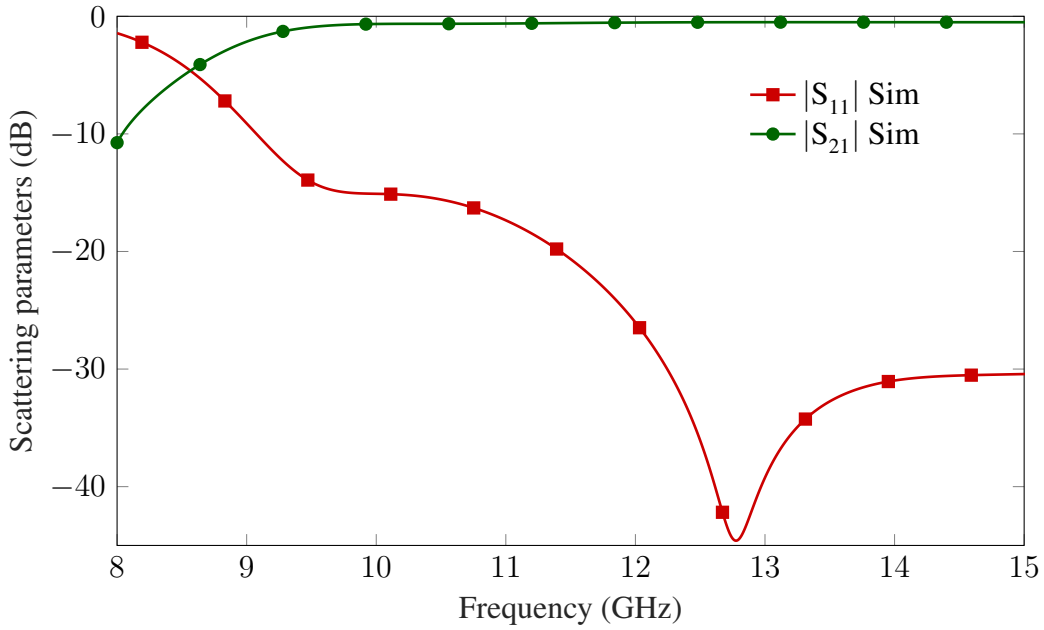

Figure 5.4: Simulated frequency response of the linearly tapered transition from microstrip to DESIW.

Exponential tapered transition

The work developed in [5] presents the opposite to the aforementioned solution. It is a transition formed by a dielectric substrate slab that penetrates in the empty waveguide. This slab is of the same substrate as the micorstrip substrate, and its width is exponentially reduced in order to match to a completely empty waveguide. This exponential taper is improved in [108] including an additional linear taper in the microstrip line to have better performance of the return loss. The transition has been also improved in this work with the mechanization of via holes to prevent possible leaky waves. The layout of this new two steps microstrip to ESIW transition is presented in Figure 5.5.

First, the transition is made of a linear taper from the width of the microstrip line (w_{ms}) to the width of a microstrip (w_{tms}) with the same impedance than the waveguide, as in the previous transition. This is followed by an exponential taper of length l_{tp}, whose initial width is w_{ti} and the end is rounded with a diameter of w_{tf}. The width of the taper exponentially decreases with the distance z as follows:

$$W(z) = \frac{w_{ti}(e^{-cl_{tp}} - e^{-cz}) + w_{tf}(e^{-cz-1})}{e^{-cl_{tp}} - 1} \tag{5.2}$$

where c is the parameter that controls the velocity of reduction of the taper width. As can be

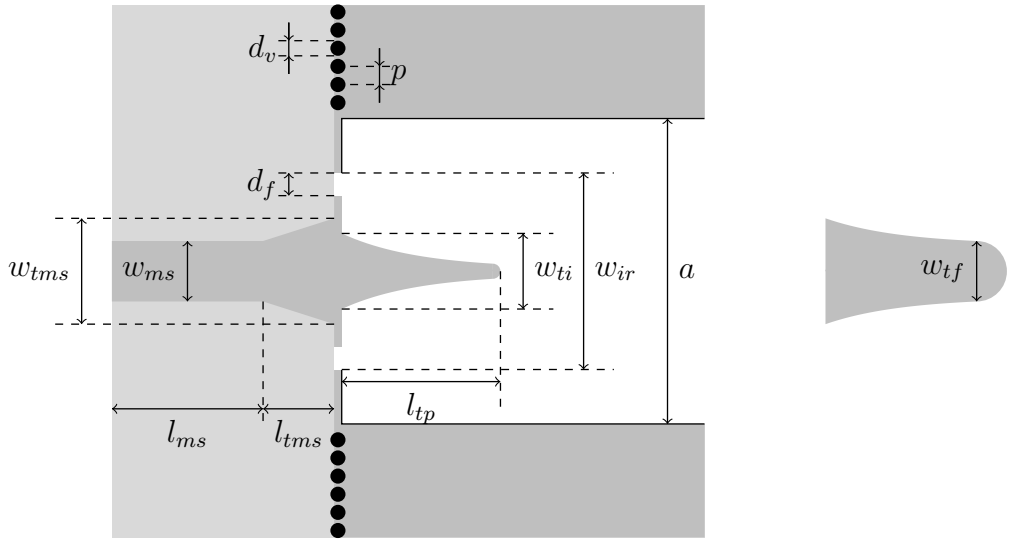

Figure 5.5: Layout of the new exponential tapered transition and details of the taper end. In black the metallized vias and the border copper metallization, in dark gray the copper metallization on top of the layer, in light gray the dielectric substrate, and in white the air-filled sections.

seen, at the beginning of the taper, the width is $W(z = 0) = w_{ti}$, and at the end, $W(z = l_{tp}) = w_{tf}$.

The mechanization of the two holes of diameter d_f with the drilling machine, ensures that the size of the iris in the back wall of the ESIW is exactly of the desired width (w_{ir}). This avoids large tolerances in the drilling process and deviations between the measurements and the simulations. Finally, via holes of diameter d_v and pitch p are mechanized in order to prevent possible leaky waves travelling through the substrate outside the ESIW. The parameters d_v and p are chosen to avoid radiation leakage with the same design rules as for the vias in a standard SIW.

In order to design the proposed transition, it is convenient to find a good initial point for the design parameters. The expressions that provide good approximations for the design parameters, and that can be used to obtain a good initial point, are detailed in (5.3). These expressions have been obtained experimentally after designing the transition for different frequency bands and different substrates, with long optimization processes using the robust genetic algorithms. The proposed initial point can speed up significantly the optimization process for new designs, regardless of the frequency band, or the specific substrate that is chosen for each case. The initial point of the microstrip taper (l_{tms} and w_{tms}) take the values given by the expressions of (5.1), and the rest of parameters are described in (5.3).

$$
\begin{aligned}
l_{tp} &= \frac{\lambda_g(f_0)}{4}, \\
w_{ti} &= 1.2 w_{tms}, \\
w_{ir} &= \frac{a + w_{ti}}{2}, \\
c &= \frac{2}{l_t}.
\end{aligned}
\tag{5.3}
$$

The transition has been designed with the initial point of expressions (5.1) and (5.3) and, afterwards, optimized to maximize the return loss. The calculated optimum values are detailed in Table 5.2. The obtained reflection coefficient is greater than 20 dB, as shown in Figure 5.6, for the substrate RO4003C of ε_r = 3.55, height of 0.508 mm, and copper cladding of 17.5 μm; whereas the insertion loss value is about 0.5 dB in the whole frequency range.

Parameter	Dimension
a	19.050 mm
w_{ms}	1.100 mm
l_{ms}	10.000 mm
w_{tms}	2.280 mm
l_{tms}	3.640 mm
w_{ir}	12.915 mm
d_f	1.000 mm
d_v	0.500 mm
p	1.320 mm
w_{ti}	2.574 mm
l_{tp}	10.088 mm
w_{tf}	0.500 mm

Table 5.2: Dimensions of the exponential tapered transition from microstrip to DESIW.

5.2 Design and manufacturing of a transmission line

An X-band DESIW transmission line has been designed for testing the performance of the proposed structure. The design of the line only consists of calculating a width that enables the propagation of the fundamental mode over 8 GHz. For an empty waveguide, a = 19.05 mm.

Moreover, concerning the patches, they are not completely squared, so their sides can have different lengths. As mentioned before, the length of the patch sides must achieve

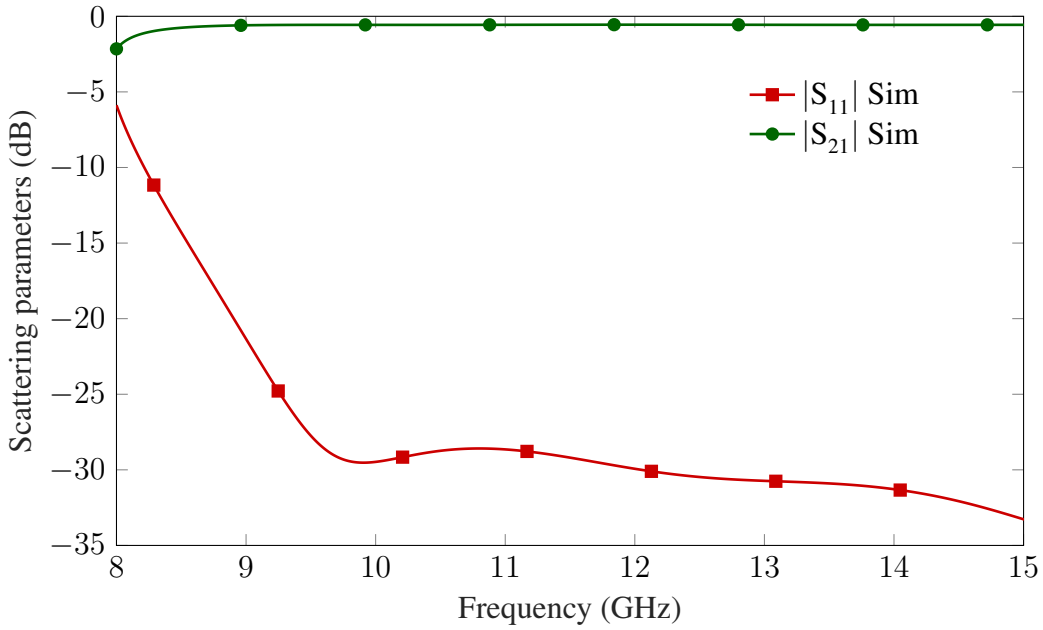

Figure 5.6: Simulated frequency response of the exponential tapered transition from microstrip to DESIW.

the passband of the FSS to be outside the desired passband of the transmission line. The mono-mode frequency band of the designed line is from 8 to 16 GHz, so in order to have a guard band, the passband of the FSS should be over 20 GHz. Therefore, the biggest side length of the patch must be smaller than 3.75 mm. However, there are some limitations for manufacturing the cover that must be taken into account in the design process: the size of the squares and the diameter of the via holes cannot be as small as desired, since the milling machine has some limitations in the accuracy and the diameter of the drill bit. The patches length in both dimensions must be greater than 0.5 mm. Thereby, these are the two optimization maximum and minimum values, respectively.

Considering all the limitations described above, the starting point of the dimensions of the squares is the average of the minimum and maximum size. The length of the squares can be different in the transmission line itself (acl) and the squares placed around the transition (acl_{input}), while the width is the same to ensure a flowing straight way for the surface currents as depicted in Figure 5.7(a). Other parameters to be optimized are the distance between adjacent squares in both directions (d_a and d_l). Finally, the gap (g) used to isolate the inner squares is fixed to the minimum manufacturable. All these dimensions are optimized in CST Studio Suite obtaining the results depicted in Table 5.3 for the linearly and exponential tapered transitions. The placement of the patches is different for each transition, as shown in

Figures 5.7 and 5.8.

Exponential taper		Linear taper	
Parameter	Dimension	Parameter	Dimension
ac_a	1.421 mm	ac_a	1.335 mm
ac_l	1.220 mm	ac_l	1.068 mm
d_a	0.950 mm	d_a	0.980 mm
d_l	0.700 mm	d_l	0.700 mm
g	0.150 mm	g	0.150 mm

Table 5.3: Dimensions of the square grid of the DESIW transmission line.

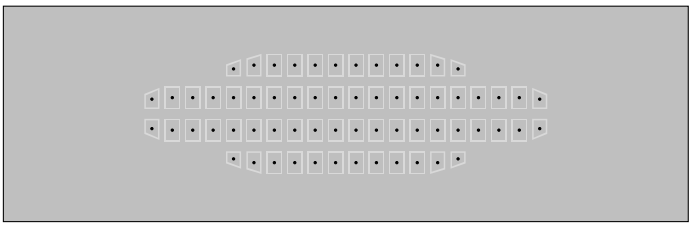

(a)

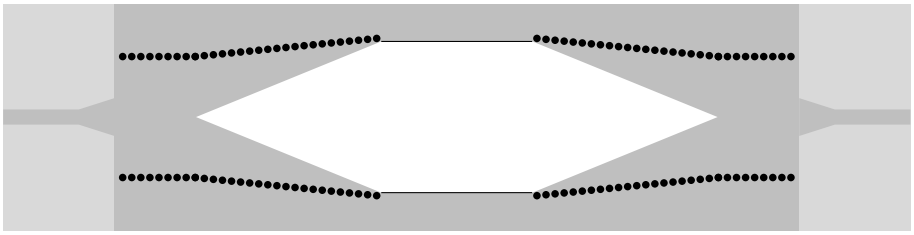

(b)

Figure 5.7: Layout of the DESIW line with the linearly tapered transition. (a) Bottom view of the top cover. (b) Top view of the central body.

Moreover, before manufacturing, it must be considered the possible influence of the top cover substrate in the structure behaviour due to the leakage through the squares. For that, the electromagnetic response of the line has been simulated for different cover substrates: FR4 with ε_r = 4.7, RO4003C with ε_r = 3.55, TMM6 with ε_r = 6 and TMM10i with ε_r = 9.8. These simulations, shown in Figure 5.9, demonstrate that the substrate of the top cover barely influences on the performance of the line.

With all the previous aspects, a DESIW transmission line is manufactured for each transition. For the central body, Rogers RO4003C substrate with height h = 0.508 mm, ε_r = 3.55, and copper cladding of 17.5 μm is used. For both (top and bottom) covers of the line, a

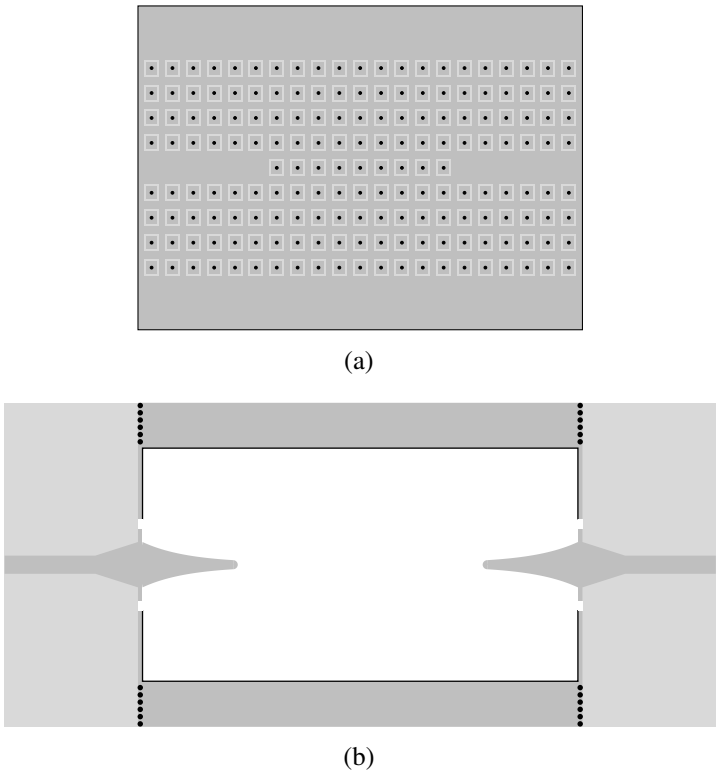

(a)

(b)

Figure 5.8: Layout of the DESIW line with the exponential tapered transition. (a) Bottom view of the top cover. (b) Top view of the central body.

Rogers RO4003C substrate with height h = 0.813 mm, ε_r = 3.55 and copper cladding of 17.5 μm has been finally chosen because its influence in the response is negligible.

During the manufacturing procedure, the first stage is related to the DESIW body: the substrate is partially emptied to conform the line and its sides are covered with copper by electro-deposition, then the transition is milled. Next, the top cover is manufactured: the via holes that connect the inner squares to the outside of the cover are drilled and electro-deposited with copper. Then, the inner squares are milled, as well as the decoupling big square of the upper side. The bottom cover acts just as a whole copper foil. The structure is welded to ensure electric continuity and it is fastened by screws. Figures 5.10 and 5.11 show the manufactured layers (central body and two view of the top cover) of the structure before assembling for both linearly and exponential tapered transition, respectively. It is remarkable that the line with linear taper is longer since the length of the transition is three times the length of the exponential taper.

The frequency responses of the manufactured prototypes of the new DESIW line are compared with the simulated data obtained with CST Studio Suite.

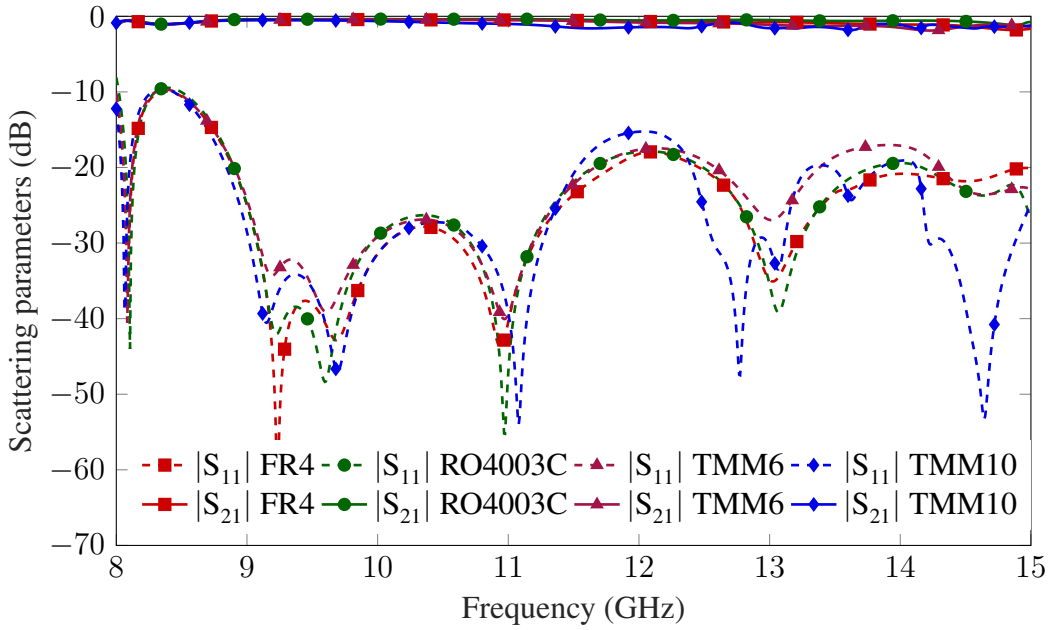

Figure 5.9: Simulates frequency response of a DESIW line with different cover substrates.

Figure 5.12 shows the comparison for the linearly tapered transition. The measurement does not match with the simulation, since return loss are only greater than 15 dB in a small bandwidth, and IL values are greater than simulation, around 1.5 dB.

Figure 5.13 shows the frequency response of the exponential tapered transition . As it can be observed, simulation and measurement are in good agreement. In the whole frequency range the return loss are greater than 15 dB, and IL values are lower than 0.5 dB.

A comparison between the results of the DESIW line with exponential tapered transition and previous works in the field is provided in Table 5.4, since the linear tapered transition does not meet the specifications and was dismissed. It can be seen that DESIW results are similar to those of the ESIW, and much better than the results of other integrated decoupled lines. The low attenuation of the line ensures a good performance of this structure for different applications.

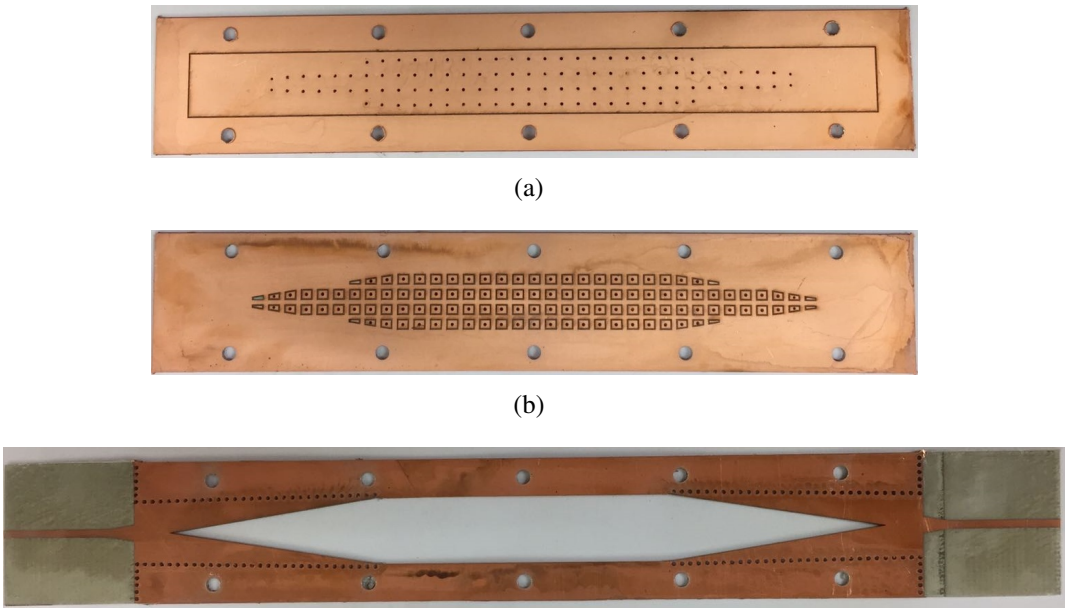

(a)

(b)

(c)

Figure 5.10: Layers of the manufactured DESIW line prototype with linearly tapered transition. (a) Top view of the top cover. (b) Bottom view of the top cover. (c) Central body of the line.

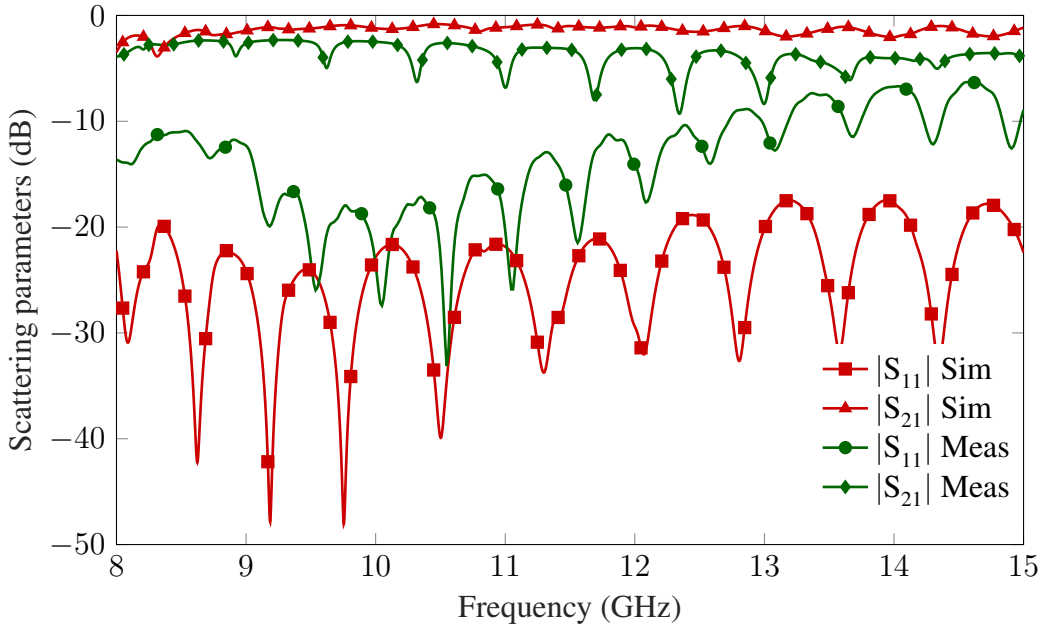

Figure 5.12: Comparison between simulation and measurement results for the DESIW line with linearly tapered transition.

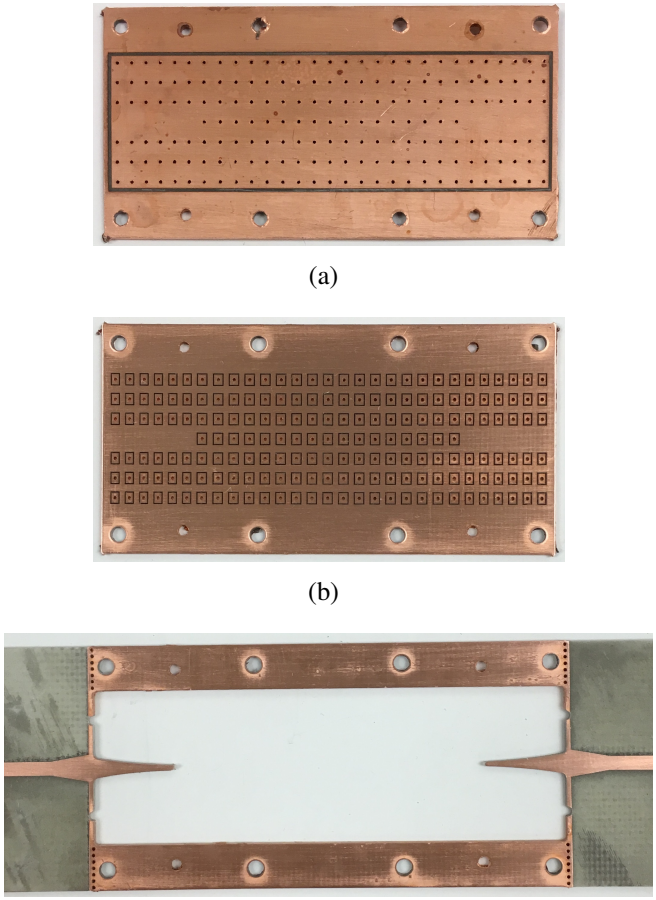

(a)

(b)

(c)

Figure 5.11: Layers of the manufactured DESIW line prototype with exponential tapered transition. (a) Top view of the top cover. (b) Bottom view of the top cover. (c) Central body of the line.

	AC/DC decoupled	Return Loss	Insertion Loss
DESIW	Yes	15 dB	0.5 dB
ESIW [5]	No	20 dB	0.3 dB
CSIW [102]	Yes	10 dB	3.5 dB
SBFSS-SIW [105]	Yes	12 dB	1 dB

Table 5.4: Comparison of scattering parameters between DESIW and other SIWs.

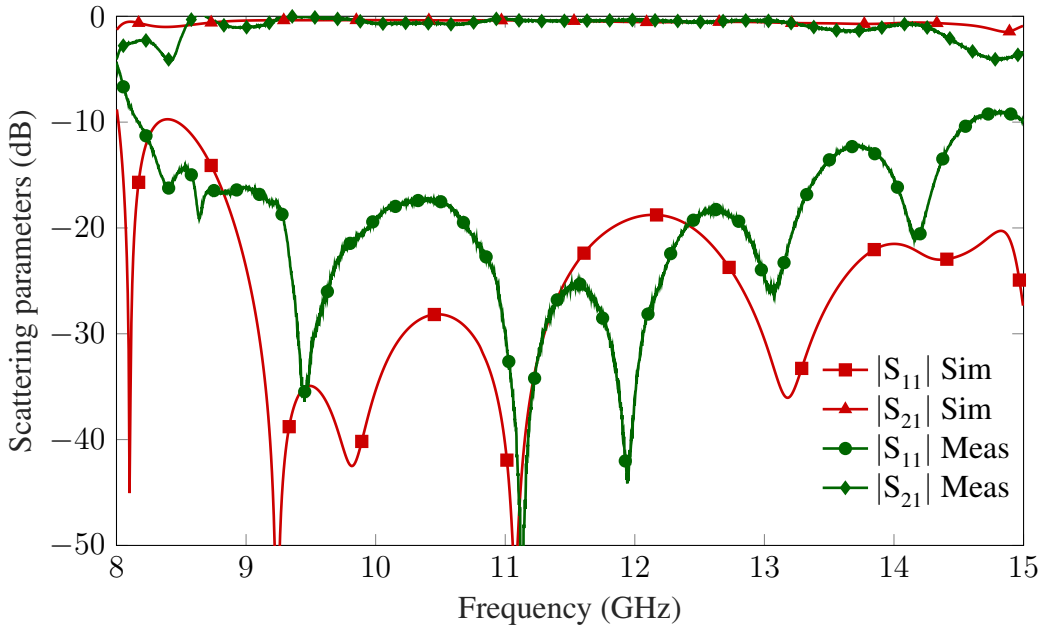

Figure 5.13: Comparison between simulation and measurement results for the DESIW line with exponential tapered transition.

5.3 Design and manufacturing of a resonator

In order to test the validity of the proposed structure as a filter, and to establish a consistent design procedure, a simple filter with only one resonator is designed using the standard procedure of [53], which uses an equivalent ideal network composed of ideal inverters and resonators as a reference. Exponential tapered transition is used for its better performance. The layout of this 1-pole filter is shown in Figure 5.14. In this case, the layout of the squares grid follows the shape of the resonator. The squares with the gaps in the coupling windows have the same length than the iris ($acl_w + 2g = l_{win}$). Furthermore, there are no squares in the zone of the iris, as in the case of the transition, for avoiding short-circuits.

The optimized dimensions detailed in Table 5.5 for both the square grid and the central body are calculated for providing a Chebyshev response with the following specifications:

- Number of cavities: N = 1 cavity.
- Central frequency: f_0 = 11 GHz.
- Bandwidth: 300 MHz.
- Dielectric permittivity: air $\rightarrow \varepsilon_r$ = 1.

Parameter	Dimension
a	19.050 mm
a_{win}	8.000 mm
l_{in}	12.000 mm
l_{res}	15.975 mm
l_{win}	1.000 mm
g	0.150 mm
ac_a	1.336 mm
ac_l	1.216 mm
ac_{linput}	0.918 mm
ac_{lw}	0.700 mm
da	0.950 mm
dl	0.670 mm

Table 5.5: Dimensions of the the central body and the square grid of the DESIW resonator.

For manufacturing the central body and the covers, Rogers RO4003C substrate with height h = 0.813 mm, ε_r = 3.55, and copper cladding of 17.5 μm is used. Figure 5.15 shows manufactured layers of the structure before assembling. In this case, in the central body layer there is a footprint for using an end-launch connector [109] instead of a welded connector.

This prototype has been measured and its frequency response is compared with the simulation in Figure 5.16. There is a slight frequency shift due to the manufacturing tolerances and the galvanic metallization thickness. This thickness influences the size of the resultant structure, hence modifying the final frequency response.

Once the performance of a transmission line and a resonant structure based on DESIW technology is validated, the next step is the use of these prototypes to get reconfigurable devices. As stated in previous chapters, the reconfiguration method utilized in this work is the Liquid Crystal (LC), analyzed in depth before.

5.4 Reconfiguration of the resonator with Liquid Crystal

5.4.1 Filling process

One important issue is how to fill the reconfigurable devices with LC. This process is not trivial since it cannot be done by capillarity from one side of the device, as in the case of LC cells, and the devices are not transparent, not being able to see if the device is completely full or not. In order to check the best method to fill the devices, a line and a two poles filter implemented in ESIW have been manufactured. Instead of using a metallic cover, a transparent glass has been used for covering these structures as shown in Figure 5.17. Different patterns

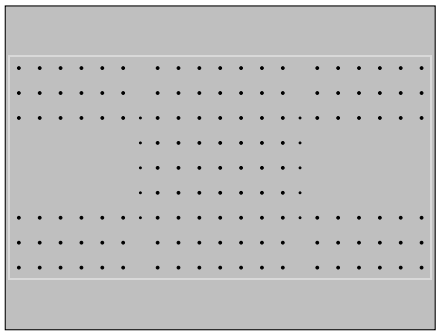

(a)

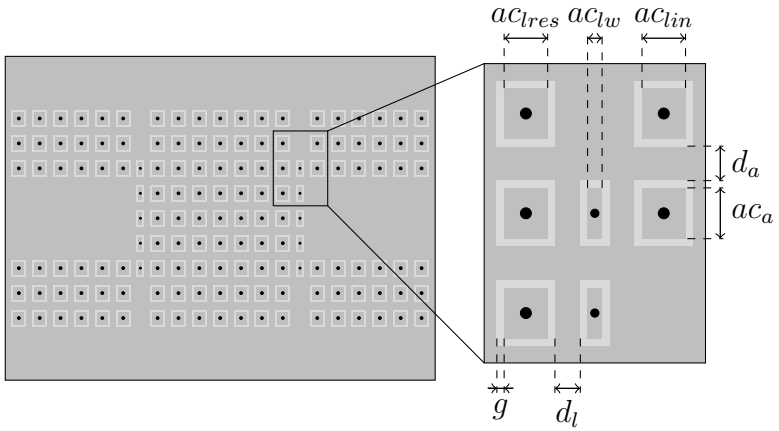

(b)

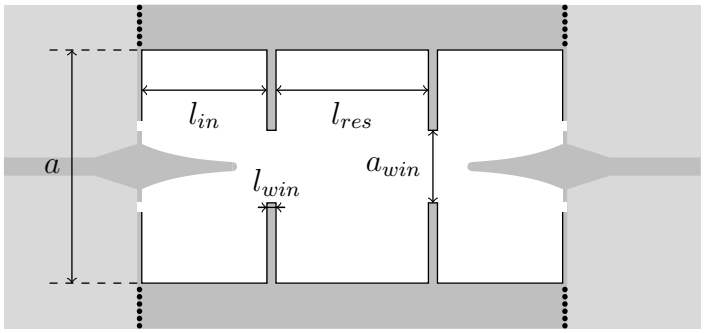

(c)

Figure 5.14: Layout of a DESIW resonator with the top cover cut in small squares. In black the metallized vias and the border copper metallization, in dark gray the copper metallization on top of the layer, in light gray the dielectric substrate, and in white the air-filled sections. (a) Top view of the top cover. (b) Bottom view of the top cover with detail of the squares. (c) Top view of the central body.

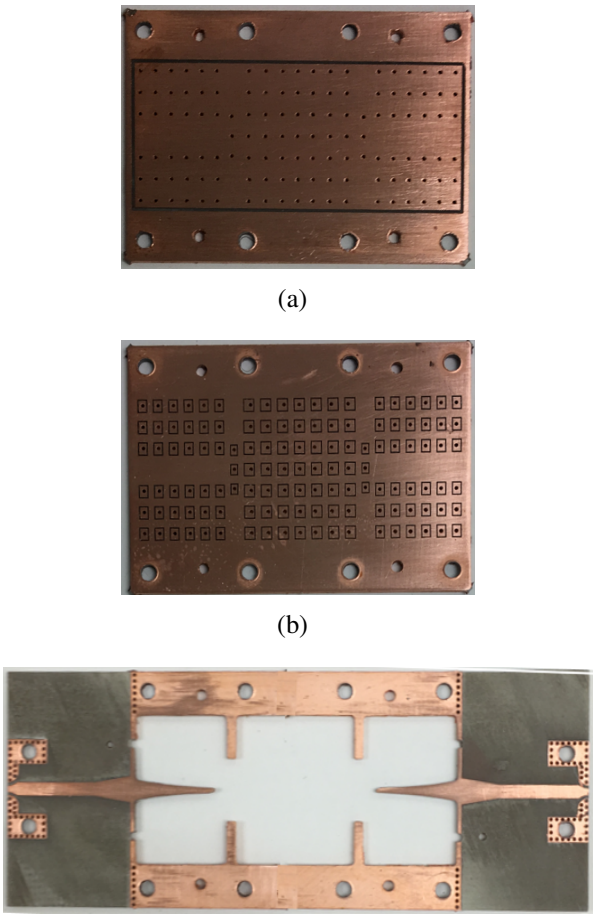

(a)

(b)

(c)

Figure 5.15: Layers of the manufactured DESIW resonator prototype. (a) Top view of the top cover. (b) Bottom view of the top cover. (c) Central body of the resonator.

of holes have been made in the glasses to test how the LC flows inside the device. Figure 5.17 shows the distribution that achieves a better filling of the whole device. It consists of two holes, one for filling and the other for allowing the air to get out. These two holes are placed in the center of the line and in the center of each resonant cavity in the filters. Additionally, four holes can be made in the four corners of each resonator to improve the filling, although the field in these zones is negligible. The maximum of electric field is placed in the center of the cavity, so this is the important zone that must be filled to get better frequency response and reconfiguration features.

Furthermore, to get the highest available anisotropy of the LC molecules, the initial alignment is essential. In this case, polyimide should not be used since it produces an isolation between the layers and, consequently, the conduction currents are cut avoiding wave propa-

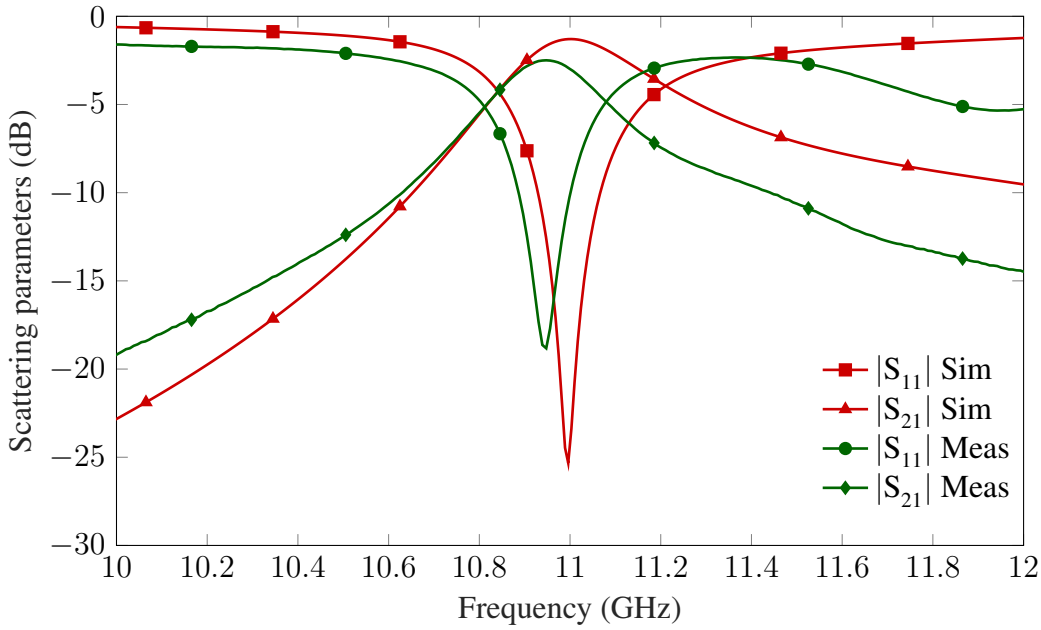

Figure 5.16: Comparison between simulation and measurement results for the DESIW resonator.

gation. However, if no alignment surface is implemented, the dielectric permittivity of the LC could only vary from a random value to the parallel case. Therefore, a velvet rubbing strategy has been followed to achieve the maximum initial alignment. As in the case of the polyimide of the LC cells, the metallic covers are rubbed with a natural silk velvet. It is very important to perform rubbing in a unique way, since this will determine the initial inclination of the molecules. The microgrooves implemented in copper do not have the same anchoring force than the ones of polyimide because of the characteristics of the material. Copper surface is harder, so the velvet does not produce the same effect.

Finally, the filling process is finished by the sealing of the device. The via holes of the top cover are sealed with high temperature solder wire for keeping the electric contact between all the squares. The via holes pattern indicated before is not sealed in order to use it to fill the device with LC, as shown in Figure 5.18.

After soldering, the decoupling is again checked, and the device can be assembled and welded. For this welding, a low temperature soldering paste is used, to avoid the cover sealing to melt. For assuring that there are not leaks, the borders are sealed with optical glue (Norland UV Sealant 91). Furthermore, after filling the structure with LC, the filling holes are also sealed with optical glue. In this moment, either solder paste or wire can not be used since the temperature needed for soldering is over the clearing temperature of the LC, i.e.,

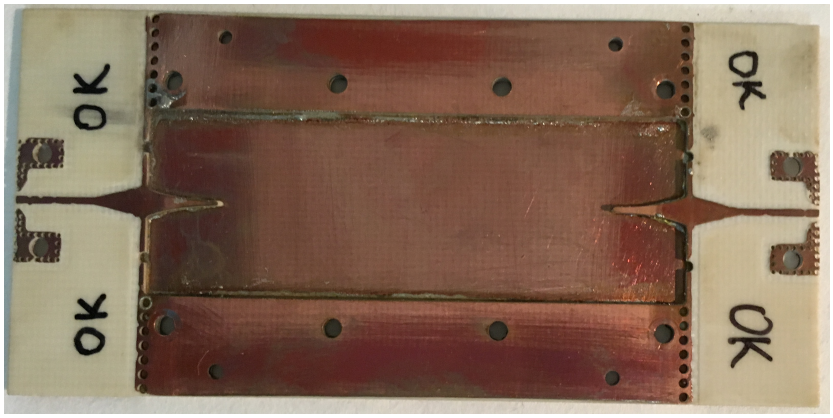

(a)

(b)

Figure 5.17: Filling process of the reconfigurable DESIW devices. (a) Transmission line. (b) Two poles filter.

the temperature at which the transition between the mesophase and the isotropic phase occurs (about 150°C).

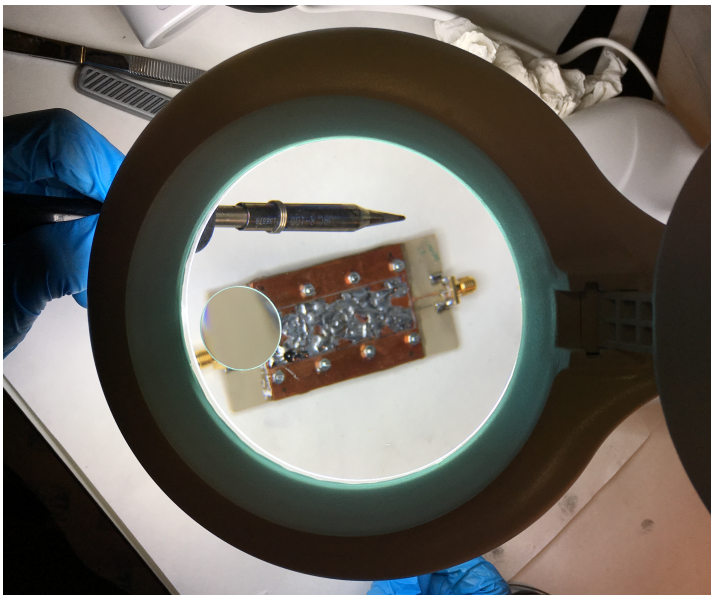

Figure 5.18: Soldering process of the top cover of a DESIW structure.

5.4.2 Biasing

Taking into account the behaviour of the LC molecules, the dielectric anisotropy of the material is achieved by applying an external DC (or low frequency) bias field, either electric or magnetic.

The $\varepsilon_{r\perp}$ state is achieved by using the anchoring force (physical alignment) or a magnetic bias field, while the $\varepsilon_{r\parallel}$ state is achieved by applying electric or magnetic bias field [3].

Magnetic biasing

Two magnets can be used for obtaining the two states, since the molecules are aligned parallel to the magnetic field lines. First, the perpendicular permittivity ($\varepsilon_{r\perp}$) is achieved by two magnets repelling each other, as shown in Figure 5.19(b). Then, the molecules are aligned orthogonally to the RF electric field ($\vec{E}$). Next, the molecules can be aligned vertically, i.e. parallel to the same RF electric field ($\varepsilon_{r\parallel}$), if the two magnets are placed in attracting mode, as shown in Figure 5.19(a). When the device is placed between the two magnets, the perpendicular and the parallel LC states can be alternatively measured, by changing the position of the magnets.

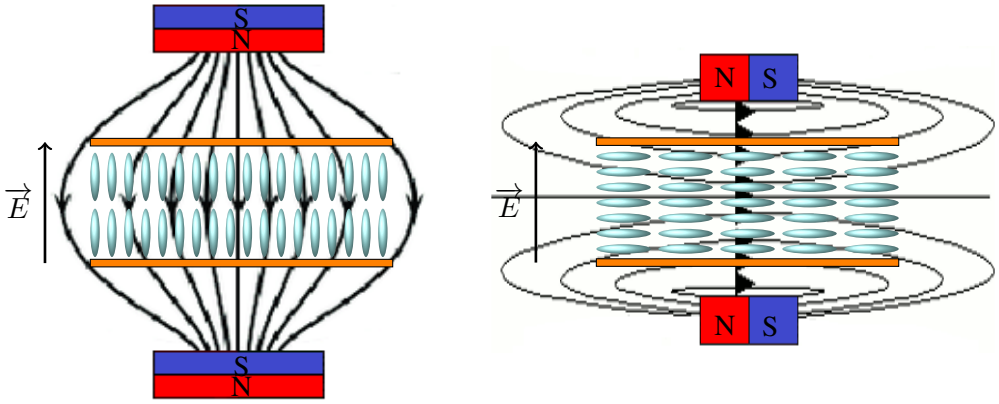

(a) (b)

Figure 5.19: Cross section of magnetic field biasing states. (a) Attract: parallel permittivity. (b) Repel: perpendicular permittivity.

Electric biasing

For electric biasing, a low frequency voltage is applied between the grid of squares and the rest of the structure. When no voltage is applied, the molecules are in repose state, forced by the anchoring surface, obtaining a pseudo-perpendicular permittivity value. When starting to apply a voltage higher than the threshold value (which is different for each LC mixture) [3], the molecules start rotating to the vertical position. Depending on the applied voltage, continuous values of permittivity can be obtained, until $\varepsilon_{r\|}$ is achieved.

5.4.3 Reconfigurable resonator results

In order to test the variation of the frequency response, two manufactured DESIW resonators are filled with QYPDLC-036 and GT3-23002. The first resonator has been measured applying both magnetic and electric bias fields, but the second one has only been measured applying magnetic field since its practical realization was short-circuited unintentionally. The measurement set-up is shown in Figure 5.20.

Figure 5.21 shows the frequency response for the two states of the magnetic biasing, and the continuous reconfiguration response for the electric biasing of the resonator filled with QYPDLC-036 mixture.

The repose measurement, without any biasing field, shows a resonance at 6.74 GHz. There is a frequency shift with regard to the simulation data, due to the non-perfect perpendicular alignment of the LC molecules, thus decreasing the resonance frequency. When the

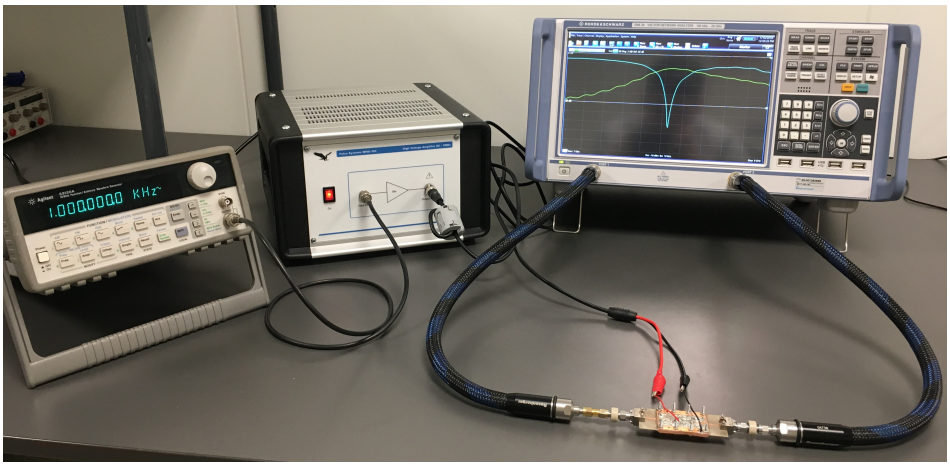

Figure 5.20: Measurement set-up using electric bias field.

bias voltage (from 25 Vpp to 100 Vpp in 25 Vpp steps) is applied, the molecules start rotating from the repose state to the parallel position, where the resonance frequency is located at 6.52 GHz. The tuning achieved is continuous in a frequency range of 220 MHz, which in relative terms corresponds to 3.38%.

Alternatively, a magnetic biasing field is applied, as shown in Figure 5.19. For the perpendicular mode, the resonance frequency is 6.85 GHz, and for the parallel one it is 6.3 GHz. This tuning range of 550 MHz corresponds to a relative value of 8.5% that compares rather well with the simulated value of 11%.

The magnetic biasing achieves a wider tuning range (extreme states) than the electric one (continuous intermediate states). There are two main reasons for such results. For the parallel case, the voltage is not applied between the whole top cover and the bottom cover, but between the squares and the bottom cover, leaving some spaces without polarization. For the perpendicular case, non electric field can be applied, so the alignment is limited to the repose state configuration. In the magnetic case, the polarization is applied in the whole surface of the device and for both states.

The measured IL are between 5.7 dB and 7.4 dB in the passband over the whole tuning range, including the loss of both transitions and connectors. The extracted unloaded quality factor Q_u ranges between 80 to 30, as shown in Table 5.6.

Figure 5.22 shows the frequency response for the two states of the magnetic biasing of the resonator filled with GT3-23002 mixture.

The repose measurement shows a resonance at 7.27 GHz. As in the previous case, there is a shift with regard the simulation due to the non-perfect initial alignment of the LC molecules. When the magnetic biasing field is applied, the two extreme states are achieved. For the

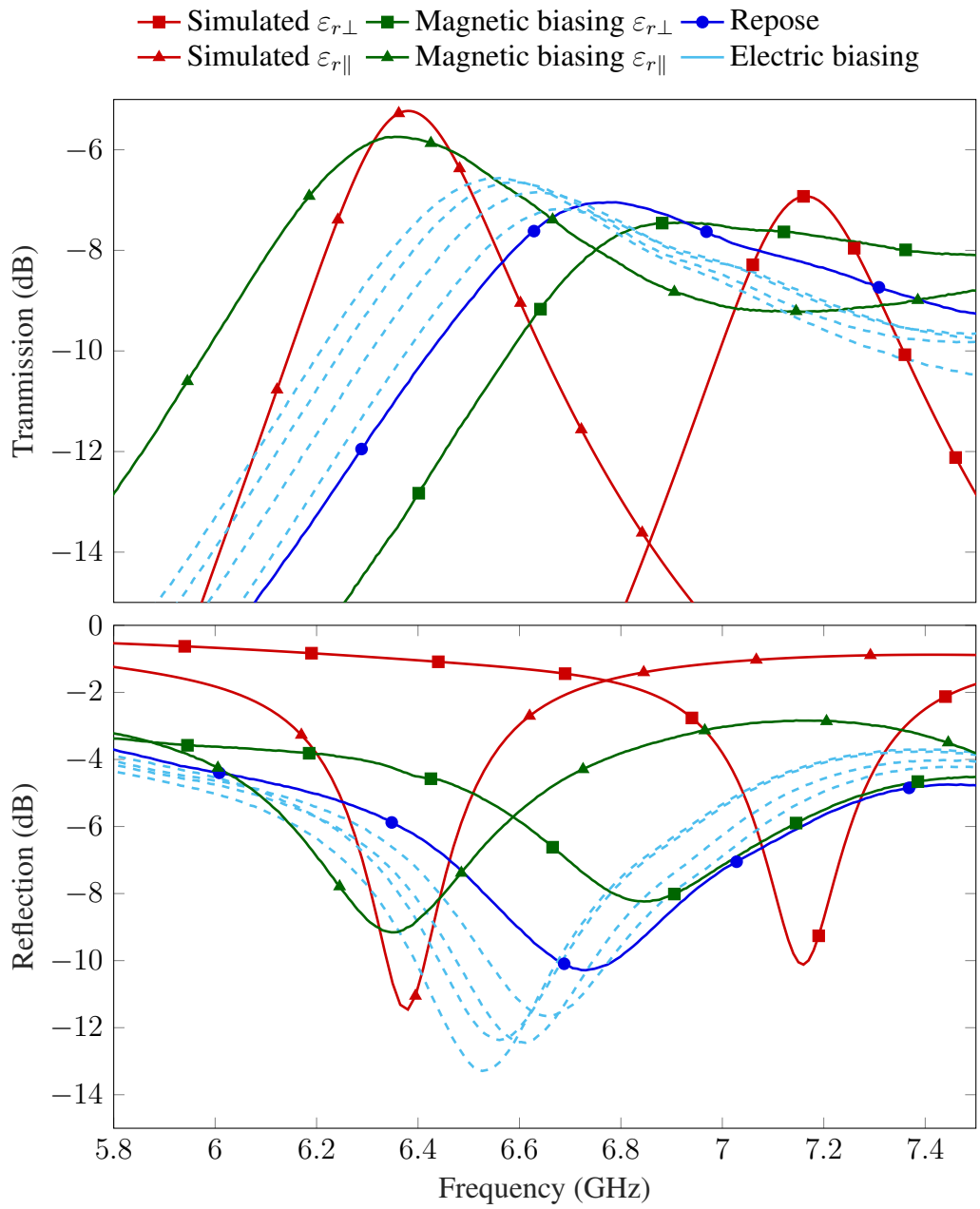

Figure 5.21: Measurement results for the DESIW resonator filled with QYPDLC-036 applying magnetic and electric biasing fields.

perpendicular case, the resonance frequency is 7.3 GHz, and for the parallel one it is 6.7 GHz. This tuning range of 600 MHz corresponds to a relative value of 8.5% that compares rather well with the simulated value of 13.85%. The measured IL is between 4.3 dB and 6.8 dB in the passband over the whole tuning range, including the loss of both transitions and

connectors. The extracted unloaded quality factor Q_u ranges between 190 and 172, as shown in Table 5.6.

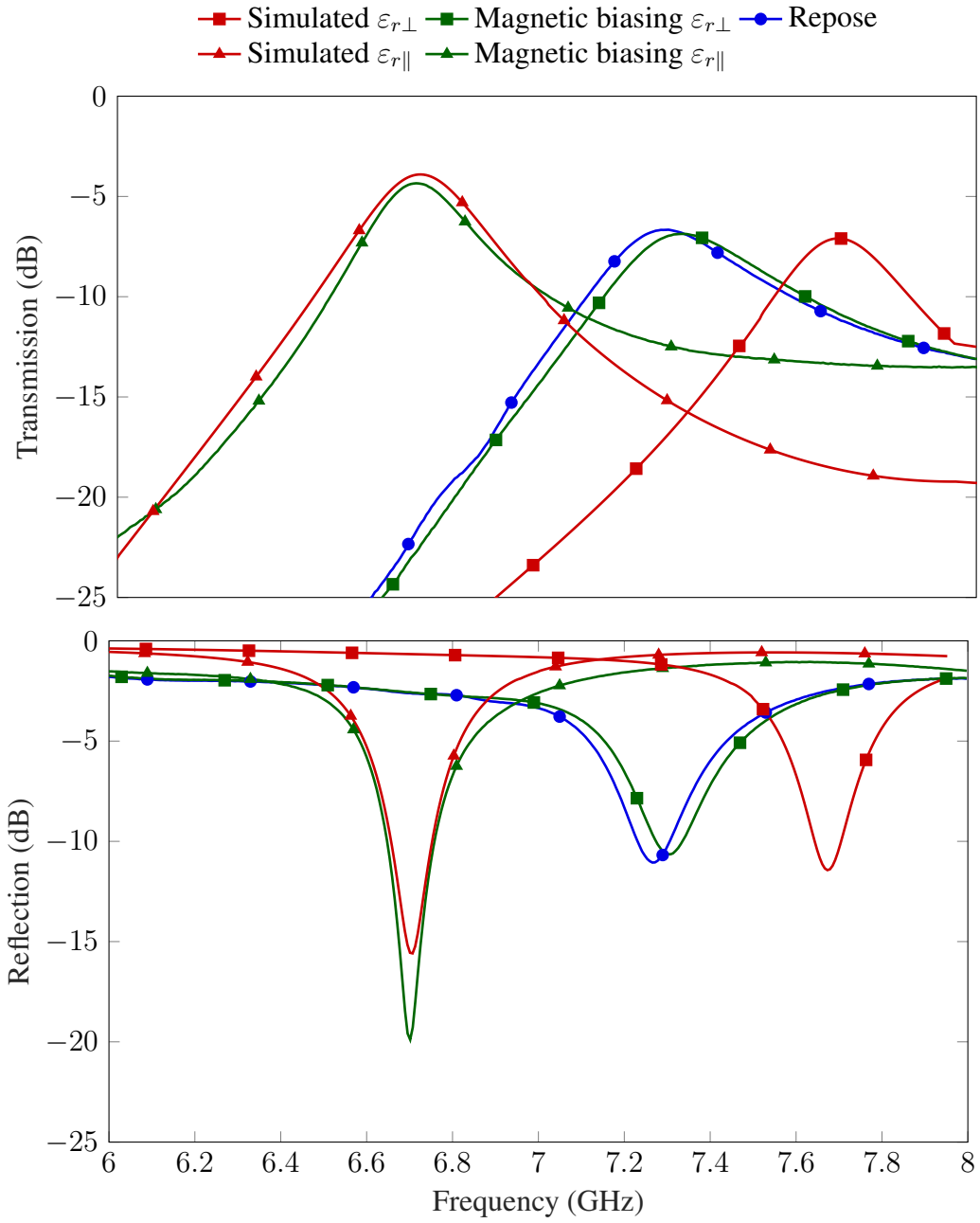

Figure 5.22: Measurement results for the DESIW resonator filled with GT3-23002 applying magnetic biasing field.

These results are mostly determined by the LC properties, so that for a fair comparison

with other works, the LC mixture should be the same one. However, a comparison with other tunable resonators using LC material is included in Table 5.6. The use of other LC mixtures can change both the tunabilitiy range and the insertion loss of the proposed structure.

Work	f (GHz)	Tunability (%)	IL (dB)	Q_u-factor
DESIW (QYPDLC-036)	6.5	8.50	5.7-7.4	80-30
DESIW (GT3-23002)	7.0	8.50	4.3-6.8	190-172
Waveguide [110]	23.5	2.10	Not given	256-170
SIW [18]	23.5	1.75	27-28	105-102
Microstrip [19]	2.8	8.20	0.97-1	Not given

Table 5.6: Comparison of tunable LC resonators on planar technology.

Chapter 6

Conclusions and future research lines

Current communication systems face the advent of spectrum saturation caused by new applications, like Internet of Things (IoT) or 5G access technology. They are defined to provide extremely high capacity, high bandwidth, and robust integrity. Thereby, RF and microwave systems must provide, among others, enhancements in terms of spectral efficiency and adaptable resource management. The thesis arises from this increasing need in recent years for development of reconfigurable microwave devices (i.e. devices with a frequency-agile response).

The work starts with an exhaustive bibliography search of the microwave filter topologies and the technologies for implementing them. It has been concluded that SIW technology is the perfect candidate for developing new filter structures. Since these devices are integrated on a dielectric substrate, it is possible to use manufacturing processes based on milling techniques. This allows to reduce costs and guarantee excellent mechanical tolerances, together with high performance characteristics. The achieved features are between those of classic metallic waveguide and planar technology.

In the literature review the possibilities to reconfigure these integrated filters has also been studied. There are many possibilities in the bibliography, but the LC features, molecular behaviour, and macroscopic properties have been further investigated, since it is a promising material for reconfiguration of filters, phase shifters and other microwave devices.

The dielectric properties of LC mixtures are not well characterized at microwave frequencies due to their recent use in this frequency band. As a solution to this problem, four different LC samples have been characterized for obtaining their dielectric permittivity and loss tangent. For this purpose, a research about methods of material characterization has been completed in order to select the best one for characterizing this particular material.

It has been concluded that the split-cylinder resonator method is the best candidate. It is based on the measurement of the resonance frequency and the Q-factor of the two states of

the LC molecules. For achieving these two states, no electric or magnetic fields are needed, just the cell is physically turned 90° inside the cavity. The values have been extracted by using two techniques, a modal method and a numerical one. The values of the dielectric anisotropy are presented for the considered samples, together with the values of loss tangent factors. Furthermore, it is observed that the loss tangent decreases and the dielectric anisotropy increases at higher frequencies.

Next, the influence of the dielectric permittivity in the frequency response has been studied, obtaining a promising filtering structure based on alternating dielectric SIW sections. One of the advantages of the proposed topology is that it can be easily analyzed with a full-wave modal technique, thus allowing its fast and accurate CAD design. As it was proved, using the modal method for obtaining an optimized point instead of a commercial software, a drastical reduction of the computational cost is achieved. The new proposed filter topology provides an enhanced Q-factor when compared to a classical SIW technology (due to the absence of dielectric material in coupling sections), is smaller than the same filter in ESIW, and presents a good out-of-band response. The study of the out-of-band response shows that the width of the rejected band can be controlled by the substrate permittivity, reaching values up to $2f_0$, moreover its depth can be controlled by the filter order. The results are consistent for different frequencies, substrates and filter orders.

Finally, an evolution within the development of reconfigurable devices has been carried out. It has been presented a decoupled topology (DESIW), that has two isolated conductors. This allows for performing a tunable resonator using LC. Two concepts for polarizing the LC molecules into the resonant cavity have been presented for achieving a wider tunability range. A combination of both magnetic and electric biasing fields have been used. The magnetic biasing allows to get the extreme states, whereas the electric biasing achieves the continuous intermediate states. The results are very satisfactory, achieving a tunability range of 8.5% with unloaded quality factor values between 190 and 172 in the best case.

The results obtained in this work validate the followed design procedures and confirm the use of DESIW technology and LC as an excellent alternative to conventional technologies and topologies for implementing reconfigurable filters.

In conclusion, all the main goals initially proposed for this PhD Thesis have been accomplished successfully. As a result, this Thesis work has generated multiple international publications in relevant journals and conferences dedicated to microwave engineering, as it is summarized in Appendix A.

This work lays the foundations of a new research field in the development of reconfigurable high frequency devices. Among the many future research lines related to this work, it should be noted the study of either alternative LC mixtures or other decoupled structures

for their biasing. There is a continuous advance in the development of new LC mixtures with better performance in terms of higher dielectric anisotropy and lower loss tangent.

Concerning the reconfigurable topologies, the design of bandpass filters with dynamically adjustable permittivity by sections is of great interest. Theoretically, it could control the central frequency and the bandwidth independently.

Furthermore, the development of new empty decoupled structures, where the polarization surface is wider without cutting the RF currents, is a promising research area. For instance, a preliminary study has been performed to implement a structure with three layers, where a decoupled metallic layer is introduced in the middle of the device to have a fully polarizable sheet.

Appendix A

List of publications

A.1 International journal publications

- J. R. Sánchez, C. Bachiller, V. Nova, V. E. Boria, “A novel continuously-tunable reconfigurable microwave resonator based on Liquid Crystal materials," *Electronics Letters*, vol. 55, no. 16, pp. 871, August 2019.

- J. R. Sánchez, C. Bachiller, V. Nova, V. E. Boria, “Reconfigurable resonator in decoupled empty SIW technology using liquid crystal material," *Electronics Letters*, vol. 55, no. 16, pp. 907-910, August 2019.

- J. R. Sánchez, V. Nova, C. Bachiller, B. Villacampa, A. de la Rua, R. Kronberger, F. Peñaranda, V. E. Boria, “Characterization of nematic liquid crystal at microwave frequencies using split-cylinder resonator method," *IEEE Transactions on Microwave Theory and Techniques*, vol. 67, no. 7, pp. 2812-2820, June 2019.

- J. R. Sánchez, C. Bachiller, V. Nova, V. E. Boria, “Controlled out-of-band rejection of filters based on SIW with alternating dielectric line sections," *IEEE Microwave and Wireless Components Letters*, vol. 29, no. 4, pp. 258-260, April 2019.

- J. R. Sánchez, C. Bachiller, M. Juliá, V. Nova, H. Esteban, V. E. Boria, “Microwave filter based on substrate integrated waveguide with alternating dielectric line sections," *IEEE Microwave and Wireless Components Letters*, vol. 28, no. 11, pp. 990-992, November 2018.

- J. M. Merello, V. Nova, C. Bachiller, J. R. Sánchez, A. Belenguer, V. E. Boria, “Miniaturization of power divider and 90° hybrid directional coupler for C-Band applications

using empty substrate integrated coaxial lines.," *IEEE Transactions on Microwave Theory and Techniques*, vol. 66, no. 6, pp. 3055-3062, June 2018.

- H. Esteban, A. Belenguer, J. R. Sánchez, C. Bachiller, V. E. Boria, "Improved low reflection transition from microstrip line to empty substrate integrated waveguide," *IEEE Microwave and Wireless Components Letters*, vol. 27, no. 8, pp. 685-687, August 2017.

- J. R. Sánchez, C. Bachiller, H. Esteban, A. Belenguer, V. Nova, V. E. Boria, "New decoupled empty substrate integrated waveguide realisation," *Electronics Letters*, vol. 53, no. 17, pp. 1203-1205, August 2017.

A.2 International conference publications

- J. R. Sánchez, V. Nova, C. Bachiller, B. Villacampa, A. de la Rua, R. Kronberger, F. Peñaranda, V. E. Boria, "Measurement of the dielectric properties of liquid crystal material for microwave applications," in *17th International Conference on Microwave and High Frequency Heating*, September 2019, pp. 43.

- J. R. Sánchez, C. Bachiller, M. Juliá, H. Esteban, V. E. Boria, "Modal method for the efficient analysis and design of microwave filters based on multiple discontinuities," in *2017 19th Mathematical Modelling in Engineering and Human Behaviour Conference*, July 2017, pp. 284-289.

A.3 National journal publications

- C. Bachiller, J. R. Sánchez, V. Nova, J. M. Merello, V. E. Boria, "Development of substrate integrated passive microwave circuits," *WAVES magazine, iTEAM-UPV*, no. 10, pp. 35-45, 2018.

A.4 National conference publications

- J. R. Sánchez, C. Bachiller, V. Nova, V. E. Boria, "Estudio de la capacidad de configuración del ancho de banda de rechazo en filtros basados en secciones dieléctricas alternas," in *2019 24th Simposium Nacional de la Unión Científica Internacional de Radio*, September 2019, pp. 1-4.

- V. Nova, C. Bachiller, J. R. Sánchez, M. L. Marín, V. E. Boria, “Implementation of a 3D printed microwave waveguide using plated PLA," in *2019 24th Simposium Nacional de la Unión Científica Internacional de Radio*, September 2019, pp. 1-4.

- C. Bachiller, J. R. Sánchez, V. Nova, V. E. Boria, “Fabricación e integración de resonador reconfigurable con cristal líquido en tecnología SIW," in *2019 24th Simposium Nacional de la Unión Científica Internacional de Radio*, September 2019, pp. 1-4.

- J. R. Sánchez, C. Bachiller, M. Juliá, V. Nova, H. Esteban, V. E. Boria, “Análisis, diseño e implementación de un nuevo filtro SIW basado en secciones dieléctricas alternas," in *2018 23rd Simposium Nacional de la Unión Científica Internacional de Radio*, September 2018, pp. 1-4.

- J. R. Sánchez, C. Bachiller, V. Nova, V. E. Boria, “Microwave filter on a decoupled empty substrate integrated waveguide," in *2018 23rd Simposium Nacional de la Unión Científica Internacional de Radio*, September 2018, pp. 1-4.

- V. Nova, C. Bachiller, J. R. Sánchez, V. E. Boria, “A novel reconfigurable phase shifter based on substrate integrated coaxial line using liquid crystal," in *2018 23rd Simposium Nacional de la Unión Científica Internacional de Radio*, September 2018, pp. 1-4.

- J. M. Merello, V. Nova, C. Bachiller, J. R. Sánchez, V. E. Boria, “Power divider and 90° hybrid directional coupler in empty substrate integrated coaxial line," in *2018 23rd Simposium Nacional de la Unión Científica Internacional de Radio*, September 2018, pp. 1-4.

A.5 Patents

- C. Bachiller, J. R. Sánchez, V. Nova, M. L. Marín, J. M. Merello, V. E. Boria. “Método de fabricación de dispositivos de microondas basado en guía de onda vacía integrada en sustrato," Patent Number: P201830647, Priority date: 2018-06-28, Publication date: 2019-03-26, Original Assignee: Universitat Politècnica de València.

Bibliography

[1] D. M. Pozar, *Microwave Engineering, 4th ed.* Hoboken, NJ, USA: John Wiley & Sons Inc., 2012.

[2] D. Deslandes and K. Wu, "Integrated microstrip and rectangular waveguide in planar form," *IEEE Microwave and Wireless Components Letters*, vol. 11, no. 2, pp. 68–70, February 2001.

[3] D. Yang and S. Wu, *Fundamentals of Liquid Crystal Devices*. West Sussex, England: John Wiley & Sons, Ltd., 2006.

[4] D. Deslandes and K. Wu, "Integrated transition of coplanar to rectangular waveguides," *2001 IEEE MTT-S International Microwave Symposium Digest*, vol. 2, pp. 619–622, 2001.

[5] A. Belenguer, H. Esteban, and V. E. Boria, "Novel empty substrate integrated waveguide for high performance microwave integrated circuits," *IEEE Transactions on Microwave Theory and Techniques*, vol. 62, no. 4, pp. 832–839, 2014.

[6] A. Petosa, "An overview of tuning techniques for frequency-agile antennas," *IEEE Antennas and Propagation Magazine*, vol. 54, no. 5, pp. 271–296, Oct 2012.

[7] E. Abiri, M. R. Salehi, S. Kohan, and M. Mirzazadeh, "Multi-application PIN diode," in *2010 Second Pacific-Asia Conference on Circuits, Communications and System*, vol. 1, Aug 2010, pp. 60–62.

[8] M. Armendariz, V. Sekar, and K. Entesari, "Tunable SIW bandpass filters with PIN diodes," in *2010 40th European Microwave Conference*, 2010.

[9] S. Sirci, J. D. Martínez, and V. E. Boria, "Low-loss 3-bit tunable SIW filter with PIN diodes and integrated bias network," in *2013 43rd European Microwave Conference*, Oct 2013, pp. 1211–1214.

[10] S. Sirci, J. D. Martínez, M. Taroncher, and V. E. Boria, "Varactor-loaded continuously tunable SIW resonator for reconfigurable filter design," in *2011 41st European Microwave Conference*, Oct 2011, pp. 436–439.

[11] D. E. Senior, X. Cheng, and Y. Yoon, "Electrically tunable evanescent mode half-mode Substrate-Integrated-Waveguide resonators," *IEEE Microwave and Wireless Components Letters*, vol. 22, no. 3, pp. 123–125, March 2012.

[12] Y. Ding and K. Wu, "SIW varactor-tuned phase shifter and phase modulator," in *2012 IEEE MTT-S International Microwave Symposium Digest*, June 2012, pp. 1–3.

[13] V. K. Varadan, K. J. Vinoy, and K. Jose, *RF MEMS and their applications*. West Sussex, England: John Wiley & Sons Ltd., 2003.

[14] E. Fourn, C. Quendo, E. Rius, A. Pothier, P. Blondy, C. Champeaux, J. C. Orlianges, A. Catherinot, G. Tanne, C. Person, and F. Huret, "Bandwidth and central frequency control on tunable bandpass filter by using MEMS cantilevers," in *2003 IEEE MTT-S International Microwave Symposium Digest*, vol. 1, June 2003, pp. 523–526 vol.1.

[15] V. Sekar, M. Armendariz, and K. Entesari, "A 1.2–1.6 GHz substrate integrated waveguide RF MEMS tunable filter," *IEEE Transactions on Microwave Theory and Techniques*, vol. 59, no. 4, pp. 866–876, April 2011.

[16] K. Wang and K. Wu, "Liquid crystal enabled substrate integrated waveguide variable phase shifter for millimeter-wave application at 60 GHz and beyond," in *2015 IEEE MTT-S International Microwave Symposium*, May 2015, pp. 1–4.

[17] S. Strunck, O. H. Karabey, C. Weickhmann, A. Gaebler, and R. Jakoby, "Continuously tunable phase shifters for phased arrays based on liquid crystal technology," in *2013 IEEE International Symposium on Phased Array Systems and Technology*, Oct 2013, pp. 82–88.

[18] A. E. Prasetiadi, O. H. Karabey, C. Weickhmann, T. Franke, W. Hu, M. Jost, M. Nickel, and R. Jakoby, "Continuously tunable Substrate Integrated Waveguide bandpass filter in liquid crystal technology with magnetic biasing," *Electronics Letters*, vol. 51, no. 20, pp. 1584–1585, 2015.

[19] P. Yaghmaee, C. Fumeaux, B. Bates, A. Manabe, O. H. Karabey, and R. Jakoby, "Frequency tunable S-band resonator using nematic liquid crystal," *Electronics Letters*, vol. 48, no. 13, pp. 798–800, June 2012.

[20] K. W. Eccleston, "Mode analysis of the corrugated substrate integrated waveguide," *IEEE Transactions on Microwave Theory and Techniques*, vol. 60, no. 10, pp. 3004–3012, Oct 2012.

[21] P. Kildal, E. Alfonso, A. Valero-Nogueira, and E. Rajo-Iglesias, "Local metamaterial-based waveguides in gaps between parallel metal plates," *IEEE Antennas and Wireless Propagation Letters*, vol. 8, pp. 84–87, 2009.

[22] K. Hirabayashi and T. Kurokawa, "Liquid crystal devices for optical communication and information processing systems," *Liquid Crystals*, vol. 14, no. 2, pp. 307–317, 1993.

[23] C. C. Vela, "Diseño y fabricación de dispositivos basados en cristal líquido polimérico," Ph.D. dissertation, Universidad Politécnica de Madrid, Madrid, 2012.

[24] O. H. Karabey, *Electronic Beam Steering and Polarization Agile Planar Antennas in Liquid Crystal Technology (Springer Theses)*. Springer, 2013.

[25] R. Fletcher, *Practical Methods of Optimization. 2nd Edition*. John Wiley & Sons, 1987.

[26] J. Nelder and R. Mead, "A simple method for function minimitazion," *The Computer Journal*, vol. 7, pp. 308–313, 1965.

[27] M. D. Janezic and J. Baker-Jarvis, "Full-wave analysis of a split-cylinder resonator for nondestructive permittivity measurements," *IEEE Transactions on Microwave Theory and Techniques*, vol. 47, no. 10, pp. 2014–2020, Oct 1999.

[28] S. B. Cohn, "Properties of ridge wave guide," *Proceedings of the IRE*, vol. 35, no. 8, pp. 783–788, Aug 1947.

[29] G. J. Cunningham and P. A. Blenkinsop, "A 29 GHz microstrip end-coupled filter," in *IEEE Colloquium on Electronic Filters*, June 1989, pp. 6/1–6/4.

[30] A. O. Lindo, A. P. Mathews, M. Gopikrishna, N. Osman, R. Leigh, C. Free, and A. Chandroth, "Parallel and end coupled microstrip band pass filters at W-band," in *2009 Asia Pacific Microwave Conference*, Dec 2009, pp. 345–348.

[31] E. G. Cristal and S. Frankel, "Design of hairpin-line and hybrid hairpin-parallel-coupled-line filters," in *1971 IEEE MTT-S International Microwave Symposium Digest*, May 1971, pp. 12–13.

[32] G. L. Matthaei, "Interdigital, band-pass filters," in *PGMTT Natioanl Symposium Digest*, vol. 62, no. 1, May 1962, pp. 41–45.

[33] C. K. C. Tzuang and W.-T. Lo, "ı," in *1990 IEEE MTT-S International Microwave Symposium Digest*, vol. 1, May 1990, pp. 131–134.

[34] M. Gat, "Commensurate-line, microstrip, band-pass filters," in *1988 IEEE MTT-S International Microwave Symposium Digest*, May 1988, pp. 423–426 vol.1.

[35] K. Wu, "Integration and interconnect techniques of planar and non-planar structures for microwave and millimeter-wave circuits - current status and future trend," in *APMC 2001. 2001 Asia-Pacific Microwave Conference (Cat. No.01TH8577)*, vol. 2, Dec 2001, pp. 411–416 vol.2.

[36] A. Belenguer, A. L. Borja, H. Esteban, and V. E. Boria, "High-performance coplanar waveguide to empty substrate integrated coaxial line transition," *IEEE Transactions on Microwave Theory and Techniques*, vol. 63, no. 12, pp. 4027–4034, Dec 2015.

[37] S. Adhikari, Y. Ban, and K. Wu, "Magnetically tunable ferrite loaded substrate integrated waveguide cavity resonator," *IEEE Microwave and Wireless Components Letters*, vol. 21, no. 3, pp. 139–141, March 2011.

[38] I. Hunter, *Theory and Design of Microwave Filters*. England: The Institution of Electrical Engineers, 2001.

[39] A. Tasic, W. Serdijn, and G. Setti, *Circuits and Systems for Future Generations of Wireless Communications*. Springer Netherlands, 2009.

[40] K. Rawat, M. S. Hashmi, and F. M. Ghannouchi, "Dual-band RF circuits and components for multi-standard software defined radios," *IEEE Circuits and Systems Magazine*, vol. 12, no. 1, pp. 12–32, Firstquarter 2012.

[41] D. Budimir, *Generalized Filter Design by Computer Optimization*. Norwood, MA, USA: Artech House, Inc., 1998.

[42] E. Diaz, J. V. Morro, H. Esteban, V. E. Boria, C. Bachiller, and A. Belenguer, *Simulation-Driven Design Optimization and Modeling for Microwave Engineering*. Singapore: Imperial College Press, 2013, ch. Simulation-Driven Design of Microwave Filters for Space Applications.

[43] J. Uher and J. Bornemann, *Waveguide Components for Antenna Feed Systems: Theory and CAD*. Artech Print on Demand, December, 1993.

[44] R. Levy, "Theory of direct-coupled-cavity filters," *IEEE Transactions on Microwave Theory and Techniques*, vol. 15, no. 6, pp. 340–348, June 1967.

[45] R. M. Barrio-Garrido, S. Llorente-Romano, A. Garcia-Lamperez, and M. Salazar-Palma, "Design of broadband directly coupled non-centred resonant irises filters," in *2003 33rd European Microwave Conference Proceedings*, vol. 1, Oct 2003, pp. 219–222 Vol.1.

[46] C. Bachiller, H. Esteban, F. Díaz, J. V. Morro, and V. E. Boria, "Radio-frequency performance comparison of several H-plane rectangular waveguide filters loaded with circular dielectric posts," *IET Microwaves, Antennas Propagation*, vol. 10, no. 5, pp. 536–545, 2016.

[47] V.E.Boria, D.Camilleri, A.Coves, H.Esteban, B.Gimeno, M.Guglielmi, and L.Polini, "Contributions to the analysis and design of all-inductive filters with dielectric resonators," *2003 33rd European Microwave Conference Proceedings*, 2003.

[48] M. Capurso, M. Piloni, and M. Guglielmi, "Resonant aperture filters: Improved out-of-band rejection and size reduction," in *2001 31st European Microwave Conference*, Sept 2001, pp. 1–4.

[49] G. F. Craven and C. K. Mok, "The design of evanescent mode waveguide bandpass filters for a prescribed insertion loss characteristic," *IEEE Transactions on Microwave Theory and Techniques*, vol. 19, no. 3, pp. 295–308, Mar 1971.

[50] C. Bachiller, "Métodos híbridos para el análisis y diseño eficiente de filtros avanzados para sistemas de comunicaciones espaciales," Ph.D. dissertation, Universidad Politécnica de Valencia, Valencia, 2010.

[51] E. Rajo-Iglesias and P. . Kildal, "Numerical studies of bandwidth of parallel-plate cut-off realised by a bed of nails, corrugations and mushroom-type electromagnetic bandgap for use in gap waveguides," *IET Microwaves, Antennas Propagation*, vol. 5, no. 3, pp. 282–289, Feb 2011.

[52] J. S. Hong and M. J. Lancaster, *Microstrip filters for RF/Microwave Applications*. Hoboken, NJ, USA: John Wiley & Sons Inc., 2001.

[53] G. Matthaei, E. Jones, and L. Young, *Microwave Filters Impedance-Matching Networks, and Coupling Structures*. Artech House Publishers, February, 1980.

[54] D. N. Kedia and G. B. Morgan, "The design of integrated circuit microstrip hairpin-line band pass filters for short millimetre waves," in *IEE Colloquium on Microwave Filters and Multiplexers*, Nov 1990, pp. 10/1–10/5.

[55] D. Deslandes, "Design equations for tapered microstrip-to-substrate integrated waveguide transitions," in *2010 IEEE MTT-S International Microwave Symposium*, May 2010, pp. 704–707.

[56] D. Deslandes and K. Wu, "Accurate modeling, wave mechanisms, and design considerations of a substrate integrated waveguide," *IEEE Transactions on Microwave Theory and Techniques*, vol. 54, no. 6, pp. 2516–2526, June 2006.

[57] X. Chen and K. Wu, "Substrate integrated waveguide filter: Basic design rules and fundamental structure features," *IEEE Microwave Magazine*, vol. 15, no. 5, pp. 108–116, July 2014.

[58] J. B. R. Hajri, S. Ghnimi, and N. Sboui, "Design of SIW iris-coupled-cavity band-pass filter circuit using wave concept iterative process method," in *2016 7th International Conference on Sciences of Electronics, Technologies of Information and Telecommunications (SETIT)*, Dec 2016, pp. 209–212.

[59] B. Potelon, J. Bohorquez, J. Favennec, C. Quendo, E. Rius, and C. Person, "Design of Ku-band filter based on substrate-integrated circular cavities (SICCs)," in *2006 IEEE MTT-S International Microwave Symposium Digest*, June 2006, pp. 1237–1240.

[60] W. Bo, Z. Xu, L. Hao, X. Meijuan, and J. Liao, "Substrate integrated waveguide cross-coupling filter with multilayer hexagonal cavity," in *2013 International Workshop on Microwave and Millimeter Wave Circuits and System Technology*, Oct 2013, pp. 221–224.

[61] S. Qiu, F. Xu, and J. Pu, "A compact bandpass filter with SIW triangular cavities," in *2015 Asia-Pacific Microwave Conference (APMC)*, vol. 3, Dec 2015, pp. 1–3.

[62] L. Wu, X. Zhou, and W. Yin, "Evanescent-mode bandpass filters using folded and ridge substrate integrated waveguides (SIWs)," *IEEE Microwave and Wireless Components Letters*, vol. 19, no. 3, pp. 161–163, March 2009.

[63] S. Adhikari, A. Ghiotto, S. Hemour, and K. Wu, "Tunable non-reciprocal ferrite loaded SIW phase shifter," in *2013 IEEE MTT-S International Microwave Symposium Digest*, June 2013, pp. 1–3.

[64] Y. J. Cheng, Q. D. Huang, Y. R. Wang, and J. L. Li, "Narrowband substrate integrated waveguide isolators," *IEEE Microwave and Wireless Components Letters*, vol. 24, no. 10, pp. 698–700, Oct 2014.

[65] M. Almalkawi, L. Zhu, and V. Devabhaktuni, "Magnetically tunable substrate integrated waveguide bandpass filters employing ferrites," in *2011 International Conference on Infrared, Millimeter, and Terahertz Waves*, Oct 2011, pp. 1–2.

[66] A. Ghiotto, S. Adhikari, and K. Wu, "Ferrite-loaded substrate integrated waveguide switch," *IEEE Microwave and Wireless Components Letters*, vol. 22, no. 3, pp. 120–122, March 2012.

[67] Q. D. Huang and Y. J. Cheng, "Ferrite-loaded substrate integrated waveguide frequency-agile bandpass filter," in *2015 IEEE MTT-S International Microwave Workshop Series on Advanced Materials and Processes for RF and THz Applications (IMWS-AMP)*, July 2015, pp. 1–3.

[68] S. Adhikari, A. Ghiotto, and K. Wu, "Simultaneous electric and magnetic two-dimensional tuning of substrate integrated waveguide cavity resonator," in *2012 IEEE MTT-S International Microwave Symposium Digest*, June 2012, pp. 1–3.

[69] ——, "Simultaneous electric and magnetic two-dimensionally tuned parameter-agile SIW devices," *IEEE Transactions on Microwave Theory and Techniques*, vol. 61, no. 1, pp. 423–435, Jan 2013.

[70] C. V. Brown, *Handbook of Visual Display Technology*. Springer, Berlin, Heidelberg, 2012, ch. Physical Properties of Nematic Liquid Crystals.

[71] R. G. Priest, "Theory of the frank elastic constants of nematic liquid crystals," *Phys. Rev. A*, vol. 7, pp. 720–729, Feb 1973.

[72] L. F. Chen, C. K. Ong, C. P. Neo, V. V. Varadan, and V. K. Varadan, *Microwave Electronics: Measurement and Materials Characterization*. West Sussex, England: John Wiley & Sons, Ltd., 2004.

[73] R. James, F. A. Fernandez, S. E. Day, S. Bulja, and D. Mirshekar-Syahkal, "Accurate modeling for wideband characterization of nematic liquid crystals for microwave applications," *IEEE Transactions on Microwave Theory and Techniques*, vol. 57, no. 12, pp. 3293–3297, Dec 2009.

[74] S. Mueller, A. Penirschke, C. Damm, P. Scheele, M. Wittek, C. Weil, and R. Jakoby, "Broad-band microwave characterization of liquid crystals using a temperature-controlled coaxial transmission line," *IEEE Transactions on Microwave Theory and Techniques*, vol. 53, no. 6, pp. 1937–1945, June 2005.

[75] S. Bulja, D. Mirshekar-Syahkal, R. James, S. E. Day, and F. A. Fernandez, "Measurement of dielectric properties of nematic liquid crystals at millimeter wavelength," *IEEE Transactions on Microwave Theory and Techniques*, vol. 58, no. 12, pp. 3493–3501, Dec 2010.

[76] A. Penirschke, S. Muller, P. Scheele, C. Weil, M. Wittek, C. Hock, and R. Jakoby, "Cavity perturbation method for characterization of liquid crystals up to 35 GHz," in *2004 34th European Microwave Conference*, vol. 2, Oct 2004, pp. 545–548.

[77] R. Kowerdziej, J. Krupka, E. Nowinowski-Kruszelnicki, M. Olifierczuk, and J. Parka, "Microwave complex permittivity of voltage-tunable nematic liquid crystals measured in high resistivity silicon transducers," *Applied Physics Letters*, vol. 102, no. 10, p. 102904, 2013. [Online]. Available: https://doi.org/10.1063/1.4795534

[78] R. Kowerdziej, J. Parka, J. Krupka, M. Olifierczuk, E. Nowinowski-Kruszelnicki, L. Jaroszewicz, and O. Chojnowska, "Dielectric properties of highly anisotropic nematic liquid crystals for tunable microwave components," *Applied Physics Letters*, vol. 103, no. 17, p. 172902, 2013. [Online]. Available: https://doi.org/10.1063/1.4826504

[79] M. Yazdanpanahi, S. Bulja, D. Mirshekar-Syahkal, R. James, S. E. Day, and F. A. Fernandez, "Measurement of dielectric constants of nematic liquid crystals at mm-wave frequencies using patch resonator," *IEEE Transactions on Instruments and Measurements*, vol. 59, no. 12, pp. 3079–3085, Dec 2010.

[80] L. Silvestri, E. Massoni, C. Tomassoni, A. Coves, M. Bozzi, and L. Perregrini, "Substrate Integrated Waveguide filters based on a dielectric layer with periodic perforations," *IEEE Transactions on Microwave Theory and Techniques*, vol. 65, no. 8, pp. 2687–2697, Aug 2017.

[81] N. Marcuvitz, *Waveguide Handbook*. New York, NY, USA: McGraw Hill Book Company, Inc., 1951.

[82] H. H. Rosenbrock, "An automatic method for finding the greatest or least value of a function," *The Computer Journal*, vol. 3, no. 3, pp. 175–184, 1960.

[83] W. T. V. W. H. Press, S. A. Teukolsky and B. P. Flannery, *Numerical Recipes 3rd Edition: The Art of Scientific Computing*. Cambridge University Press., September 2007.

[84] E. Diaz, A. Belenguer, H. Esteban, O. Monerris, and V. Boria, "A novel transition from microstrip to a substrate integrated waveguide with higher characteristic impedance," in *2013 IEEE MTT-S International Microwave Symposium Digest*, June 2013, pp. 1–4.

[85] A. Coves, G. Torregrosa, G. Vicent, E. Bronchalo, A. A. S. Blas, and M. Bozzi, "Modeling of perforated SIW structures and their application to the design of step-impedance microwave filters," in *2017 IEEE MTT-S International Conference on Numerical Electromagnetic and Multiphysics Modeling and Optimization for RF, Microwave, and Terahertz Applications (NEMO)*, May 2017, pp. 293–295.

[86] G. Kent, "Nondestructive permittivity measurement of substrates," *IEEE Transactions on Instrumentation and Measurement*, vol. 45, no. 1, pp. 102–106, Feb 1996.

[87] M. T. Ali, M. Farid, A. Khalid, and N. Amirudin, "Dielectric sheet perturbation to metallic air-filled cavity - technique of microwave non-destructive testing (MNDT)," in *2006 International RF and Microwave Conference*, Sept 2006, pp. 434–438.

[88] D. Marques-Villarroya, F. L. Penaranda-Foix, B. Garcia-Banos, J. M. Catalá-Civera, and J. D. Gutiérrez-Cano, "Enhanced full-wave circuit analysis for modeling of a split cylinder resonator," *IEEE Transactions on Microwave Theory and Techniques*, vol. 65, no. 4, pp. 1191–1202, April 2017.

[89] F. L. Penaranda-Foix and J. M. Catala-Civera, *Passive Microwave Components and Antennas*. IN-TECH, April 2010, ch. Circuital analysis of cylindrical structures applied to the electromagnetic resolution of resonant cavities.

[90] F. L. Penaranda-Foix, M. D. Janezic, J. M. Catala-Civera, and A. J. Canos, "Full-wave analysis of dielectric-loaded cylindrical waveguides and cavities using a new four-port ring network," *IEEE Transactions on Microwave Theory and Techniques*, vol. 60, no. 9, pp. 2730–2740, Sept 2012.

[91] F. L. Penaranda-Foix, J. M. Catala-Civera, A. J. Canos-Marin, and B. Garcia-Banos, "Circuital analysis of a coaxial re-entrant cavity for performing dielectric measurement," in *2009 IEEE MTT-S International Microwave Symposium Digest*, June 2009, pp. 1309–1312.

[92] J. Krupka, "Frequency domain complex permittivity measurements at microwave frequencies," *Measurement Science and Technology*, vol. 17, no. 6, pp. 55–70, April 2006.

[93] M. D. Janezic, "Nondestructive relative permittivity and loss tangent measurements using a split-cylinder resonator," Ph.D. dissertation, University of Colorado at Boulder, 2003.

[94] S. Zinal and U. Arz, "An extended mode-matching model for improved relative permittivity measurements using a split-cylinder resonator," *Advances in Radio Science*, vol. 12, pp. 267–272, 11 2014.

[95] M. D. Janezic, U. Arz, S. Begley, and P. Bartley, "Improved permittivity measurement of dielectric substrates by use of the TE111 mode of a split-cylinder cavity," in *2009 73rd ARFTG Microwave Measurement Conference*, June 2009, pp. 1–3.

[96] U. Arz, J. Leinhos, and M. D. Janezic, "Broadband dielectric material characterization: A comparison of on-wafer and split-cylinder resonator measurements," in *2008 38th European Microwave Conference*, Oct 2008, pp. 913–916.

[97] M. D. Janezic, E. F. Kuester, and J. B. Jarvis, "Broadband complex permittivity measurements of dielectric substrates using a split-cylinder resonator," in *2004 IEEE MTT-S International Microwave Symposium Digest*, vol. 3, June 2004, pp. 1817–1820 Vol.3.

[98] D. C. Zografopoulos, A. Ferraro, and R. Beccherelli, "Liquid-crystal high-frequency microwave technology: Materials and characterization," *Advanced Materials Technologies*, vol. 4, no. 2, p. 1800447, 2019. [Online]. Available: https://onlinelibrary.wiley.com/doi/abs/10.1002/admt.201800447

[99] J. R. Baker-Jarvis, M. D. Janezic, B. F. Riddle, R. T. Johnk, C. L. Holloway, R. G. Geyer, and C. A. Grosvenor, *Measuring the Permittivity and Permeability of Lossy Materials: Solids, Liquids, Metals, and negative-Index Materials*. Boulder, CO, USA: National Institute of Standards and Technology, 2005.

[100] J. P. Dunsmore, *Handbook of Microwave Component Measurements: with Advanced VNA Techniques*. England: John Wiley & Sons, Ltd, 2012.

[101] J. Taylor, *An Introduction to Error Analysis*. Sausalto, CA, USA: University Science Books, 1997.

[102] D. G. Chen and K. W. Eccleston, "Substrate integrated waveguide with corrugated wall," in *2008 Asia-Pacific Microwave Conference*, Dec 2008, pp. 1–4.

[103] M. Abdolhamidi, A. Enayati, M. Shahabadi, and R. Faraji-Dana, "Wideband single-layer DC-decoupled substrate integrated waveguide (SIW) - to - microstrip transition using an interdigital configuration," in *2007 Asia-Pacific Microwave Conference*, Dec 2007, pp. 1–4.

[104] N. Esparza, P. Alcon, L. F. Herran, and F. Las-Heras, "Design of substrate integrated waveguides structures based on stop-band response FSSs (SBFSS-SIW)," in *2016 46th European Microwave Conference*, Oct 2016, pp. 9–12.

[105] N. Esparza, P. Alcón, L. F. Herrán, and F. Las-Heras, "Substrate integrated waveguides structures using frequency selective surfaces operating in stop-band (SBFSS-SIW)," *IEEE Microwave and Wireless Components Letters*, vol. 26, no. 2, pp. 113–115, Feb 2016.

[106] B. A. Munk, *Frequency Selective Surfaces. Theory and Design*. New York, N. Y.: John Wiley and Sons, Inc., 2000.

[107] F. Parment, A. Ghiotto, T. Vuong, J. Duchamp, and K. Wu, "Broadband transition from dielectric-filled to air-filled substrate integrated waveguide for low loss and high power handling millimeter-wave substrate integrated circuits," in *2014 IEEE MTT-S International Microwave Symposium (IMS2014)*, June 2014, pp. 1–3.

[108] H. Peng, X. Xia, J. Dong, and T. Yang, "An improved broadband transition between microstrip and empty substrate integrated waveguide," *Microwave and Optical Technology Letters*, vol. 58, no. 9, pp. 2227–2231, 2016.

[109] *SMA End Launch Connector*, Southwest Microwave, Inc., Tempe, Arizona, January 2012. [Online]. Available: http://mpd.southwestmicrowave.com/products/product.php?need=endLaunch&item=3

[110] T. Franke, A. Gaebler, A. E. Prasetiadi, and R. Jakoby, "Tunable Ka-band waveguide resonators and a small band band-pass filter based on liquid crystals," in *2014 44th European Microwave Conference*, Oct 2014, pp. 339–342.